Analysis and Design of Link Slabs in Jointless Bridges with Fibre-Reinforced Concrete

by

Yu Hong

A thesis

presented to the University of Waterloo

in fulfilment of the

thesis requirement for the degree of

Master of Applied Science

in

Civil Engineering

Waterloo, Ontario, Canada, 2014

Author's Declaration

I hereby declare that I am the sole author of this thesis. This is a true copy of the thesis, including any required final revisions, as accepted by my examiners.

I understand that my thesis may be made electronically available to the public.

Yu Hong

Abstract

Many transportation agencies in Canada and the United States have explored alternatives to expansion joints in bridges due to high maintenance costs and poor joint durability. One of the alternatives is the use of link slab in a jointless bridge, which connects the adjacent bridge deck slabs at the pier, forming a continuous slab across the bridge spans. While the link slab system can provide the benefits of a continuous bridge deck, refinement of the design and detailing of the link slab itself is needed to optimize this bridge deck system and ensure long-term performance. Materials with high tensile strain capacity, such as fibre reinforced concrete (FRC), can be used for application in the link slab to improve the strength, durability and cracking characteristics of the link slab.

In this study, four steps are used to address the research objectives. The first step of this research is to establish a computational model of an existing bridge (Camlachie Road Underpass). It is found that the model and modelling approach in SAP2000 closely predicted the field test results obtained by the Ministry of Transportation of Ontario (MTO). Additionally, it is established that the horizontal stiffness of the elastomeric bearings is very low and therefore the supports are representative of roller supports. Therefore, axial forces are not generated when there are no horizontal restraints in the supports.

The second step is to examine the properties of FRC from experimental tests. Four-point bending tests are used to estimate the ultimate and service stresses of FRC using procedures from the *fib* Model Code (2010). It is found that the results from the *fib* Model Code are in agreement with the experimental beam tests by Cameron. Therefore, it is concluded that the *fib* Model

Code procedures are valid for calculating the ultimate and service stresses in FRC, and are used in the computational and analytical models.

The third step is to conduct a parametric study to provide a better understanding of link slab bridge behaviour to assess the impact of design decisions on the bridge response. It is found that the use of hooked steel fibres minimized the crack width of the link slab, and a debonded length a 5% to 7.5% is found to be optimal based on cost and serviceability. Moreover, it is found that fibres are more effective when less steel reinforcements are used in the link slab. Lastly, a parametric study is conducted on the computational model using non-linear analysis by including FRC in the computational model in the form of plastic hinges. It is concluded that the computational model has shown signs of cracking at the pier supports, which is consistent with the site observations during the MTO field test for the Camlachie Road Underpass.

The final step is developing an analytical model (i.e., design guideline) on the analysis and design of link slab bridges with FRC. It is found that the proposed analytical model is able to closely represent the link slab bridge behaviour with very small difference (2-3%), whereas the current method of analysis using Caner and Zia's approach shows a larger prediction error (16%). For the link slab design with FRC, it is found that fibres in reinforced concrete helped increase the bending moment capacity of the link slab by more than 10% compared to normal reinforced concrete (without fibres). The use of polypropylene fibres and hooked steel fibres in the link slab reduces the required steel reinforcement by 3.5% and 21%, respectively, and the crack width of the link slab reduces by more than 3 times with the addition of fibres.

Acknowledgements

I would like to express my sincerest gratitude to my supervisors Dr. Jeffrey S. West, from the Civil and Environmental Engineering Department at the University of Waterloo, for his advice, enthusiasm and patience throughout the writing of this thesis. I enjoyed my time working with Dr. West and I have learned many valuable lessons during my stay at Waterloo. I would like to share my sincerest gratitude for his guidance throughout my MASc program.

I would also like to thank Dr. Carolyn M. Hansson and Dr. Ralph C. G. Haas for their recommendations and aid in the writing of this thesis. The completion of my thesis and degree would not have been possible without their support. I would like to thank Mr. James F. Cameron for his hard work and contributions for his experimental studies on fibre-reinforced concrete. Mr. Cameron's experimental results contributed largely in the completion of this thesis.

I would like to thank the Ministry of Transportation of Ontario for their funding of the project. I would like to express my gratitude towards Mr. David Reed, Mrs. Hannah Schell, Mr. Clifford Lam, Mr. David Lai and Mr. Alexander Au from the Ministry of Transportation of Ontario for their input and aid in the research. I would also like to thank the Ministry of Training, Colleges and Universities of Ontario for the Ontario Graduate Scholarship Program funding of my studies at the University of Waterloo.

Finally, I would like to extend my sincere gratitude to my family and friends. My place today would not have been possible without my mom and dad. I would also like to express my gratefulness towards my wife Judy for supporting me throughout my years at the University of Waterloo.

Table of Contents

List of Figures

List of Tables

Chapter 1 Background and Literature Review

1.1 Background

1.1.1 Jointless Bridge Technology

Many transportation agencies in Canada and the United States have explored alternatives to using expansion joints in bridges because of the high maintenance costs and poor durability of expansion joints [1] [2]. Debris from the bridge deck accumulates at the joints, which restrains the movement of the joint and causes damage to the joints [3]. Conventional bridges are designed with simply-supported structures between the piers and abutments with expansion joints between the adjacent spans. Expansion joints are used to provide a smooth passage and prevent contamination (such as water and de-icing salts) from reaching the underside of the bridge girder, while accommodating bridge deck movement to relieve the accumulation of stresses due to thermal changes and concrete shrinkage. Although the size of the expansion joint is miniscule compared to the bridge structure, it serves an important purpose in preserving the integrity of the bridge structure. As the joint deteriorates, it may threaten the durability of the structure by enabling corrosion damage, cracking in the slabs and substructure, as well as corrosion in the steel girders. Due to the severity of the problems and associated costs, transportation agencies face the challenge of maintaining bridge joints [1]. Figure 1-1 demonstrates two examples of bridge deterioration due to contamination leakage demonstrated by the United States Department of Transportation (USDOT) and Ministry of Transportation Ontario (MTO).

(a) (b)

Figure 1-1 – Superstructure deterioration from (a) USDOT [4] and (b) MTO [5]

In response to the problems associated with poor-performing expansion joints, transportation agencies are now exploring the design of jointless decks as an alternative to the expansion joints. Some researchers have concluded that the repairs of jointless decks are more economical than the repair of expansion joints [1] [6] [7]. Thus, transportation agencies are advocating the use of jointless bridges. One form of a jointless bridge is the link slab bridge. The concept of the link slab bridge is to provide a continuous deck across the bridge, while the girders remain simply-supported between the abutments and piers, as shown in Figure 1-2.

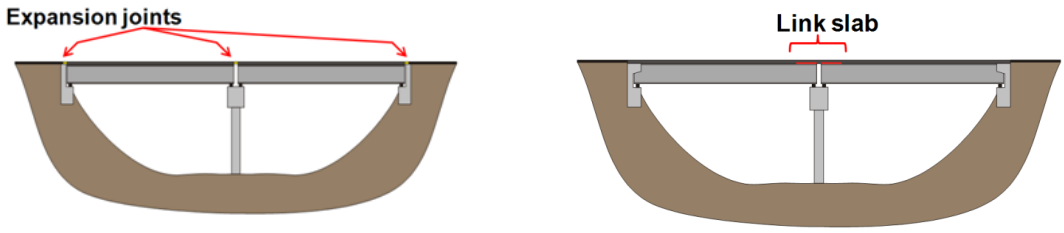

(a) (b)

Figure 1-2 – Conventional expansion joint bridge (a) and link slab bridge (b) (Courtesy of Dr. J. S. West from The University of Waterloo)

The continuous slab that links adjacent bridge spans is called the link slab. The link slab typically requires more reinforcement than the bridge deck to accommodate the large rotations and forces at the pier [1]. A typical link slab configuration is shown in Figure 1-3.

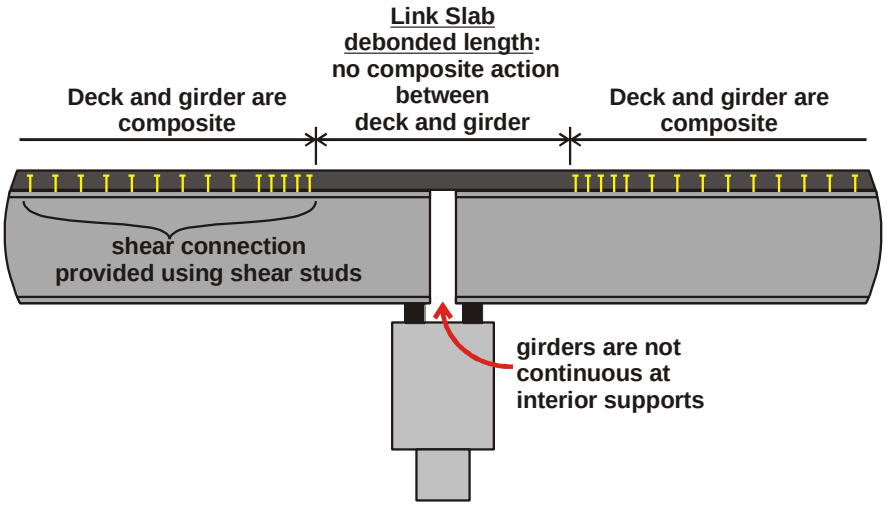

Figure 1-3 – Link slab configuration at the bridge pier (Courtesy of Dr. J. S. West from The University of Waterloo)

Since the link slab is continuous over the pier, it closes the gap between the adjacent spans and prevents contamination from reaching the girders and substructure. The link slab system can be implemented in both existing bridges or used in new bridge designs. In Canada, some bridges that were originally constructed with expansion joints had been retrofitted into link slab bridges by the Ontario Ministry of Transportation (MTO) [8]. Figure 1-4 shows the Camlachie Road Underpass that was retrofitted into a link slab bridge from the conventional expansion joint bridge [8].

While the link slab system can provide the benefits of a continuous bridge deck, refinement of the design and detailing of the link slab itself are needed to optimize this type of bridge deck system and ensure long-term performance. An additional method of improving the design of

link slabs is the use of fibre-reinforced concrete (FRC). FRC can be used to improve the strength, durability and cracking characteristics of the link slab, which inhibits contamination leakage and ensuring the structural integrity of the bridge [2].

(a) (b)

Figure 1-4 – Link slab bridge (a) elevation view and (b) continuous link slab at the bridge pier [8]

1.1.2 Current State of Jointless Bridge Technology

The design methods of a link slab bridge were first established by Caner and Zia [1]. Caner and Zia provided a detailed design guideline using concrete mechanics and verified their theory with experiments on scaled link slab bridges in the laboratory. Design recommendations were established for the link slab bridge based on existing methods of concrete design and the findings from their research. Later, Ulku et al. [6] and Okeil and El-Safty [3] used principles of structural analysis to explain the structural behaviour of the link slab bridge and improved on some of the design aspects that were not covered by Caner and Zia. In recent research, Lepech and Li [9] have researched the use of engineered cementitious composite containing fibres in link slabs as a

method of mitigating the poor tensile and cracking characteristics of conventional reinforced concrete.

A review of the published literature shows that there are numerous contributions in the design of link slab bridges, however the use of FRC in link slabs has not been widely explored [6] [7]. The remainder of this chapter presents a detailed literature review on link slab bridges and related topics. This literature review is used to develop the research objectives described in Chapter 2.

1.2 Literature Review

This literature review contains an overview of topics relevant to the link slab bridges and FRC, including:

- analyses and experiments of link slab bridges;
- tensile behaviour of FRC;
- tension stiffening behaviour of FRC; and
- compressive behaviour of FRC.

The literature review on the analyses and experiments of link slab bridges covers the state-of-the-art research on link slab bridges, using structural analyses principles and scaled bridge experiments to determine the behaviour of the link slab bridges. The literature review on tensile behaviour, tension stiffening behaviour and compressive behaviour of FRC examines the various changes in concrete property as fibres are added to concrete.

1.2.1 Analyses and Experiments of Link Slab Bridges

1.2.1.1 Caner and Zia

Caner and Zia [1] were one of the first research groups to establish methods for designing the link slab. The steps in their research were:

- Laboratory experiment on scaled models of a link slab bridges were conducted and the force effects, deflection and rotations of the link slab bridge were examined.
- Computational models were developed (i.e., structural analysis program) to predict the force effects, deflection and rotation of the link slab bridge.
- Equations were derived for the link slab bridge force effects and results were compared to the computational model and experimental results.

The laboratory experiments carried out by Caner and Zia were point load tests on laboratory samples of two-span link slab bridges with various support configurations. The supports were modelled at the piers and abutments, which were either hinges that restrained vertical and lateral movements (denoted as "H") or rollers that restrained only vertical movements (denoted as "R"). The three support conditions selected in the research were RHHR, RHRH and HRRH. The measured results were bridge mid-span deflection, support reactions, reinforcing bar stresses and the link slab crack widths.

Computational models were developed using a computer software called "Jointless Bridge Deck Link" [1], which predicted the behaviour of the link slab bridge models used in the experiments. Caner and Zia concluded that the experimental and computational results were close in comparison. Thus, equations for reinforced concrete analysis were valid for the analysis of the

link slab bridge. It was also concluded that the link slab behaviour was independent of the support condition [1]. Thus, a simple beam analysis was assumed to be valid. However, the axial forces (tension) in the link slab were neglected in the analysis.

The analytical model (i.e., equations) developed by Caner and Zia were based on existing analytical methods for bridges from The American Association of State Highway and Transportation Officials (AASHTO) Specification [10] and PCI Design Handbook [11]. From Caner and Zia, the bending moment of the link slab is found by determining the end girder rotation of the bridge using Equation 1-1,

$$M_a = 2 \cdot E_c \cdot I_d \cdot \theta / L \qquad 1\text{-}1$$

where M_a is the maximum bending moment in the link slab, E_c is the concrete Modulus of Elasticity, I_d is the link slab moment of inertia, and L is the length of the link slab.

1.2.1.2 Okeil and El-Safty

Following the work of Caner and Zia, Okeil and El-Safty [3] identified that simple beam analysis was invalid for the analysis of link slab due to the discontinuity of girder and link slab at the bridge pier. Okeil and El-Safty suggested the possibility of tension in the link slab due to the hinged support at the pier. The support conditions examined by Okeil and El-Safty were RHHR and HRRH, and the loading was focused on live loads (i.e., truck loads). A systematic analytical model was developed for both RHHR and HRRH models based on a force-displacement compatibility analysis of the structure, as shown in Figure 1-5.

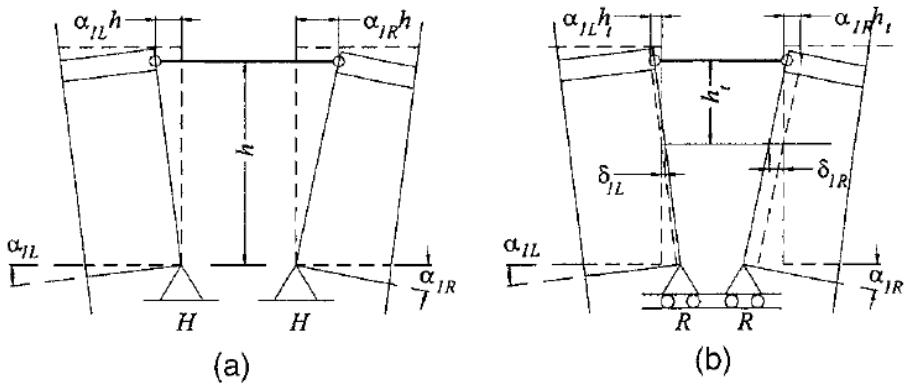

Figure 1-5– Force method for RHHR and HRRH link slab bridge [3]

The analytical model was established by Okeil and El-Safty using the force method. The RHHR and HRRH analytical models are presented in Equations 1-2 and 1-3, respectively,

$$M_0 \cdot \frac{L_L}{E_g \cdot I_{gL}} + 2M_1 \left[\frac{L_L}{E_g \cdot I_{gL}} + \frac{L_R}{E_g \cdot I_{gR}} + 3 \frac{L_{link}}{h^2 \cdot E_s \cdot A_s} \right] + M_2 \cdot \frac{L_R}{E_g \cdot I_{gR}} = -6 \left[\frac{r_{1L}}{E_g \cdot I_{gL}} + \frac{r_{1R}}{E_g \cdot I_{gR}} \right] \quad 1\text{-}2$$

$$\frac{M_0 \cdot L_L}{E_g \cdot I_{gL}} + \left[\frac{2 \cdot M_1 \cdot L_L}{E_g \cdot I_{gL}} + \frac{2 \cdot M_1 \cdot L_R}{E_g \cdot I_{gR}} + \frac{18 \cdot M_1}{h_t^2} \left(\frac{L_L}{E_g \cdot A_{gL}} + \frac{L_R}{E_g \cdot A_{gR}} + \frac{L_{link}}{E_s \cdot A_s} \right) \right] + \frac{M_2 \cdot L_R}{E_g \cdot I_{gR}} = -6 \left[\frac{r_{1L}}{E_g \cdot I_{gL}} + \frac{r_{1R}}{E_g \cdot I_{gR}} \right] \quad 1\text{-}3$$

where M is the bending moment in the link slab (subscripts 0, 1 and 2 are for bending moment at the left abutment, in the mid-span and at the right abutment, respectively), L is the length of the bridge span (subscripts L and R are for the left-span and right-span, respectively), L_{Link} is the length of the link slab, E is the Elastic Modulus of the bridge girder (subscript g and s are for the gross bridge cross-section and the steel reinforcement in the link slab, respectively), I is the moment of inertia, A is the area of the section, h is the distance from the girder bottom to the

neutral axis of the link slab, and h_t is the distance from the neutral axis of the bridge span to the neutral axis of the link slab.

The RHHR model was assumed to be restrained laterally at the pier. Thus, the rotation of the girder caused elongation in the link slab, and therefore tension forces were developed in the link slab. Moreover, the hinged support was eccentric to the centroid of the link slab. Thus, bending moment was generated in the link slab due to the tension force and the eccentricity between the hinged support and the centroid of the link slab. The HRRH model was restrained laterally at the abutment and the pier was allowed to freely translate. Therefore, the eccentricity was found to be between the link slab and the centroid of the adjacent bridge span (rather than the support).

Okeil and El-Safty verified the model using the bridge dimensions in the studies by Caner and Zia. It was found that the HRRH model had good agreement with the results from Caner and Zia, but the RHHR model did not. In conclusion, Okeil and El-Safty found that the support conditions had a large effect on the force effect in the link slab than originally anticipated by Caner and Zia.

1.2.1.3 Ulku et. al.

Ulku et al. [6] expanded on the works of Caner and Zia [1] and Okeil and El-Safty [3] by investigating the effects of link slab with strain loads (i.e., temperature) and modelling of elastomeric bearings spring supports. The steps from Ulku et al.'s research were:

- Computational models in ABAQUS (a finite element analysis software) were developed for the link slab bridges with HRRR, RHHR and RRHR support conditions;

- In addition to the models with hinges and rollers, models with spring supports were also constructed in ABAQUS to represent link slab bridge with effects of elastomeric bearing supports.
- Force effects in the link slab were compared between the various support conditions from steps 1 and 2.

The elastomeric bearing supports from the models were based on guidelines from the Michigan Department of Transportation (MDOT) [12] [13]. From the computational models, it was found that axial forces were negligible for the HRRR and RRHR models, even with spring supports. It was found that the RHHR model had large axial forces in the link slab, but the bending moment was less than the HRRR and RRHR models. It was concluded that thermal load produced force effects that were the same magnitude as the truck (live) load.

Ulku et al. proposed to design the link slab for both the HRRR and RHHR support configurations. An axial-moment interaction diagram for the link slab was produced and the link slab would be determined adequate if the force effects from both HRRR and RHHR models were bounded by the axial-moment diagram (i.e., yield surface). Since thermal load was found to be significant, Equation 1-4, a modified equation by Saadeghvaziri and Hadidi [13], was used to account for the thermal load,

$$M_{cont,T} = \left(F_{slab} \cdot d_g - M_g\right)(3 \cdot E_t \cdot I_t) / \left(2 \cdot E_g \cdot I_g\right) \qquad 1\text{-}4$$

where F_{slab} is the axial force in the link slab, d_g is the distance from the girder neutral axis to the girder top fibre, M_g is the bending moment in the girder, E_t and E_g are the Elastic Modulus of the bridge cross-section and bridge girder, respectively, and I_t and I_g are the moment of inertia of the bridge cross-section and bridge girder, respectively.

1.2.2 Tensile Behaviour of Fibre-Reinforced Concrete

1.2.2.1 fib Model Code (2010)

The European method for concrete analysis and design using FRC follows the International Federation for Structural Concrete (*fib*) Model Code 2010 [14]. From Clause 5.6.2 of the *fib* Model Code, a uniaxial test is suggested to determine the properties of FRC in compression. The expected behaviour of the FRC in compression from *fib* Model Code is demonstrated in Figure 1-6, which shows that the FRCs have greater ductility than normal concrete even though the fibres themselves are only effective in tension.

Regarding FRC in tension, the *fib* Model Code has suggested a bending test on rectangular FRC specimens for the calculation of the stress as a function of the crack mouth opening displacement (CMOD). In the *fib* Model Code, the Reunion Internationale des Laboratoires et Experts des Materiaux Technical Committee (RILEM TC) 162 has proposed a standardized three-point bending set-up to determine bending stress in FRC samples, as shown in Figure 1-7.

To determine the bending stress in FRC, the applied load and crack mouth opening of the specimen is measured and compared as shown in Figure 1-8. To convert the load to stress, the *fib* Model Code assumes elastic cross-sectional behaviour at the mid-span of the specimen, and the assumption is that the extreme tensile stress equals to the bending moment divided by the section modulus, which is also assumed for loading past the peak of the load versus CMOD curve.

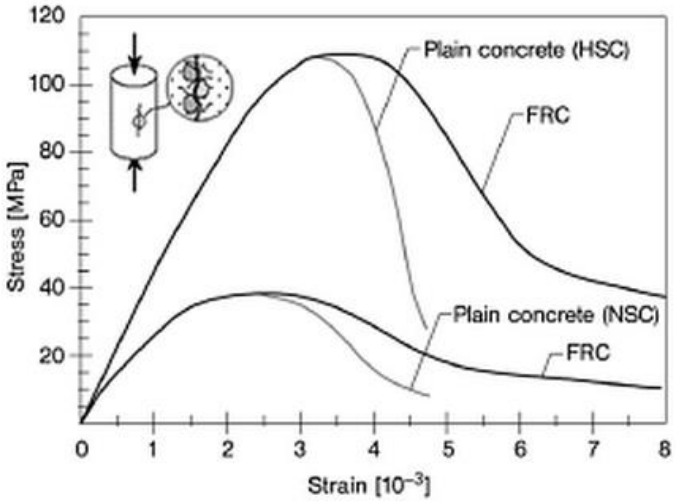

Figure 1-6 – Compression behaviour of FRC [14]

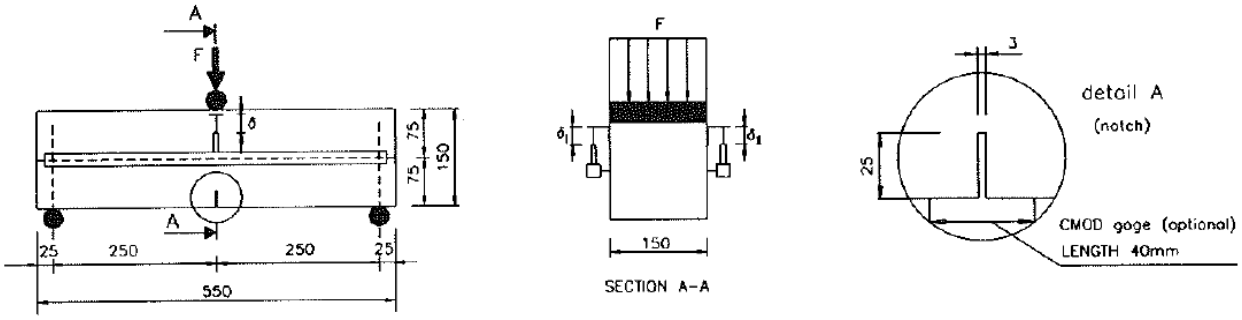

Figure 1-7 – Three point bending best on RILEM TC 162 [15]

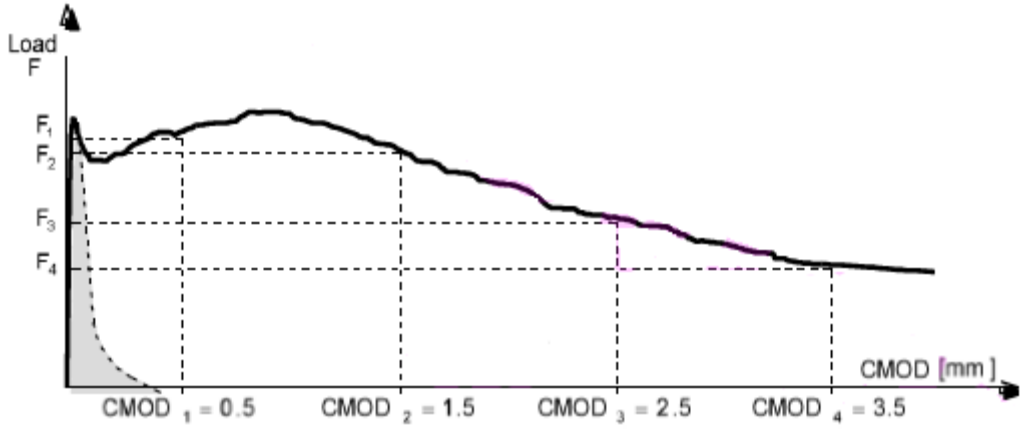

Figure 1-8 – Load versus CMOD results from bending test [14]

The stress block for FRC design can be determined based on the load (or stress) versus CMOD plot, described in Clause 5.6.4 of the *fib* Model Code. The compression and tension stresses can be treated as rectangular stress blocks to simplify the analysis of the fibre-reinforced concrete section. From the *fib* Model Code, the equation to calculate the stress at service (f_{Fts}) and ultimate (f_{Ftu}) are shown in Equations 1-5 and 1-6, respectively. The terms f_{R1} and f_{R3} refer to the stress obtained from the RILEM-TC 162 bending test corresponding to CMOD at 0.5 mm and 2.5 mm from the test, respectively, and w_u is the ultimate crack width acceptable in design. Figure 1-9 shows the stress of a FRC cross-section as suggested by the *fib* Model Code.

$$f_{Fts}=0.45\cdot f_{R1} \quad \text{1-5}$$

$$f_{Ftu}=f_{Fts}-\frac{w_u}{CMOD_3}\left(f_{Fts}-0.5\cdot f_{R3}+0.2\cdot f_{R1}\right)\geq 0 \quad \text{1-6}$$

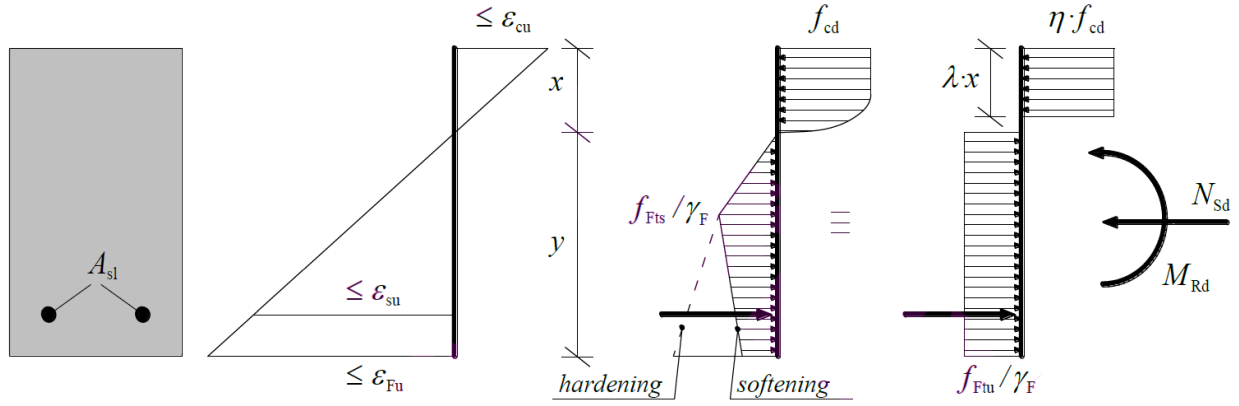

Figure 1-9 – *fib* Model Code section stress for fibre-reinforced concrete [16]

1.2.2.2 Lepech and Li

Lepech and Li [9] examined the use of fibres in the link slab to increase the constructability, durability and sustainability of the link slab structure. Polyvinyl alcohol fibres with sand, cement and fly ash were used as the main compositions of the Engineered Cementitious Composite

(ECC) [7] [9], which differed from conventional concrete mixes. The ECC was found to strain harden under large axial loads and form many micro-cracks rather than increasing the size of existing cracks as the strain of the structure increased. Figure 1-10 shows the material behaviour of ECC. The large strain capacity of the ECC was found to be 400 times that of normal concrete.

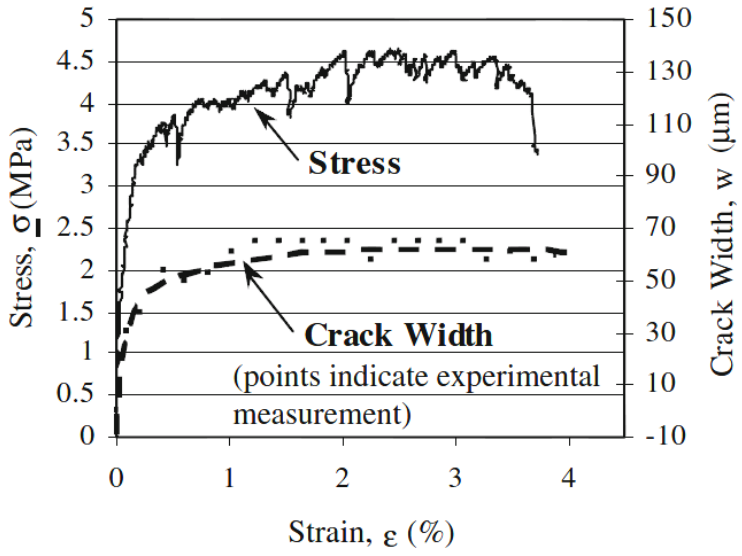

Figure 1-10 – Material behaviour of ECC [9]

The durability and superior mechanical properties of the ECC were then employed in the construction of link slabs, which replaced the use of expansion joints in an existing bridge. The Michigan Department of Transportation (MDOT) constructed several ECC link slabs following the design procedures based on Caner and Zia [1]. In previous link slab analyses, the tensile strain capacity of concrete was not accounted for because conventional concrete did not possess large tensile capacity, and as such large amounts of reinforcements were needed to limit crack widths [2]. Figure 1-11 shows the cross-section stress proposed by Lepech and Li, which reduces the requirement for steel requirement in the link slab. A rectangular stress block was assumed for the post-cracking ECC behaviour.

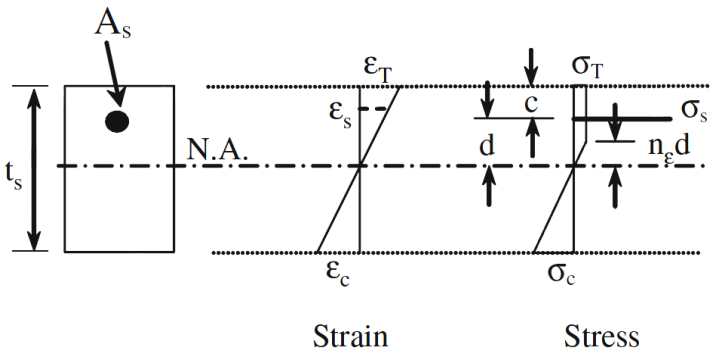

Figure 1-11 – Post-cracking flexural behaviour of ECC [9]

After the construction of the ECC link slabs in 2005, static load tests were conducted on the demonstration project. A finite element model was developed to compare the ECC model against the field measurements. It was found that the girder rotation from the finite element model was 0.00076 rad, while the field measurement was 0.00056 rad. Although the error was approximately 30%, it was considered acceptable since the rotations itself were quite small, and the model underestimated the Elastic Modulus of the concrete since the actual as-constructed material properties were unknown [7]. In conclusion, it was found that the ECC had strain-hardening properties in tensile loading, which helped mitigate cracking and reduced the need for steel reinforcement in the link slab design [9].

1.2.2.3 Jansson

In the study by Jansson [17], it was suggested that a three or four-point bending test could be used to determine the residual stress in FRC. This was consistent with the method proposed by RILEM TC 162 [15], which used three point bending. Jansson also suggested methods proposed by Deutscher Ausschuss für Stahlbeton (DAfStb) [18], the German Committee for Structural Concrete, which determined the flexural strength from three point bending. The stresses in the concrete at service and ultimate conditions were determined from the force-deflection result of

the beam test, as shown in Figure 1-12. At service and ultimate loads, the stresses were taken from deflections of 0.5 mm and 3.5 mm, respectively.

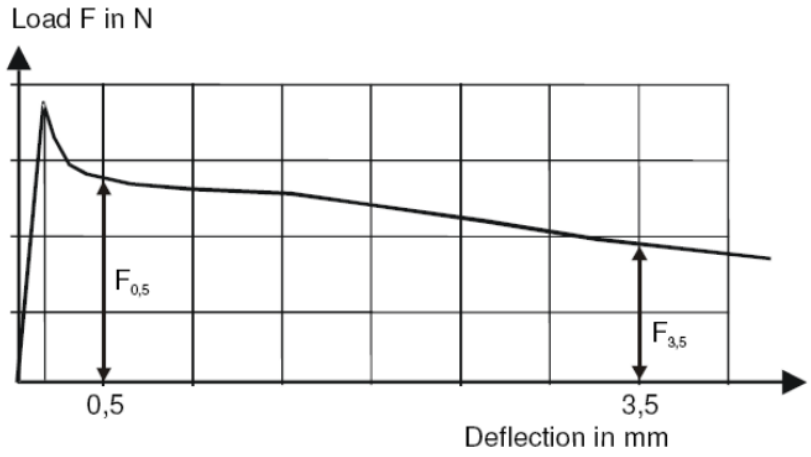

Figure 1-12 – Qualitative force-deflection plot from DAfStb [18]

1.2.2.4 Gribniak, Kaklauskas, Kwan, Bacinskas and Ulbinas

In the study by Gribniak et al. [19], four-point bending test was carried out on 3 meter long beam specimens that were lightly reinforced with steel bars (less than 0.3% reinforcing). The concrete was made using hooked steel fibres with fibre volumes of 0.5%, 1.0% and 1.5%. The FRC compressive strength was approximately 50 MPa. It was found that at tensile strains past 0.002, the tensile stresses of the FRC were stabilizing. For normal concrete without fibres, it was found that there were no tensile stresses past a strain of 0.002. For strains greater than 0.002, the FRC tensile stresses were 1.2 MPa, 2.0 MPa and 2.7 MPa for fibre volumes of 0.5%, 1.0% and 1.5%, respectively.

A layer-section (also referred to as layer-by-layer) analysis approach was used to predict the behaviour of the fibre-reinforced concrete beam, as shown in Figure 1-13. In Figure 1-13a, h and b are the dimensions of the beam, A_s is the steel reinforcement area, and d is the depth of

steel reinforcement. In Figure 1-13b, the concrete section is subdivided into many layers, and t_i is the thickness of each layer. The stress distribution of the section is shown in Figure 1-13c. Using strain compatibility from Figure 1-13d, the strain in each layer ε_i is used to calculate the stress in each layerσ_i. It was found by Gribniak et al. that the layer-by-layer analysis was accurate in calculating the stresses in the FRC section.

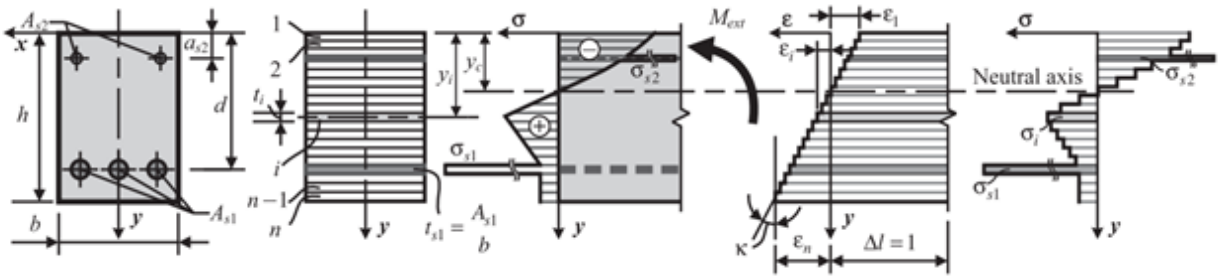

(a) (b) (c) (d) (e)

Figure 1-13 – Layer-by-layer analysis of FRC showing (a) cross-section of reinforced concrete (b) subdivision of layers (c) stress distribution (d) strain compatibility and (e) layer stresses [19]

1.2.2.5 Löfgren

Löfgren suggested that the crack opening in the FRC beam could be treated as a non-linear hinge [20], which could be used to study the flexural behaviour of FRC in its post-cracking configuration. Löfgren suggested that the non-linear hinge concept could be used to define a fictitious crack and therefore an average strain or elongation could be approximated at the location of the crack. This concept can be used to back-calculate the crack width "*w*" of the concrete beam, given the applied load and bending stiffness for a non-linear hinge. If the stiffness of the plastic hinge is known, the curvature (or inverse of the rotation θ) can be found since the curvature is equal to the bending moment divided by the stiffness. Given the crack

length "a" or the concrete compression zone "y_0", the crack width can then be calculated for the cracked section.

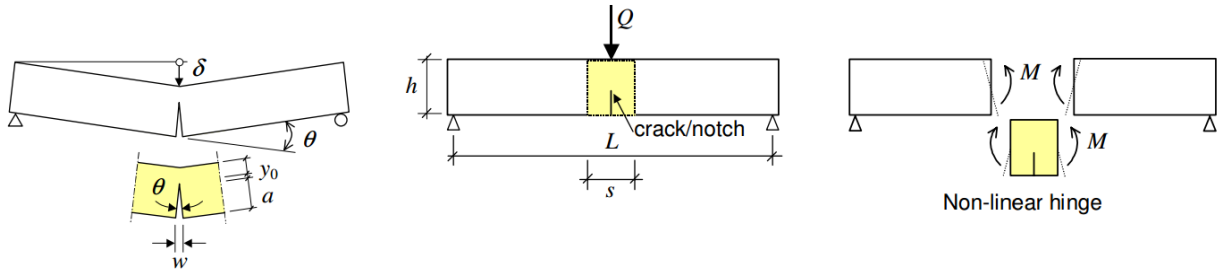

Figure 1-14 – Plastic hinge behaviour in FRC after cracking [20]

1.2.3 Tension Stiffening Behaviour of Fibre-Reinforced Concrete

1.2.3.1 Abrishami and Mitchell

Abrishami and Mitchell [21] investigated the tension stiffening and crack controlling response of reinforced concrete tension members. The specimens were loaded in pure tension to determine the cracking and tension stiffening behaviour of the reinforced concrete specimens. The equation that is proposed to predict the stress in the concrete is shown in Equation 1-7,

$$f_c = (N - E_s \cdot A_s \cdot \varepsilon)/A_c \qquad 1\text{-}7$$

where ε is the strain in the specimen, f_c is the stress in the concrete, A_c is the area of concrete, E_s is the Elastic Modulus of the steel reinforcement, A_s is the area of steel reinforcement, N is the normal (tension) force in the specimen. For FRC, the tensile force is separated into the contributions of the steel bars and fibres, where N_f is the normal force carried by the fibre and N_y is the normal force of the steel at yielding. The normal force in the specimen is described in Equation 1-8,

$$N = N_f + N_y = E_f \cdot A_f \cdot \varepsilon_f + N_y = E_f \cdot A_f(\varepsilon - \varepsilon_y) + N_y \quad \text{1-8}$$

where E_f is the Elastic Modulus of the fibre, A_f is the total area of the fibres in the concrete cross-section, ε_y is the steel yield strain and ε_f is the strain in the fibre. Assuming that 50% of the fibres are orientated ineffectively at any cross-sectional cut, the effective area of the fibre (A_f) is shown in Equation 1-9,

$$A_f = \frac{1}{2} \cdot \frac{1}{3} V_f A_c \quad \text{1-9}$$

where V_f is the volume percentage of fibre in the concrete. The tension force carried by the fibre, up to the yield strength of the fibre (f_{yf}), can be described using Equation 1-10.

$$N_f = min\left[\frac{1}{6} \cdot V_f \cdot A_c \cdot E_f(\varepsilon - \varepsilon_y),\ \frac{1}{6} \cdot V_f \cdot A_c \cdot f_{yf}\right] \quad \text{1-10}$$

The tension stiffening models developed by Abrishami and Mitchell showed good agreement with the test results, although the number of specimens were limited.

1.2.3.2 Bischoff

Bischoff [22] proposed a model for tension stiffening with steel fibres, defined by Equation 1-11,

$$P_{c,m} = 0.6 \cdot P_{max} = 0.6 \cdot \frac{2}{3} \cdot P_{cr} = 0.4 \cdot P_{cr} \quad \text{1-11}$$

where P_{cr} is the axial cracking load of the FRC, $P_{c,m}$ is the additional axial load carried by the cracked concrete, and P_{max} is the axial ultimate capacity of the FRC. Equation 1-11 assumed that 60% of the maximum load was transferred to the concrete (P_{max}) and 2/3 of the concrete cracking force (P_{cr}) was effective in stabilizing the crack [14]. The tension stiffening effect was

described in terms of the bond factor of concrete (β_c) which equals to the ratio of cracked concrete load capacity to the cracking load, defined by Equation 1-12.

$$\beta_c = \frac{P_{c,m}}{P_{cr}} = \frac{0.4 \cdot P_{cr}}{P_{cr}} = 0.4 \qquad 1\text{-}12$$

A similar expression was derived for the tension stiffening of fibre-reinforced concrete. Assuming that with the addition of fibres, the capacity of the cracked concrete is the sum of fibre capacity (P_f) plus the load transferred to the concrete $0.6(P_{max}\text{-}P_f)$. The load in the cracked fibrous concrete due to an applied load P_{max} is shown in Equation 1-13.

$$P_{c,m} = P_f + 0.6(P_{max} - P_f) = 0.6 \cdot P_{max} + 0.4 \cdot P_f = 0.4 \cdot P_{cr} + 0.4 \cdot P_f \qquad 1\text{-}13$$

The bond factor for fibrous concrete (β_f) can be described by Equation 1-14.

$$\beta_f = \frac{P_{c,m}}{P_{cr}} = \frac{0.4 \cdot P_{cr}}{P_{cr}} + \frac{0.4 \cdot P_f}{P_{cr}} = \beta_c + 0.4 \cdot \frac{P_f}{P_{cr}} \qquad 1\text{-}14$$

The tension stiffening effect is demonstrated in Figure 1-15. From laboratory experiments, it was found that the crack spacing was reduced with the presence of steel fibres as a result of tension stiffening, which helped control cracking of the concrete.

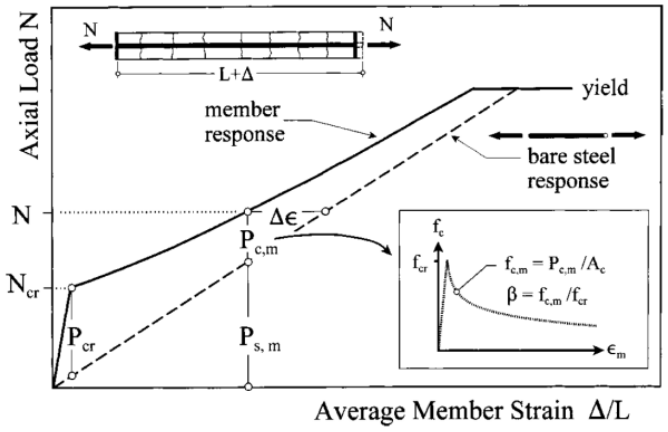

Figure 1-15 – Tension stiffening effect of FRC [22]

1.2.3.3 Deluce and Vecchio

Deluce and Vecchio [23] investigated the tension stiffening behaviour of steel fibre-reinforced concrete (SFRC). The test study was on the uniaxial tension tests of SFRC specimens and the fibres were hooked-end steel fibres. Deluce and Vecchio concluded that steel fibres with reinforcement improved the post-cracking load capacity, the cracking characteristics (i.e., crack width and spacing) and tension stiffening of reinforced concrete. A model was developed by Deluce and Vecchio to estimate the mean crack spacing of SFRC, which was developed based on an equation from Moffatt (2001) [24] and the RILEM Technical Committee 162 equation from Eurocode 2 (Dupont and Vandewalle 2003) [25]. The Eurocode 2 equation to estimate mean crack spacing is shown in Equation 1-15,

$$s_m = 50+0.25 \cdot k_1 \cdot \frac{d_b}{\rho_{eff}} \left(\frac{50}{l_f/d_f} \right) \frac{\varepsilon_1+\varepsilon_2}{2\varepsilon_1} \qquad 1\text{-}15$$

where k_1 is taken as 0.8 for deformed reinforcing bars and 1.6 for smooth bars, ε_1 and ε_2 are the largest and smallest tensile strains, respectively, d_b is the reinforcing bar diametre, ρ_{eff} is the reinforcing ratio to the effective tension zone (e.g., steel area in the tension zone divided by the effective tension area), and l_f/d_f is the aspect ratio of the fibre (length of fibre l_f over its diametre d_f). The modified mean crack spacing equation by Moffatt (2001) is shown in Equation 1-16,

$$s_m = 50+0.25 \cdot k_1 \cdot k_2 \cdot \frac{d_b}{\rho_{eff}} \left(1 - \frac{f_{res}}{f_{cr}} \right) \qquad 1\text{-}16$$

where f_{res} and f_{cr} are the post-cracking residual concrete stress and the crack stress of concrete, respectively. Deluce and Vecchio's crack spacing model for crack spacing is described in Equation 1-17 and 1-18,

$$s_m = 2\left(c_a + \frac{0.5\sqrt{\pi \cdot d_b / s_{mi}}}{10}\right) + 0.125 \cdot \frac{k_1 \cdot k_2}{s_{mi}} \qquad 1\text{-}17$$

$$s_{mi} = \frac{d_b}{\rho_{eff}} + k_{eff} \cdot \frac{\alpha_f \cdot V_f}{d_f}\left(\frac{l_f / d_f}{50}\right) \qquad 1\text{-}18$$

where c_a and s_b are minimum concrete cover and effective average distance between reinforcements, respectively. The contribution of fibre in the equation for mean crack spacing is in the variable s_{mi}. In the equation for s_{mi}, the variables α_f, V_f and d_f are the fibre orientation factor, fibre volume ratio and the fibre diametre, respectively. The variable k_{eff} is the effectiveness factor of fibres. It was concluded that the steel fibres improved the cracking characteristics and tension stiffening of the reinforced concrete compared to conventional reinforced concrete.

1.2.3.4 Lee, Cho and Vecchio

Lee, Cho and Vecchio [26] have established a tension-stiffening model for steel FRC, as demonstrated in Equations 1-19, 1-20 and 1-21,

$$f_{c,TS} = \frac{f_{cr}}{1 + \sqrt{3.6 \cdot c_f \cdot M \cdot \varepsilon_{t,avg}}} \qquad 1\text{-}19$$

$$c_f = 0.6 + \frac{1}{0.058}\left(\frac{l_f}{d_f}\right)^{0.9} \frac{100 \cdot V_f}{M^{0.8}} \quad (straight\ fibres) \qquad 1\text{-}20$$

$$c_f = 0.6 + \frac{1}{0.034}\left(\frac{l_f}{d_f}\right)\frac{\left(100 \cdot V_f\right)^{1.5}}{M^{0.8}} \quad (\textit{hooked-end fibres}) \qquad 1\text{-}21$$

where $f_{c,TS}$ is the stress of concrete for tension stiffening, f_{cr} is the cracking stress of concrete matrix, c_f is coefficient as a function of the fibre properties and volume, $\varepsilon_{t,avg}$ is the average strain in the steel reinforcement, M is the bond parameter of the steel reinforcement (decreases with higher reinforcement size), l_f/d_f is the fibre aspect ratio and V_f is the fibre volume.

The conclusion drawn by the tension stiffening model suggested that tension stiffening in the concrete was reduced as fibres were added to the concrete matrix. From Equation 1-19, the tension stiffening model suggested that as the fibre volume or aspect ratio increased, the tension stiffening in the concrete decreased. This was because the steel fibres were assumed to carry the tensile stresses rather than the tension stiffening from concrete.

1.2.4 Compressive Behaviour of Fibre-Reinforced Concrete

1.2.4.1 Dhakal, Wang and Mander

In the study by Dhakal et al. [27], concrete with steel fibres were tested in compression at fibre volumes between 0 to 2% at increments of 0.5%. Both hooked end and straight steel fibres were used in the study, with results shown in Figure 1-16. Comparing the concrete samples with fibres to normal concrete (without fibres), it is evident that FRC has a larger crushing or failure strain than normal concrete, and the strain can be as large as 3.5%. Therefore, not only does FRC provide post-cracking tension capacity in the concrete, it also provides a large strain capacity in compression, which agrees with *fib* Model Code for FRC in compression [14]. It was found that adding steel fibres also increased the peak stress and strain of the normal concrete.

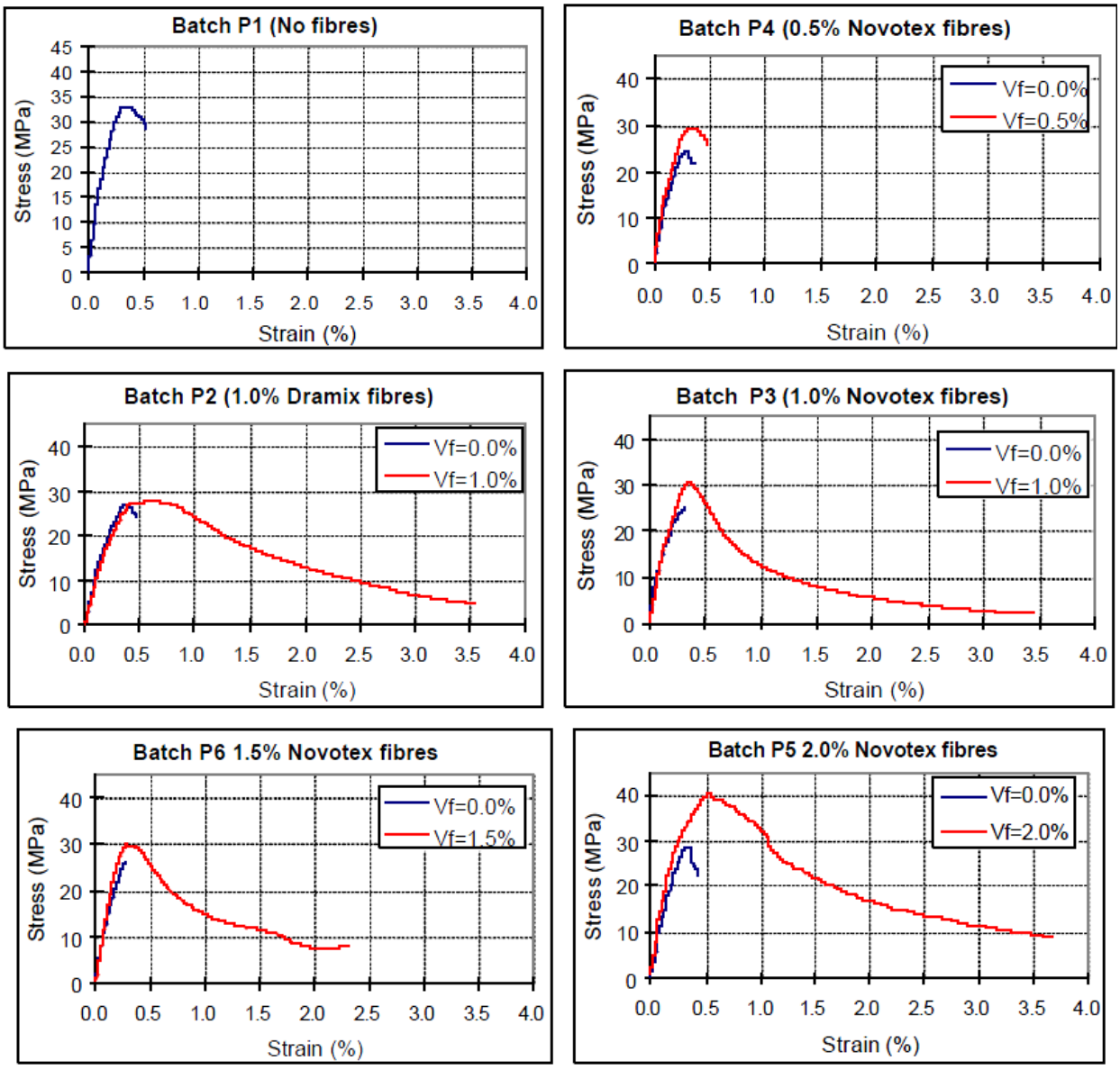

Figure 1-16 – Stress versus strain curves for steel FRC of 0 to 2% fibre volumes [27]

1.2.4.2 Neves and Fernandes de Almeida

Neves and Fernandes de Almeida [28] examined the compressive behaviour of steel FRC. Concrete strengths of 35 and 60 MPa were tested with fibre rations between 1 to 5%. Figure 1-17 shows the results for fibres at 1.5%, where A0 and B0 were the normal concrete samples

(without fibres) and A120Z and B120R were FRC samples. It was found that with fibres, the compressive strain increased significantly. For both normal concrete and FRC, the concrete crushed at a strain of 0.0035, but normal concrete was found to be brittle and decreased to zero stress at a low strain, while the ultimate compressive (crushing) strain of FRC could be as high as 0.025. It was concluded that the peak stress and maximum compressive strain increased with steel fibres.

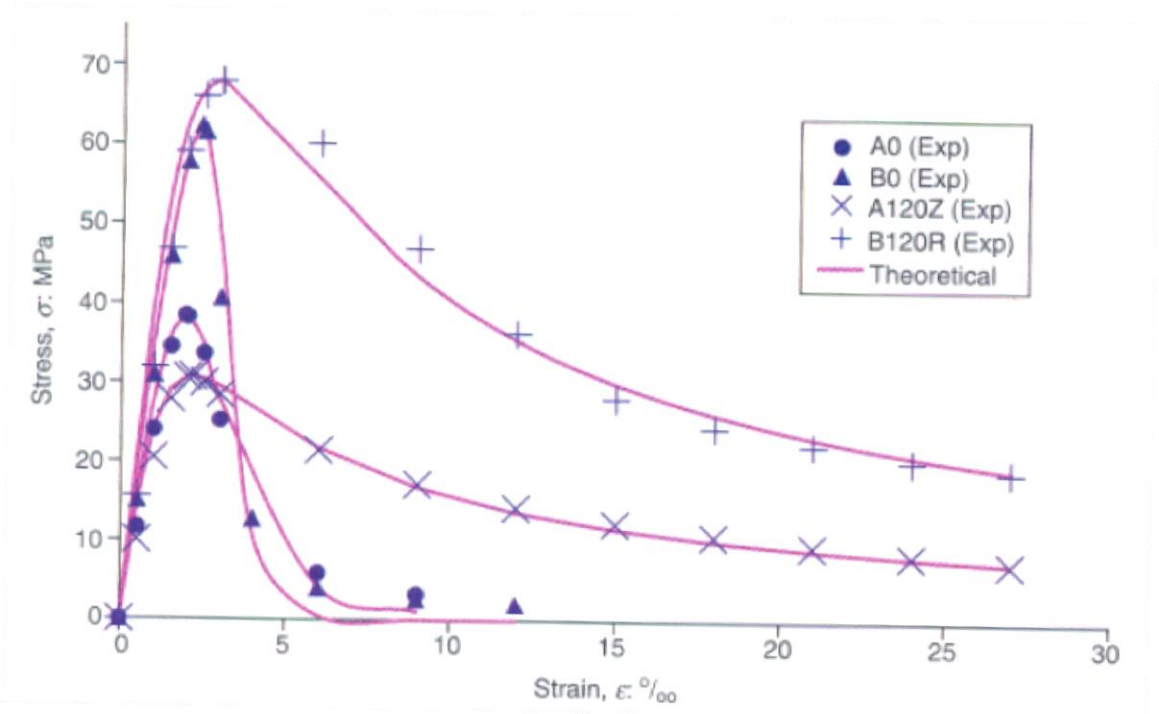

Figure 1-17 – Stress-strain relationship for 1.5% fibre volume [28]

1.2.4.3 Wang, Liu and Shen

A study was conducted by Wang et al. [29] on steel FRC under dynamic compression. Short steel fibres at various fibre volumes were used in cylinders with concrete strength of 40 to 60 MPa. Figure 1-18 is the experimental stress-strain relationship of the specimens at quasi-static

state for 30 MPa concrete with 0%, 1.5% and 4.5% fibres. From Figure 1-18, it can be seen that normal concrete (without fibres) fails at a much lower strain, whereas specimens with fibres have a larger strain before failure.

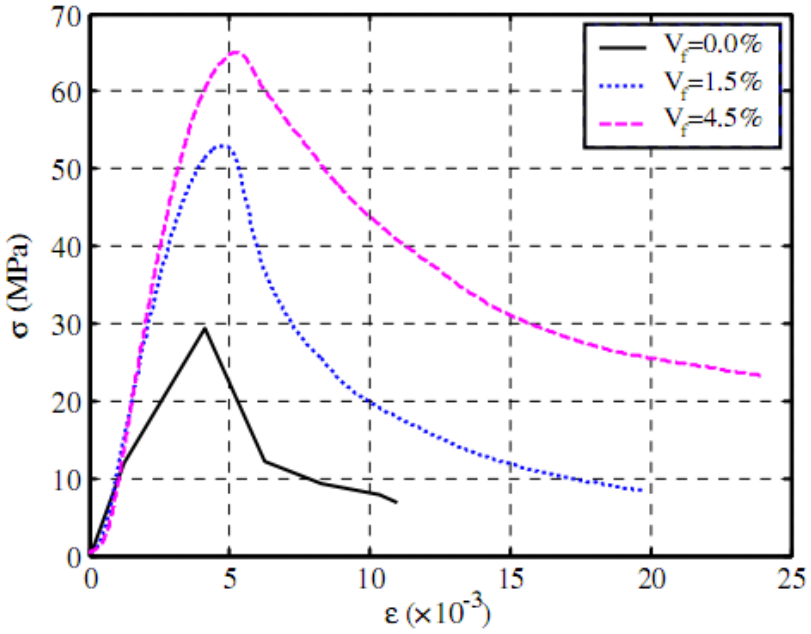

Figure 1-18 – Stress-strain curves of steel FRC in quasi-static state [29]

The stress-strain relationship of FRC past the crushing strain varies depending on the concrete mix and fibre type, but the shape of the FRC stress-strain relationship can be approximated using a concrete stress-strain model called the Hognestad model [30]. In the Hognestad model, the descending branch of concrete stress is approximated linearly, such that the stress of concrete decreases linearly to zero. Figure 1-19 illustrates an example for 30 MPa concrete. Comparing the Hognestad model (i.e., Figure 1-19) to the compressive stress-strain relationship of FRC from Wang, Liu and Shen, (i.e., Figure 1-18), the Hognestad is conservative and therefore valid for approximating the compressive stress-strain relationship of FRC.

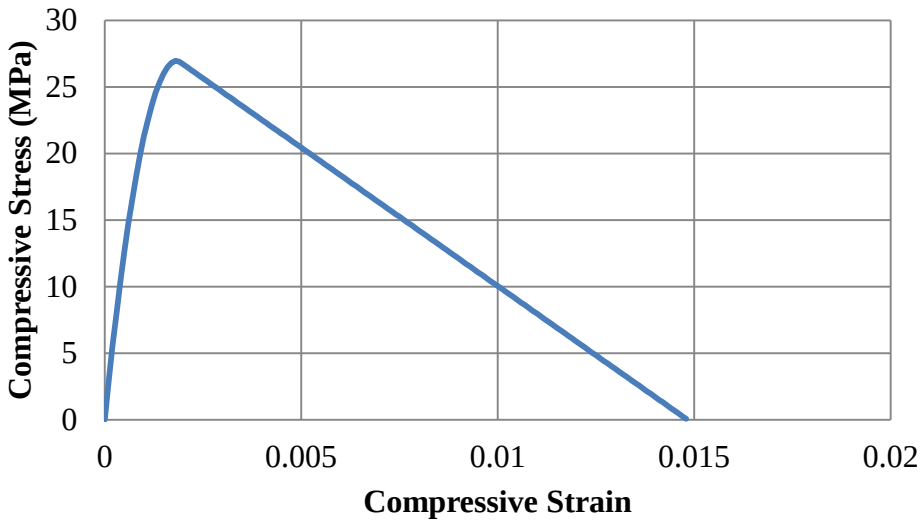

Figure 1-19 – Hognestad model for 30 MPa concrete with extended stress-strain relationship past concrete crushing

1.3 Research Objectives

Based on the preceding literature review, and considering the research needs expressed by the Ministry of Transportation of Ontario, the following research tasks were identified as the research needed to be addressed in this thesis:

- A computational model for a link slab bridge needs to be developed, and the computational model needs to be compared with field test data to assess the accuracy of the modeling method.
- The behaviour of FRC needs to be examined through experimental tests.
- The behaviour of a link slab bridge needs to be investigated parametrically in a computational model considering loading based on the Canadian Highway Bridge Design Code (CHBDC).

- An analytical model needs to be derived to predict the force effects in the link slab due to imposed loading, and determine methods to design link slabs with FRC using existing design codes (i.e., *fib* Model Code).

The first task was to determine a computational model that represented a link slab bridge. An accurate computational model was necessary to examine and predict the behaviour of the link slab bridge. In Caner and Zia [1], a similar approach was adopted, where a computational model was developed to predict the behaviour of the link slab bridge prior to experiments on scaled link slab bridges. Similarly, Okeil and El-Safty [3] also constructed computational models to examine the behaviour of the link slab bridge. However, the computational models by these researchers had their limitations. In Caner and Zia's model, the structural behaviour of the link slab was not explained in full when the support condition was varied (i.e., from RHHR to HRHR). The axial force in the link slab was also neglected by Caner and Zia. Okeil and El-Safty [3] explained the behaviour of the link slab very well with the choice of support conditions RHHR and HRRH by using the force method in an analytical hand model. However, the computational model developed by Okeil and El-Safty did not completely agree with the theoretical computations. Ulku et al. [6] took the similar approach as Okeil and El-Safty by including axial force in the design of link slab, but did not explain the effects of the support condition through statics or mechanics such as the reason for the similarity between the RHRR and HRRR models. Therefore, there was still a lack of understanding of the link slab bridge and its support conditions, and research was needed to better understand and predict the behaviour of the link slab bridge.

The second task was to examine the behaviour of FRC through experimental tests and determine methods of using the experimental data computationally (e.g., computer models) and analytically

(e.g., stress-strain analysis). This step was necessary to incorporate the effects of FRC in the design of link slabs, which were used in the computational model and the analytical model of this thesis. The Canadian design codes for buildings (CSA A23.3-04 [31]) and bridges (CSA S6-06 [32]) did not provide guidance or provisions on the use of fibres for structural purposes. Therefore, it was necessary to develop a method to use experimental results of FRC and incorporate the data in FRC design. In Europe, the *fib* Model Code [14] was used to calculate stress values from FRC experiments (in bending). Thus, the *fib* Model Code equations were also examined in this thesis.

The third task was to parametrically examine the link slab bridge behaviour using a computational model. This step was used to determine the behaviour of the link slab bridge due to various loadings from the CHBDC. The cost of the link slab with the use of FRC was compared to conventional bridges in order to determine the economic feasibility of the link slab bridge with FRC. Finally, the effects of FRC were incorporated into the computational model to observe the behaviour of link slab bridges with FRC.

The final task was to develop analytical models for analysis and design of link slab bridges. The first step in the analytical model was to derive a relationship between the force effects in the link slab and the imposed loading. The rationale was to examine the behaviour of the link slab bridge using structural analysis (i.e., force method), circumventing the need for complicated computational models. This approach was similar to studies by Okeil and El-Safty [3] and Ulku et al. [6] who also developed analytical models for link slab bridges through structural analysis. The next step was to formulate a method of designing link slab with FRC. The purpose of FRC was to improve the cracking characteristic of the link slab to prevent leakage to the underside of the bridge. Additionally, the use of FRC was considered to reduce the required steel reinforcing

bars in the link slab. In analyzing the FRC link slab in design, a stress-strain relationship was derived using existing equations from both the *fib* Model Code and the CHBDC so that the design was tailored specifically to Canadian standards. Although there were many researchers (such as Lepech and Li [9] and Deluce and Vecchio [33]) who investigated the use of FRC, methods of incorporating the effects of FRC in reinforced concrete could be better elaborated for use under Canadian jurisdiction.

1.4 Organization of Thesis

This thesis is organized into seven chapters and five appendices. Chapter 1 presents background information, literature review on link slab bridges, the use of fibre-reinforced concrete (FRC) in structural applications, and justification of research. Chapter 2 summarizes the research objectives and research approach. Chapter 3 describes the development of a computational model of a link slab bridge using SAP2000 and assessment of the model accuracy using field test results. Chapter 4 contains an experimental study on FRC, and the use of *fib* Model Code to derive the stresses in FRC from the results of the experimental data. Chapter 5 provides parametric studies on the computational model with various loads and use of the FRC in non-linear analysis. Chapter 6 develops analytical models for analyzing the force effects in the link slab and the design procedure of the link slabs with the use of FRC. Chapter 7 provides a summary of conclusions, contributions and recommendations for future work. Appendix A contains calculations for the parametric studies of the computational model and FRC experimental results in Chapter 4. Appendix B contains calculations for the analytical model of the first part of Chapter 5, which focuses on the relationship of force effect and imposed loading of the link slab bridge using structural analysis. Appendix C contains calculations for the

analytical model in the second part of Chapter 5 that focuses on the design of link slab with FRC using stress-strain equations. Appendix D presents the step-by-step design calculation for the analytical model of link slab with FRC in Chapter 5. Appendix E presents the drawings from MTO for the Camlachie Road Underpass that is used in the computational model in Chapter 3.

Chapter 2 Research Approach

2.1 Research Approach

The overall objective of this research is to improve the design and performance of link slabs. This can be achieved by investigating the behaviour of link slab bridges, for new construction and retrofit conversions of existing simple-span girder bridges. The research needs identified by the literature review were used to develop the research objectives for this thesis. The research approach that is used to address these objectives is described in the following sections.

2.1.1 Computational Model and Assessment of Modeling Method

The first step of this research was to develop a computational model the link slab bridge of the Camlachie Road Underpass [8]. A truck load test was previously carried out by MTO to study the behaviour of the link slab bridge, and the results of this load test were available to assess the modelling approach of the computational model. The purpose of the computational model was to help understand the behaviour of the link slab through a parametric study:

- The force effects in the link slab were investigated under various loading conditions, such as live load, thermal load and shrinkage load.
- Various design parameters, such as bridge bearing supports, FRC in the link slab, and the debonded length of the link slab, were investigated for the link slab bridge.
- Design guidelines for link slab bridges for both retrofit and new bridges were developed.

Better estimation of the force effects in the link slab will allow engineers to make better decisions on the detailing of the link slab, such as the proportioning of reinforcement and use of

concrete materials with post-cracking strength (i.e., FRC) for the link slab design. The computational model is described in detail in Chapter 3.

2.1.2 FRC Experimental Study

The second step of this research was the investigation of FRC in the design of link slabs. A laboratory study on FRC was conducted by Cameron [34] in parallel with this research to characterize the flexural and durability properties of FRC. Results from the FRC study by Cameron were used in the non-linear analysis component of the parametric study in Chapter 4 and development of the analytical model in Chapter 6. The *fib* Model Code [14] was used in determining the tensile stresses in FRC from the experimental data. See Chapter 4 for a detailed investigation of experimental results with FRC.

2.1.3 Parametric Study of Link Slab Bridge Behaviour

Following the establishment of FRC properties, the next step was to conduct a parametric study on the computational model of the link slab bridge. Various parameters were changed in the computational model to determine their influence on the link slab; such as the support conditions, loadings from the CHBDC, length of the debonded link slab and effect of FRC modelled as plastic hinges in link slab bridges. With better knowledge of the link slab behaviour, design guidelines can be developed for link slab bridges in the analytical model. The current design provisions, assumptions and practices for link slab bridges were reviewed to identify possible gaps in knowledge or potential for design improvements. The parameters selected for investigation were:

- CHBDC loads including dead load, live load (CL-625-ONT truck load) and strain load (temperature and concrete shrinkage);
- CHBDC Ultimate Limit State (ULS) and Serviceability Limit State (SLS) load combinations using linear elastic behaviour;
- effects of varying the link slab debonded length and cost estimate of link slab construction with various debonded lengths;
- application of FRC in link slab design with ULS and SLS load combination using non-linear behaviour; and
- inclusion of FRC in the analysis of link slab bridge and its influence on link slab force effects, deflection and cracking.

The parametric study is described in detail in Chapter 5.

2.1.4 Analytical Model for Link Slab Design

A simplified analytical model was developed to better represent the link slab bridge behaviour for design purposes with a series of equations. This step was intended to simplify the analysis of the link slab bridge so that complicated computational models were not needed for design purposes. The analytical model was covered in two aspects, which were:

- derivation of force effects in the link slab due to imposed loading using the force method; and
- derivation of stress-strain relationship of the FRC link slab using equations and recommendations from existing codes.

The first aspect of the analytical model was to develop equations to analyze the load effects in the link slab bridge using the force method. The goal was to propose equations that would capture the effects of various loads without the need for complicated computational models. The loads from the parametric study in Chapter 5 were used to validate the analytical model.

The second aspect of the analytical model was to derive a stress-strain relationship of the FRC link slab for design using *fib* Model Code and CSA A23.3 [31] (Canadian Standard Association for the design of concrete structures). In the current design provisions, the CHBDC does not include effects of tension stress in concrete for structural concrete sectional design. However, the *fib* Model Code [14] suggested that the tensile stress in FRC could be considered as a rectangular stress block, which could be derived from bending tests of FRC specimens. Therefore, derivation of new equations was needed in an effort to incorporate *fib* Model Code by modifying the current Canadian practices for reinforced concrete analysis and design. The analytical model is described in detail in Chapter 6.

Chapter 3 Computational Model for Link Slab Bridge

3.1 Introduction

A computational model is a very powerful tool for engineers to estimate the behaviour of the structure due to various applied loading. The link slab bridge is an indeterminate and non-trivial structure, as explained in Section 1.1.1. One method of examining the behaviour of such a complicated structure is to develop a computational model and understand the structure through various studies of the structure, including modifying the support conditions of the structure and changing the imposed loading on the structure. To accurately represent a link slab bridge using a computational model, the results of the computational model should ideally be compared to truck load test results from an existing bridge. The computational model in this thesis was achieved in a progression of two steps:

1. the development of a computational model based on the as-designed conditions of an existing bridge; and
2. the study of idealized support conditions with rollers and hinges using a parametric study.

The first step was to develop a computational model based on the as-designed construction drawings for the Camlachie Road Underpass [8]. This Camlachie Road Underpass is an existing bridge in Ontario under the management of MTO. The bridge was retrofitted in 2007 that replaced the expansion joint with link slabs, and was subjected to a truck load test by the Ministry of Transportation Ontario (MTO), which provided a good opportunity for the study of the link slab bridge. In this research, spring supports were used to model the bearing supports in the shear (horizontal) and rotational degrees of freedom, which were based on the designed shear

and rotational stiffness of the bearing, respectively. The abutment-end restraint, approach slab and parapet walls were not modelled in the computational model due to their connection details from the as-designed drawings (to be discussed in Section 3.2).

The next step was to determine the idealized support combinations (i.e., roller and hinge supports) used in the subsequent parametric study. This step was taken as a design consideration for various idealized supports used more typically in design (i.e., hinges and rollers), rather than the use of spring supports. The idealized supports were also compared to the MTO truck load results in order to determine which combinations of idealized supports were similar to elastomeric bearing. This was consistent with the works of Caner and Zia [1], Okeil and El-Safty [3] and Ulku et al. [6], where the models were investigated based on idealized support combinations.

SAP2000 [35] was selected for computational modelling of the link slab bridge behaviour. SAP2000 is a general purpose, commercial structural analysis program with capabilities in non-linear geometric responses and non-linear material responses in the form of plastic hinges (plastic hinges to be discussed further in non-linear computational model in Section 5.4).

3.2 Camlachie Road Underpass Background

The computational model was developed based on the Camlachie Road Underpass as-designed drawings. The Camlachie Road Underpass is a two-span semi-integral abutment bridge that crosses Highway 402 in the township of Plympton-Wyoming, Lambton County, in Ontario [8]. The Camlachie Road Underpass, shown in Figure 3-1, was constructed in 1975 with expansion joints at the pier and abutment, and was retrofitted in 2007 to a link slab bridge. In 2009, a truck load test was carried out by the Ministry of Transportation Ontario (MTO) to study the behaviour of the link slab bridge. The truck load test results from the Camlachie Road Underpass were

used to assess the accuracy of the computational model. The as-designed drawings for the retrofitted Camlachie Road Underpass are included in Appendix E.

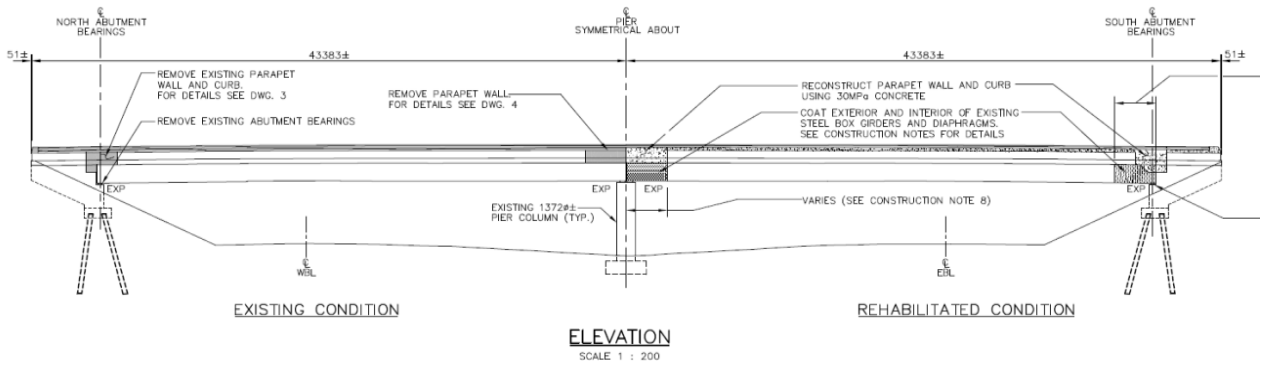

Figure 3-1 – Elevation view of the Camlachie Road Underpass [8]

Each span of the Camlachie Road Underpass is a slab-on-girder structure made up of a cast-in-place concrete slab (or deck) on two steel U-girders. Figure 3-2 is a cross-section view of the Camlachie Road Underpass Bridge and the detail of the parapet wall connection. Each U-girder is approximately 1300 mm in height and 2000 mm in width with steel plate thickness of 16 mm. The concrete deck is 190 mm in thickness and it is reinforced with four layers of reinforcement. The top and bottom layers are transverse reinforcements, and the two middle layers are longitudinal reinforcements. The top and bottom longitudinal reinforcements are 15M bars spaced at approximately 400 mm and 200 mm centre to centre, respectively. The depths of the top and bottom longitudinal reinforcements from the top of deck are 50 mm and 120 mm, respectively.

The design of the parapet wall suggests that the parapet wall is not composite with the bridge deck. For one, the parapet wall is quite long relative to its cross-section, and it will be subject to lateral torsional buckling and significant reduction in bending effectiveness since the stiffness of

this parapet wall is quite low. Moreover, the shear lag effect of the parapet wall is unknown and not specified in the drawings or report (i.e., reduction of parapet wall effectiveness). Thus, it is acceptable to not include the parapet wall in the computational model. Typically, the parapet wall is designed for impact loading due to vehicles and not accounted for as a structural component of the bridge unless it is purposely intended. Therefore, the parapet wall was not considered as part of the bridge span in the model.

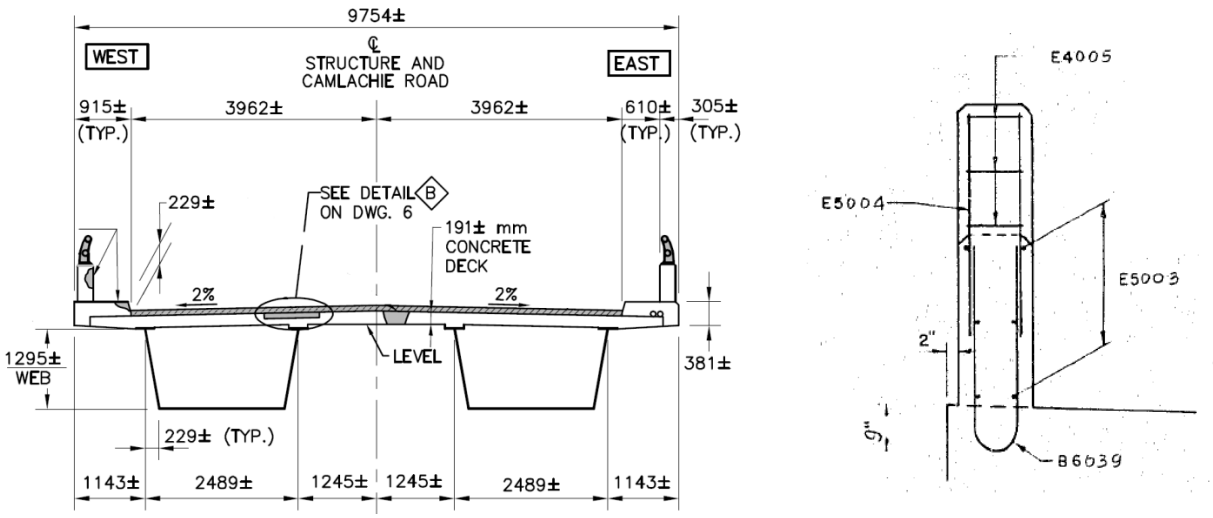

(a) (b)

Figure 3-2 – Camlachie Road Underpass Bridge (a) cross-section view and (b) parapet wall details [8]

For the link slab bridge, the girders are simply-supported beams between the pier and the abutment, but the deck is continuous over the length of the bridge. Figure 3-3 is a partial elevation view of the link slab and girder at the pier. The link slab is also designed with four layers of steel reinforcement, similar to the bridge deck design. The top and bottom reinforcement layers are transverse reinforcements, and the two middle layers are longitudinal reinforcements. The longitudinal reinforcement consists of 15M bars spaced at 200 mm centre

to centre (in both layers). The depths of the longitudinal reinforcement layers (from the top of deck) are 70 mm and 120 mm, respectively, also similar to the bridge deck. The link slab is debonded over a total length of 6000 mm, as shown in Figure 3-3, which is approximately 7.5% of one of the bridge span length. The debonded length between the link slab and girder is achieved using roofing paper in-between the link slab and the girder to prevent bonding. As a result, the link slab cannot compress into the girder; otherwise, the link slab is allowed to freely rotate or separate from the girder.

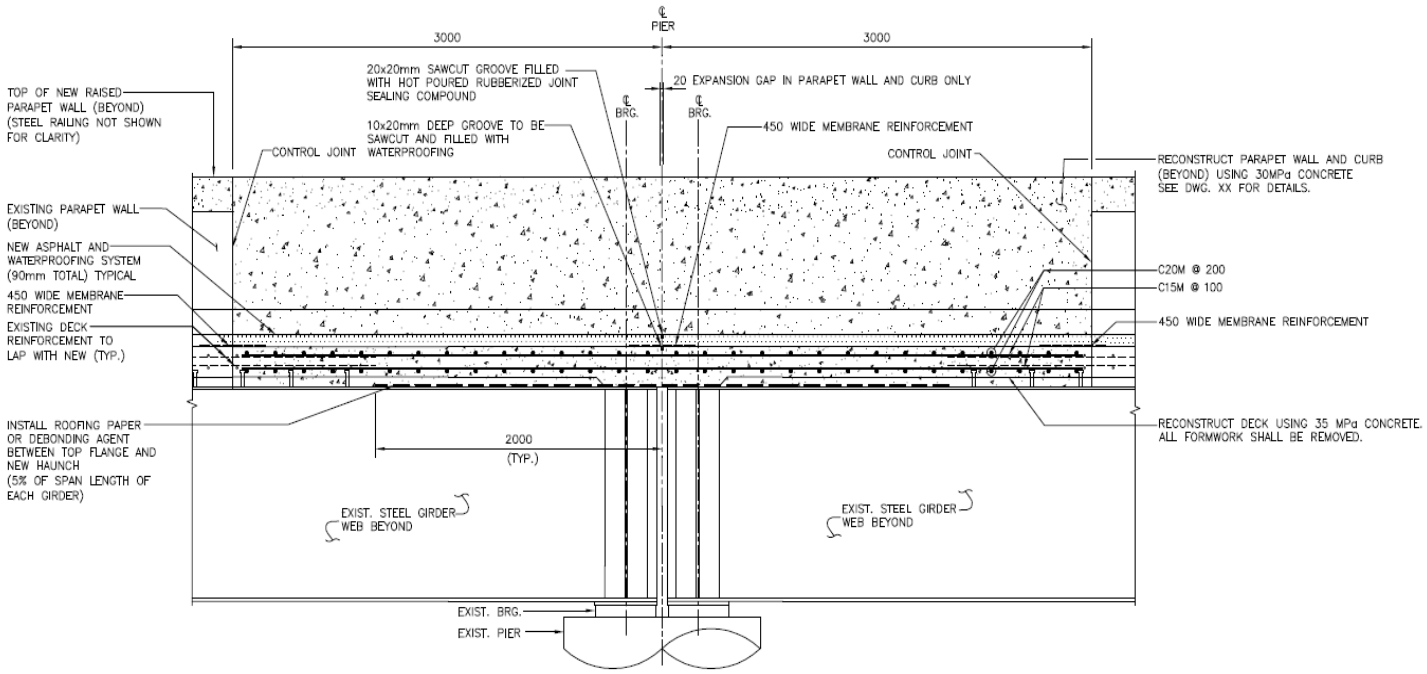

Figure 3-3 – Link slab rehabilitation details [8]

The semi-integral abutment detail of the Camlachie Road Underpass is shown in Figure 3-4. Based on the design of the semi-integral abutment, it is representative of discontinuity between the bridge deck and the abutment piles due to the flexible elastomeric bearing strip separating the bridge deck and the abutment. Thus, the bridge span is mostly supported by the elastomeric bearing pad at the girder-end. The approach slab was also not considered as a restraint because

the detail of the approach slab showed a construction joint with only one layer of reinforcement connection between the approach slab and bridge deck. This means the approach slab does not provide significant restraint on the bridge deck, where typically construction joints are used to prevent restraints between two elements (i.e., to separate the approach slab from the bridge [36]), so the assumption is valid. Therefore, under the circumstances that the soil condition is unknown, the abutment-end restraint should be neglected so that the restraint at the abutment is not over-compensated as a conservative means in modelling.

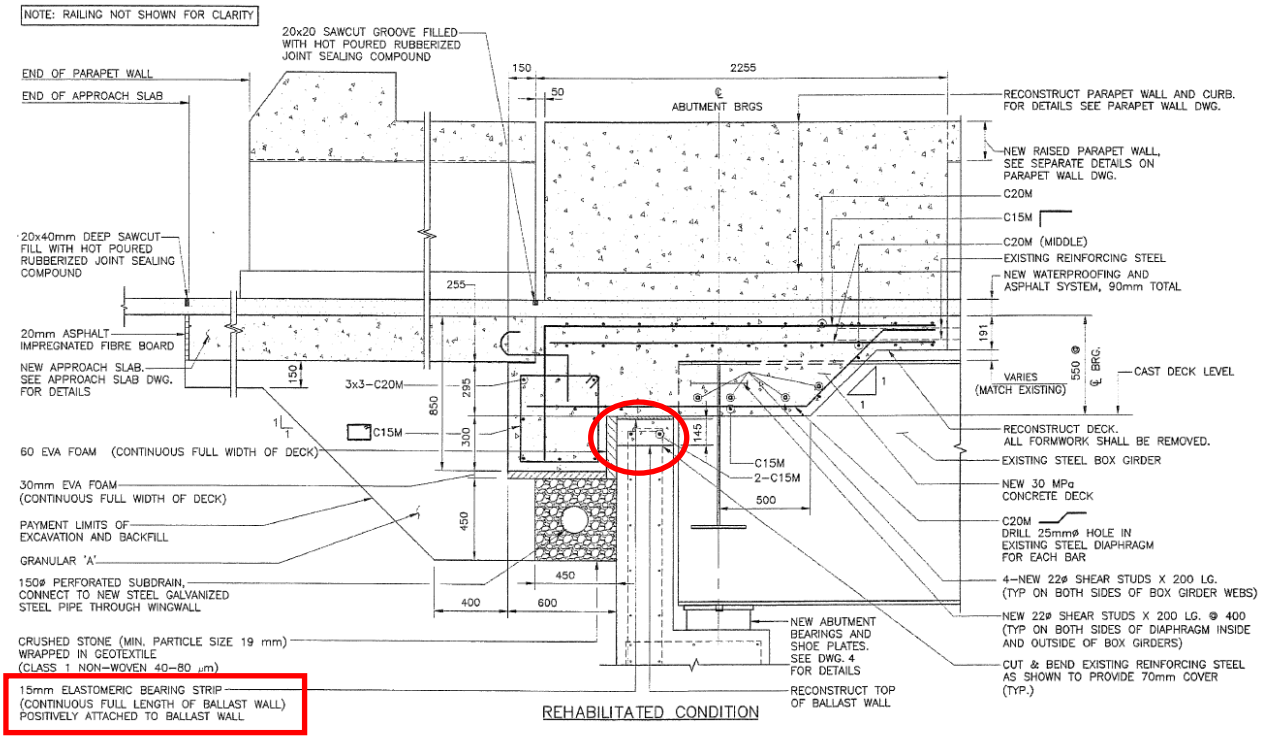

Figure 3-4 – Semi-integral abutment detail for Camlachie Road Underpass [8]

The link slab bridge is not a trivial structure because it is neither a simply-supported bridge nor a continuous bridge. The link slab bridge cannot be modelled as a simply-supported bridge because the link slab provides restraint to the girder-end at the pier. Moreover, the link slab bridge cannot be modelled as a continuous bridge because only the link slab is continuous across

the bridge and the girders are not continuous. The approach taken to model this behaviour is described in Section 3.2.2.

From the Camlachie Road Underpass observations, it was found by MTO that the cracking occurred at the pier supports, as shown in Figure 3-5. Therefore, it is expected that the highest force effects are at the pier supports rather than at the centre of the link slab. This will be confirmed later from the results of the Camlachie Road Underpass computer model in Section 3.3 and the parametric study in Section 5.2.

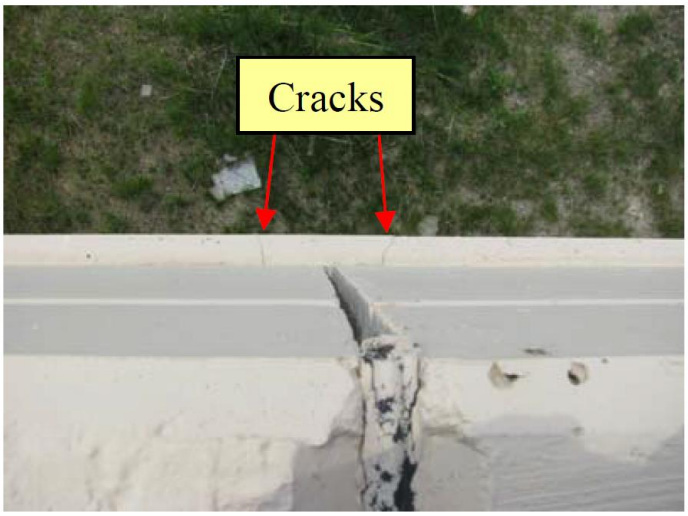

Figure 3-5 – Crack observations from Camlachie Road Underpass link slab [8]

3.2.1 Camlachie Road Underpass Load Test

The MTO conducted truck load tests on the Camlachie Road Underpass in 2009, two years after the link slab retrofit, to study the behaviour of the link slab bridge after its retrofit [8]. The load test results were based on static load testing with truck loads in various positions along the span of the bridge. The truck positions were labelled as Step 1 to Step 10. From Step 1 to Step 9, two trucks were placed side-by-side and moved along the bridge span. In Step 1, the trucks were

positioned near the abutment and in Step 9 the two trucks were positioned near the link slab. The intermediate steps were trucks in other positions between the abutment and pier. In Step 7, the position of the two trucks was such that they were near the middle of one span that generated the greatest positive moment in the bridge span. Step 10 was a special loading case where a truck was placed on each of the spans on either side of the centre pier that generated the largest negative bending moment in the link slab. Figure 3-6 shows the two test trucks used in the MTO field test, and Figure 3-7 shows the SAP2000 representation of Step 7 and Step 10 loading with arrows that represent the axle load positions of the trucks from Figure 3-6.

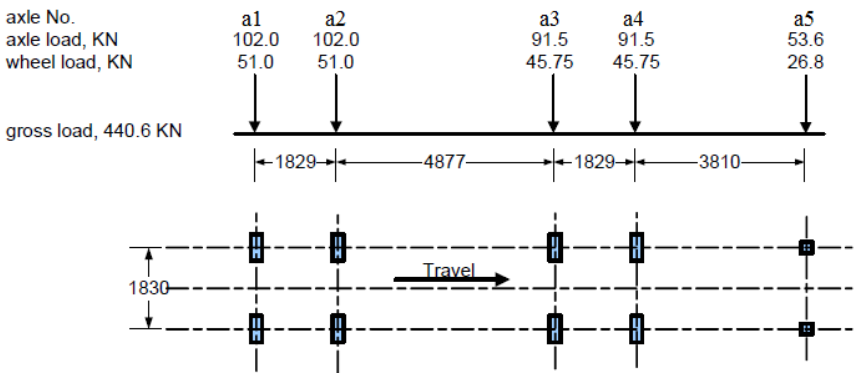

(a)

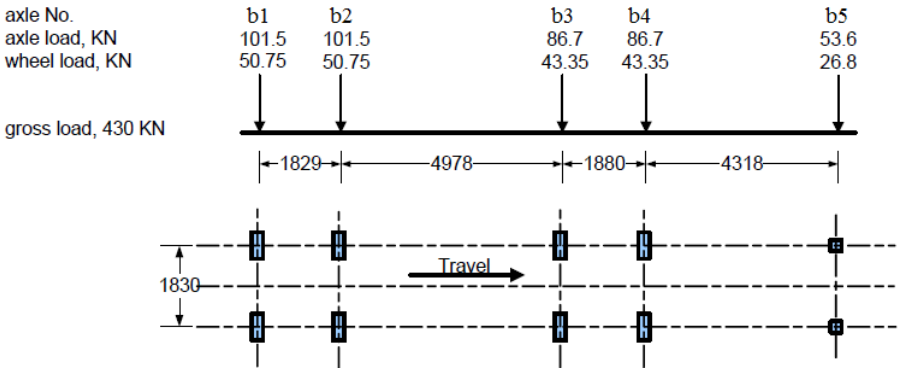

(b)

Figure 3-6 – MTO field test vehicles (a) Western Star Truck and (b) Volvo Auto-Car Truck

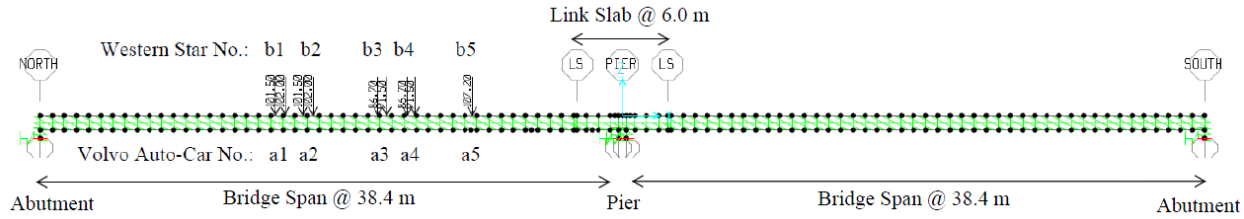

(a)

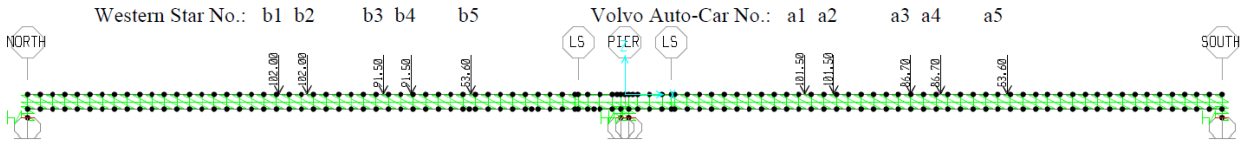

(b)

Figure 3-7 – Bridge model with (a) Step 7 and (b) Step 10 load positions in SAP2000

The MTO truck load test included strain readings from the reinforcements in the link slab, bottom flange of the girder and vertical deflection of the bridge girder near the pier. The vertical deflection of the girder measurement was used assess the accuracy of the SAP2000 computational model of the bridge. The strain in the reinforcement and girder were not used because the measured strain values were very small (less than 50 micro strains) and distinguishing actual trends in the data from noise may not be reliable at these levels. Therefore, only the model deflection profiles were compared to the measured results.

3.2.2 Modelling of Camlachie Road Underpass in SAP2000

The model that is developed in this section is used to determine force effects in the longitudinal direction and deflection profiles along the length of the bridge. Given that the bridge does not have a skew and the truck loads from Camlachie Road Underpass load are symmetric about the centroid of the span, torsional effects in the response of the bridge are not significant. As such, it

was decided to model the link slab bridge using a 2-D model with beam elements, similar to the approaches by Kim and Laman [37] and Civjan et al. [36].

Modelling of link slab bridges is different than modelling of regular steel girder-concrete deck composite bridges. A typical bridge (without the link slab) can be modelled using a single beam element that represents both the concrete slab and the steel girder. The shear studs between the concrete deck and girder create composite action, and thus the deck and girder act as one composite cross-section. If the cross-section design of the bridge is consistent between the abutments and piers (i.e., no abrupt changes in cross-section geometry and material), a single beam element can be used to represent each span of the composite deck and girder cross section between the abutments and piers. In simply-supported composite steel-concrete girder bridges with expansion joints, the expansion joint provides a smooth vehicle transition between the spans while accommodating for thermal expansion of the bridge, and preventing leakage through the deck that would otherwise cause damage to the substructure underneath. The expansion joint at the pier does not transfer axial force, shear and bending moment between the spans; this is to say that there is no structural continuity between spans, and each bridge span is considered a simply-supported element when modelling expansion joint bridges. For continuous bridges, there are no expansion joints between adjacent spans. If the cross-section of the bridge is consistent for the entire bridge, then a single continuous composite beam element can be used to represent the bridge with intermediate supports. However, the link slab at the debonded region (near the pier) is not composite with the girder.

For link slab bridges, the expansion joint is replaced with a link slab that transfers axial force and bending moment between bridge spans. At the debonded region of the link slab, the link slab is not composite with the girder (on a sectional basis) as illustrated in Figure 1-3. As such, the link

slab can separate (lift off) from the girder and experience longitudinal slip relative to the girder, but cannot compress into the girder. Away from the link slab region, composite action between the deck and girder is provided by shear studs. These conditions must be accounted for in order to accurately model the link slab bridge behaviour.

To model the link slab bridge, the centroid locations for the bridge deck, link slab and girder must be considered along with the compatibility conditions within each region. Within the length of the link slab, the link slab is not composite with the steel girder since there are no shear studs. For the remainder of the bridge, the deck and girder can be treated as a composite section since there are shear studs. This means that a single continuous beam section cannot be used to model the link slab bridge. Additionally, the model must account for the eccentricity of the link slab centroid relative to the girder section.

In the bridge model, the bridge deck, link slab and the girder have been modelled as separate elements to account for the debonded region of the link slab. The composite behaviour between the bridge deck and the girder is enabled by restraining the translational and rotational degrees of freedom using "link elements" between the deck and the girder beam elements along the bridge span. The link elements represent shear studs between the bridge deck and steel girder. Constraining the translational and rotational degrees of freedom between the deck and the girder creates a deck-girder composite section. Within the debonded region of the link slab section, the compatibility between link slab and girder is provided using "gap elements", which only restrains the compression degree of freedom in the vertical direction, while the rotational, shear (in the horizontal direction), and tension (in the vertical direction) degrees of freedom are not constrained. This allows the link slab to freely separate and slip relative to the steel girder. The only constraint is that the link slab is prevented from crushing into the girder. Therefore,

modelling the link slab, the deck and the girder as separate beam elements can be used to account for the debonded region and eccentric behaviour of the link slab relative to the deck-girder composite. Figure 3-8 shows the overall bridge model in SAP2000 and a detailed view of the link slab at the pier. The debonded region of the link slab is approximately 6000 mm in length, and is the region indicated with the "gap elements" (or "gap links") in Figure 3-8.

Post-processing is required to obtain bending moment results for the overall model cross section in Figure 3-8 since there are coupling axial forces in the deck and girder sections created by modelling the deck and girder as separate beam elements. Therefore, to obtain the actual bending moment in the bridge section, the axial force in the elements must be multiplied by the moment arm (distance between the deck and girder centroid) and included in addition to the bending moment in both the deck and girder beam elements.

The cross-section of the bridge steel U-girder and the link slab are shown in Figure 3-9, which are modelled using the custom section definer in SAP2000. These cross-sections are used for the beam elements in Figure 3-8. There are two steel U-girders supporting the bridge deck, and the approximate dimension of a U-girder is 2000 mm in width and 1300 in height (at a small angle), with plate thicknesses of 16mm. The bridge deck (and link slab) is 190 mm in depth with two layers of steel reinforcements. The link slab reinforcing bars are spaced at 200 mm, which is equivalent to 91 numbers of 15M at depths 50 mm and 120 mm from the top of the slab (in both layers). The top and bottom concrete deck reinforcements are spaced at 200mm and 400mm, respectively, which is equivalent to 22-15M in the top layer and 44-15M in the bottom layer (also at depths 50mm and 120mm from the top of the slab). In SAP2000, the steel layer is modelled as a rectangular steel layer. Although rectangular sections would contribute to torsional stiffness of the section, there is no torsion in a beam element (for 2D analysis). Thus,

modelling the reinforcement as a rectangular steel section is deemed valid. The transverse reinforcement layers are not modelled because the 2D bridge model will not consider out-of-plane action of the structure.

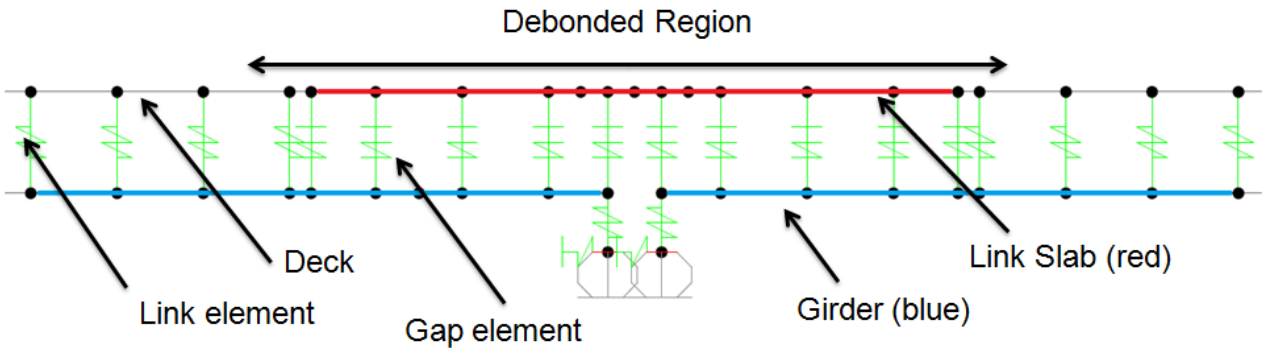

Figure 3-8 – SAP2000 model with the bridge detail at the pier support

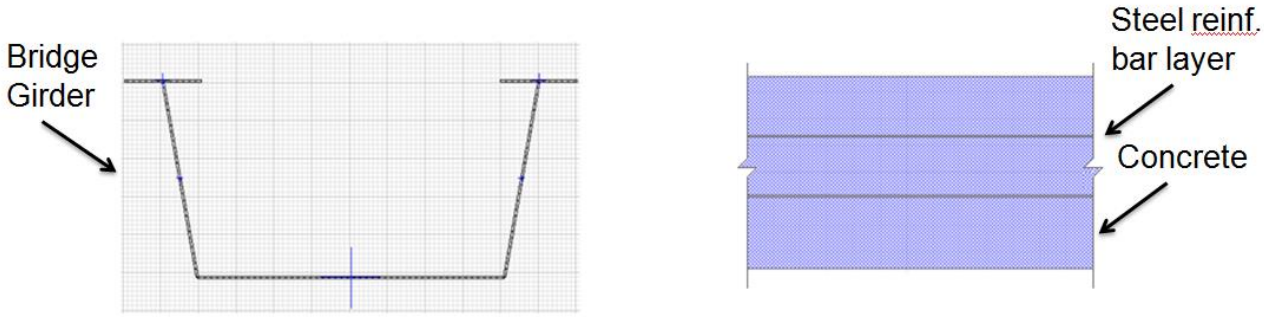

(a) (b)

Figure 3-9 – SAP2000 (a) girder cross-section and (b) link slab cross-section

The support condition was modelled by using spring supports with horizontal spring stiffness of 5.0 kN/mm and 7.5 kN/mm at the pier and abutment, respectively, based on the lateral stiffness

specified for the elastomeric bearing pads as indicated on the design drawings for the retrofitted Camlachie Road Underpass. The rotational stiffness of the bearing pads were very small and therefore its effects were deemed negligible.

The effective moment of inertia of the link slab was calculated for every load case [1]. This was used to model the softening of the link slab if the applied bending moment is large (based on Caner and Zia [1]). The equation is defined in Clause 8.13.3.3 of the CHBDC and is used to calculate the effective moment of inertia, which is defined by Equation 3-1,

$$I_{eff} = I_{cr} + \left(I_g - I_{cr}\right)\left(\frac{M_{cr}}{M_a}\right)^3 \leq I_g \qquad 3\text{-}1$$

where I_{eff} is the effective moment of inertia, I_{cr} is the moment of inertia after concrete cracking, I_g is the gross moment of inertia, M_{cr} is the cracking moment and M_a is the applied moment. The properties of the link slab and steel girder sections for the Camlachie Road Underpass are summarized in Table 3-1 (note: the concrete bridge deck properties are similar to the link slab). These properties are provided with the SAP2000 custom section definition.

Table 3-1 – Properties used in SAP2000 model for the Camlachie Road Underpass

Gross Moment of Inertia of steel girder	126 (10^9) mm^4
Gross Moment of Inertia of link slab	5.58 (10^9) mm^4
Elastic Modulus of steel girder	200 (10^8) Nmm^2
Elastic Modulus of link slab	26.6 (10^8) Nmm^2
Area of steel girder	181 (10^3) mm^2
Area of link slab	1945 (10^3) mm^2
Centroid distance between girder and link slab	865 mm

3.3 Assessment of Modelling Approach

The modelling approach described in the preceding section was designed to represent key features of the link slab bridge, including link slab debonding and varied bridge support conditions. In order to gain some measure of the accuracy of the modelling approach, the predicted response of the Camlachie Road Bridge using the computational model developed in this thesis was compared to the MTO field results and the MTO computational model from the load test on the bridge (conducted previously). The MTO field and model load test results represent a partial response of the bridge under truck loading. Thus, comparison of the computational model to the MTO results is not sufficient to validate the model completely for all load types and model variables. However, this limited comparison was important to demonstrate whether the modelling approach was suitable for further use in the parametric study later in this thesis (see Section 5.2).

The computational model was constructed in SAP2000 using the properties summarized previously in Table 3-1 along with the following key assumptions (for detailed explanations, see Section 3.2.2):

- The elastomeric bearing support at the abutment and pier supports were modelled using spring supports, rather than idealized supports (i.e., hinges and rollers).
- The parapet wall of the bridge was not included in the bridge model because it was deemed that the parapet wall should not be considered to be composite with the deck.
- The abutment ends of the bridge model were not restrained in the rotational degree of freedom, because it was deemed that the connection detail did not represent a moment connection, even though the abutments were semi-integral.

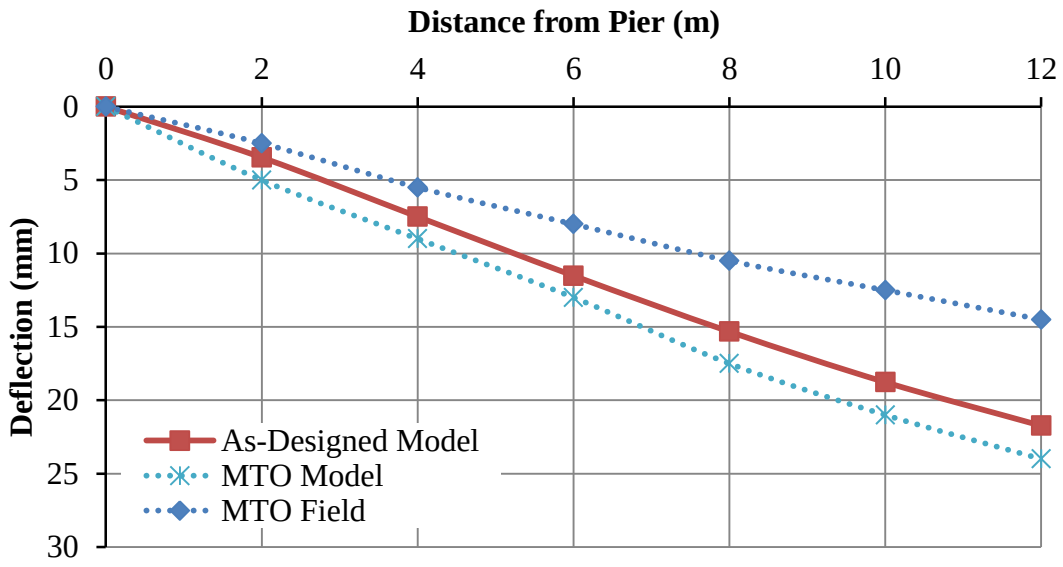

(a)

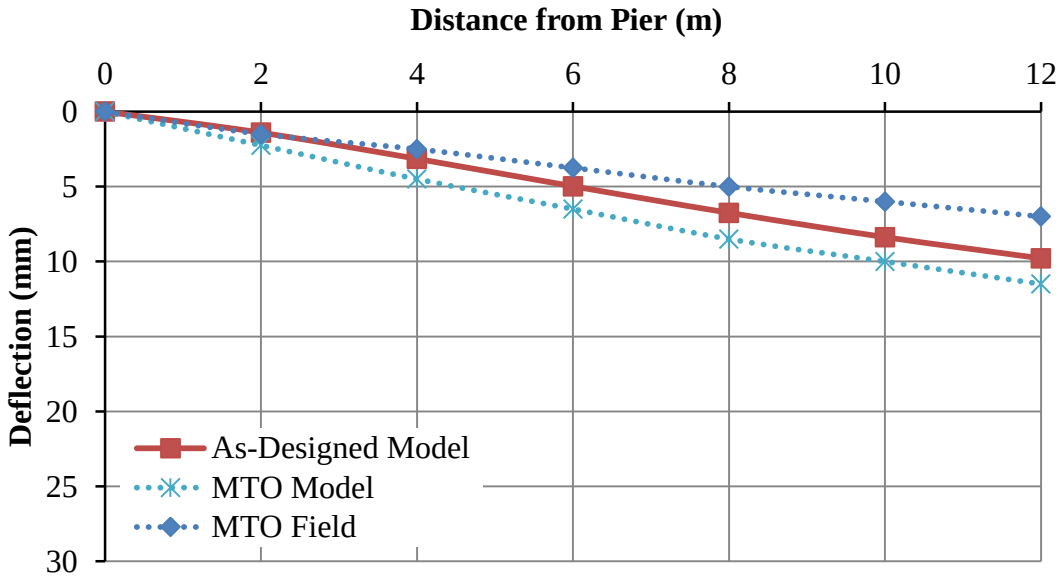

(b)

Figure 3-10 – As-designed model deflection results versus MTO model and field results for (a) Step 7 maximum positive moment and (b) Step 10 maximum negative moment

The model results were compared to the MTO field results, which was the measured response of the bridge subjected to a truck load test. Figure 3-10 shows the deflection results of the computational model versus the MTO field results and the MTO model. The computational model that is used to plot Figure 3-10 can be referred to as the "as-designed" model, because the model is representative of the bridge in the design drawing (see Appendix E for design drawings).

As described previously by Equation 3-1, the effective moment of inertia of the link slab (as a function of applied moment) was calculated in the model, as suggested by Caner and Zia [1]. However, reduction was not needed in the moment of inertia of the link slab because the force effects in the link slab were not large enough to influence the effective moment of inertia (i.e., to cause cracking at the load levels encountered during the load test). From Figure 3-10, the average difference between the SAP2000 computational model and MTO field results were approximately 44% and 28% for Step 7 and Step 10 loading, respectively. Note that the MTO field data shown were extrapolated from the data reported in the MTO report and plotted at 2 m intervals for comparison with the model predictions.

The as-designed model consistently over-predicted the deflections measured during the MTO truck load test, although the predictions are slightly better than those from the MTO model. The over-prediction of deflections suggests that the actual bridge response is stiffer than that of the model. Several modelling assumptions and other factors may have influenced the effective stiffness of the bridge in the model, leading to the over-prediction of deflections. For example, not including the parapet wall or semi-integral abutment restraint in the model resulted in a bridge model with reduced stiffness. Moreover, the material strength of the concrete could have been higher than the as-designed drawings, and therefore would have increased the stiffness of

the bridge. Since the information from the MTO report and field test was limited, assumptions had to be made during the development of the computational model.

Although the relative error in the predicted deflections appears large at first glance (e.g., up to 44% error for Step 7 loading), the largest magnitudes of the errors were 6 mm and 2 mm for Step 7 and Step 10, respectively. Deflection errors of these magnitudes are small in comparison to the overall scale of the bridge (e.g., deflection error of 6 mm for Step 7 loading compared to the bridge span of more than 38 m). Additionally, the computational model from SAP2000 had a slightly better prediction than the MTO model. Therefore, it was deemed that the deflection predicted by the as-designed computational model showed good correlation with the MTO field results for truck loading at Step 7 and Step 10, and it was concluded that the model and modelling approach were sufficiently accurate for further use in this thesis.

3.4 Influence of Support Idealization on Response of Model

In structural analysis and design, it is common to use idealized supports (i.e., hinges and rollers) to represent the support rather than to use spring supports. The use of idealized supports in bridge analysis has been studied by others such as Caner and Zia [2] and Aktan et al. [38]. Researchers that used spring supports, such as Okeil and El-Safty [3] and Ulku et al. [6], also tried to compare computational models with spring supports to that of idealized supports. Therefore, it is needed to investigate the effect of different idealized support combinations on the bridge response to identify which support types should be considered in the parametric study.

The use of spring supports had not been explored in the research by Caner and Zia, but had been by Ulku et al. and Okeil and El-Safty, and it was found that modelling with the spring supports and various idealized support combinations had a large influence on the force effects of the link

slab. From their research, it was also found that a combination of various pinned and roller support conditions led to different deflection results in both the bridge computational model and the laboratory tests. Therefore, the study of support conditions followed the development and computational model for investigation of the link slab bridge. The following parameters were selected for investigation:

- The deflection results between the computational models with idealized support and the spring supports were compared; and
- Determine the combinations of idealized support for further investigation in the parametric study in Chapter 5 and analytical model in Chapter 6.

As part of the study in this thesis, the support conditions at the pier and abutments were idealized in a variety of combination of hinge (pinned) and roller supports to investigate the effect of assumed support conditions on the model response in terms of the bridge deflections and the forces and bending moments in the bridge and link slab. The support configurations investigated are denoted as "R" to indicate a roller support and "H" to indicate a hinge or pinned support. For example, the "HRRH" support configuration represents roller supports at the piers and hinge/pin supports at the abutments, which would mean that the abutment bearings have significantly higher horizontal stiffness than the pier bearings. Similarly, the "RHHR" model represents rollers at the abutments and pins at the piers, representing a stiffer pier bearing than the abutment bearing. This study considered the truck loading in the Step 7 and Step 10 positions, which were determined to be the most relevant load cases from the MTO truck load test. In this study, positive and negative axial force refers to tension and compression forces, respectively. Positive and negative bending would cause the member to bend in positive curvature (bend downwards) and negative curvature (bend upwards), respectively.

3.4.1 Support Combinations Investigated

The study on support combinations included spring supports and the idealized supports (i.e., pins and rollers). In total, this study examined four idealized support models and two spring support models. The idealized support models were "RHRR", "RHHR", "HRRH" and "HHHH". The "RHHR" condition assumed that the pier support is stiffer and provides more restraint than the abutment, while the "HRRH" model assumed that the abutment is stiffer than the pier. The "RHRR" model assumes that all support conditions are rollers (one hinge "H" is provided for static stability and it does not matter where the hinge is placed). The two spring support models were the as-designed computational model in SAP2000 from Section 3.3, which will be referred to as the "elas" model (short for elastomeric bearing support). The second spring support model was the "elas10" model, which increased the stiffness of the elastomeric bearing by 10 times. The "elas10" model was to observe effects of elastomeric bearing stiffening overtime. As discussed previously in Section 3.2.2, the spring stiffnesses were 5.0 kN/mm and 7.5 kN/mm at the pier and abutment, respectively, based on the design values for the elastomeric bearing pads from the design drawings (see Appendix E).

3.4.2 Deflection and Force Effect Results

The six different support conditions (i.e., elas, elas10, RHRR, RHHR, HRRH and HHHH) were modelled in SAP2000 and subjected to the truck loading in the Step 7 and Step 10 positions. The predicted vertical deflection profiles are shown in Figure 3-11 along with the measured deflection results reported by MTO.

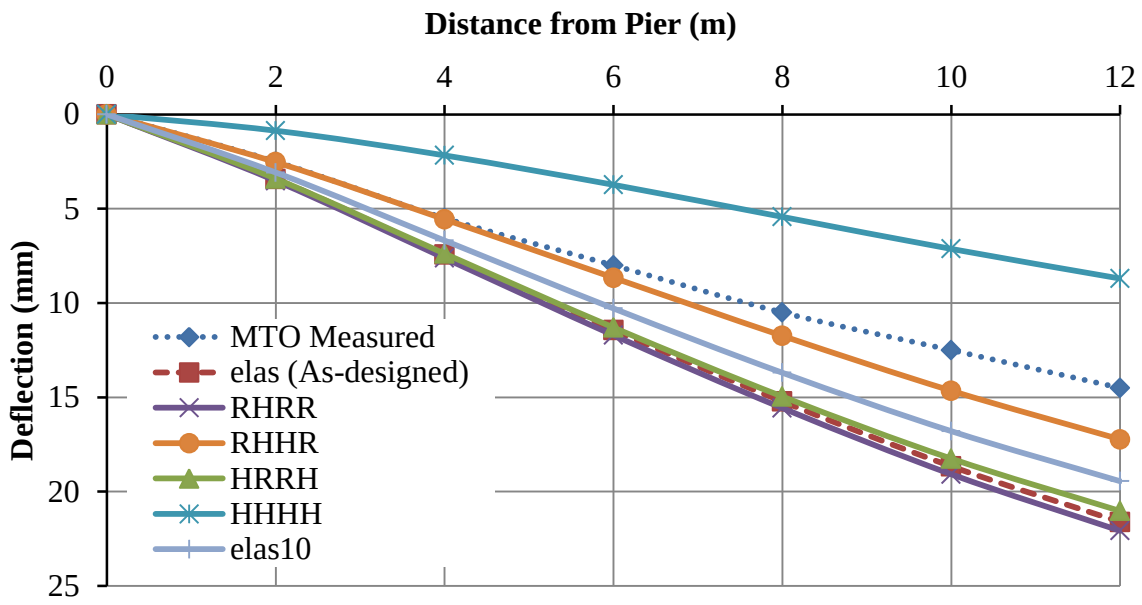

(a)

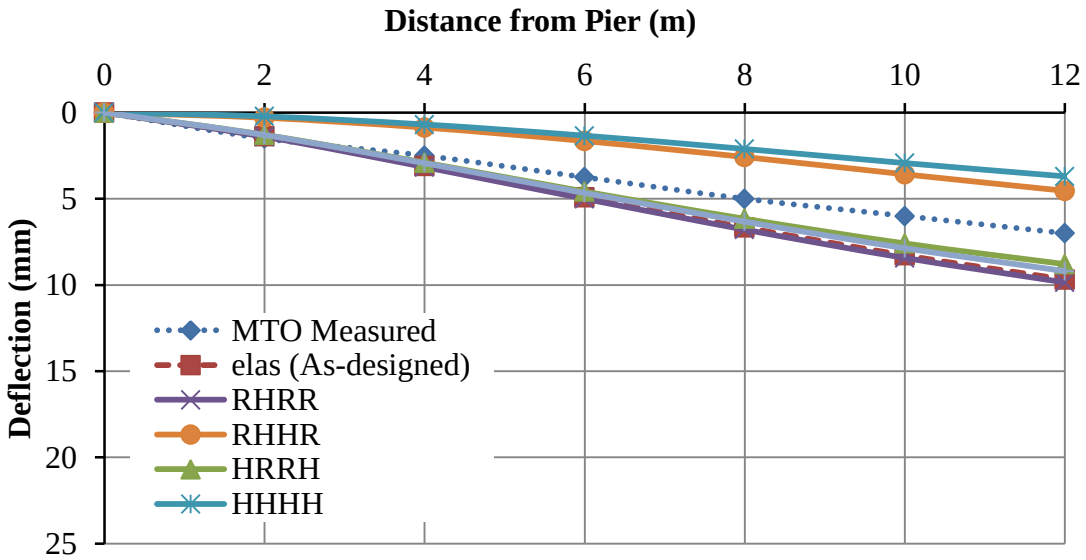

(b)

Figure 3-11 – Comparison of deflections for (a) Step 7 Truck Load Position (max. positive moment) and (b) Step 10 Truck Load Position (max. negative moment)

For Step 7 and Step 10 loading, it was found that the deflection of the RHRR model (Roller-Hinge-Roller-Roller) was the closest to the as-designed "elas" model with spring supports. This indicates that the elastomeric bearing is quite flexible so that horizontal movement is essentially unrestrained as expected.

The elastomeric bearing with 10 times the stiffness (elas10) stiffened the supports and decreased the deflection by approximately 20%, but overall the deflection was still very similar to the RHRR model. The all hinge model "HHHH" showed severe under-prediction of the deflections, and therefore was not analyzed further in this thesis. The differences between the deflections for the various support conditions compared to the as-designed model are summarized in Table 3-2

Table 3-2 – Summary of percent error average for support condition deflection results

Percent Error (%) deflection compared to as-designed ("elas") model	Step 7 (max. positive moment.)	Step 10 (max. negative moment.)
elas10 (10 times elastomeric bearing stiffness)	13	6.3
RHRR (Roller-Roller-Roller-Roller)	2.3	1.8
RHHR (Roller-Hinge-Hinge-Roller)	22	61
HRRH (Hinge-Roller-Roller-Hinge)	19	7.9
HHHH (Hinge- Hinge- Hinge- Hinge)	63	67

Interestingly, the "RHHR" model gave inconsistent deflection predictions for the Step 7 and Step 10 loading. For Step 7, the deflection of the RHHR model was between the RHRR and HHHH models. However, for Step 10 loading, it was closer to the HHHH model. For Step 10 loading, the bridge was loaded symmetrically, which caused the link slab to stretch similar to an axial

spring, producing tension in the link slab. Since the hinge supports restrained the horizontal movement at the pier, the axial force in the link slab acted eccentrically to the hinged support and therefore a moment arm effect was developed, as shown in Figure 3-12.

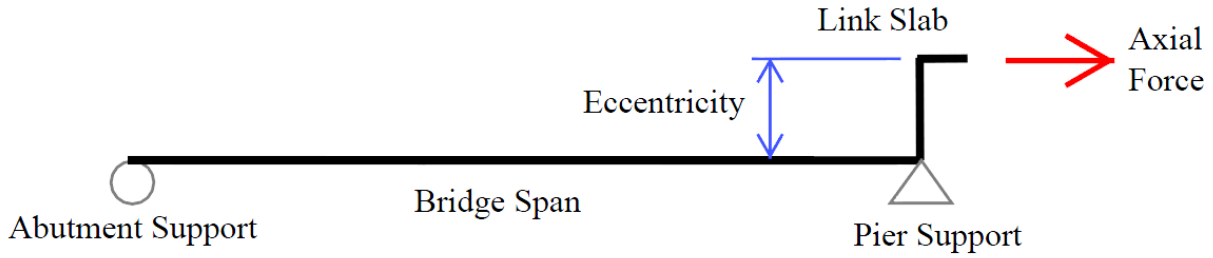

Figure 3-12 – Eccentricity of link slab with axial force

For Step 7 loading, the loading was on one span only. Thus, the link slab resisted the rotation of the girder end and minimal tension was generated in the link slab. The highest bending moment was observed in the link slab right above the pier supports (maximum bending moment at North pier for Step 7 and Step 10 loading), which was consistent with the MTO report findings.

Table 3-3 – Maximum bending moment and axial force in link slab

	Step 7		Step 10	
Model	Axial (kN)	Bending (kN-m)	Axial (kN)	Bending (kN-m)
elas	5.44	-270.21	5.78	-224.13
elas10	48.78	-206.54	51.50	-171.30
RHRR	0.00	-280.16	0.00	-232.37
RHHR	2080.43	-69.50	2103.86	-39.26
HRRH	-1028.13	-259.49	-1005.95	-214.09

The maximum bending moment and axial forces in the link slab are summarized in Table 3-3. From Table 3-3, the "RHRR" and "elas" model showed similar values of maximum axial force and bending moment and had the greatest bending moment compared to the other models. The "RHHR" model showed the greatest tension force (negative axial force) in the link slab. This was because the horizontal restraint at the pier support restricted the movement of the link slab, as discussed previously. The "HRRH" model represents the case with very stiff abutment that restricts horizontal movement. Compression was generated in the link slab in the HRRH model because the pier supports were allowed to move closer to each other. Thus, compression force was generated in the link slab.

Figure 3-13 shows the bending moment diagram for Step 7 and Step 10 loading of the support condition parametric models. As expected, the highest negative moment was found at the pier, which meant that the most probable location for cracking would be in the link slab at the pier. This was consistent with the MTO report that identified cracking a seen previously in Figure 3-5. The bending moment diagram in Figure 3-13 shows that the as-designed "elas" model was very similar to the all roller "RHRR" model and the 10 times stiffness of elastomeric bearing "elas10" model. Even though the "elas10" model had a large implication on the deflection results compared to the as-designed "elas" model, the force effects in the bridge were not significantly affected. The "RHHR" model had the largest negative bending moment in the bridge section (but not at the link slab itself), while the "HRRH" model showed a similar bending moment to the "RHRR" and "elas" model, but also generated a compression force in the link slab. This was because the hinge (or pinned) support at the abutments did not allow the horizontal moment. As the bridge deformed downwards, the girder ends and link slab at the pier moved closer together, generating compressive forces in the link slab.

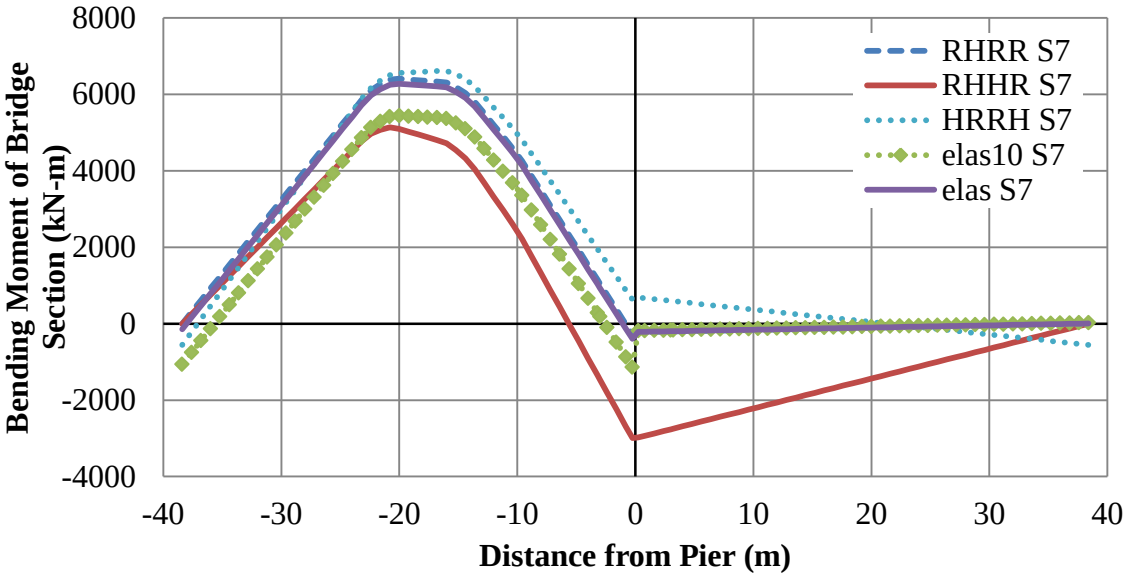

(a)

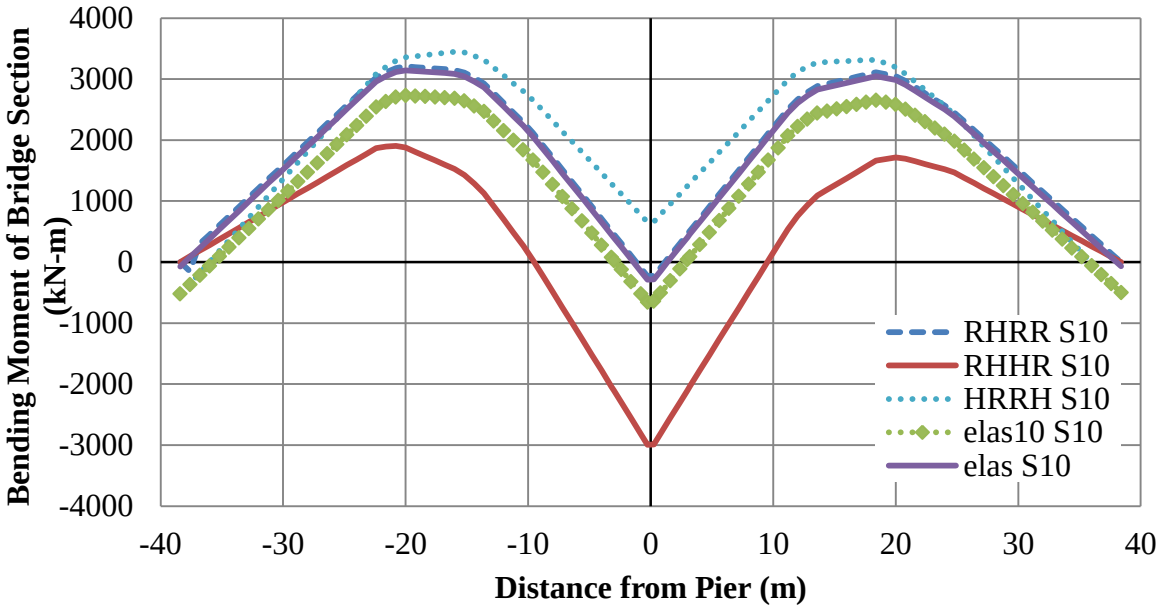

(b)

Figure 3-13 – Bending moment diagrams for (a) Step 7 Truck Load Position (max. positive moment) and (b) Step 10 Truck Load Position (max. negative moment)

3.4.3 Summary of Support Condition Analysis Results

In this study, it was determined that the as-designed model ("elas") was closely represented by the RHRR support combination. The RHRR model was a bridge model with no horizontal restraints (i.e., all rollers) at the supports, except for one horizontal restraint that was required for the structural stability. Other cases that were investigated were RHHR and HRRH support combinations that showcased supports with high stiffness at the pier and abutment, respectively. However, the RHHR and HRRH support conditions did not predict the deflection as well as the RHRR model when compared to the MTO field results. Therefore, the RHRR, RHHR and HRRH support conditions were adopted in the parametric study in Chapter 5 and the analytical model Chapter 6.

3.5 Summary of Computational Model Findings

The findings from the development and assessment of the computational model for the Camlachie Road Underpass are:

- Based on a review of the as-designed drawings for the Camlachie Road Underpass, it was deemed that the abutment-end restraint, approach slab and parapet wall did not need to be included in the computational model. The SAP2000 computational model was found be in agreement with the MTO model, but over-predicted the deflection compared to the MTO field results. The computational model for Step 7 and Step 10 over-predicted the deflection by 6 mm and 2 mm, respectively, which were small in comparison to the scale of the bridge. In conclusion, the results were still within reasonable limits, and the computational model was deemed to be an accurate representation of the link slab bridge.

- The Camlachie Road Underpass model with elastomeric bearing stiffness (i.e., as-designed model) was similar to the RHRR model when deflection and force effects were compared. This was because the RHRR model represented a bridge with no horizontal restraint at the supports. Thus, these results indicated that the elastomeric bearing provided little or no horizontal restraint. It was therefore concluded that the RHRR model would be a good representation of the as-designed condition, and it was not necessary to reconsider the "elas" model in the remainder of this thesis.
- The support conditions investigated were shown to have a significant effect on the force effects developed in the link slab. In particular, significant axial forces were developed in the link slab when there were two or more horizontal restraints at the supports, such as the RHHR and HRRH cases. This highlighted the importance of correctly modelling the supports for representing the actual or designed supports to accurately estimate the force effects in the link slab.
- Models with support idealization "RHRR", "RHHR" and "HRRH" were identified for further use in the parametric study in Chapter 5 and the analytical model Chapter 6.

Chapter 4 Effect of FRC on the Response of Reinforced Concrete Elements

4.1 Introduction

The purpose of the link slab bridge is to provide continuity between adjacent spans and prevent leakage of moisture and chlorides from the bridge deck onto the supporting girders and bridge substructure. In current link slab design, a large amount of steel reinforcement is used to control crack widths and spacing, making placement and compaction of the concrete very difficult. A primary objective of this research is to examine the use of fibre-reinforced concrete (FRC) to further limit cracking in the link slab, and to determine whether the FRC would allow the amount of reinforcing bars to be reduced while still providing adequate crack control. The analysis has two aspects:

- The effect of the FRC on the strength and serviceability of the link slab. Specifically, the tension-stiffening effects of FRC, as a function of fibre type and amount, must be accounted for in the calculation of the ultimate strength of the link slab, and in the expected cracking response (crack width and spacing) under service loading conditions.
- The influence of the post-cracking tensile response of an FRC link slab on the overall response of the bridge. Specifically, since the FRC will change the flexural and tensile behaviour of the reinforced concrete link slab, the effect of this changed behaviour on the design force effects in the link slab and girders must be assessed.

The effect of the FRC on the strength and serviceability of reinforced concrete elements can be assessed analytically by adapting the established mechanics of reinforced concrete behaviour to incorporate the tension stiffening from FRC. This requires a correlation with the actual mechanical properties of the FRC obtained through testing. Once the behaviour of the FRC link

slab is established analytically (incorporating experimentally determined FRC properties), this behaviour can be incorporated into the computational model of the link slab bridge to determine the effect of the FRC on the overall response of the bridge.

In a related study, Cameron [34] conducted an experimental investigation of FRC made with polypropylene fibres and hooked steel fibres. One of the tests performed by Cameron was American Society for Testing and Materials (ASTM) C1609, which investigated FRC prism specimens (without steel reinforcement) in four-point bending. The purpose of the ASTM C1609 tests was to determine the tensile properties and toughness of FRC in flexure. Cameron also tested reinforced concrete beams made using both FRC types to observe the effect of fibres in combination with steel reinforcing bars on the flexural and cracking characteristics of reinforced concrete beams.

The results from Cameron were used in the current thesis research for the analysis and design of link slab with FRC. The two experimental results from Cameron were used to validate theoretical equations from *fib* Model Code [14] that predicted the FRC stress blocks used in analysis and design. The FRC properties were also used to define the plastic hinge properties for the non-linear models in described in Section 5.4 and were used in the Analytical Model in Chapter 6. A brief summary of the FRC experimental study by Cameron is provided in the following sections, along with an analysis of the results for the purposes of defining an analytical process to assess the expected flexural behaviour of a reinforced concrete element made using FRC.

4.2 Experimental Results from Cameron [34]

4.2.1 Four-point Bending Test of FRC Prisms (ASTM C1609 test)

A four-point bending test was conducted by Cameron [34] on FRC prism specimens following ASTM C1609. This test is very similar to the RILEM TC 162 [15] test for characterizing the FRC in four-point bending, which is also designed to characterize the flexural performance of FRC. Fibre volumes of 1.5% for polypropylene and hooked steel fibres were recommended by Cameron based on characteristics of workability and FRC strength [34]. Concrete strengths of 40-50 MPa were used with beam length of 450 mm and cross-section dimension of 150 mm by 150 mm. The averaged force versus displacement relationship is shown in Figure 4-1 for normal concrete (no fibre), polypropylene FRC and hooked steel FRC. Steel reinforcing bars were not used in the concrete specimens of the C1609 experiment.

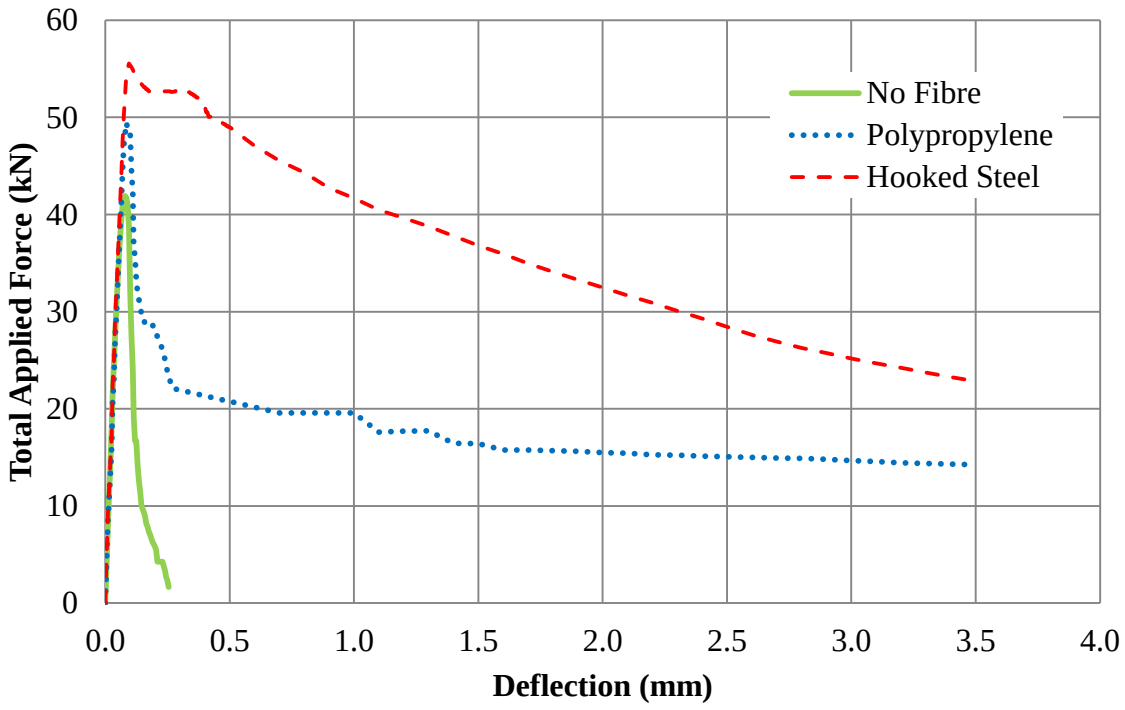

Figure 4-1 – Averaged force versus deflection plot for C1609 test [34]

4.2.2 Four-point Bending Test of Reinforced Concrete Beams with FRC

Cameron [34] also conducted a series of tests on small reinforced concrete beams containing conventional steel reinforcing bars. The beams were 1500 mm in length, 100 mm in width by 150 mm in height. The beam was reinforced with two 10M reinforcing bars with nominal yield strength of 400 MPa at an effective depth of 100 mm. Six specimens were tested in total, two of which were normal concrete specimens without fibres (named "NF"), two were hooked-steel FRC (named "HS"), and two were polypropylene FRC (named "PP"). The compression strengths of the concrete specimens were 40 MPa. The beams were loaded in four-point loading at 500 mm intervals. Figure 4-2 is the load versus deflection plot of the lab specimens. Figure 4-3 is an example of the deformed shape of the concrete beam specimens. From Figure 4-2, the normal concrete beam reached its ultimate load at about 34 kN, which is equivalent to 8.5 kN-m bending moment at mid-span. The polypropylene and hooked-steel FRC reached their ultimate loads at 40 kN, which corresponds to a midspan moment of 10 kN-m.

The results from Cameron showed that the normal concrete (no fibre) beams had larger crack widths than the FRC beams, which tended to have narrower cracks with closer crack spacing along the beam length. In both cases, the beam reached its maximum load when concrete crushed at the top compression fibre. This ultimate behaviour is representative of the formation of plastic hinges. The hooked-steel (HS) and polypropylene (PP) FRC beams were able to carry load past its peak load at higher deflection, showing significantly higher ductility compared to normal concrete (NF) beams. The deformed beam at failure (see Figure 4-3) showed that the concrete compression zone of the FRC beams was still intact and effective after crushing of concrete, whereas normal concrete (NF) showed immediate crushing and breaking of the concrete compression zone. This is consistent with the findings of Dhakal et al. [27], Neves and

Fernandes de Almeida [28], and Wang et al. [29], where the compression strain of FRC is much higher than normal concrete (without fibres). Therefore, in developing a theoretical curve for fibre-reinforced concrete beams, it is important to account for the compressive strength and strain beyond the normally assumed crushing strain of 0.0035.

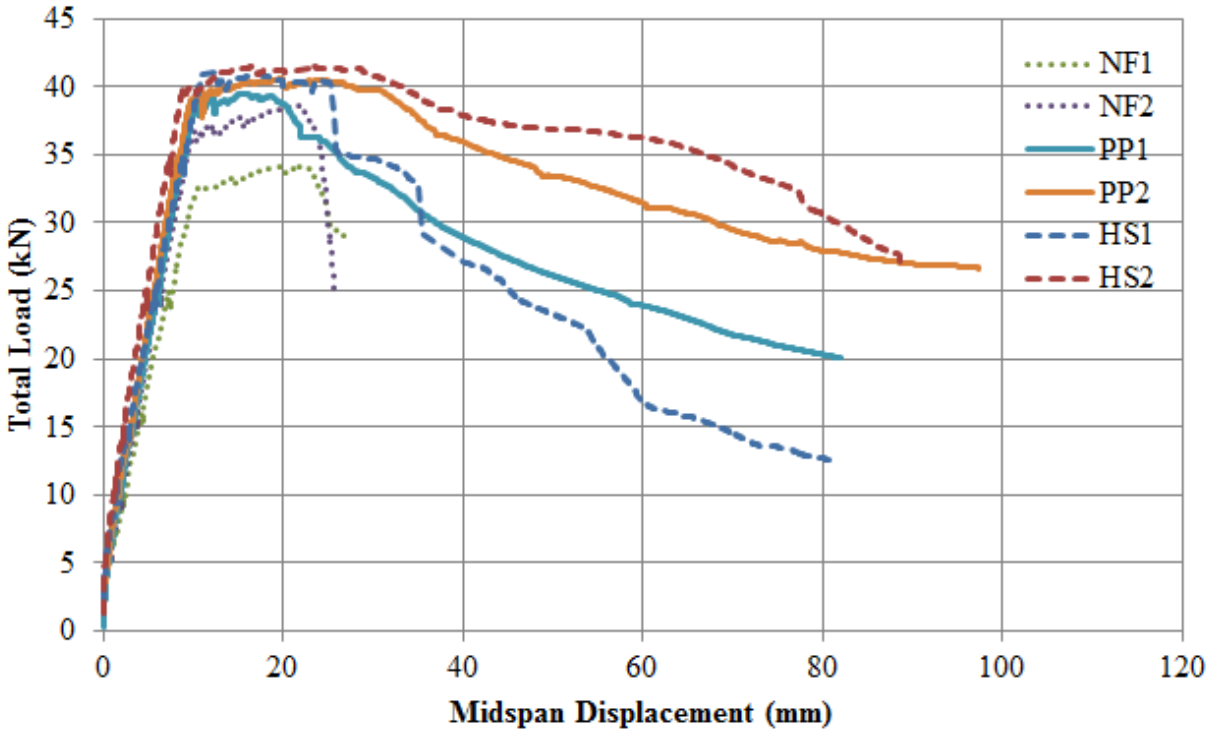

Figure 4-2 – Load versus deflection of beam in four-point loading [34]

Figure 4-3 – Deformed shape of PP1 beam at failure [34]

4.3 Calculation of FRC Stress Block Parameters using ASTM C1609 Results

To calculate the FRC tensile stress blocks using the *fib* Model Code [14], a stress versus Crack Mouth Opening Displacement (CMOD) relationship is required. For example, one can find the relationship through the RILEM TC 162 flexural test setup [15]. Unfortunately, the CMOD results were not measured by Cameron [34] as these results are not part of ASTM C1609. Thus, an alternate method was developed in the current study to establish the stress versus CMOD relationship based on the given information of force and displacement relationship from the C1609 test in Figure 4-1. From Jansson [17] and RILEM TC 162 [15], the stress f_i in a cross-section can be found using Equation 4-1, which is the bending moment divided by the section modulus. F is the total applied force, l is the distance between the support and the load, b is the width of the beam, and h is the height of the beam. Equation 4-1 is adjusted for post-cracking analysis based on recommendation from Jansson [17] and RILEM TC 162 [15].

$$f_i = \frac{3Fl}{bh^2} \qquad 4\text{-}1$$

To convert the displacement to CMOD, the approach by Löfgren [20] was used, which suggested that the portion of the FRC under the load could be treated as a non-linear hinge (or plastic hinge), while the remainder of the FRC beam maintains its linear elastic properties, as shown in Figure 4-4. The crack width "w" is the CMOD, and given the crack length "a" or the concrete compression zone "y_0", the CMOD can be calculated using geometry or a more rigorous method of determining the plastic modulus (and curvature) of the cracked section. In this study, the latter was used in combination with the layer-by-layer analysis and virtual work method presented in Appendices A.4 and A.5, respectively. Sample calculations can be found in Appendices A.5 and A.6.

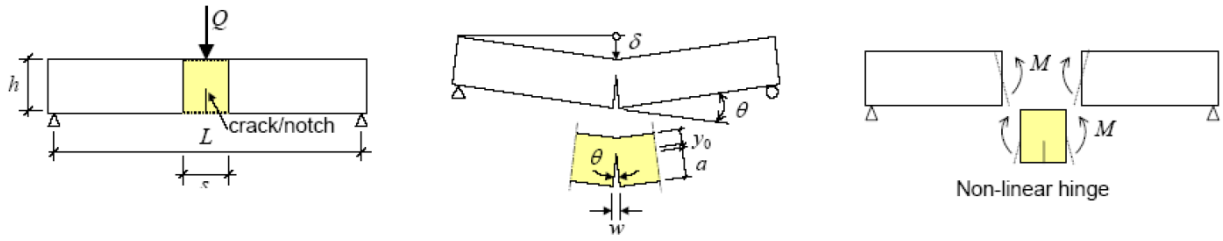

Figure 4-4 – CMOD model from flexural test [20]

Assuming a concrete compression depth "y_0", Figure 4-5 shows the CMOD versus stress relationship of a section, which can be derived based on the force versus displacement relationship from Figure 4-1. A compression depth was assumed based on RILEM TC 162 guidelines [15], which suggested a compression depth of 0.50, 0.34 and 0.10 of the beam in linear elastic behaviour, plastic behaviour and large displacements, respectively. Figure 4-5 is the tensile stress versus CMOD response of the beam calculated based on the measured response from Cameron and the procedure described above.

As mentioned previously, the *fib* Model Code [14] includes provisions for estimating the effective tensile stress block in FRC after cracking for use in analysis and design of reinforced concrete elements made using FRC. The *fib* Model Code defines the FRC tensile stresses at service (f_{Fts}) and ultimate (f_{Ftu}) using Equations 4-2 and 4-3 to calculate the section resistance at service and ultimate loads,

$$f_{Fts} = 0.45 \cdot f_{R1} \qquad 4\text{-}2$$

$$f_{Ftu} = f_{Fts} - \frac{w_u}{CMOD_3}\left(f_{Fts} - 0.5 \cdot f_{R3} + 0.2 \cdot f_{R1}\right) \geq 0 \qquad 4\text{-}3$$

where f_{R1} and f_{R3} are the stresses at CMOD of 0.5 mm and 2.5 mm from the stress versus CMOD relationship, respectively. w_u is the maximum crack width and $CMOD_3$ is 2.5 mm. The crack width equation from the *fib* Model Code is the same as Clause 8.12.3.2 of the CHBDC [32].

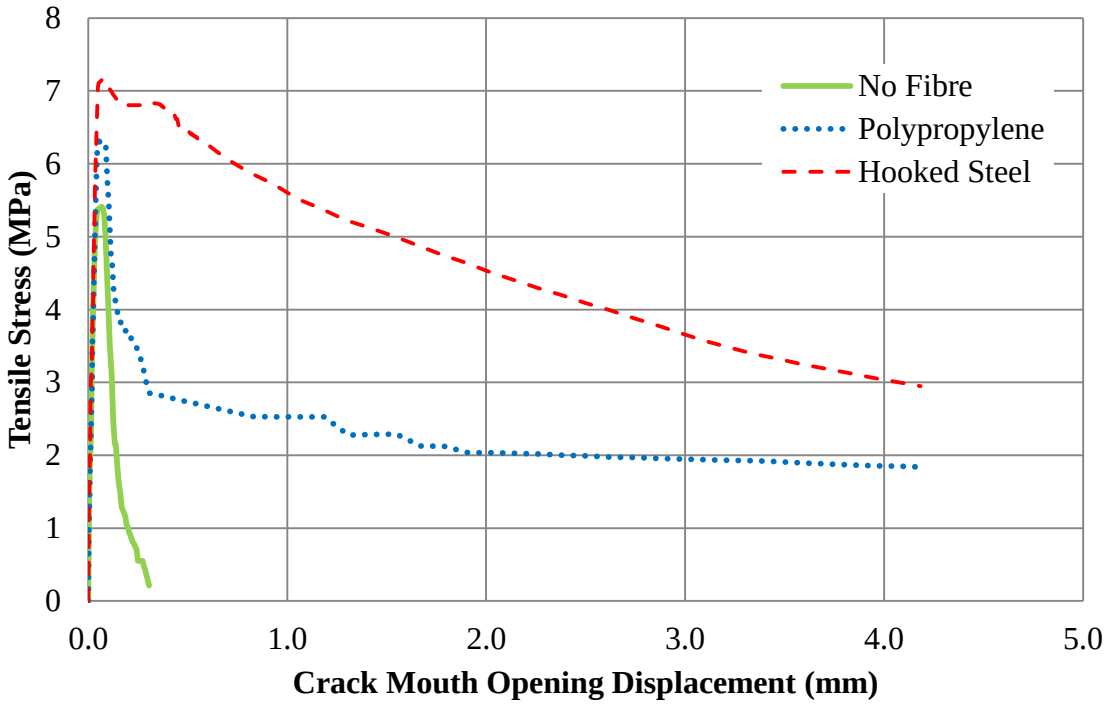

Figure 4-5 – Averaged tensile stress versus crack mouth opening displacement for C1609 test

Using the *fib* Model Code [14] and RILEM TC 162 [15] approaches along with the stress versus CMOD results in Figure 4-5, the rectangular stress block parameters can be estimated. From Figure 4-5, the CMOD at 0.5 mm and 2.5 mm were used for the service and ultimate loads, respectively. The stresses at CMOD 0.5 mm were 2.8 MPa and 6.7 MPa for polypropylene and hooked steel FRC, respectively, and the stresses at CMOD 2.5 mm were 2.0 MPa and 4.3 MPa for polypropylene and hooked steel FRC, respectively. Note that the residual tensile stress for normal concrete (e.g., no fibres) was zero since it did not have any values at 0.5 mm and 2.5 mm CMOD.

Equations 4-2 and 4-3 from the *fib* Model Code were used to define the service and ultimate stress blocks in design. For polypropylene fibres, the service and ultimate stresses were 1.3 MPa and 1.2 MPa, respectively. For the hooked steel, the service and ultimate stresses were 3.0 MPa and 2.8 MPa, respectively. See Appendix A.8 for sample calculations. The results are summarized in Table 4-1.

Table 4-1 – Results for *fib* Model Code FRC Tensile Stress Block determined from C1609 test

	Effective Tension Stress Block (MPa)			
	CMOD = 0.5 mm	CMOD = 2.5 mm	Service Stress	Ultimate Stress
Polypropylene	2.8	2.0	1.3	1.2
Hooked Steel	6.7	4.3	3.0	2.8

4.4 Prediction of Load-Deflection Behaviour for FRC Beams

The FRC tensile stress block parameters derived in the preceding section are appropriate for estimation of the reinforced concrete beam capacity at ultimate and for service-load stress calculations. However, a more rigorous analysis is needed to establish the predicted moment-curvature and load-deflection responses for the beams accounting for the properties of the concrete section before and after the onset of plasticity. As well, development of a more rigorous analysis method was needed to validate the *fib* Model Code method for determining the FRC tensile stress block parameters, in conjunction with the results from the ASTM C1609 test described in Section 4.2.1. The steps taken to predict the load-deflection response of a FRC beam were as follows:

1. define the stress-strain relationship for the FRC;

2. develop the moment-curvature response of the section; and
3. calculate the load-deflection response using the predicted moment-curvature relationship.

The first step was to define the FRC stress-strain relationship. Since the compressive stress and strain relationship for the FRC was not determined experimentally by Cameron [34], the "Modified Hognestad model" was assumed in this thesis to provide an established means of predicting the stress and strain relationship of FRC. From the literature review of compression behaviour of FRC in Section 1.2.4, it was found that the Hognestad model was valid (and conservative) for approximating the stress-strain behaviour of FRC after concrete crushing. The difference between the Hognestad model and the "Modified Hognestad model" in this research is the maximum compressive strain. In the Hognestad Model, the maximum strain is 0.0038, which is close to the crushing strain, whereas the maximum strain of the "Modified Hognestad model" is obtained when stress in concrete is equal to zero. The concrete compress stress (f_c) are shown in Equations 4-4, 4-5 and 4-6.

$$f_c = 0.9 \cdot f_c' \left[2\frac{\varepsilon_c}{\varepsilon_c'} - \left(\frac{\varepsilon_c}{\varepsilon_c'}\right)^2 \right] \text{ for } \varepsilon_c \leq \varepsilon_c' \quad \text{4-4}$$

$$f_c = 0.9 f_c' - \left(\frac{0.135 \cdot f_c'}{0.0038 - \varepsilon_c'} \right) (\varepsilon_c - \varepsilon_c') \text{ for } \varepsilon_c > \varepsilon_c' \quad \text{4-5}$$

$$\varepsilon_c' = 1.62 \cdot f_c' / (12411 + 460 \cdot f_c') \quad \text{4-6}$$

The "Modified Hognestad model" in this research agreed with findings by researchers such as Dhakal et al. [27], Neves and Fernandes de Almeida [28], and Wang et al. [29] (see Section 1.2.4), with represented concrete with large ductility in compression in comparison to normal concrete. In this research, the maximum strain used in the The Modified Hognestad model was 1.3%, which was still very conservative compared to the other researchers. This was deemed a

reasonable approximation because the concrete strength was not over-predicted and ductility was accounted for by using a 1.3% strain. The Modified Hognestad stress-strain curve for a 40 MPa specimen is shown in Figure 4-6.

The next step was to develop the moment-curvature relationship of the reinforced concrete section. A layer-by-layer strain compatibility analysis was used to determine the properties of concrete sections as proposed by Gribniak et al. [19]. This was achieved by subdividing the beam section into rectangular layers and defining a strain in each layer based on strain compatibility. The concrete and reinforcement stresses were then computed based on the strains using the modified Hognestad stress-strain curve for concrete in compression and an elastic-plastic stress-strain curve for steel. The tensile stresses in the FRC were taken based on the *fib* Model Code approach as described in Section 4.3. The service level tensile stress (Equation 4-2) was assumed up until the steel reinforcing bars yielding, after which the ultimate tensile stress (Equation 4-3) was used. Tensile stresses were neglected in the normal concrete. To complete the analysis, the strain profile was varied until equilibrium of the section was achieved, at which time the corresponding moment and curvature on the section were computed. An example of the algorithm for layer-by-layer strain compatibility analysis is presented in Appendix A.4. The moment-curvature diagram was generated by increasing the top fibre concrete strain for the beam section incrementally in the layer-by-layer analysis from 0.001 to 0.0134, and then computing the corresponding bending moment and curvature once equilibrium was satisfied by iteration for a given strain level.

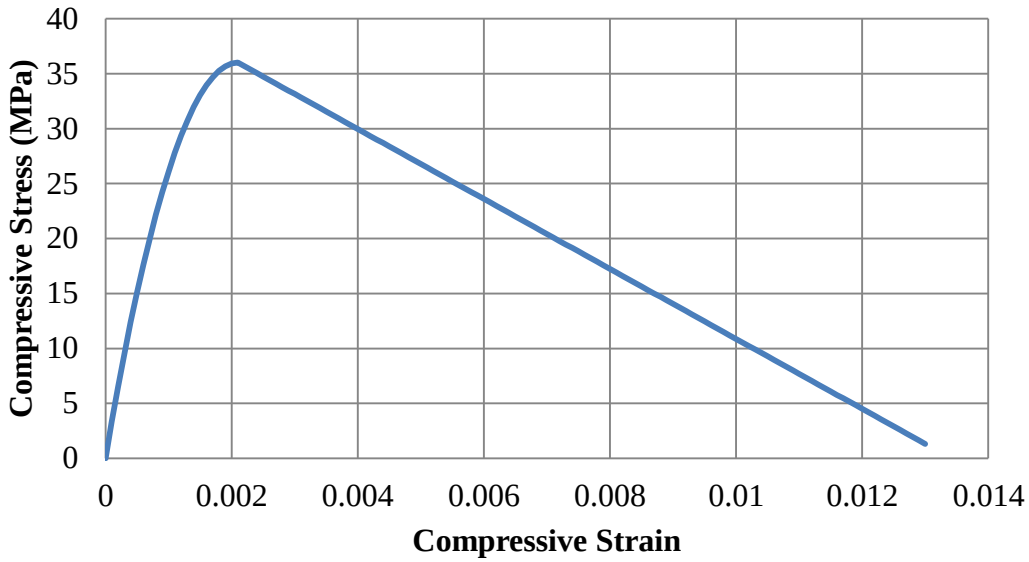

Figure 4-6 – Stress-strain relationship of concrete using the "Modified Hognestad model"

The final step was to compute the load-deflection relationship for a given beam using virtual work. The bending moment diagram of the beam in four-point bending is shown in Figure 4-7. The curvature diagram for the beam at a given load level was determined using the bending moment diagram and the moment-curvature relationship. The curvature diagram was then be used to compute the beam deflection at that load level using virtual work (or any other deflection calculation method). The calculation of deflection using virtual work is shown in Appendix A.5.

Calculation for the load-deflection behaviour of the beams tested by Cameron [34] was completed using the procedures described above in a step-by-step analysis up to failure. Figure 4-8 shows the averaged beam specimen deflection from the experimental results (Cameron [34]) in comparison with the theoretical deflections for the beams with normal concrete (no fibres), polypropylene FRC and hooked steel FRC.

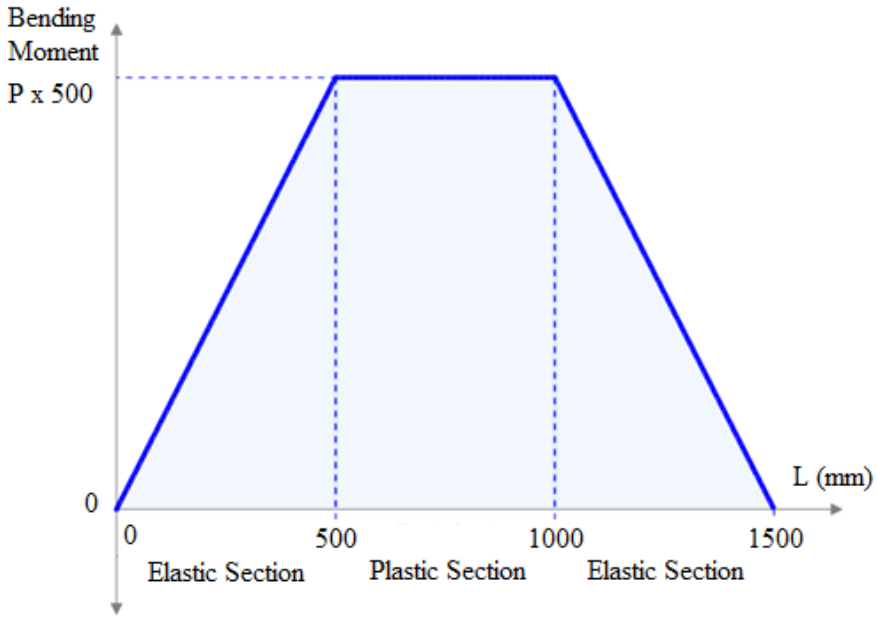

Figure 4-7 – Bending moment diagram for four-point bending

From Figure 4-8, up to a crushing strain of 0.0035, the theoretical load versus displacement agreed with the experimental results. Past the crushing strain, the results predicted using the Modified Hognestad equation also show good correlation with the measured responses for the FRC beams. As mentioned previously, the post-cracking tensile stresses in the polypropylene and hooked steel FRC were obtained using the *fib* Model Code approach from as described Section 4.3, with the appropriate use of service and ultimate stresses. Based on the ASTM C1609 results, the *fib* Model Code tensile stresses for the hooked steel fibre FRC were higher than for the polypropylene fibre FRC, and the effect of this on both the experimental and theoretical results is evident in Figure 4-8.

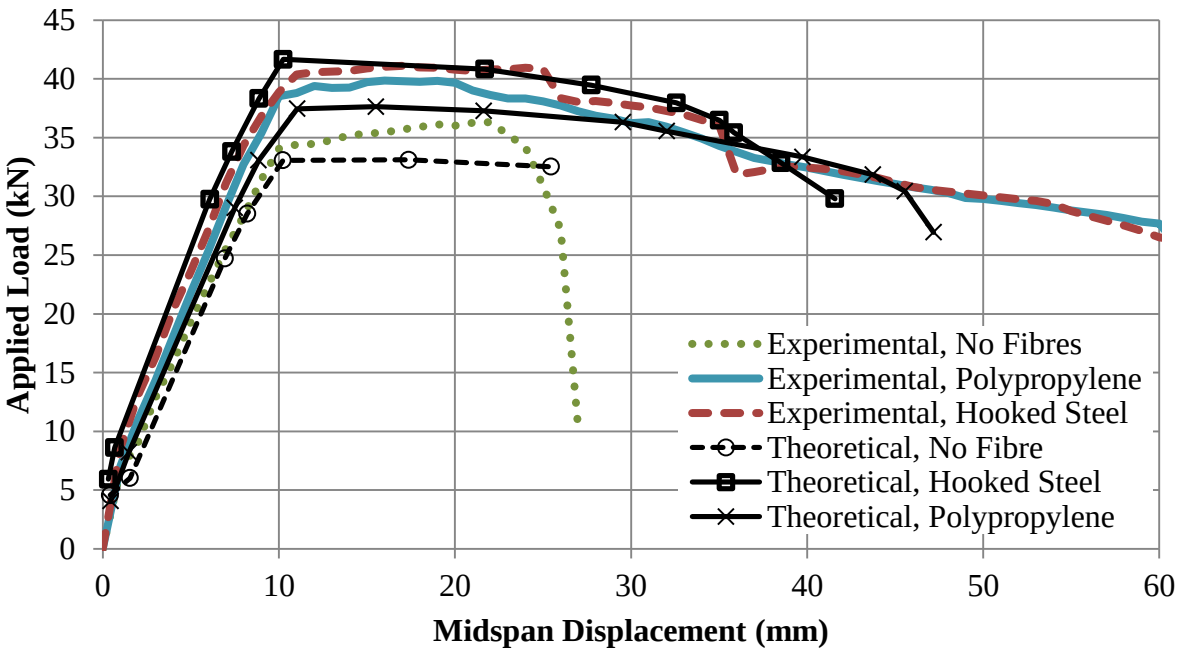

Figure 4-8 – Load-deflection plot of averaged experimental deflection versus theoretical

Up to 40 mm of deflection, the error between the experimental data and the theoretical plots were 9% and 4% for polypropylene fibres and hooked steel fibres, respectively. After a deflection of 40 mm, the theoretical results under-predicted the deflection compared to the experimental results. This was deemed reasonable because the Modified Hognestad equation conservatively estimated the post-peak stress-strain relationship of FRC. Overall, the descending branch of the experimental data had good alignment with the theoretical predictions up to 40 mm of deflection. The theoretical load at yield also showed good correlation with the experimental data. In conclusion, the tensile stress in concrete due to fibres is important in predicting the behaviour of FRC, and the proposed methodology described Section 4.3 based on the *fib* Model Code appears to lead to good results.

4.5 Prediction of Crack Width and Spacing for FRC Beams

Crack width and spacing were measured by Cameron [34] for the four-point bending test for steel reinforced beams with fibres (see Section 4.2.2). Figure 4-9 is the measured load versus crack width relationship for the tested beam specimens. The average crack data were measured at 10 kN, 15 kN, 25 kN, 35 kN and 40 kN. The yield load is about 35 kN and 40 kN for normal concrete and FRC, respectively.

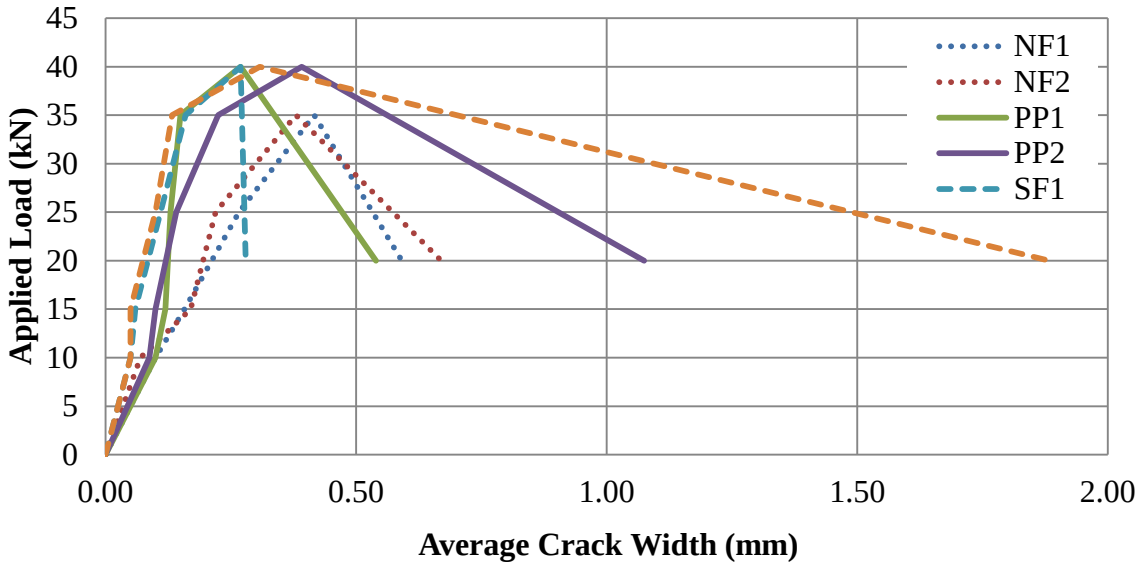

Figure 4-9 – Measured Load versus Crack Width of Specimens [34]

The mean crack width equation from the CHBDC Clause 8.12.3.2 [32] is presented in Equation 7, which takes the same form as the *fib* Model Code [14] and RILEM TC 162 [15]. This equation is also used in the Analytical Model in Section 6.3.2 and Section 6.4.4 of Chapter 6 (to be discussed later),

$$w = k_b \cdot \beta_c \cdot s_{rm} \cdot \varepsilon_{sm} \qquad 4\text{-}7$$

where k_b is 1.2 for epoxy-coated bars and 1.0 for all other components, β_c is 1.7 if the crack is due to loading or if the minimum cross-section dimension exceeds 800 mm, s_{rm} is the average spacing of cracks, and ε_{sm} is the average strain in the reinforcement. The strain in the steel reinforcement was determined using the layer-by-layer analysis described in the preceding section. The *fib* Model Code and RILEM Committee TC 162 methods were used to predict the crack spacing since the CHBDC does not include methods to calculate crack spacing for fibre-reinforced concrete. The *fib* Model Code equation to calculate the mean crack spacing for normal concrete (without fibres) is shown in Equation 4-8,

$$s_m = 2\left(c+\frac{s}{10}\right)+k_1\frac{d_b}{\rho_{eff}}\left(\frac{\varepsilon_1+\varepsilon_2}{2\cdot\varepsilon_1}\right) \qquad 4\text{-}8$$

where c is the concrete cover, s is the spacing of reinforcements, k_1 is 0.8 for deformed reinforcing bars and 1.6 for smooth bars, d_b is the diametre of steel reinforcement, ρ_{eff} is the effective reinforcement, and ε_1 and ε_2 are the maximum and minimum tensile strains in the specimen, respectively. The RILEM Committee TC 162 [25] equation to calculate the spacing with fibres is shown in Equation 4-9,

$$s_m = 50+0.25\cdot k_1\cdot\frac{d_b}{\rho_{eff}}\left(\frac{50}{l_f/d_f}\right)\left(\frac{\varepsilon_1+\varepsilon_2}{2\cdot\varepsilon_1}\right) \qquad 4\text{-}9$$

where l_f/d_f is the fibre aspect ratio, which is the fibre length to fibre diametre. Using Equations 7 to 4-9 and the layer-by-layer analysis, it was found that without fibres, the theoretical mean crack widths were 0.81 mm and 1.4 mm at loads of 15 kN and 25 kN, respectively. With polypropylene fibres, the crack widths were 0.084 mm, 0.22 mm and 0.36 mm at loads 15 kN, 25 kN and 35 kN, respectively. With hooked steel fibres, the crack widths were 0.0089 mm, 0.093 mm and 0.26 mm at loads 15 kN, 25 kN and 35 kN, respectively. The calculations are shown in

Appendix A.6. The theoretical and experimental values are summarized in Table 4-2. From Table 4-2, it could be seen that by using the *fib* Model Code, the equations over-predicted the crack width by 390% and 470% for normal concrete (without fibres) for 15 kN and 25 kN loading, respectively, and a load of 35 kN exceeded the theoretical load capacity of the concrete beam. For polypropylene FRC, the crack width was under-predicted by 24% for 15 kN load, but over-predicted by 63% and 9.1% for 25 kN and 35 kN loading, respectively. Therefore, the predictions for polypropylene FRC were in reasonable agreement with the experimental data. For hooked steel FRC, the crack widths were over-predicted by 84%, 11% and 10% for 15 kN, 25 kN and 35 kN loading, respectively. Therefore, the predictions for hooked steel FRC were in agreement with the experimental data for larger loads. In conclusion, the equations from the *fib* Model Code and RILEM TC 162 provided a reasonable estimate of the crack widths for FRC at high loads.

Table 4-2 – Crack width comparing experimental data to theoretical predictions

	Crack width (mm) at 15 kN		Crack width (mm) at 25 kN		Crack width (mm) at 35 kN	
	Experimental	Theoretical	Experimental	Theoretical	Experimental	Theoretical
No Fibre	0.164	0.81	0.245	1.4	0.400	-
Poly-propylene	0.11	0.084	0.135	0.22	0.330	0.36
Hooked Steel	0.055	0.0089	0.105	0.093	0.290	0.26

4.6 Summary of FRC Experimental Study Findings

Based on the experimental results presented by Cameron [34] and subsequent analysis of FRC beam behaviour described in this Chapter, the following conclusions and observations were made:

- A methodology was demonstrated for calculating the stress versus crack-mouth opening displacement (CMOD) for FRC prisms using the measured load-deflection response from the ASTM C1609 four-point bending test data reported by Cameron.
- The FRC tensile stress block parameters at ultimate and service were obtained from the stress versus CMOD results of the C1609 test, following guidelines from RILEM TC 162 and the *fib* Model Code.
- Based on RILEM TC 162, it was estimated that the service stresses were 1.3 MPa and 3.0 MPa for polypropylene and hooked steel FRC, respectively, and the ultimate stresses were 1.2 MPa and 2.7 MPa, respectively.
- The assumed stress and strain relationship of the Hognestad equation (i.e., Modified Hognestad model) was consistent with experimental results by other researchers such as Dhakal et al. and Wang et al. Thus, the Hognestad equation was used to model FRC with large strains in a layer-by-layer strain compatibility analysis in the research.
- It was found that the theoretical predictions of load-deflection by including the fibre effects and tension stiffening showed close resemblance with the experimental beam test with fibres reported by Cameron. Therefore, a methodology was developed for calculating the tensile stress in FRC using C1609 test results.
- The effects of fibres and tension stiffening will subsequently be used in the non-linear analysis in SAP2000 and the Analytical Model in Chapter 6.

Chapter 5 Parametric Study

5.1 Introduction

The purpose of the parametric study using the computational model is to provide a better understanding of link slab bridge behaviour, and to assess the impact of design decisions on the bridge response and design force effects on the link slab. Current design provisions, assumptions and practices for link slab bridges were reviewed to identify possible gaps in knowledge or potential for design improvements.

The first parameter examined was the various loads types from the CHBDC on the computational model developed in Chapter 3 (i.e., RHRR, RHHR and HRRH). This was to better understand the link slab bridge behaviour. The second parameter examined was the debonded length to allow optimization of the design of the link slab with FRC based on cost and serviceability. The third and last parameter examined was the effect of FRC in non-linear analysis of computational models using plastic hinges. The non-linear analysis was carried out to determine the behaviour of the bridge incorporating the post-cracking responses from FRC. In summary, the parameters covered in this study were the following:

- computational model of link slab bridge with ULS and SLS loads were examined;
- the cost estimate and serviceability analysis of the link slab debonded length were analyzied; and
- Non-linear computational model of link slab bridge with FRC link slab was modelled.

5.1.1 Parametric Study of ULS and SLS Load Cases

The CHBDC [32] loads used in the parametric study were dead load (*D*), live load (*L*) and strain (thermal and shrinkage) load (*K*). The loads were studied independently to determine their effects on the link slab, as well as in possible combinations that would cause the greatest adverse effect on the link slab. The applicable Ultimate Limit State (ULS) and Serviceability Limit State (SLS) load combinations from the CHBDC were chosen. The ULS load combination equations are defined by Equation 5-1,

$$\begin{aligned} ULS\ 1 &= \alpha_D \cdot D + 1.7 \cdot L \\ ULS\ 2 &= \alpha_D \cdot D + 1.6 \cdot L + 1.15 \cdot K \\ ULS\ 4 &= \alpha_D \cdot D + 1.25 \cdot K \end{aligned} \qquad 5\text{-}1$$

where α_D is the safety factor of the dead load defined by CHBDC and varies with the material. The SLS load combination equation is shown in Equation 5-2.

$$SLS\ 1 = D + 0.9 \cdot L + 0.8 \cdot K \qquad 5\text{-}2$$

The ULS and SLS load combinations were applied to the computational model developed in Chapter 3, and a linear elastic analysis was conducted. The study of CHBDC loads and ULS and SLS load combinations are discussed in Section 5.2. The governing load combinations identified in this analysis were then used in the study of debonded length analysis in Section 5.3, non-linear analysis in Section 5.4, and the analytical model in Chapter 6.

5.1.2 Debonded Length

The debonded length study was based on a linear elastic analysis using the ULS loading with the greatest load effect on the link slab. In this parametric study, the debonded lengths investigated

were 0.5%, 2.5%, 5%, 7.5% and 10% of the bridge span length, which were similar to Caner and Zia [1] and Ulku et al. [6]. The calculated force effects were used to determine the required steel reinforcement (bars) in the link slab. The cracking characteristics of normal concrete and FRC were evaluated to determine the serviceability design aspect of the link slab bridge using SLS load combination. A cost estimate of the link slab in Section 5.3 was used to compare the economic benefits of the various debonded lengths with FRC.

5.1.3 Parametric Study of FRC and Non-Linear Analysis using Plastic Hinges

Plastic hinges were introduced into the computational model to model the non-linear response of the link slab bridge to observe the effect of FRC after cracking and the force redistribution for both ULS and SLS. The plastic hinge properties were calculated based on the results of the experimental and analytical study in Chapter 4. The non-linear parametric analysis with the plastic hinges is described Section 5.4.

5.2 Computational Model of Link Slab Bridge with ULS and SLS Loads

The load types investigated in the parametric study were dead load, live load and strain load, and the load values were based on the CHBDC [32]. The CHBDC load combinations considered were presented previously in Section 5.1.1. Note that in the results presented in the following sections, positive and negative bending moments refer to the link slab deformed in positive and negative curvatures, respectively. Positive and negative axial forces are tension and compression forces in the link slab, respectively. The Camlachie Road Underpass from Chapter 3 was used as the model bridge in this analysis, and all results are shown for a linear elastic analysis.

5.2.1 Load Types

5.2.1.1 Dead Load

The dead load of the bridge includes of the reinforced concrete (deck and parapet wall), asphalt wearing surface and steel girder. The cross-section of the Camlachie Road Underpass is shown in Figure 3-2. The unit weights of the materials are provided in Clause 3.6 of the CHBDC. The dead load for the reinforced concrete, steel girder and asphalt wearing surface on the Camlachie Road Underpass are 61.2 kN/m, 14.0 kN/m and 16.8 kN/m, respectively. Calculations of the dead loads are provided in Appendix A.1. The dead loads of the bridge are summarized in Table 5-1. The maximum and minimum load factors (α_D) are provided in Clause 3.5.1 of the CHBDC.

Table 5-1 – Camlachie Road Underpass Dead Load

	Load (kN/m)	α_D Factor Max	α_D Factor Min
Reinforced Concrete	61.2	1.20	0.90
Asphalt Surface	16.8	1.50	0.65
Girder Steel	14.0	1.10	0.95

5.2.1.2 Live Load

The bridge live loads are CL-625-ONT truck loads and uniformly distributed lane loads defined by Clause 3.8.3.2 and Clause 3.8.3.3 in the CHBDC, respectively. For a two-lane bridge with two girders, it is expected that each girder will take a live load of one truck, as implied by Clause 5.7.1.2 from the CHBDC. The CL-625-ONT truck load and the truck load with lane load from the CHBDC are shown in Figure 5-1.

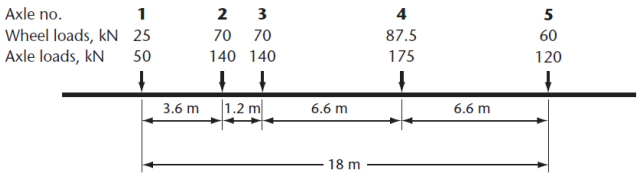

Figure A3.4.1
CL-625-ONT Truck
(See Clause A3.4.1.)

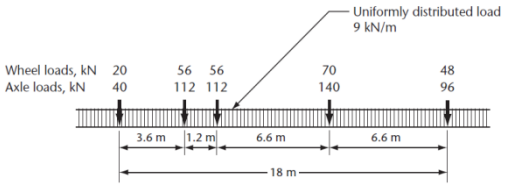

Figure A3.4.2
CL-625-ONT Lane load
(See Clause A3.4.1.)

(a) (b)

Figure 5-1 – CHBDC (a) CL-625-ONT truck load and (b) CL-625-ONT truck load with lane load [32]

The two types of live loads investigated were CL-625-ONT truck load or 80% of CL-625-ONT truck load plus 9 kN/m lane load, as defined by Clause 5.7.1.2 of the CHBDC with Dynamic Load Allowance of 1.25. It was found that the truck live load with DLA was governing. From an influence line generated using SAP2000, it was found that placing "axle 1" from Figure 5-1 at 12.4 m from the abutment-end and "axle 5" near the bridge pier produced the greatest bending moment in both the link slab and the girder. The location with the largest influence was found to be at 17.8 m from the abutment. This is very similar to the influence line without a link slab, where the influence is near the mid-span at 19.2 m from the abutment. See Appendix A.2 for influence line outputs from SAP2000. The load placement that caused the largest bending moment is shown in Figure 5-2.

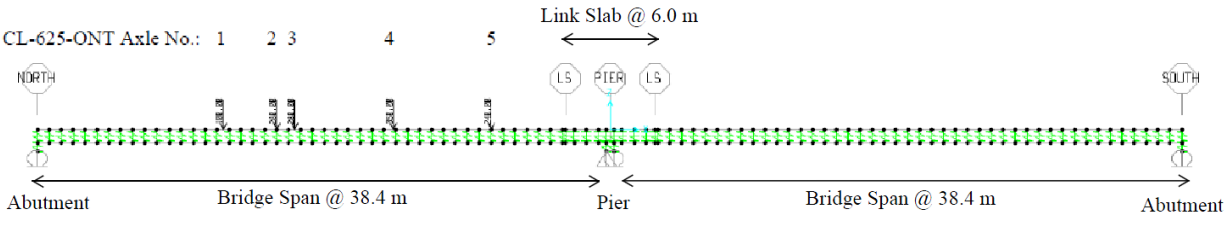

Figure 5-2 – Live load causing largest bending moment in bridge span and link slab

5.2.1.3 Strain Load – Shrinkage

The shrinkage and thermal loading effects on the link slab have not been fully explored in current link slab design literature. In Caner and Zia [1], the shrinkage and thermal loading were converted into an applied bending moments without considering axial force effects. It is important to account for all possible force effects from concrete shrinkage and thermal loading so that the link slab can be designed to accommodate these loadings.

Concrete shrinkage can be calculated based on Section 8.4.1.5.2 of the CHBDC. From the CHBDC, the ultimate shrinkage (ε_{cs0}) can be calculated to represent long term effects of shrinkage, such that as time goes to infinity, the shrinkage is equal to the ultimate shrinkage. The equation for ultimate shrinkage ε_{cs0} (from Section 8.4.1.5.2 of the CHBDC) is defined in Equation 5-3,

$$\varepsilon_{cs0} = \beta_{RH}\left[160 + 50\left(9 - \frac{f_c' + a}{10}\right)\right] 10^{-6};\ \beta_{RH} = -1.55\left[1 - \left(\frac{RH}{100}\right)^3\right] \qquad 5\text{-}3$$

where *RH* is the relative humidity of the location (obtained from Figure A3.1.3 in CHBDC) and a is the difference between the actual concrete strength and the specified strength. From calculations, the ultimate shrinkage is approximately -529(10^{-6}) for the Camlachie Road Underpass. The calculations are provided in Appendix A.3.

The shrinkage of concrete was considered in two separate cases. The first case was if the bridge deck was cast with the link slab, which resulted in shrinkage of the bridge deck affecting the link slab, referred in this research as the "full bridge shrinkage". The second case was if the link slab was cast some time after the casting the bridge deck, such that shrinkage of the deck did not

affect the link slab, referred to as “link slab shrinkage”. The link slab shrinkage represented the case for rehabilitation of conventional bridge into a link slab bridge.

5.2.1.4 Strain Load – Thermal

Thermal loading was examined for both daily and seasonal loading based on Clause 3.9.4 of the CHBDC, with a reference construction temperature at 15 degrees. Daily thermal loading for composite bridges is a gradient temperature, which is 30^{o}C at the surface of the concrete deck to 0^{o}C at the bottom of the bridge deck. For seasonal loading, a uniform thermal load of +31.0^{o}C and -42.5^{o}C were used to represent the extreme values of high and low temperatures, respectively, based on the geographic location of the Camlachie Road Underpass (in Clause C3.9.4 of the CHBDC, a change in temperature of 25 degrees was recommended for the design of bearings and joints, therefore the selected values were conservative).The thermal loads were applied to the entire structure.

5.2.2 Analysis Results for Load Types

5.2.2.1 Dead Load Results

Figure 5-3 is the bending moment diagram of the link slab bridge for the dead load case without load factors (i.e., nominal loads). The maximum bending moments in the link slab for the RHRR, RHHR and HRRH models were -1330 kN-m, -249 kN-m and -1216 kN-m, respectively. Axial forces were 0 kN, 11646 kN and -6312 kN, respectively. The bending moments and axial forces are summarized in Table 5-2 and Table 5-3, respectively. Figure 5-4 is the deflection diagram of the dead loads for the RHRR, RHHR and HRRH models.

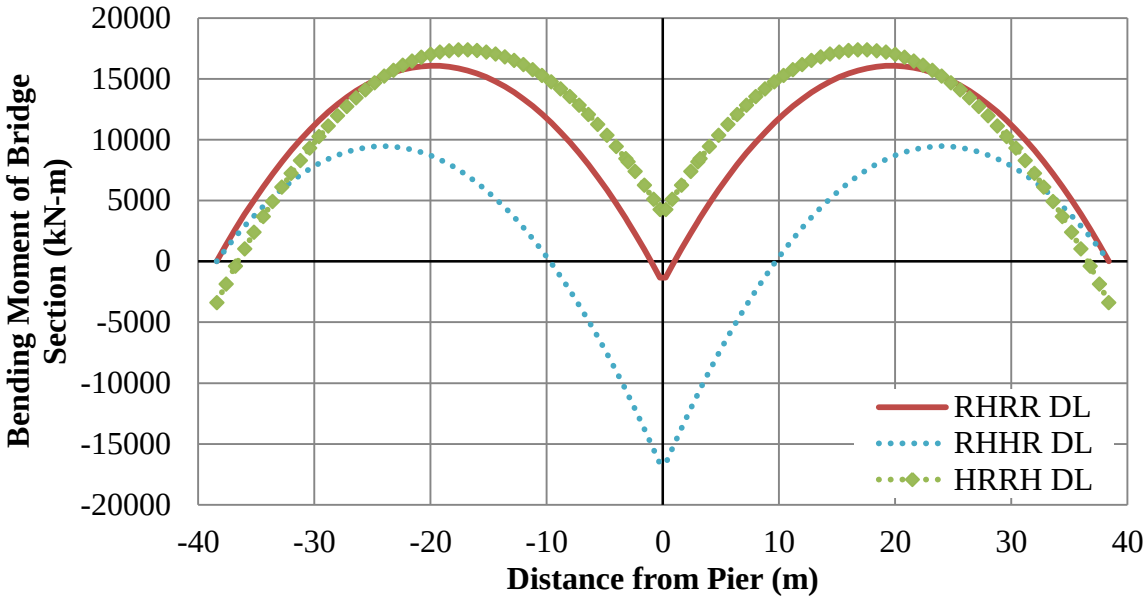

Figure 5-3 – Dead load bending moment diagram

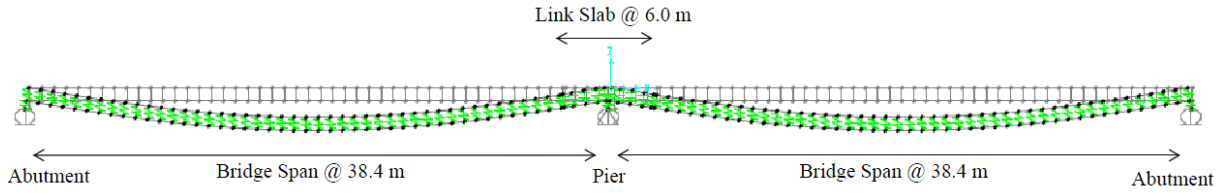

(a)

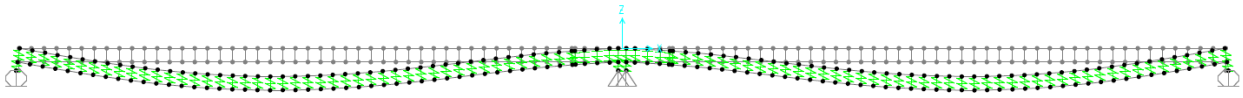

(b)

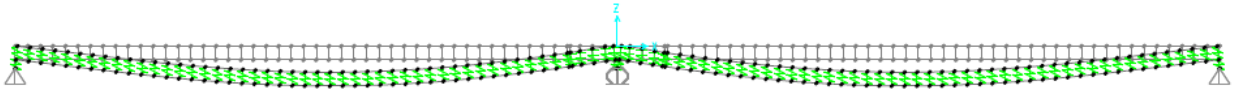

(c)

Figure 5-4 – Dead load qualitative deflection for (a) RHRR, (b) RHHR and (c) HRRH

The deflection diagram shows that the dead load causes the bridge to deflect downwards, generating positive bending in the bridge span. Negative bending is generated in the link slab because the deflection of the girder forces the link slab at the pier to bend in negative curvature.

5.2.2.2 Live Load Results

Figure 5-5 is the bending moment diagram of the link slab bridge due to the truck live load (nominal case) as described in Section 5.2.1. The maximum bending moments in the link slab for the RHRR, RHHR and HRRH models were -383 kN-m, -96 kN-m and -355 kN-m, respectively. Axial forces were 0 kN, 2836 kN and -1435 kN, respectively. Figure 5-6 is the deflection diagram of the live load case.

The deflection diagram shows that the live load causes the bridge span to deflect downwards in the loaded span, generating positive bending in the loaded bridge span. Negative bending is generated in the link slab since the link slab is resisting the rotation of the girder at the pier, similar to that of the dead load.

5.2.2.3 Strain Load Results – Shrinkage

Figure 5-7 is the bending moment diagram of the link slab bridge for the full bridge shrinkage (nominal load). The maximum bending moments in the link slab for the RHRR, RHHR and HRRH models were -855 kN-m, -20 kN-m and -1007 kN-m, respectively. Axial forces were 0 kN, 10259 kN and -8379 kN, respectively. Figure 5-8 is the deflection diagram of the full bridge shrinkage load case.

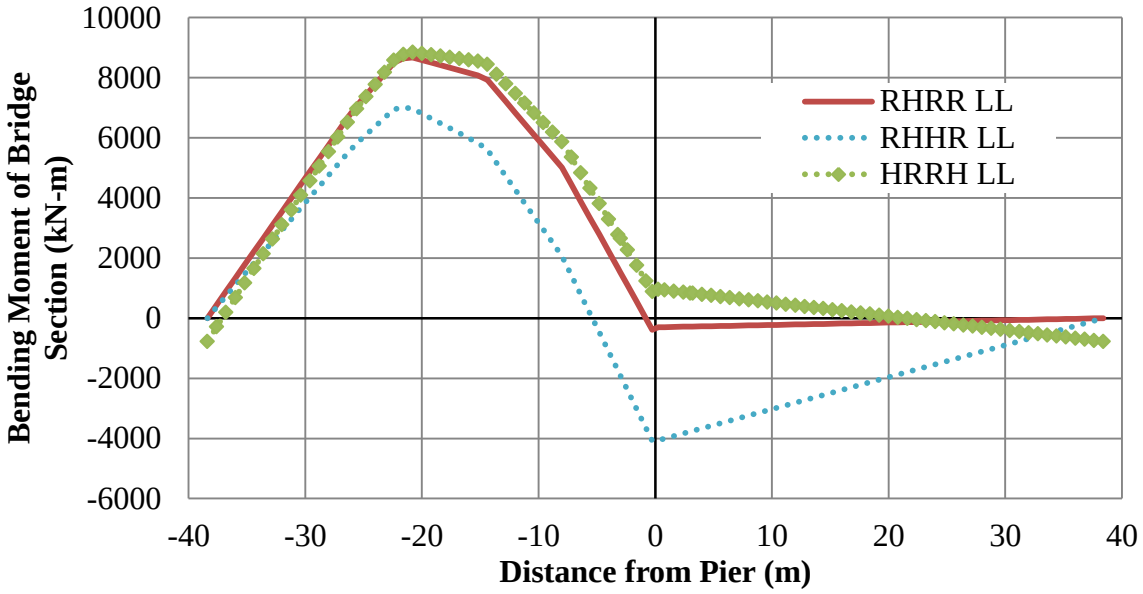

Figure 5-5 – Live load bending moment diagram

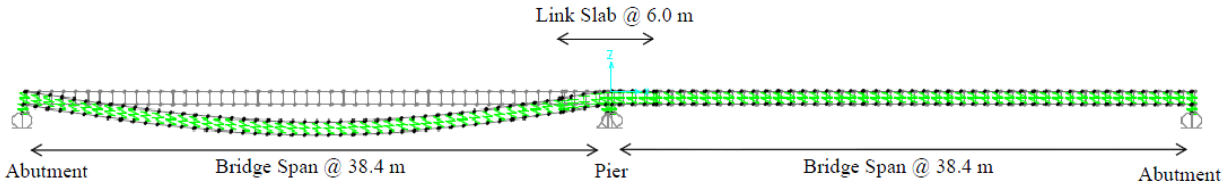

(a)

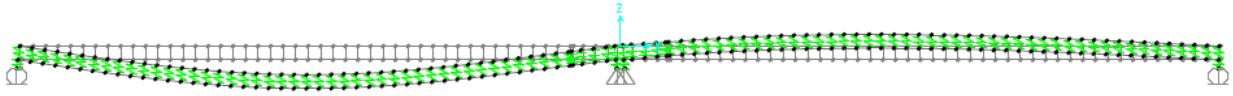

(b)

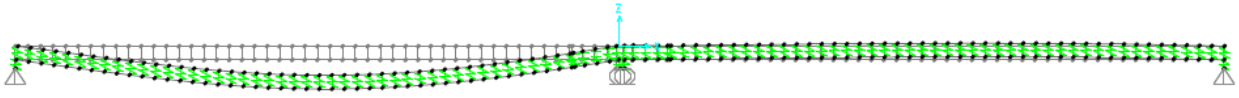

(c)

Figure 5-6 – Live load qualitative deflection for (a) RHRR, (b) RHHR and (c) HRRH

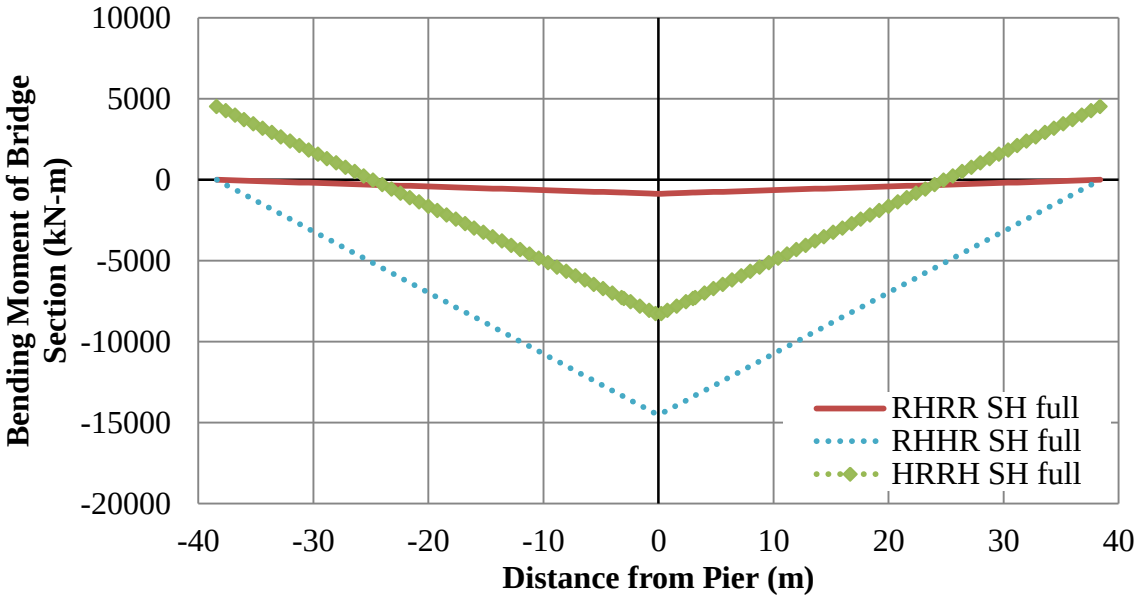

Figure 5-7 – Full bridge shrinkage (strain) load bending moment diagram

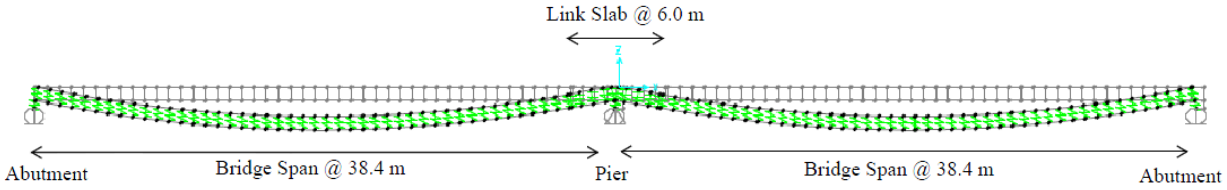

(a)

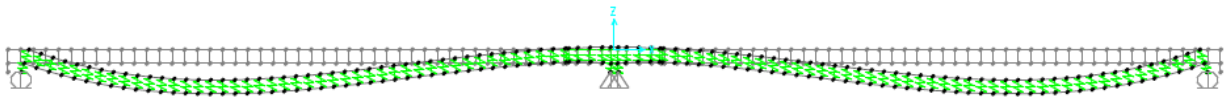

(b)

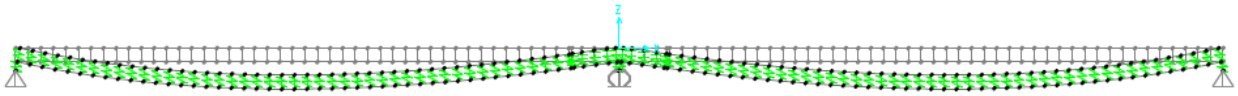

(c)

Figure 5-8 – Full bridge shrinkage qualitative deflection for (a) RHRR, (b) RHHR and (c) HRRH

The deflection diagram shows that the full bridge shrinkage causes the bridge to deflect downwards similar to the dead load case. In the deck-girder cross-section, the bridge deck is shortening due to shrinkage. Thus, the shortening of the top fibre (i.e., concrete deck) produces positive curvature in the bridge section. Similar to the dead and live load, negative bending is generated in the link slab due to the reaction of the link slab at the pier.

Figure 5-9 is the bending moment diagram of the link slab bridge for the case where only the link slab experiences shrinkage (nominal load). The maximum bending moments in the link slab for the RHRR, RHHR and HRRH models were 0 kN-m, 43 kN-m and -33 kN-m, respectively. Axial forces were 0 kN, 1620 kN and 1801 kN, respectively. Figure 5-10 is the deflection diagram of the link slab shrinkage load case.

The deflection diagram of the bridge link slab shrinkage is different than the deflection of the full bridge shrinkage. The RHRR case shows no deflection in the vertical direction because at the link slab, there is no composite action between the link slab and the girder. Thus, the shortening of the link slab does not affect the girder and only shortens the link slab. Since there are no horizontal support restraints at the pier or abutment, they are free to move and zero axial forces are developed in the link slab due to the free movement of the pier supports.

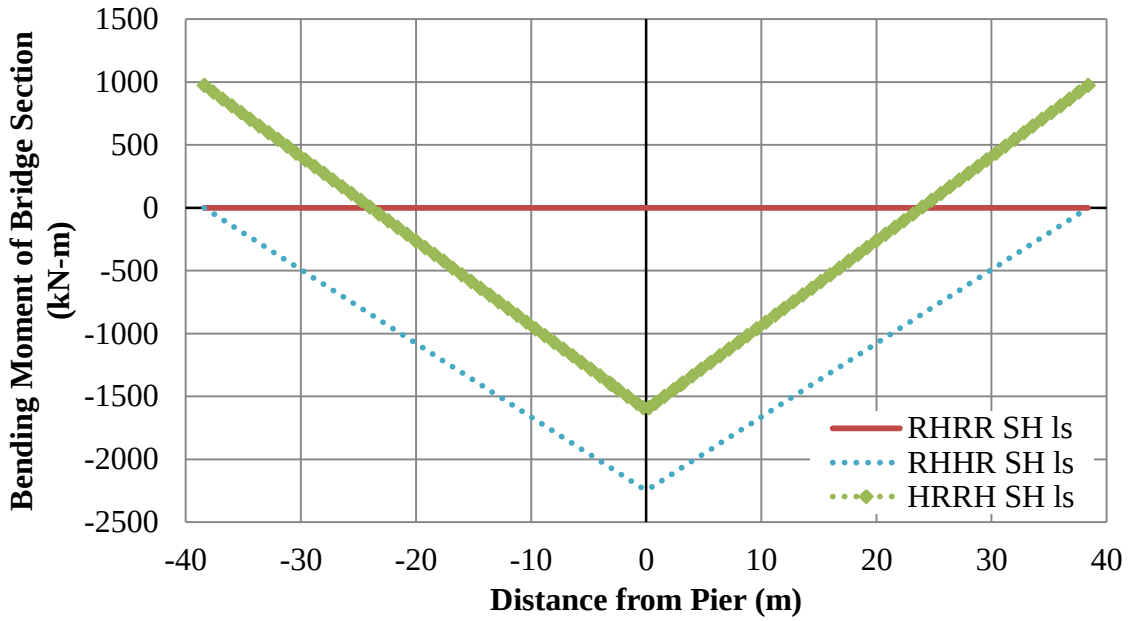

Figure 5-9 – Link slab shrinkage (strain) load bending moment diagram

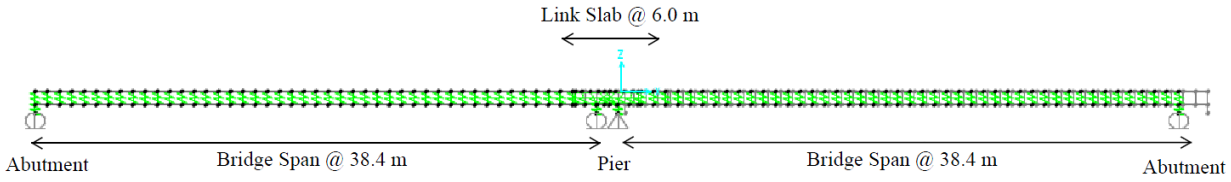

(a)

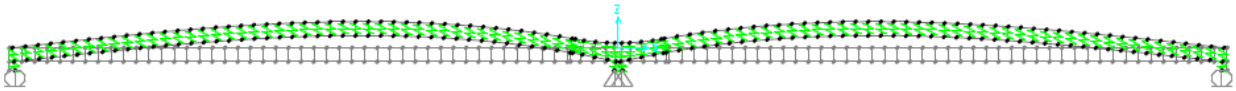

(b)

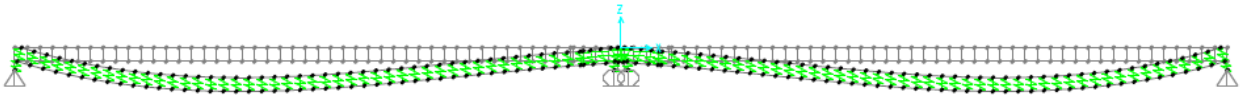

(c)

Figure 5-10 – Link slab shrinkage qualitative deflection for (a) RHRR, (b) RHHR and (c) HRRH

The RHHR model shows a different behaviour with bridge span deflection upwards. This is because there are horizontal restraints at the pier, which restrains the pier supports from freely moving with the shrinkage of the link slab. The restraint at the pier generates internal forces in the link slab as shrinkage is applied. Since there is tensile axial force in the link slab, the eccentricity between the link slab and the pier support act as a moment arm that generates a bending moment in the adjacent spans. The shrinkage of the link slab generates tension at the adjacent bridge deck, producing negative curvature in the adjacent bridge spans and bending moment opposite to that of the dead and live loads.

The HRRH model shows deflection of the bridge spans downwards. In the HRRH model, the hinged supports are at the abutments, the moment arm is at the abutment support. The shrinkage in the link slab pulls at the adjacent bridge spans causes bending in the positive direction, which is analogous to shortening of the bridge deck. The shortening of the bridge deck generates positive curvature in the deck-girder section. Thus, the deflection of the bridge span is downwards.

5.2.2.4 Strain Load Results – Thermal

Figure 5-11 is the bending moment diagram of the link slab bridge for the positive thermal case (nominal case). The positive thermal load maximum bending moments in the link slab for the RHRR, RHHR and HRRH models were -90 kN-m, -4.3 kN-m and 44 kN-m, respectively. Axial forces were 0 kN, 990 kN and -14908 kN, respectively. Figure 5-12 is the deflection diagram of the positive thermal load case.

The RHRR model shows downwards deflection in the vertical direction. This is because with positive thermal load, the girder elongates more than the concrete deck since the steel girder

expands more than the concrete (i.e., higher thermal expansion coefficient). The supports are free to move, so there are no internal forces generated due to the supports. Since the girder elongates more than the concrete, this is analogous to positive curvature and bending where the top fibre shortens and the bottom fibre elongates. The deflection is in the same direction as the dead and live load.

The RHHR case shows a deflection downwards as well, similar to the RHRR model. This is analogous to full bridge shrinkage because the concrete shortens relative to the steel girder, which is similar to shrinkage in the concrete deck. The deflection is in the same direction as the dead and live load.

The HRRH model, however, is not the same as the model with shrinkage load, even though concrete shortens relative to the steel girder. This is because both the concrete and girder are elongating due to the positive thermal load. If the girder deflects downwards, the section is in positive curvature and the concrete deck must shorten to satisfy geometric compatibility between the concrete deck and steel girder. Therefore, in order for both the steel and concrete to elongate, the bridge span must deflect upwards. Deflection of the bridge span upwards elongates the concrete deck and steel girder. This is possible because the hinged support is located below the girder centroid, which means deflection upwards will elongate both the steel girder and concrete deck. The bending moment in the link slab shows negative bending for the RHRR and RHHR models, and positive bending for the HRRH models, which are in the same direction as the dead and live loads.

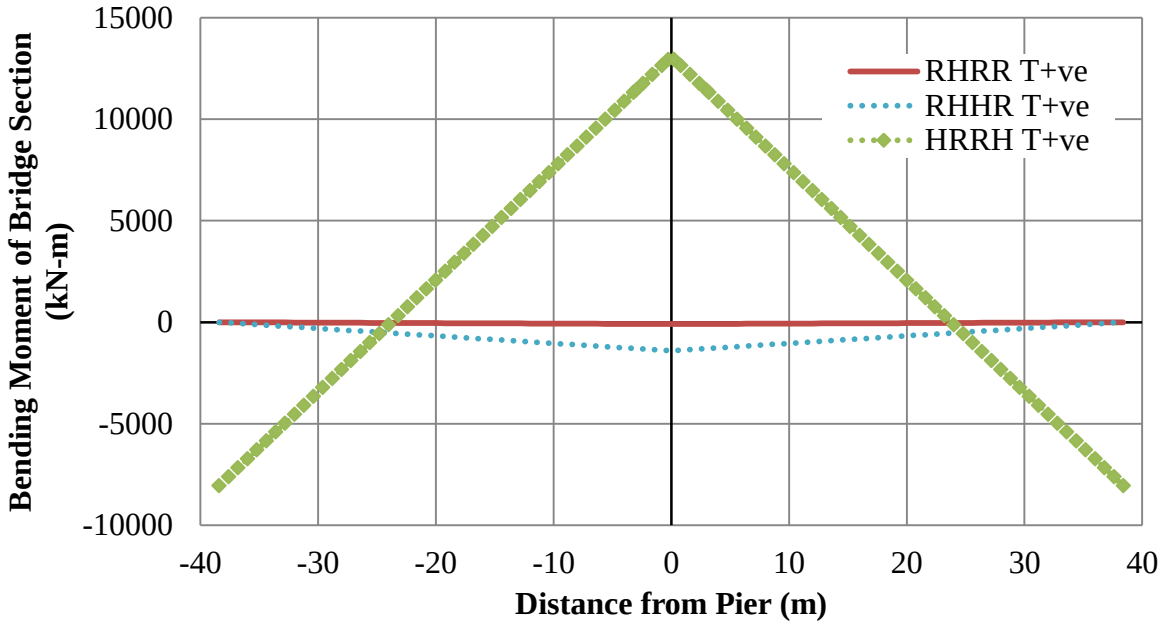

Figure 5-11 – Positive thermal (strain) load bending moment diagram

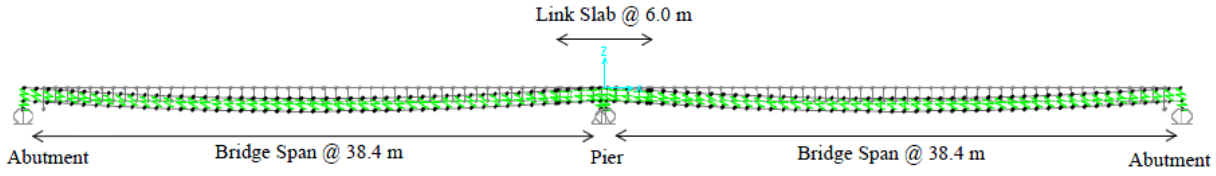

(a)

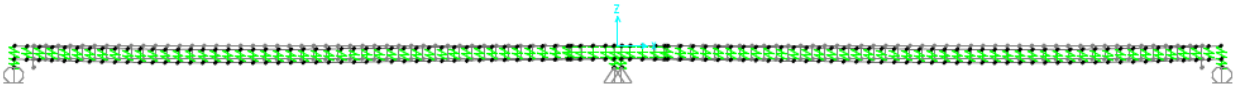

(b)

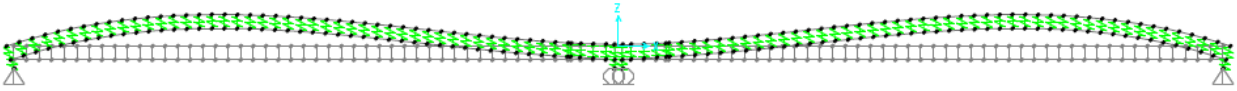

(c)

Figure 5-12 – Positive thermal qualitative deflection for (a) RHRR, (b) RHHR and (c) HRRH

Figure 5-13 is the bending moment diagram of the link slab bridge for the negative thermal case (nominal load). The negative thermal load maximum bending moments in the link slab for the RHRR, RHHR and HRRH models were 42 kN-m, -0.44 kN-m and -248 kN-m, respectively. Axial forces were 0 kN, -1362 kN and 20468 kN, respectively. Figure 5-14 is the deflection diagram of the negative thermal load case.

The deflection diagram of the negative thermal load is the opposite of the positive thermal load. The RHRR case shows upwards deflection in the vertical direction. This is because the girder shortens more than the concrete since the steel has a higher thermal expansion coefficient. The pier supports move to satisfy section compatibility. The deflection is opposite to the direction of the positive thermal load.

The RHHR model shows a deflection upwards as well. The pier supports move to satisfy section compatibility for shortening of both the concrete deck and steel girder. The deflection is opposite to the direction of the positive thermal load.

The HRRH model shows deflection downwards, opposite to the positive thermal load. Since both the concrete deck and steel girder must shorten, the deflection is downwards to shorten the concrete deck to satisfy the geometric compatibility between the concrete deck and steel girder. Support at the pier also moves towards the abutment to shorten the girder due to the negative thermal load.

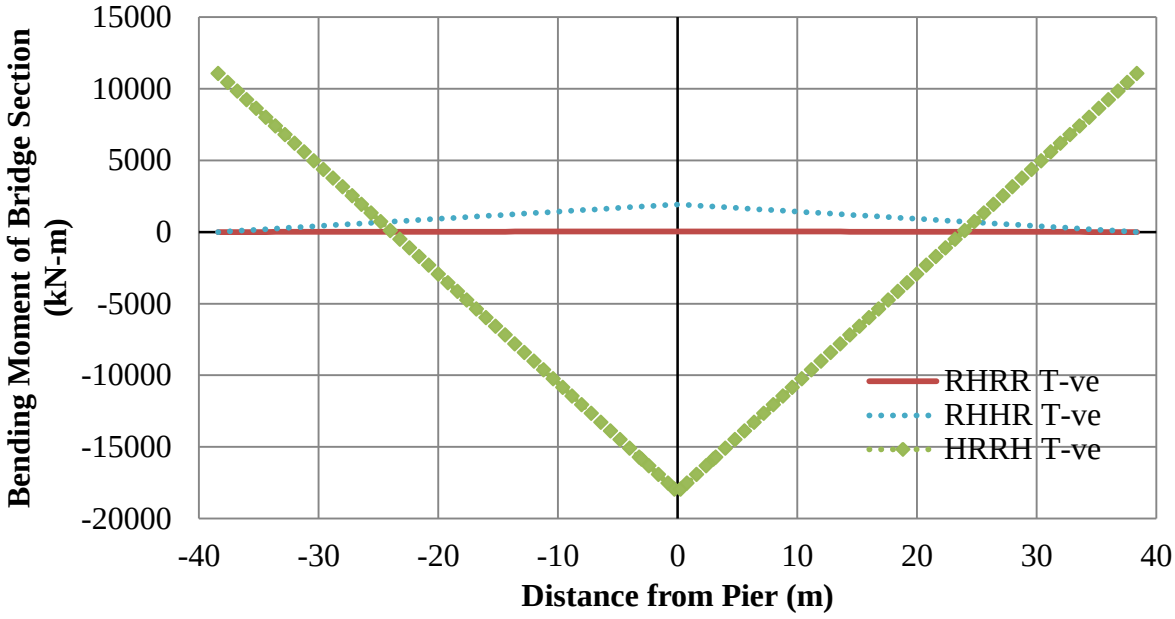

Figure 5-13 – Negative thermal (strain) load bending moment diagram

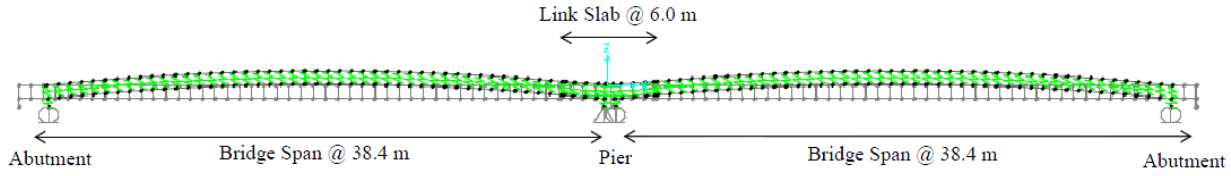

(a)

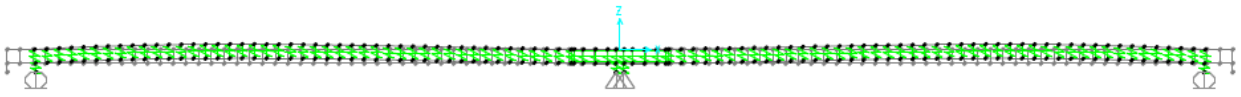

(b)

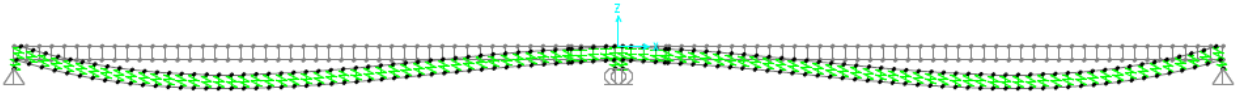

(c)

Figure 5-14 – Negative thermal qualitative deflection for (a) RHRR, (b) RHHR and (c) HRRH

Figure 5-15 is the bending moment diagram of the link slab bridge for the thermal gradient case (nominal load). The thermal gradient load maximum bending moments in the link slab for the RHRR, RHHR and HRRH models were 47 kN-m, 46 kN-m and 46 kN-m, respectively. Axial forces were 0 kN, -13 kN and 208 kN, respectively. Figure 5-16 is the deflection diagram of the gradient thermal load case.

The deflection diagram of the bridge with gradient thermal load is opposite of the dead and live loads. In all cases, the bridge deflects upwards. The thermal load is in the concrete deck only with 30^{o}C at the top of the concrete deck to 0^{o}C at the bottom of the concrete deck. There is no thermal change applied to the steel girder. Thus, the steel girder shortens or elongates only as necessary to accommodate the geometric compatibility between the concrete deck and steel girder. Since the concrete elongates due to thermal gradient, the curvature is negative for the deck-girder section, opposite of full bridge shrinkages, dead load and live loads.

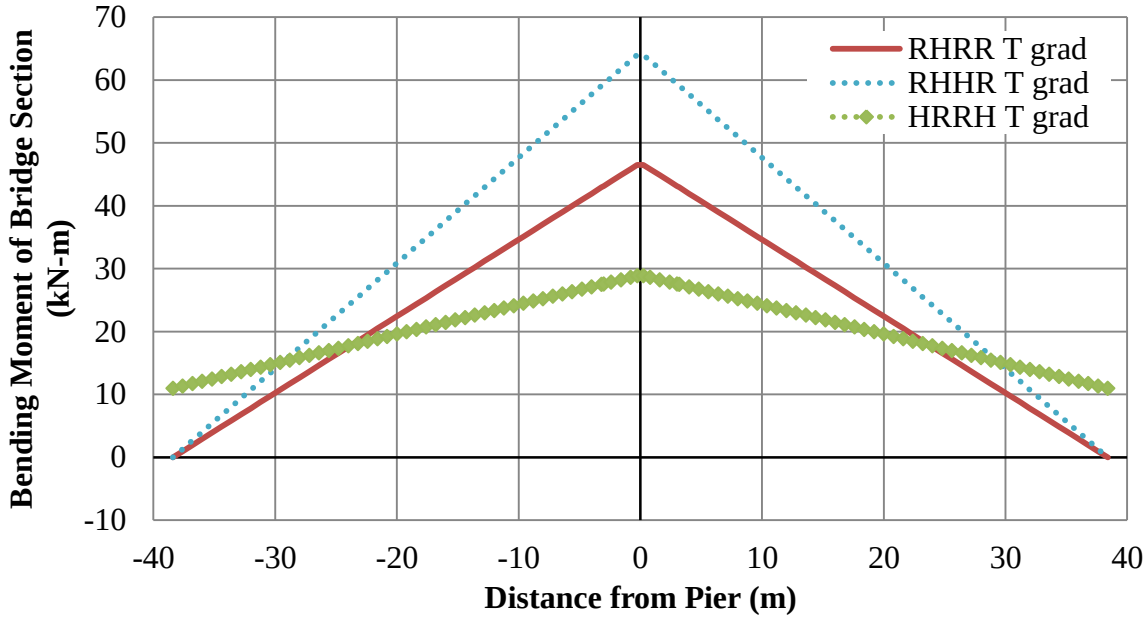

Figure 5-15 – Gradient thermal (strain) load bending moment diagram

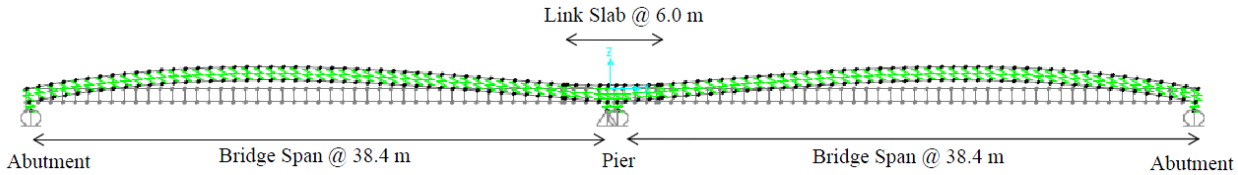

(a)

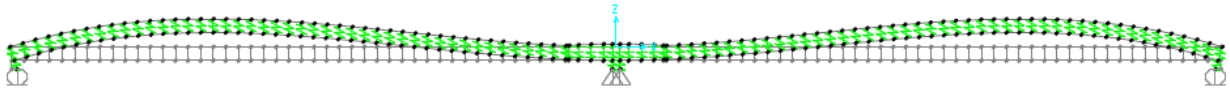

(b)

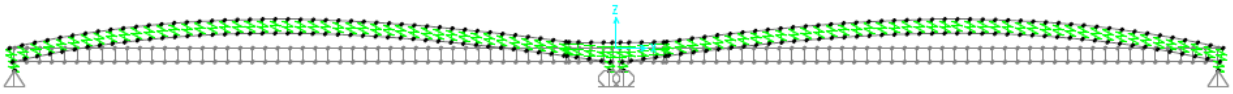

(c)

Figure 5-16 – Gradient thermal qualitative deflection for (a) RHRR, (b) RHHR and (c) HRRH

5.2.2.5 Load results and Application in ULS and SLS Combinations

The governing or critical results from the load type analyses in terms of the bending moment and axial force in the link slab are shown in Table 5-2 and Table 5-3, respectively. In the tables, "DL" is dead load, "LL" is live load, "SH Full" is full bridge shrinkage, "SH LS" is link slab shrinkage, "T +ve" is positive thermal load, "T –ve" is negative thermal load, and "T grad" is gradient thermal load. The sense of the bending moment, axial force and deflection of the loads are used to determine which loads are used in ULS and SLS combinations to produce the largest load effect in the link slab.

Table 5-2 – Link Slab bending moment results from parametric study of various load types

Bending moment in link slab (kN-m)							
	DL	LL	SH Full	SH LS	T +ve	T -ve	T grad
RHRR	-1330	-383	-855	0	-90	42	47
RHHR	-249	-96	-20	43	-4.3	-0.44	46
HRRH	-1216	-355	-1007	-33	44	-248	46

Table 5-3 – Link Slab axial force results from parametric study of various load types

Axial force in link slab (kN)							
	DL	LL	SH Full	SH LS	T +ve	T -ve	T grad
RHRR	0	0	0	0	0	0	0
RHHR	11646	2836	10259	1620	990	-1362	-13
HRRH	-6312	-1435	8379	1801	-14908	20468	20

From Table 5-2, it can be seen that the effect of the dead load (DL) is very significant, producing the largest force effects in the link slab compared to the other load types. Additionally, full bridge shrinkage (SH Full) also produced very large force effects. Both cases generated bending

moments and axial forces more than 3 times larger than the live load case. Therefore, where construction staging will permit, it is recommended to place the concrete for the link slab after the bridge deck concrete has been placed. The bridge deck concrete should be allowed to experience initial shrinkage to minimize the effect of the bridge deck shrinkage on the link slab, and to reduce the dead load effect on the link slab during early stages of construction. It is noted that this will also be the case for existing bridges where the link slab is installed (to replace an expansion joint) as part of a rehabilitation project. That is, the link slab will not experience shrinkage loading from the rest of the concrete deck, nor will it be subject to the dead load effects from the rest of the bridge since they would already be in place before the link slab was installed. For a detailed discussion of the axial forces developed in the link slab and the effects of support conditions, please refer to Section 3.4.

Other than the DL and SH Full load cases, it can be seen that live loads produces the next largest force effects in comparison to the other load types. In the ULS 1 load combination, all bridge models (i.e., RHRR, RHHR and HRRH) will only have the live load case since the dead load and full bridge shrinkage will not be present assuming the recommended construction staging described above is used (i.e, the link slab is placed after hardening of the deck concrete). In the ULS 2 load combination, all of the models will include live load in combination with thermal load, and the addition of shrinkage in the HRRH model only. The thermal load is positive for RHRR and RHHR model and negative for HRRH model. The ULS 4 load combination has no live load component in the combination; therefore loads having the same sense as the shrinkage load are used, which are negative thermal and gradient thermal loads for the RHRR and RHHR models, and only the positive thermal load for the HRRH model. The load types included in the SLS 1 load combination are similar to ULS 2 since both cases include live load and strain load.

Table 5-4 is a summary of the load types used in the ULS and SLS load combinations for the rehabilitation of existing bridges.

Table 5-4 – Loads used in the ULS and SLS combinations

Loads in Rehabilitation of Existing Bridges ULS and SLS studies				
	ULS 1	ULS 2	ULS 4	SLS 1
RHRR	LL	LL, T +ve	SH LS, T -ve, T grad	LL, T +ve
RHHR	LL	LL, T +ve	SH LS, T -ve, T grad	LL, T +ve
HRRH	LL	LL, SH LS, T -ve	SH LS, T +ve	LL, SH LS, T -ve

5.2.3 Parametric Study of ULS and SLS using Linear Elastic Model

The CHBDC load combinations presented in Section 5.2.1were applied using the load types listed in Table 5-4. Figure 5-17 shows the results of the ULS 1 analysis for the rehabilitation of existing bridge. The maximum link slab bending moments for RHRR, RHHR, and HRRH were -815 kN-m, -204 kN-m and -753 kN-m, respectively. Link slab maximum axial forces for RHRR, RHHR, and HRRH were 0 kN, 6026 kN and -3049 kN, respectively.

Figure 5-18 shows the results of the ULS 2 analysis for the rehabilitation of existing bridge. The maximum link slab bending moments for RHRR, RHHR, and HRRH were -881 kN-m, -191 kN-m and -1070 kN-m, respectively. Link slab maximum axial forces for RHRR, RHHR, and HRRH were 0 kN, 6814 kN and -22740 kN, respectively.

Figure 5-19 shows the results of the ULS 4 analysis for the rehabilitation of existing bridge. The maximum link slab bending moments for RHRR, RHHR, and HRRH were 110 kN-m, 119 kN-m and -351 kN-m, respectively. The maximum link slab axial forces for RHRR, RHHR, and HRRH were 0 kN, 312 kN and 27836 kN, respectively.

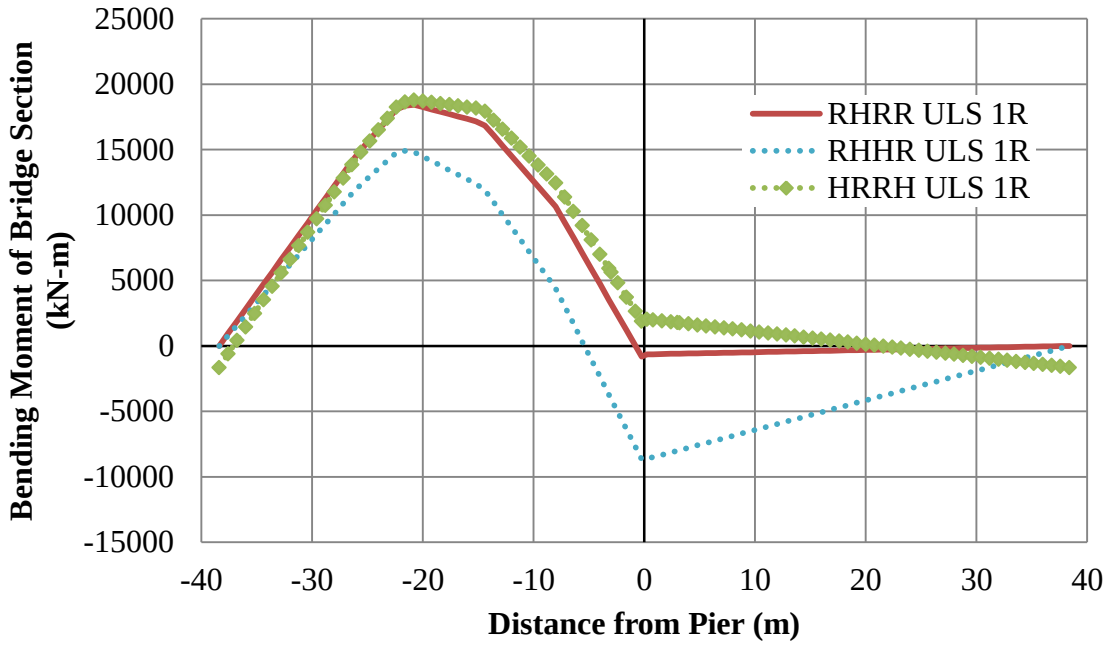

Figure 5-17 – ULS 1 Rehabilitation of Existing Bridge Analysis Results

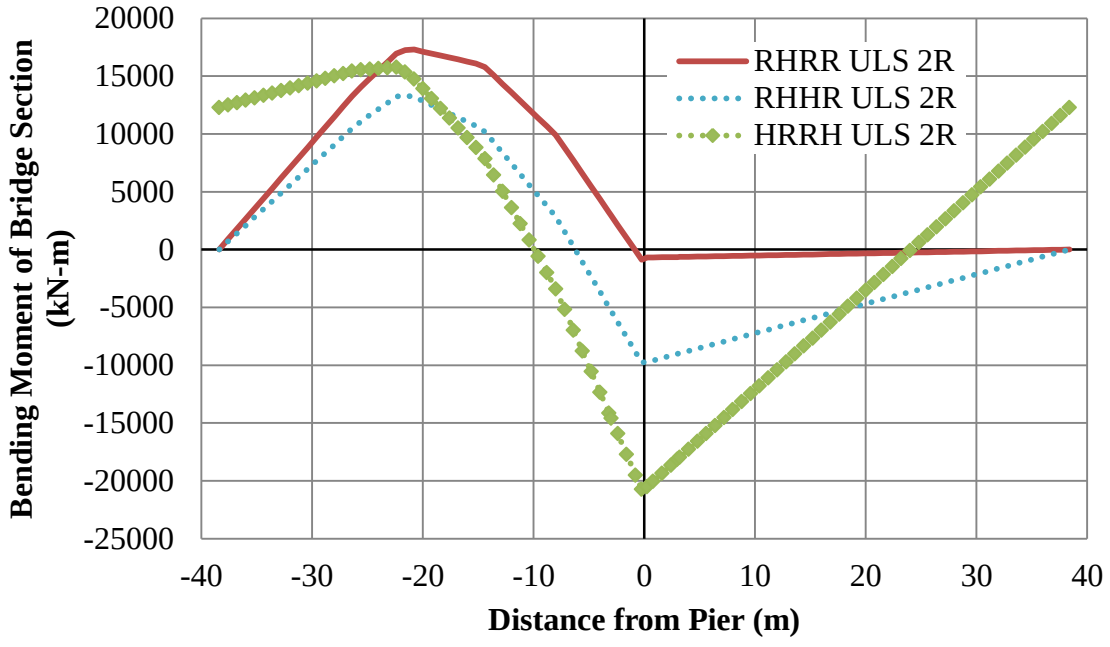

Figure 5-18 – ULS 2 Rehabilitation of Existing Bridge Analysis Results

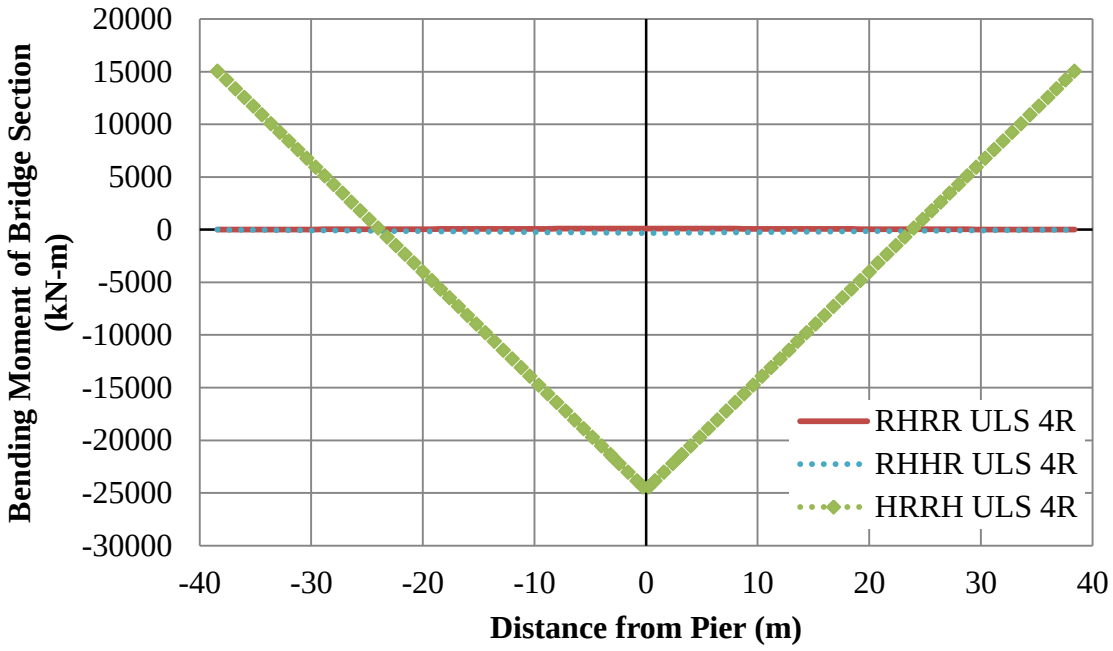

Figure 5-19 – ULS 4 Rehabilitation of Existing Bridge Analysis Results

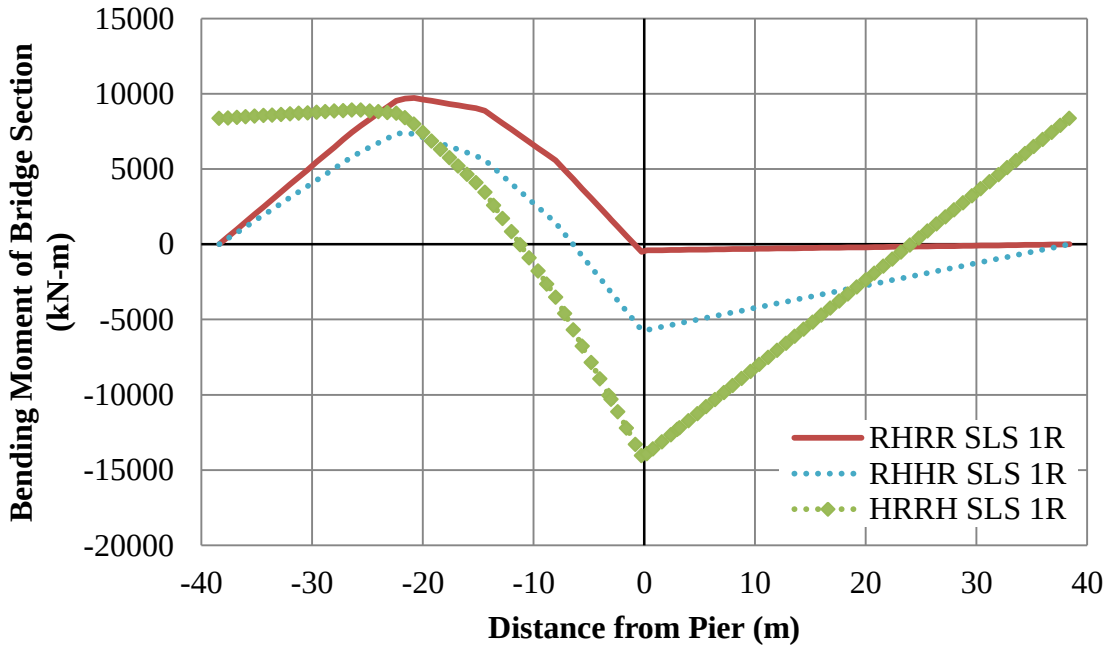

Figure 5-20 – SLS 1 Rehabilitation of Existing Bridge Analysis Results

Figure 5-20 shows the results of the SLS 1 analysis for the rehabilitation of existing bridge. The maximum link slab bending moments for RHRR, RHHR, and HRRH were -511 kN-m, -107 kN-m and -634 kN-m, respectively. The maximum link slab axial forces for RHRR, RHHR, and HRRH were 0 kN, 3985 kN and 15502 kN, respectively.

A summary of the governing bending moments and axial forces in the link slab is provided in Table 5-5. It was found that ULS 2 was the governing load combination at the ultimate limit state. The largest factored bending moment with the RHRR model is the ULS 2 combination with 881 kN-m, which is 4% greater than the MTO design capacity at 850 kN-m, meaning that the link slab design by MTO is in good agreement with the ULS 2 load combination in this study. The ULS 2 combination for HRRH model shows a bending moment at -1070 kN-m and an axial force of 22740 kN (in tension), which is greater than the capacity of the link slab.

Table 5-6 shows the girder end rotations for the ULS and SLS combinations. The girder rotation is used to determine the bending moment in the link slab using methods described by Caner and Zia [1]. In the ULS combinations, the largest girder end rotation was found using the ULS 2 load combination. Although the RHHR model showed a larger girder rotation for the ULS 1 load combination, the ULS 2 combination was governing when axial load was included. For example, the maximum tensile stress developed by the bending moment and axial forces for the ULS 1 and ULS 2 combinations were 6.73 MPa and 6.93 MPa, respectively. The girder rotations are used later in Chapter 6 of the thesis.

Table 5-5 – Governing ULS and SLS bending moment and axial force results for rehabilitation of existing bridge

	Bending moment in Link Slab (kN-m)				Axial force in Link Slab (kN)			
	ULS 1	ULS 2	ULS 4	SLS 1	ULS 1	ULS 2	ULS 4	SLS 1
RHRR	-815	-881	110	-511	0	0	0	0
RHHR	-204	-191	119	-107	6026	6814	312	3985
HRRH	-753	-1070	-351	-634	-3049	22740	27836	15502

Table 5-6 – ULS and SLS girder end rotation for rehabilitation of existing bridge

	Girder End Rotation (rad)			
	ULS 1	ULS 2	ULS 4	SLS 1
RHRR	-0.00860	-0.00876	0.00109	-0.00502
RHHR	-0.00476	-0.00442	0.00130	-0.00248
HRRH	-0.00827	-0.00965	-0.00206	-0.00560

The ULS 2 and SLS 1 load combinations are studied in the debonded length analysis (Section 5.3), non-linear analysis with FRC using plastic hinges (Section 5.4.3) and the analytical model (Chapter 6).

5.2.4 Summary of Results

From the ULS and SLS analysis:

- It was found that dead loads generated a large force effect in the link slab (bending moment and axial force). Thus, it was recommended to install the link slab after the bridge deck and girders are in place to minimize the force effect in the link slab.
- Placement of link slab concrete after the placement and hardening of bridge deck was recommended to minimize the effect of bridge deck shrinkage on the link slab.

- The CHBDC ULS 2 load combination was found to be the governing case, which was a load combination with CL-625-ONT truck load and thermal load.
- The results from the ULS 2 and SLS 1 load combinations were used in the debonded length analysis in Section 5.3, non-linear analysis with FRC in Section 5.4 and the analytical model in Chapter 6.

5.3 Link Slab Bridge Debonded Length Analysis and Cost Estimate

The debonded length of the link slab is one of the most important design aspects because it affects the reinforcement design, cost, serviceability and maintenance of the link slab bridge. For example, decreasing the debonded length of the link slab would result in reduced cost for concrete placement and removal. However, decreasing the debonded length increases the rotational and axial stiffness of the link slab, requiring more steel reinforcement in link slab compared to a more flexible link slab. Therefore, the debonded length of the link slab greatly affects the cost of constructing the link slab.

Although cost is an important factor, serviceability of the link slab should not be overlooked. The purpose of the link slab is to prevent leakage to the underside of the link slab. Thus, minimizing crack width is also important. The experimental results of FRC by Cameron [34] suggested that inclusion of fibres in concrete reduced the concrete crack widths significantly. Therefore, it is also important to assess the serviceability aspect of the link slab in addition to the construction cost. The three parameters examined in this study were:

- The force effect and required steel reinforcement in the link slab were investigated.
- The crack widths of link slab with fibre-reinforced concrete was analyzed and compared to conventional concrete.

- Cost estimate of the link slab construction was conducted between conventional concrete and FRC.

Debonded lengths of 0.5%, 2.5%, 5%, 7.5% and 10% of the bridge span length were studied, which were consistent with the debonded lengths selected by Caner and Zia [1] and Ulku et al. [6] in their studies of link slab bridges. The models that were analyzed in this study were RHRR, RHHR and HRRH, which were selected based on the results from Chapter 3, and the analysis was linear elastic.

5.3.1 Link Slab Force Effects and Required Steel Reinforcements

The results of the ULS 2 bending moment and axial forces (from Section 5.2) were used to determine the required steel reinforcement for a parametric analysis and design in this study. The debonded lengths were varied in the SAP2000 computational models to determine the force effects in the link slab, which were then used to design for the required steel reinforcement in the link slab assuming normal concrete is used. The force effect results are summarized in Table 5-7. It was found that the bending moment increased significantly as the debonded length decreased. At 0.5% debonded length, the bending moment increased by more than 600% compared to that of 10% debonded length for all models (RHRR, RHHR and HRRH); and at 2.5% debonded length, the bending moment increased more than 130% compared to 10% debonded length. Axial forces in the link slab, however, were not sensitive to variation in debonded length. The variation of bending moment and axial force with debonded length is shown in Figure 5-21and Figure 5-22, respectively.

The ULS 2 bending moments and axial forces from Table 5-7 were used to determine the required steel reinforcement in the link slab. Table 5-7 shows the amount of steel reinforcement required to satisfy the force effects of ULS 2 load combination in terms of area and reinforcement ratio. Note that Table 5-7 does not include the transverse reinforcement required for the slab, as this does not affect the slab design for the force effects considered. The variation of reinforcement required as a function of debonded length is shown in Figure 5-23 (a) and (b) in terms of reinforcement area and volume, respectively. The volume of reinforcement that is required in the link slab is also a function of the link slab length, and increases sharply for the RHHR and HRRH cases, as the reduction in reinforcement area with increasing length is not sufficient to offset the increased volume of steel associated with increasing length. This is primarily due to the significant axial force present in the link slab for these cases. This suggests that a debonded length on the order of 2.5% is desirable for link slab bridges with the RHHR and HRRH support conditions (only considering volume of steel required). For the RHRR model, the link slab axial force is negligible and the reduction in the area of reinforcement required is proportional to the increasing debonded length such that the volume of reinforcement required is essentially constant, as shown in Figure 5-23(b). This suggests that from a volume of steel perspective, the optimum debonded length for the RHRR model ranges between 2.5% to 10%. From the computational model in Chapter 3, it was found that the RHRR model was more representative of the link slab bridge with elastomeric bearings, suggesting that debonded lengths between 2.5% to 10% could be selected for design. The findings were consistent with the conclusions of Caner and Zia [1] and Ulku et al. [6], where the authors suggested debonded lengths from 5% to 7.5%.

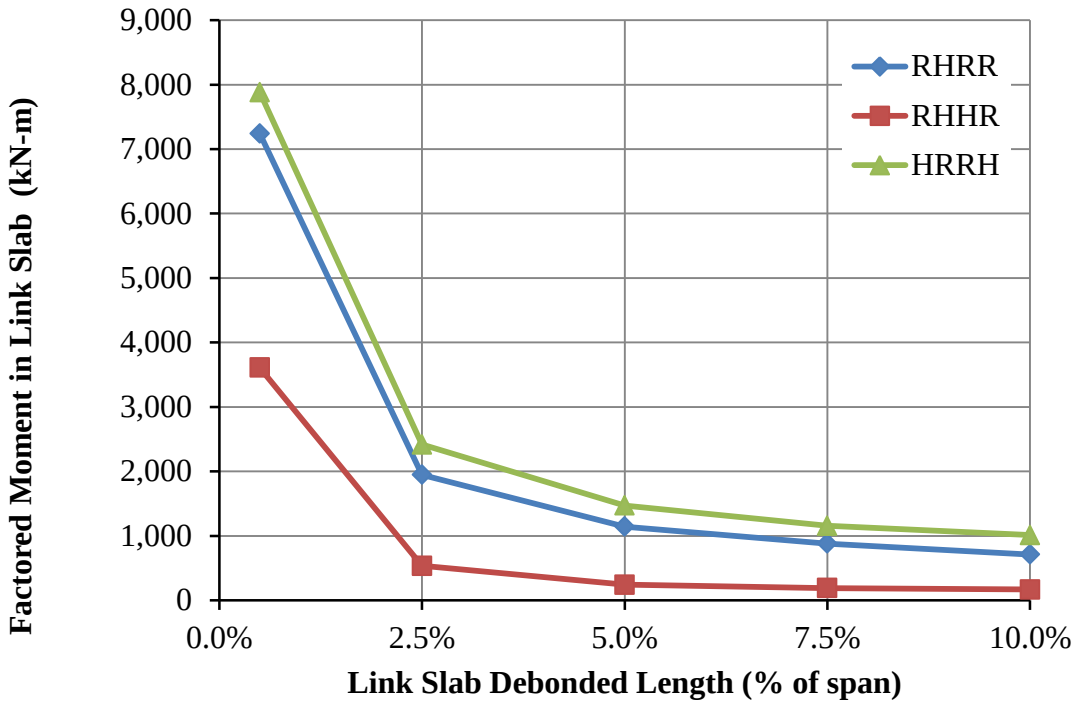

Figure 5-21– Variation of link slab moment with debonded length

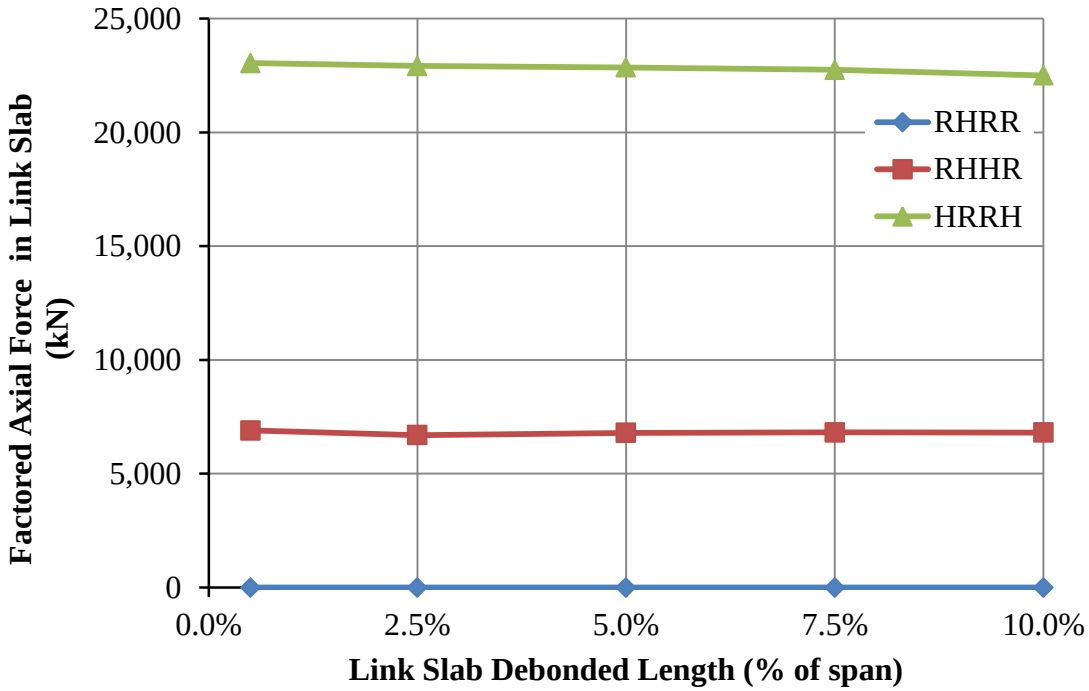

Figure 5-22– Variation of link slab axial force with debonded length

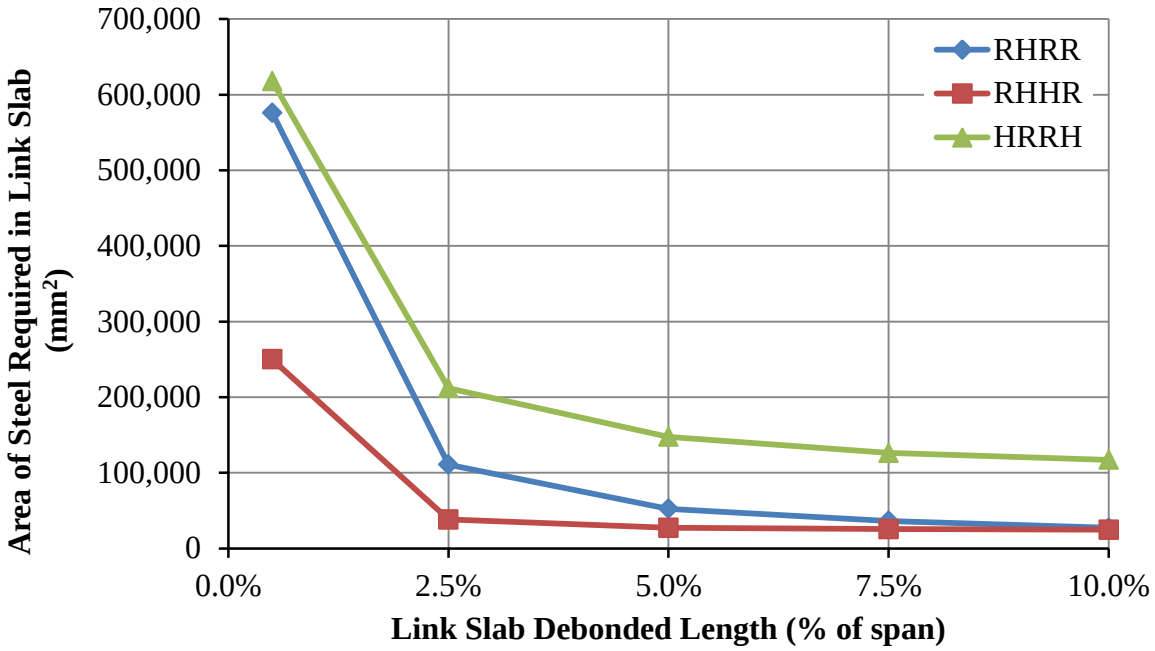

(a)

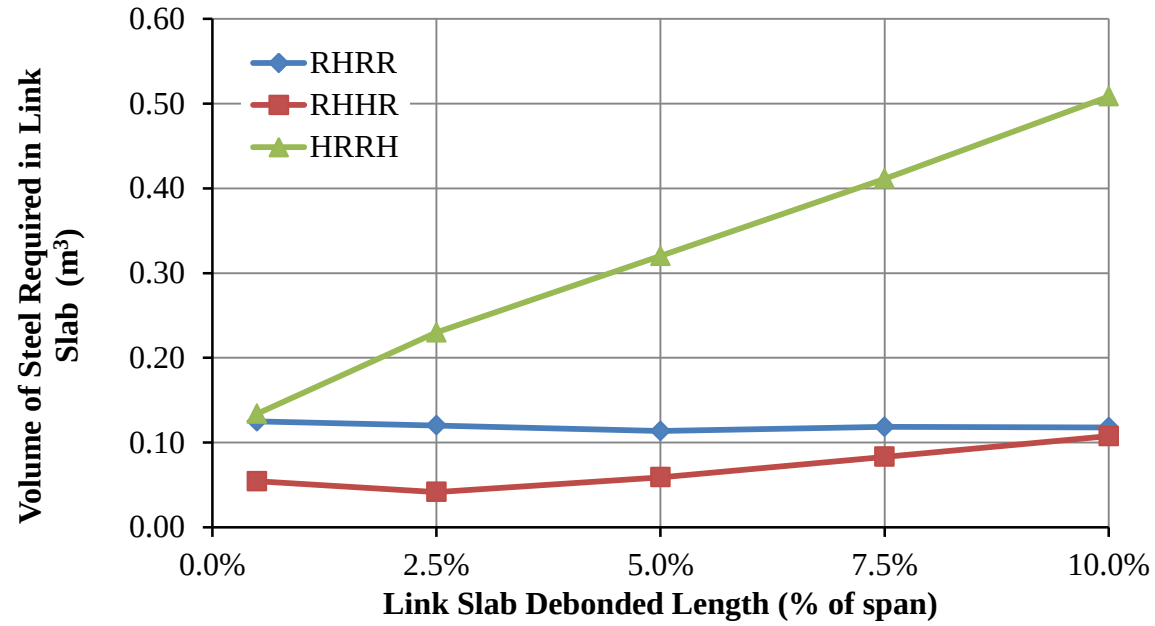

(b)

Figure 5-23 – Link slab (a) required area of steel reinforcement and (b) required volume of steel reinforcement for various debonded lengths

Table 5-7 – Bending moment and percent change for ULS 2

Bending Moment in Link Slab (kN-m), ULS 2					
Debonded Length	0.5%	2.5%	5.0%	7.5%	10.0%
RHRR	-7242	-1947	-1144	-881	-711
RHHR	-3610	-534	-243	-191	-169
HRRH	-7883	-2416	-1472	-1156	-1011
Axial Force in Link Slab (kN), ULS 2					
Debond Length	0.5%	2.5%	5.0%	7.5%	10.0%
RHRR	0	0	0	0	0
RHHR	6899	6697	6798	6814	6807
HRRH	23047	22919	22851	22751	22503

5.3.2 Crack Widths of Link Slab with FRC

The experimental and analytical study on FRC presented in Section 4.5 showed that the use of fibres greatly enhanced the link slab design by reducing crack width in reinforced concrete, which was important in minimizing leakage to the link slab underside. Table 5-8 compares the predicted crack widths for normal concrete, hooked steel FRC and polypropylene FRC as a function of debonded length. The results are shown for the RHRR support conditions which are previously found to be similar to the actual conditions for elastomeric bearings. Note that the axial force in the link slab is negligible for this support condition. Crack widths were calculated based on CHBDC [11] procedures as discussed in Section 4.5 using the SLS load combination results (Table 5-5). Calculations of the crack width can be found in Appendix A.9. Note that the reinforcement amounts listed in Table 5-8 were calculated based on a ULS 2 load combination (see Section 5.3.1 for more details), although the reinforcing steel stresses and associated crack widths were predicted for the SLS moments listed in the table.

From Table 5-8, the crack widths for the link slab with FRC did not change significantly for the polypropylene FRC, and decreased for the steel FRC as the debonded length increased. This was because the fibres were found to be more effective as the area of steel reinforcement decreased (see Section 4.5), particularly for the steel FRC. Figure 5-24 shows the variation of crack width as a function of debonded length for the RHRR model comparing normal concrete and FRC. For hooked steel FRC, 7.5% is the optimal debonded length, while for polypropylene FRC it is at 10%. The 0.5% debonded length is excluded due to its unreasonably high requirement for steel reinforcement. It is therefore recommended to use 5% to 7.5% debonded length to obtain a balance between minimizing crack width (with hooked steel FRC) and having a reasonable start-up construction cost.

Table 5-8 – Predicted crack width comparison between normal concrete and FRC

Concrete Type	Debonded Length	SLS Bending Moment	Tension Reinf. Area	Steel Reinf. Stress	Average Crack Width
	(%)	(kN-m)	(mm^2)	(MPa)	(mm)
Normal Concrete	2.5	1128	55400	215	0.110
	5.0	664	26200	250	0.149
	7.5	511	18200	267	0.177
	10.0	412	13600	286	0.205
Hooked Steel FRC	2.5	1128	55400	150	0.076
	5.0	664	26200	115	0.056
	7.5	511	18200	81	0.004
	10.0	412	13600	41	0.001
Polypropylene FRC	2.5	1128	55400	187	0.095
	5.0	664	26200	188	0.109
	7.5	511	18200	180	0.106
	10.0	412	13600	164	0.085

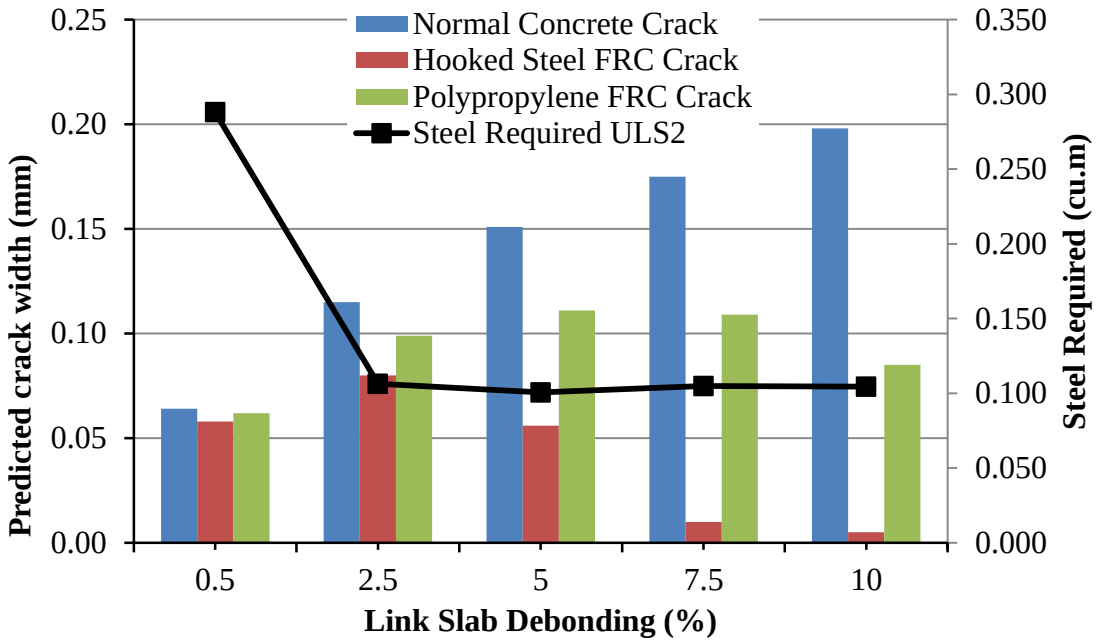

Figure 5-24 – Variation of predicted crack width with debonded length for normal concrete and FRC (RHRR model)

It should be noted that the preceding crack width analyses were based on internal steel reinforcement that was proportioned for the normal concrete case. Given the excellent crack control provided by the steel FRC in particular, it is likely that the amount of steel reinforcing bars could be reduced when used with steel FRC while still providing adequate crack control. This would allow further material savings.

5.3.3 Cost Estimate of Link Slab with FRC

The cost estimate of link slab construction was determined from data from R.S. Means [39]. Based on the 2013 data from R.S. Means for Toronto, the cost for removal of reinforced concrete is approximately $250 per cubic metre; the cost of normal concrete per cubic metre is approximately $200 per cubic metre for 35 MPa concrete (with transportation) and an additional

$100 for specialty hand mixed concrete (i.e., with fibres); and the cost of 15M steel reinforcements is approximately $1500 per metric ton and an additional $3500 per metric ton with labour and transportation cost. From these data, the initial or first cost of link slab construction considering required steel reinforcement, concrete removal and concrete placement were calculated for each link slab debonded lengths and presented in Figure 5-25. The cost estimate assumed that an existing bridge with expansion joints was converted into a link slab bridge, which had already accounted for the removal of concrete deck in the calculation.

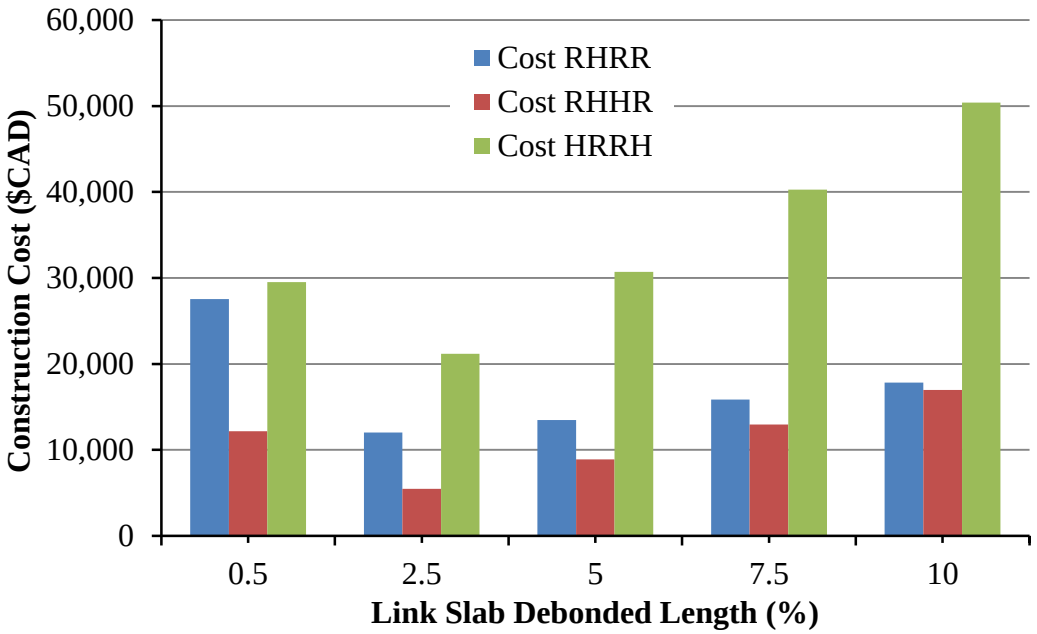

Figure 5-25 – Start-up cost of link slab construction

From Figure 5-25, the lowest construction cost for link slab construction was for the 2.5% debonded length, owing to the least volume of steel, concrete and removal of the bridge deck. For the RHRR model, the cost increased by 12% and 32% for debonded lengths of 5% and 7.5% of the bridge span, respectively. Although start-up cost was lowest for 2.5% debonded length, the long term maintenance and rehabilitation of the link slab should also be considered. Repair

of cracks in reinforced concrete could cost up to $30 per meter in slab, and for a 9.7m wide link slab, the cost was $300 per crack for large cracks up to 4mm width. Over the course of several years, the cost for maintenance could amount to more than the start-up cost based on the severity of the cracks. In addition, the damage to the underside of the link slab was also a concern and could be much greater than the start-up cost of the link slab. Therefore, considering the serviceability (i.e., crack width) and long term benefit of the hooked steel FRC link slab, it is recommended to use hooked steel FRC with a debonded length of 5% or, preferably 7.5%, in order to minimize cracking while providing a reasonable start-up cost. Due to the lack of data on link slab bridges for varying debonded length and use of FRC, more research is required to conclude the long term benefits of FRC (for future work).

As noted in the preceding section, the crack width analyses were based on internal steel proportioned for the normal concrete case. It is likely that the amount of steel reinforcing bars can be reduced when used with steel FRC in particular, while still providing adequate crack control and strength. This will allow further material cost savings for the FRC case. This additional analysis is recommended as future work.

5.3.4 Summary of Debonded Length

From the debonded length analysis:

- The required steel reinforcement for RHRR model is lowest between debonded lengths of 2.5% to 7.5%, and the required steel reinforcements for RHHR and HRRH models are lowest for debonded length of 2.5%.
- Crack width is minimized when debonded length increases, with optimal debonded lengths at 7.5% for hooked steel and 10% for polypropylene. Hooked steel FRC reduces

the crack width significantly and it is recommended for use in the link slab at 7.5% debonded length.

- Considering both initial construction cost and benefit (reduced crack widths) of the FRC link slab, a 5% to 7.5% debonded length is recommended for link slab design using hooked steel fibres.

5.4 Non-linear Computational Model of Link Slab Bridge with FRC

The differences between FRC and normal concrete are its improved ductility, tensile strength and improved cracking characteristics, which benefits the reinforced concrete once the material is loaded past its cracking and yielding capacity. The post-cracking behaviour of normal concrete is typically ignored because concrete is assumed to be ineffective in tension after cracking. However, FRCs have shown to be effective even after cracking. From the FRC tests by Cameron [34] (partial results reported in Chapter 4), it was found that the reinforced concrete beams tested with normal concrete failed after crushing of concrete at a mid-span deflection of 25mm. In contrast, beams with FRC showed resilience even after exceeding the crushing strain of concrete, and high ductility was achieved with a mid-span deflection of 100mm, all due to the post-cracking benefit of FRC and its ability to enhance steel reinforced concrete.

To include the benefits of FRC in a computational model and to determine the effect of the post-cracking behaviour in the FRC link slab on the response of the bridge, a non-linear analysis is carried out in an attempt to model the link slab bridge with post-cracking behaviour of FRC. Based on the experimental results from Cameron, it was seen that beams with FRC exhibited plastic hinge-like behaviour, where a local hinge formed at the location of concrete cracking, rather than evenly distributed cracking across the beam. In order to model this in SAP2000, FRC

post-cracking and post-yielding material behaviour was included in the computational model as plastic hinges. The plastic hinge approach has been used by others such as Löfgren [20] for studying non-linear behaviour of concrete beams with FRC (see Sections 1.2.2.5).

5.4.1 FRC and Plastic Hinges Background

In current link slab analysis and design, the effect of cracking of the link slab is calculated and modelled using an effective moment of inertia, such that the section property of the link slab is reduced as a function of the bending moment, as proposed by Caner and Zia [1]. This assumes that cracks are uniformly distributed across the link slab and the stiffness of the entire link slab will decrease due to the cracks.

The plastic hinge is a discrete plasticity or crack modelling method that models plastic behaviour, such as cracking and yielding, in a specific location within a beam element. If that particular location exceeds the cracking or yielding load, it will take the property of the post-cracking or yielding material property defined by the user. To assess plastic behaviour or cracking in the beam, the plastic hinge is typically inserted in the location with highest force effects or deformation determined from an elastic analysis.

Both the ULS and SLS load combinations from Section 5.2 were used in the non-linear analysis of the link slab bridge, although different hinge properties were used in the two analysis cases. In the ULS analysis, the ultimate capacity of the link slab was considered. The strength analysis included the plastic hinge in the link slab with linear-elastic behaviour up to yielding of the steel reinforcement, and perfectly-plastic behaviour post-yielding. This type of hinge is called the "ULS hinge" in this study. The purpose of this analysis was to determine the effect of the post-

yielding behaviour (softening) in the FRC link slab on the force effects in the link slab and girder at the ultimate limit state.

The purpose of the SLS analysis was to capture the cracking behaviour of the link slab at service load levels. In the serviceability analysis, the moment-curvature relationship for cracking, yield and ultimate loads are all considered in the plastic hinge since deformation and cracking are important design aspects for serviceability. The plastic hinge properties were defined so that the hinge was engaged once the cracking moment of the section was exceeded, creating a localized reduction in stiffness due to cracking. The hinge properties were further defined to capture yielding, although this was not expected at the SLS. This type of hinge is called the "SLS hinge" in this study.

5.4.2 Introduction to Plastic Hinge

The plastic hinge models the post-elastic (or post-cracking) behaviour of the link slab. One type of plastic hinge in SAP2000 is the axial-moment plastic hinge (PM Hinge). The PM Hinge couples together the axial force and bending moment, which describes the axial-moment yield surface of the material at the specified location in a beam element. Moment-rotation relationships are also defined as a function of the axial load. Unfortunately, the axial force and deformation of the hinge cannot be defined in the PM Hinge because it is computationally difficult in SAP2000 [35]. Thus, the plastic hinge adopts an assumed axial-deformation relationship based on the material property of the element the hinge is part of. Since the axial deformation response of the hinge is not always representative of the actual behaviour, the crack widths in the axial direction cannot be used to represent the actual crack width. Rather, the

plastic hinge is used to illustrate locations in the bridge that has reached the yield load and it would redistribute the load across the bridge system based on the properties of the PM Hinge.

The moment-rotation curve required for the plastic hinge is defined using 5 points, labelled “A”, “B”, “C”, “D” and “E” in Figure 5-26. Each point defines the normalized moment ratio versus the plastic rotation [35] at a given axial force level. The moment-rotation curve can be uniquely defined for various axial forces with the appropriate interpolation between axial forces. Point “A” is the initial point (origin) at zero moment and zero plastic rotation. Point “B” represents the onset of plasticity, which could be either the cracking moment or the yield moment depending on the intended use. Point “C”, “D” and “E” are bending moments after the onset of plasticity.

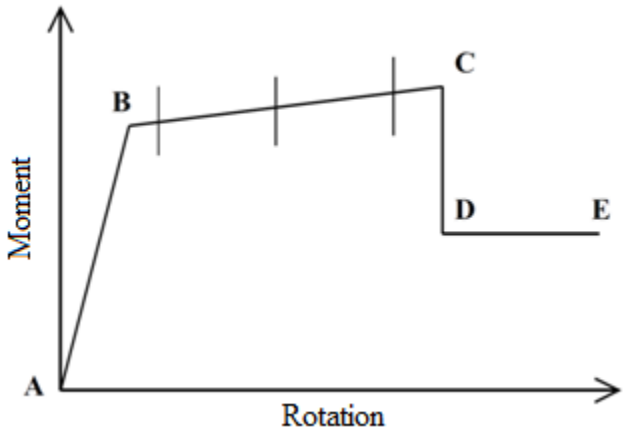

Figure 5-26 – General moment-rotation curve in plastic hinge

When the hinge yields for the first time (i.e., a combination of axial force and bending moment has reached the yield surface), a net moment-rotation curve is interpolated to provide an energy equivalent moment-rotation curve. The net moment-rotation curve will not always follow the backbone of the moment-rotation curve defined by the user, and is adjusted by taking into account the plasticity occurring in the axial direction as well. The shape of the net moment-

rotation curve (recalculated after yielding of the hinge) is influenced by the magnitude of the axial force (or strains) in the structure, and the loading sequence of axial force and bending moment. For example, applying the axial force and bending moment with equivalent ratios will generate a different net moment-rotation curve than if all of the axial force is applied to the structure first, followed by the bending moment. Without an axial force, the hinge will typically follow the backbone of the moment-rotation curve because there is no plasticity (or work done) in the axial direction in the hinge. Thus, the moment-rotation curve does not need to be recalculated in this case [40].

In the ULS analysis, the bridge model has "ULS hinges" in the link slab with linear-elastic behaviour up to the yield moment, and perfectly-plastic relationship afterwards. The onset of plasticity will be the yield load defined by point "B" in Figure 5-26. Points "C" to "E" are flat, defining a perfectly-plastic relationship. The same methods were adopted by the authors of SAP2000 in their examples for using the PM hinge [35].

In the SLS analysis, the bridge model has "SLS hinges" that models different stages of the material property from cracking moment to yield moment and to ultimate moment. The purpose of the serviceability hinge is to accurately model the rotation (and elongation) of the hinge according to the deformation of the link slab. The moment-rotation curves are also a function of the axial forces. The point "B", "C", "D" and "E" in Figure 5-26 are the cracking moment, yield moment, ultimate moment and failure moments of the link slab, respectively.

5.4.2.1 Plastic Hinge Definition for ULS

The "ULS hinge" requires the axial-moment interaction diagram to define the onset of plasticity (or yielding) of the hinge. The moment-rotation relationship is simply modelled as linearly-

elastic up to the yield load and then perfectly-plastic. Effective section modulus is used in the definition of the moment-curvature plot, as suggested by Caner and Zia [1]. The axial-moment diagram is calculated based on a layer-by-layer strain compatibility analysis of the cross-section (see Appendix A.4 for the algorithm). The layer-by-layer analysis is necessary to compute the property of the concrete section with the effects of fibres. The design of the link slab is based on the as-designed condition of the Camlachie Road Underpass (see Section 3.2) with the inclusion of polypropylene or steel FRC. The tensile stresses for FRC were found using the *fib* Model Code [16], following the procedures discussed previously in Section 4.3. Figure 5-27 shows the axial-moment interaction diagram of the link slab at ultimate for normal concrete (no fibre), polypropylene FRC and hooked steel FRC. The tension stiffening effects of the FRC are evident in the regions of the curves controlled by reinforcement yielding. Above the balanced point, the contribution of the FRC decreases rapidly until pure compression.

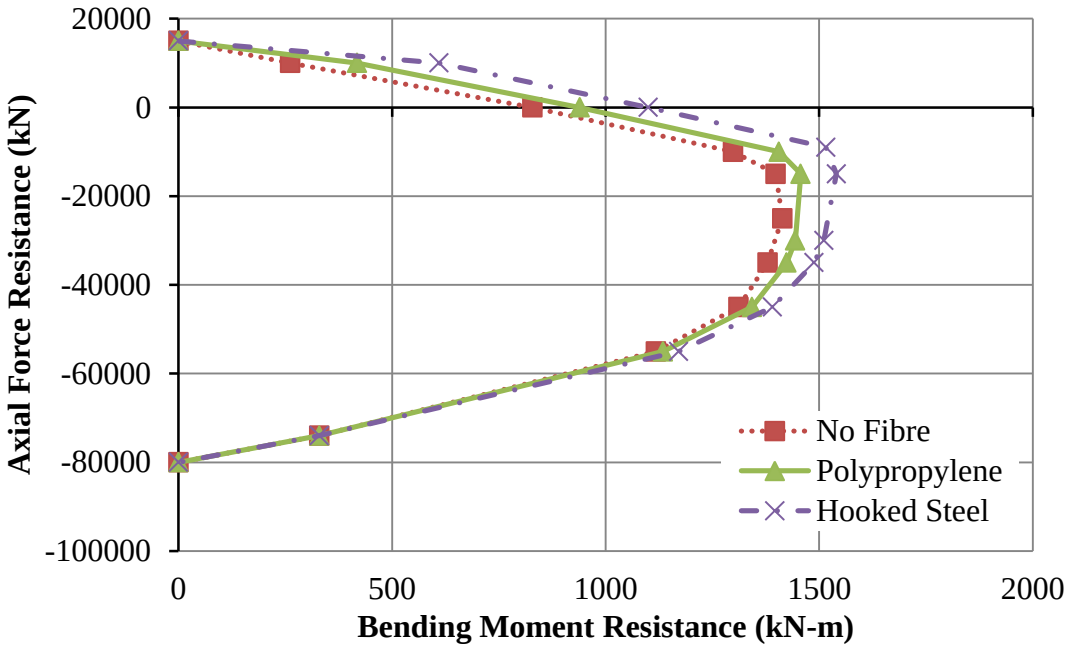

Figure 5-27– Axial-moment interaction diagram for link slab section at ultimate load

5.4.2.2 Plastic Hinge Definition for SLS

The "SLS hinge" requires an axial-moment interaction diagram that is based on the cracking load of the link slab. The tensile stress f_t at the extreme fibre of the link slab is defined by Equation 5-4 using basic mechanics,

$$-f_t = \frac{P}{A_{tr}} - \frac{M}{S_{tr}} \qquad 5\text{-}4$$

where P is the axial force, M is the bending moment, A_{tr} is the transformed gross cross-section area and S_{tr} is the gross transformed section modulus. To calculate the cracking moment M_{cr} and applied axial force P_{app}, the tensile stress can be replaced with the concrete rupture stress f_r, and the cracking moment to applied axial force relationship is defined by Equation 5-5.

$$M_{cr} = S_{tr}\left(f_r + \frac{P_{app}}{A_{tr}}\right) \qquad 5\text{-}5$$

The moment-curvature relationship of the cross-section can also be determined from the layer-by-layer strain compatibility analysis (see Appendix A.4 for the algorithm). From the layer-by-layer analysis, the neutral axis c can be found and the compressive strain ε_{top} is known, and the curvature is defined in Equation 5-6.

$$\varphi = \varepsilon_{top} / c \qquad 5\text{-}6$$

For the SLS analysis, the plastic hinge is used to describe the axial force-moment relationship of a point in a beam (or column) where first cracking occurs. Figure 5-28 is the SLS axial force-moment interaction relationship for the link slab section for the Camlachie Road Underpass for normal concrete (no fibre), polypropylene FRC and hooked steel FRC. The effect of the FRC is to increase the cracking load/moment since the modulus of rupture, f_r, is increased.

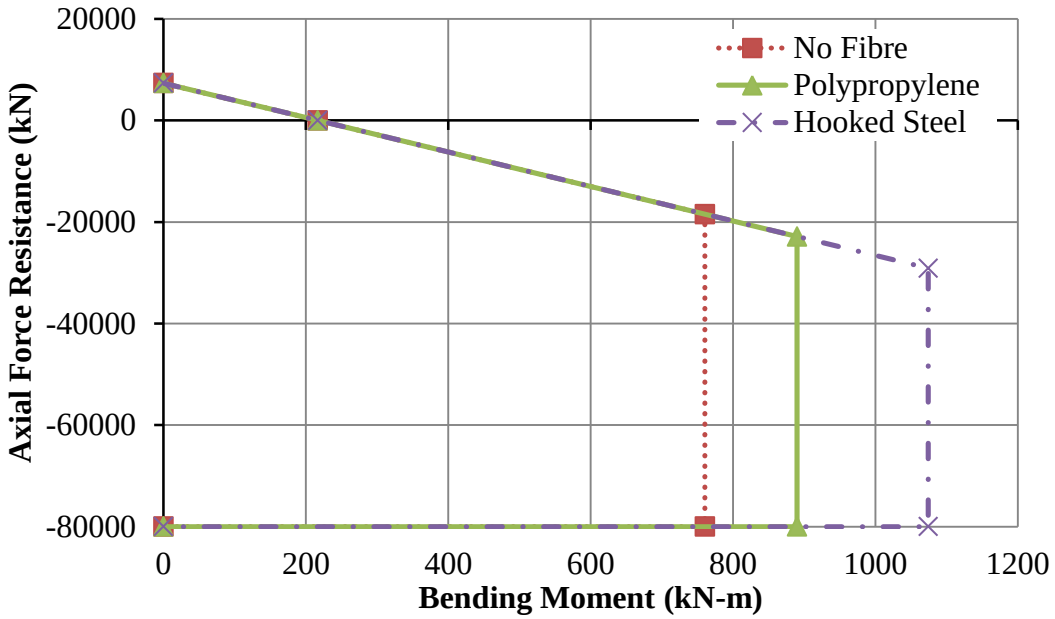

Figure 5-28 – Axial-moment interaction diagram for link slab section at service load

The moment-curvature behaviour of the link slab is a function of the axial force. Figure 5-29, Figure 5-30 and Figure 5-31 are the moment-curvature plots for reinforced concrete without fibres, with polypropylene fibres and hooked steel fibres, respectively. There are 6 moment-rotation curves in each figure corresponding axial forces of -10000 kN, -5000 kN, 0 kN, 10000 kN, 20000 kN and 30000 kN. A maximum axial load of 30000 kN was used because the linear elastic analysis did not exceed -30000 kN. Note that in the moment-curvature plots, the elastic rotations (or curvatures) must be adjusted to its plastic rotations when programmed in the plastic hinge. The polypropylene fibres are less stiff than the hooked steel FRC. Thus, the curves for the polypropylene FRC models reach larger strains and curvatures than the hooked steel FRC. The moment-curvature relationship up to yielding was generated based on the gross-section modulus of the link slab, while the moment-curvature relationship after yielding was generated using the cracked stiffness of the link slab.

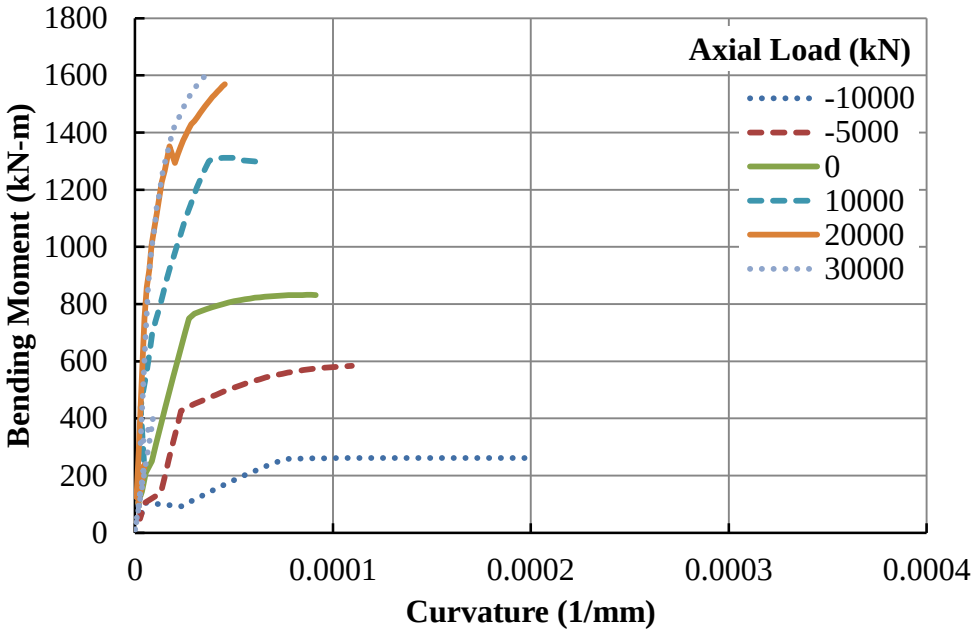

Figure 5-29 – Moment-curvature plot for normal reinforced concrete (no fibres)

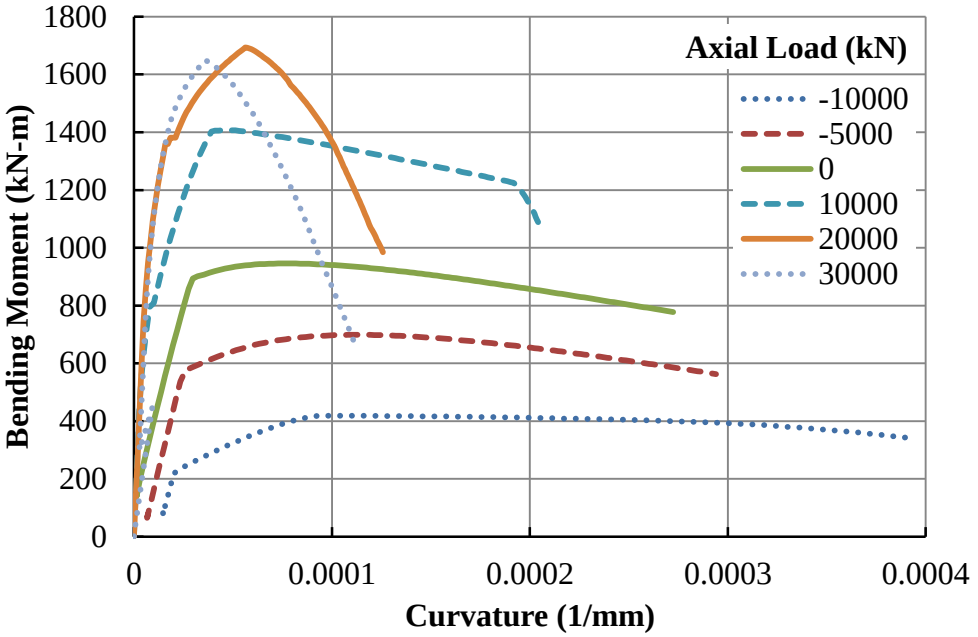

Figure 5-30 – Moment-curvature plot for reinforced concrete with polypropylene fibres

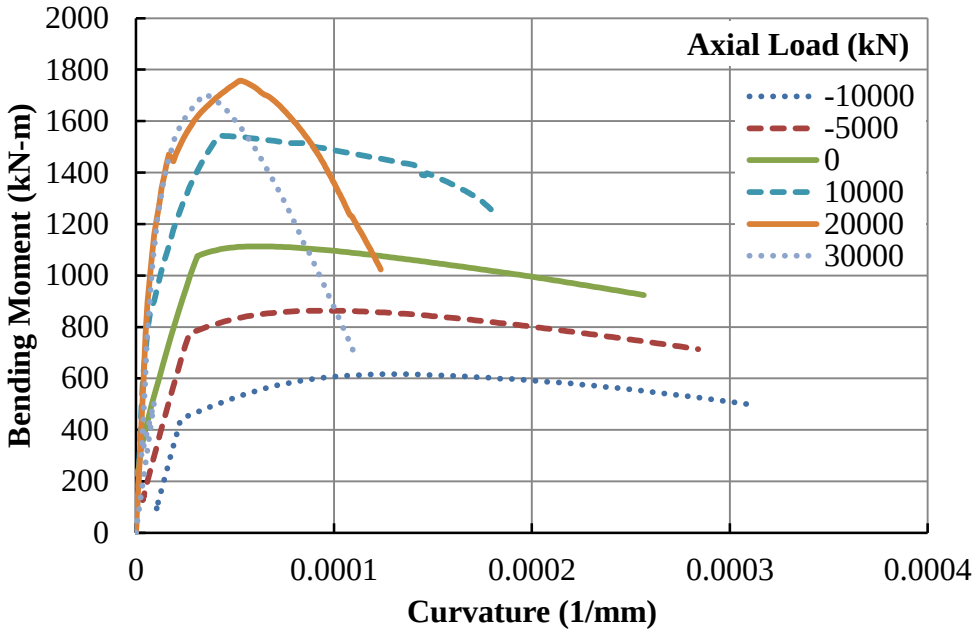

Figure 5-31 – Moment-curvature plot for reinforced concrete with hooked steel fibres

5.4.3 Parametric Study of ULS and SLS using Non-linear Model with FRC

Plastic hinges were placed at the locations of the highest bending moment and axial force in the link slab, which were found to be above the pier supports (refer to Sections 5.2.2 and 5.2.4). As described in the preceding sections, the plastic hinge behaviour is defined by the user in terms of axial force-moment interaction (yield surface) and moment-rotation response to represent the post-linear response of the link slab. The plastic hinge behaviour was calculated based on the link slab design details for the Camlachie Road Underpass.

Concrete cracking changes the elastic properties of the section and force redistribution is expected in the link slab bridge. The link slab will form cracks when the capacity of the link slab is exceeded. If force effects are increased to produce non-linear material responses in the concrete or steel, further non-linear effects may be experienced. The field observation of Ulku et

al. [6] reported a single large crack observed through the link slab, rather than uniform cracks appearing in the link slab. Similarly, MTO studies showed hairline cracks concentrated at the pier support for the Camlachie Road Underpass [8], rather than many cracks distributed across the link slab (see Figure 3-5). This is consistent with findings from Cameron [34] where plastic hinge-like behaviour was observed, with large localized compression and cracking failure at the mid-span of the beam.

For the ULS study, "ULS hinges" were inserted in the link slab above the pier support, one for each of the two pier supports in the bridge. Additional hinges were placed along the link slab to capture non-linear effects that may occur in the link slab. Figure 5-32 shows the location of the hinges placed in the link slab of the Camlachie Road Underpass. There were 9 hinges in total, labelled "H1" through to "H9". Three of the hinges were placed in the link slab at the pier supports and the middle of the link slab, labelled "H4", "H5" and "H6". Two hinges were placed at the interfaces between the link slab and the bridge deck about 3 m from the pier supports, labelled "H1" and "H9". Two hinges labelled "H2" and "H8" were placed 1.5 m from the support, half way between the pier and the link slab ends. Two other hinges labelled "H3" and "H7" were placed 0.75 m from the pier supports to capture intermediate cracks in the link slab.

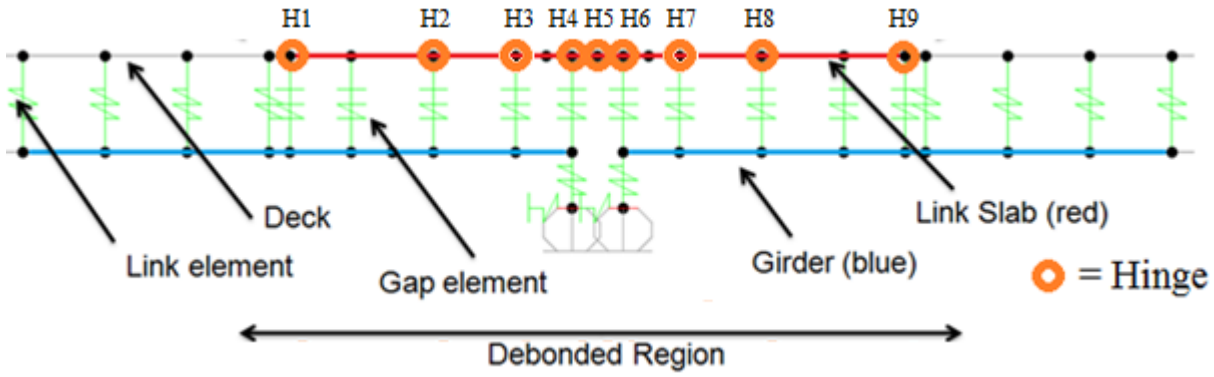

Figure 5-32 – Hinge location in the link slab

5.4.3.1 Results for ULS with Plastic Hinges

The bending moments and axial forces for the non-linear models (RHRR, RHHR and HRRH) are summarized in Table 5-9. Linear-elastic results are included in the table for comparison purposes (from Section 5.2.3 of the parametric study). The notation in Table 5-9 is "NF", "PP" and "HS" for the non-linear model with normal concrete (no fibre), polypropylene FRC and hooked steel FRC, respectively. Output of hinge results and model deflections for the ULS analysis are shown in Appendix A.10.

Table 5-9 – Link slab bending moment and axial force for ULS non-linear analysis

	Bending Moment (kN-m)				Axial Force (kN)			
ULS 2	Linear	NF	PP	HS	Linear	NF	PP	HS
RHRR	-881	-831	-881	-881	0	0	0	0
RHHR	-191	-191	-191	-191	6814	6814	6814	6814
HRRH	-1070	-2	3	-15	22740	15007	14791	14717

Figure 5-33 is the ULS bending moment diagram for the RHRR model comparing the linear elastic bending moment to the non-linear models. The non-linear models include plastic hinges with properties from normal concrete (no fibres), polypropylene FRC and hooked steel FRC, as described in Section 5.4.2.1. The bending moment diagram shows negligible change between the linear model and the non-linear models except for the no fibre model.

In the normal concrete (no fibre) model, the "H4" hinge yielded (see Figure 5-32), which was located at the support above the pier. The moment in the plastic hinge was between cracking and yielding load, which suggested that the overall impact on the link slab bridge was small. Therefore, the redistribution of forces in the link slab was negligible, and it was found that the change in bending moment was only 6%. This was consistent with the findings of the MTO

report, which showed small cracks at the pier support (see Section 3.2 and Figure 3-5). The other models (i.e., polypropylene FRC and hooked steel FRC) did not show yielding of the hinges.

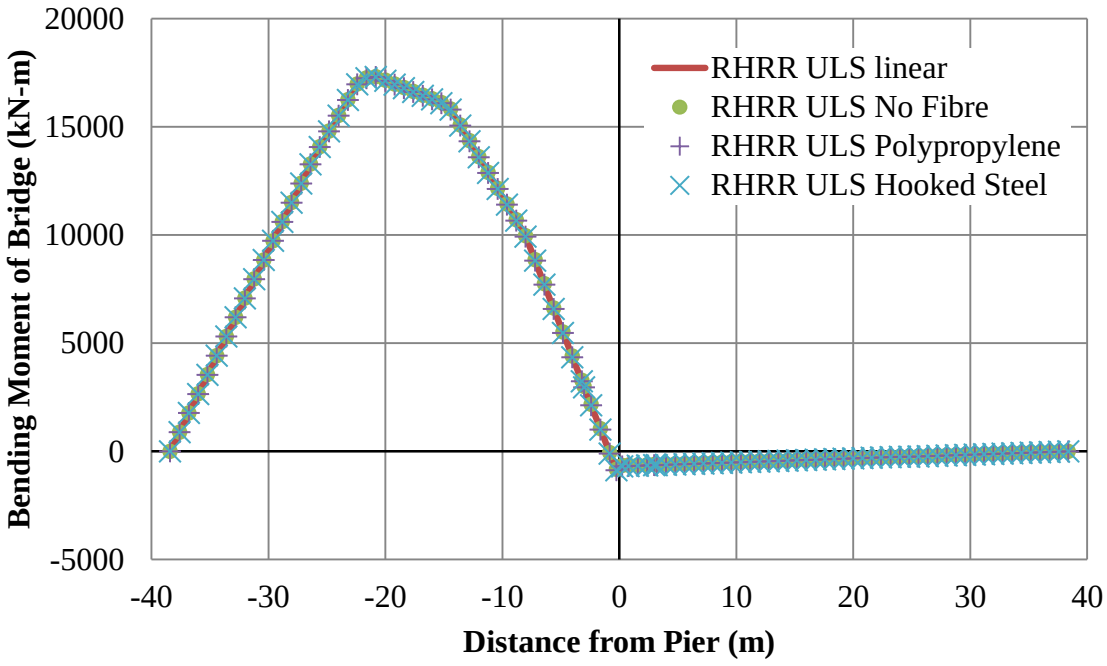

Figure 5-33 – ULS RHRR comparison of linear elastic model to non-linear models with and without FRC

Figure 5-34 is the ULS bending moment diagram for the RHHR model comparing the linear elastic bending moment to the non-linear models, with and without FRC. The bending moments and axial forces were not changed comparing the linear and non-linear models, as presented in Table 5-9. None of the plastic hinges yielded; therefore there was no redistribution of forces.

Figure 5-35 is the ULS bending moment diagram for the HRRH model comparing the linear elastic bending moment to the non-linear models, showing significant change between the linear and non-linear models.

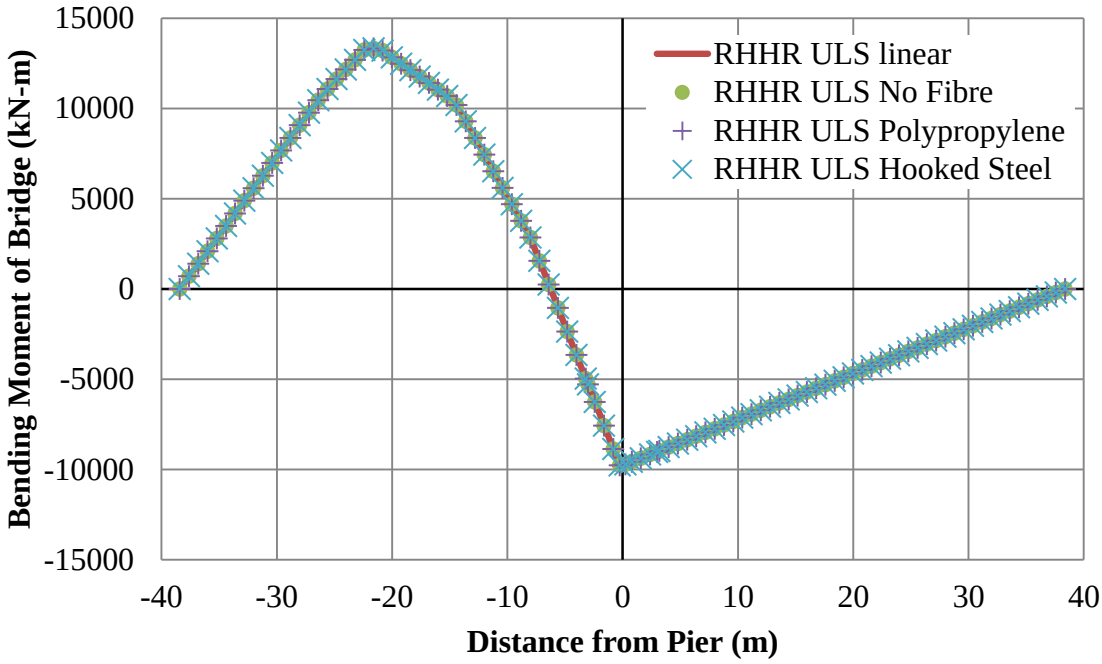

Figure 5-34 – ULS RHHR comparison of linear elastic model to non-linear models with and without FRC

From Table 5-9, the link slab bending moments and axial forces were -1070 kN-m and 22740 kN (in tension) for the linear elastic model, respectively. The bending moments were almost zero for the non-linear models. The linear elastic axial force resulted in a bending moment capacity of zero based on the axial-moment yield surface in Figure 5-27. Thus, the bending moment capacities of the hinges were zero. This was consistent with the results of the hinges in Appendix A.10, and all of the hinges showed loading exceeding the hinge capacity due to the high restraint at the bridge abutments (i.e., hinge supports rather than rollers). The yielding of the plastic hinge allowed plastic movement in the link slab, which relieved the restraint in the bridge supports (i.e., horizontal restraint at the abutment). Less internal forces were generated as a result of the plastic deformation at the link slab. Therefore, the bending moment decreased in the bridge for the non-linear models, as seen in Figure 5-35.

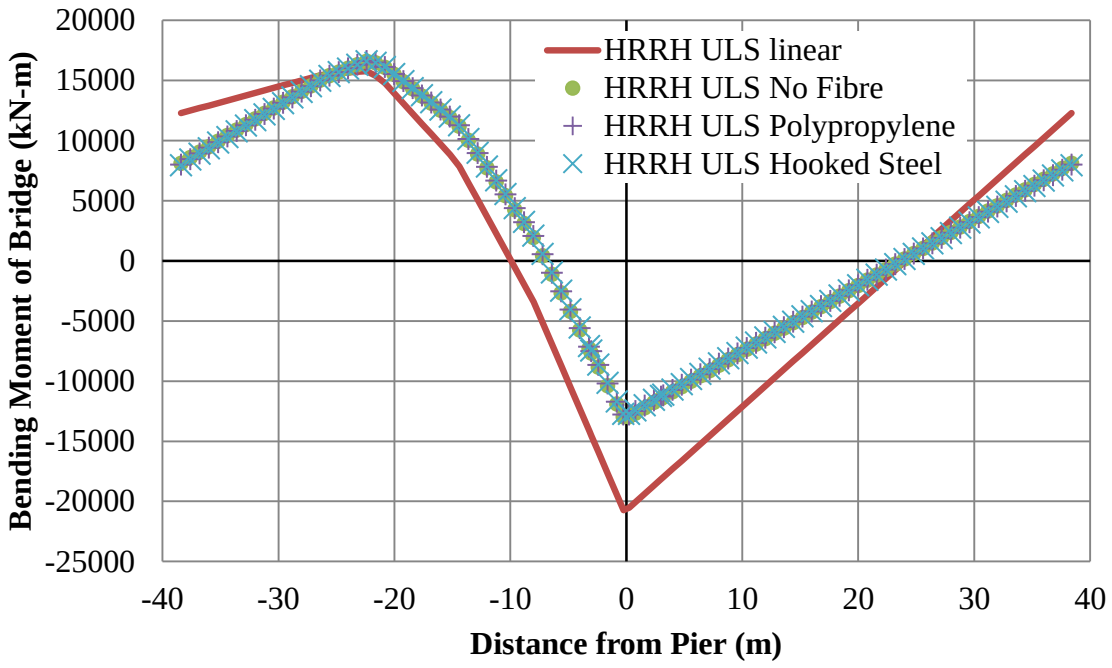

Figure 5-35 – ULS HRRH comparison of linear elastic model to non-linear models with and without FRC

5.4.3.2 Results for SLS with Plastic Hinges

The bending moments and axial forces for the non-linear models (RHRR, RHHR and HRRH) are summarized in Table 5-10. Linear-elastic results are included for comparison purposes (from Section 5.3.2 of the parametric study). The notation in Table 5-10 is "NF", "PP" and "HS" for the non-linear model with normal concrete (no fibre), polypropylene FRC and hooked steel FRC, respectively. Output of the hinge results and model deflection for SLS are shown in Appendix A.11. It is important to note that the non-linear results for the SLS analysis are essentially bi-linear, since the plastic hinges are defined to capture post-cracking behaviour; that is engagement of the hinge represents a change in stiffness due to cracking, but not necessarily plastic behaviour.

Table 5-10 – Link slab bending moment and axial force for SLS non-linear analysis

	Bending Moment (kN-m)				Axial Force (kN)			
SLS 1	Linear	NF	PP	HS	Linear	NF	PP	HS
RHRR	-511	-245	-253	-263	0	0	0	0
RHHR	-107	-89	-90	-91	3985	3993	3993	3992
HRRH	-634	-6	19	6	15502	12592	7523	10030

Figure 5-36 is the SLS bending moment diagram for the RHRR model comparing the linear elastic bending moment to the non-linear models. The link slab bending moments were -511 kN-m for the linear elastic model and approximately 250 kN-m for the non-linear models. The link slab axial forces were 0 kN for all models.

In the non-linear model hinge results (in Appendix A.11), hinges "H4" and "H5" were plastically deformed (i.e., cracking occurred at these locations). These hinges were near the pier support closer to the truck load, which was consistent with the findings of the MTO report, showing small cracking at the pier support (see Section 3.2 and Figure 3-5). The moment in the hinge was between the cracking and yield moment, which was not large. Thus, the force redistribution of the link slab bridge was negligible. From Figure 5-36, the overall bending moment of the link slab bridge did not change significantly.

Interestingly, the hooked steel FRC showed hinge yielding (section cracking) at "H6" as well. This is because the hooked steel FRC is stiffer than the polypropylene FRC, meaning it is less able to accommodate deformation than polypropylene FRC. Thus, the hooked steel FRC model showed more cracking. However, the crack widths are likely to be smaller than polypropylene FRC based on the crack analysis in Section 4.5. In conclusion, for loading in SLS load

combination, the FRC is expected to crack at the pier, but it is not expected to have a large impact on the overall response of the structure or the link slab.

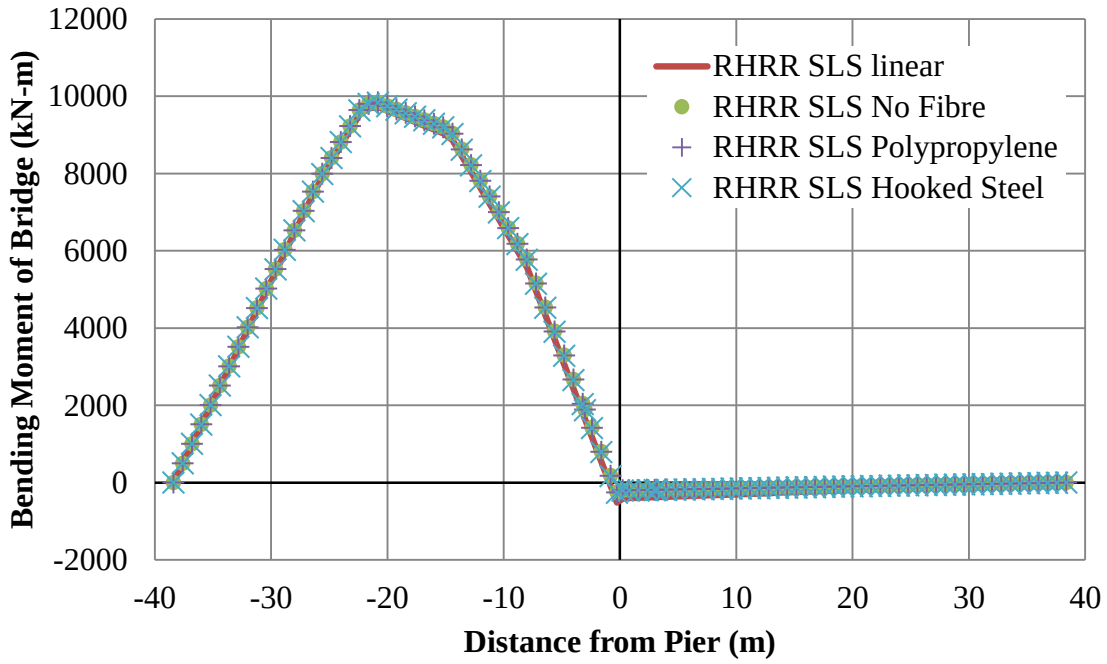

Figure 5-36 – SLS RHRR comparison of linear elastic model to non-linear models with and without FRC

Figure 5-37 is the SLS bending moment diagram for the RHHR model comparing the linear elastic bending moment to the non-linear models. From the hinge results and deflection diagram of the non-linear model (in Appendix A.11), the hinge yielded at "H4", which was above the pier support. The hinge state was close to the cracking load. Thus, the link slab bending moments did not change significantly (i.e., less than 10% change) and there was no significant force redistribution. The bending moment diagram showed no change between the linear model and the non-linear models since the effect of the hinge was negligible.

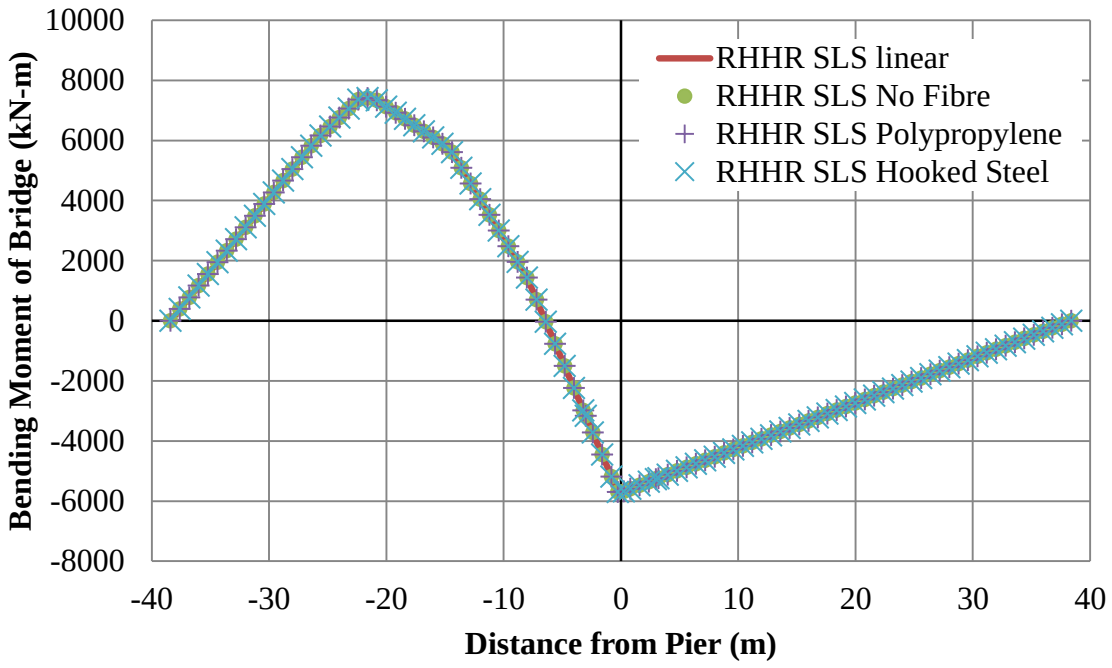

Figure 5-37 – SLS RHHR comparison of linear elastic model to non-linear models with and without FRC

Figure 5-38 is the SLS bending moment diagram for the HRRH model comparing the linear elastic bending moment to the non-linear models. The bending moment diagram showed a significant change between the linear model and the non-linear models with less bending moments in the non-linear models, similar to the HRRH in Section 5.4.3.1.

From Table 4-15, the link slab bending moment was -634 kN-m for the linear elastic model. The non-linear models showed almost zero bending moment in the link slab. The axial force in the linear elastic model was 15000 kN, which resulted in a bending moment capacity of almost zero for both ULS and SLS axial-moment yield surfaces in Figure 5-27 and Figure 5-28, respectively. This is consistent with the hinge results and deflection (see Appendix A.11) of the non-linear model, where all of the hinges show loading past and exceeding the yield load.

For the normal concrete (no fibre) model, four of the nine hinges were loaded past the cracking load and approaching the ultimate failure. For the polypropylene FRC models, hinges "H4" and "H5" were exceeding the cracking load and nearing the ultimate load. For the hooked steel FRC model, hinge "H4" exceeded the cracking load. Similar to the RHRR model, this was because the stiffness of the hooked steel was higher than the polypropylene fibres. Thus, the hooked steel FRC was not able to accommodate deformation as the polypropylene would, causing concentrated load at one location.

For the HRRH non-linear models, the hinge was not able to maintain the bending moment capacity since the axial force capacity of the hinges was exceeded, resulting in zero moment capacity in the link slab.

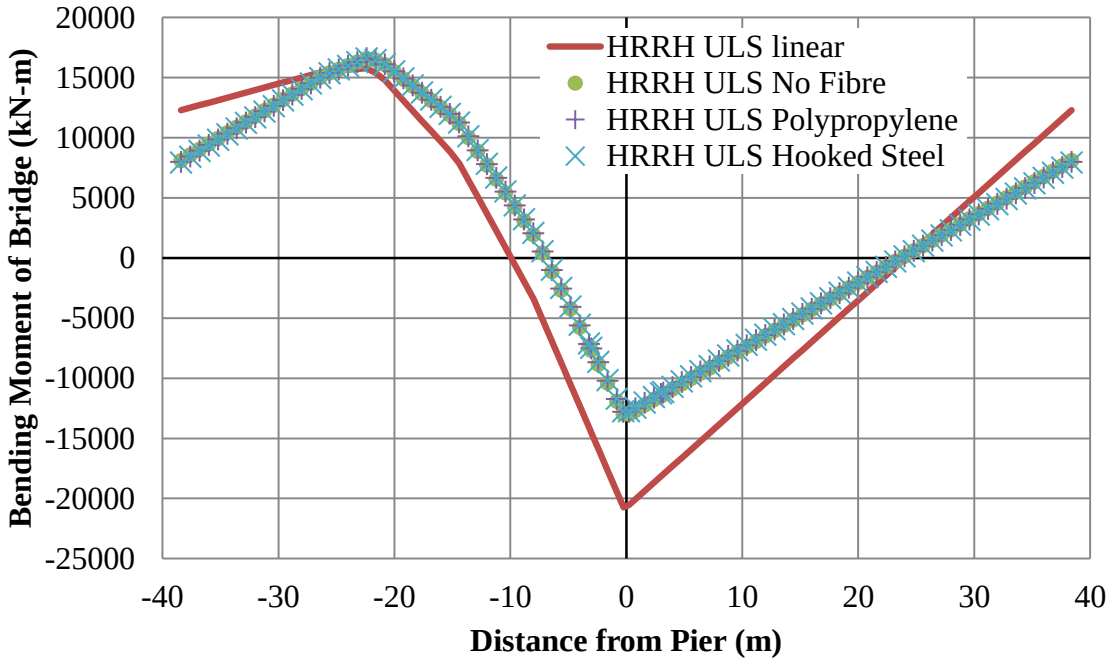

Figure 5-38 – SLS HRRH comparison of linear elastic model to non-linear models with and without FRC

5.4.3.3 Summary of Results

From the non-linear analysis to assess the effect of FRC on the link slab bridge response at the ULS and SLS:

- The bridge models with FRC showed increased bending moment resistance and better cracking characteristics than bridge models without FRC. Thus, FRC improved the strength and durability characteristics of the link slab.
- The RHRR and RHHR models with non-linear analysis showed cracking (yielding of hinges) at the pier supports, which was consistent with the site observations by MTO, where cracking of the concrete was found in the link slab at the pier support.
- The RHRR and RHHR models showed that the redistribution of force effects in the hinge was small and did not affect the overall redistribution of force effects in the link slab bridge, such that the bending moment diagram did not deviate from the linear elastic analysis.
- The model output showed that the hooked steel FRC had more severe local cracking than the polypropylene FRC link slab (with loading between the cracking and yielding capacity of the link slab). Thus, the conclusion drawn was that the polypropylene FRC was able to distribute the cracks more uniformly across the link slab than hooked-steel FRC.
- In the HRRH SLS model, the horizontal restraints at the abutments caused the resulting force effect in the link slab to be very large (similar to the conclusion drawn in 3.4.2 and 5.2.3), which led to the plastic hinge exceeding its ultimate capacity even at the service load, whereas the RHRR and RHHR models did not exceed the yield moment capacity.

- In both ULS and SLS HRRH models, multiple plastic hinges exceeded the ultimate capacity of the plastic hinges, which meant that large horizontal restraints at the abutment caused very large loads in the link slab. Thus, HRRH was not recommended for design.
- Plastic deformation of the hinges in the HRRH model allowed deformation to occur in the link slab, which relieved the bridge of the horizontal restraint in the abutments, but at the same time decreased the bending moment capacity in the link slab bridge (due to failure in the link slab).

5.5 Main Summary of Parametric Study

From the ULS and SLS analysis:

- It was found that dead loads generated large force effects in the link slab. Thus, it was recommended to install the link slab after the hardening of the bridge deck concrete to minimize the dead load force effect in the link slab.
- Similar to the dead load, placement of link slab concrete after the bridge deck concrete hardening was recommended to minimize the effect of bridge deck shrinkage on the link slab.

From the debonded length analysis:

- The required steel reinforcement for the ULS in the RHRR model was relatively insensitive to debonded length over a range of 2.5% to 7.5%.
- Hooked-steel FRC reduced the crack width (and stress in the steel reinforcement) significantly and it was recommended for use in the link slab at 7.5% debonded length.

- Considering initial construction cost and serviceability with hooked steel FRC (e.g., crack width), debonded length from 5% to 7.5% was recommended.

From the non-linear analysis with FRC:

- The bridge models with FRC showed increased bending moment resistance and better cracking characteristics than bridge models without FRC. Thus, the addition of FRC in the link slab improved its strength and durability characteristics.
- In the HRRH ULS and SLS models, the horizontal restraints at the abutments caused the resulting force effect in the link slab to exceed the ultimate capacity of plastic hinge, whereas the force effects in the link slab for the RHRR and RHHR models did not exceed the yield moment capacity at SLS or the ultimate capacity at ULS.
- Plastic deformation of the hinges in the HRRH allowed deformation to occur in the link slab, which relieved the bridge of the horizontal restraint in the abutments, but decreased the bending moment capacity in the link slab bridge since axial forces were too large.

Recommendations for designing the link slab bridge:

- The placement of the link slab concrete should be carried out after the placement and hardening of the bridge deck concrete to avoid large force effects in the link slab from dead load and bridge deck concrete shrinkage.
- The horizontal restraint at the abutment should be reduced to avoid large build-up of internal forces in the bridge and in the link slab.
- The CMOD versus applied load should be established with experiment using methods described in RILEM TC 162 in order to characterize the FRC tensile stresses at service

and ultimate, especially for FRC with different mixes and concrete strengths than described by this research.

- Based on the non-linear model developed in SAP2000, the polypropylene FRC link slab had better crack distribution than hooked-steel FRC link slab, but the hooked-steel fibres were better at reducing the tensile stress in the steel reinforcement and the mean crack width of the link slab.
- Based on the debonded length analysis, it was recommended to use hooked-steel FRC at a debonded length from 5% to 7.5%.

Chapter 6 Analytical Model for Link Slab Design

6.1 Introduction

The computational models developed in the previous chapters could be used to assess the response of a composite bridge with a link slab, and to capture the effects of support conditions and link slab properties on the design force effects. Although the computational model provides a very complete and in-depth analysis of the bridge, a considerable level of expertise and amount of effort is needed to build and validate the model, and this may not be practical for all design situations. This chapter describes the development of an analytical model to capture the primary bridge responses needed for design purposes using equations, circumventing the need for complicated computational models (e.g., SAP2000) in many design situations. The proposed modelling approach considered the results from the computational models and incorporated the findings in the development of design guidelines for FRC link slabs. From the investigation of various models and support conditions in Chapter 3, the results showed that the RHRR model closely represented the as-designed condition because the elastomeric bearing supports were representative of roller supports with little or no horizontal restraint. Therefore, the development of the analytical model in this research was based on the assumption that support conditions of the link slab bridge were similar to the RHRR model. The following aspects were considered in the analytical model:

1. Equations for the force effects in the link slab due to imposed loading needs to be derived using the force method of indeterminate analysis for the link slab bridge.
2. The stress-strain relationship of the FRC link slab needs to be determined using equations and recommendations from the *fib* Model Code and CSA A23.3 code.

Although the Canadian standard for bridge design follows the CHBDC, most of the design provisions in the CHBDC are for concrete deck slabs composite with the girders. Since the link slab is not designed to be composite with girders, CSA A23.3 is used instead for the analysis and design of the link slab, which treats the link slab a typical reinforced concrete element rather than a typical concrete bridge deck.

The derivation of the relationships between the force effects in the link slab and the imposed loading were obtained for the RHRR support configuration. Live (truck) loads and thermal loads were selected based on the results of the parametric analysis in Section 5.2, where it was found that these loads produced the governing force effect in the link slab. Shrinkage load did not need to be accounted for in the RHRR model since there were no horizontal restraints that resisted the shrinkage load. The analytical model developed in this research was a simplification of the computational model used in Chapter 3 and Chapter 5 by treating the link slab and girder as simple beam elements in structural analyses. The model derivation is described in detail in Section 6.2.

The derivation of stress-strain relationship for FRC focused on utilizing and modifying the existing equations and procedures from the *fib* Model Code and CSA A23.3 code. From the experimental study in Section 4.3, it was found that FRC provided post-cracking tensile strength in concrete. Therefore, tensile stress in reinforced concrete must be included in the equations for developing a design guideline of reinforced concrete with fibres. Two types of FRC recommended by Cameron [34] were polypropylene and hooked steel FRC, and the tensile stresses for analysis and design were obtained using the *fib* Model Code (see Section 4.3). The derivation of stress-strain relationship with FRC is presented in Section 6.3, and a step-by-step example of using the derived stress-strain equations in design is provided in Section 6.4.

6.2 Force Effect Derivation of Link Slab Bridge Model

The first part of the analytical model was to derive the relationship between the force effect in the link slab and imposed loading on the link slab bridge. From the parametric study in Section 5.2, it was found that the governing load cases were live (truck) loads and thermal loads. The link slab bridge was simplified into a series of beam elements, and the force method was used to obtain the forces in the link slab due to imposed loading.

6.2.1.1 Generalized Analytical Model for RHRR Live Load

From the computational model in Chapter 3, the RHRR model was found to be representative of bridges with elastomeric bearing supports (i.e., Camlachie Road Underpass). The current method by Caner and Zia [1] for link slab analysis simplifies the bridge into a simply-supported bridge structure, but the drawback of Caner and Zia's method is that the stiffness and eccentricity of the link slab is not considered in the analysis (see Section 1.2.1.1 for Caner and Zia's method). It was suggested by Caner and Zia that the girder end rotation of a simple beam model could be used to approximate the bending moment in the link slab [1], shown in Equation 6-1,

$$M_{ls} = 2 \cdot \frac{E_c \cdot I_g}{L} \cdot \theta \qquad 6\text{-}1$$

where M_{ls} is the bending moment in the link slab, E_c is the elastic modulus of concrete, I_g is the gross moment of inertia, L is the length of the link slab, and θ is the girder-end rotation from a simply-supported beam. From a simply-supported beam analysis in SAP2000, the girder-end rotation from the truck load was 0.00420 radians, which was equivalent to 416 kN-m using Equation 6-1. From the parametric study in Section 5.2, the link slab bending moment due to

truck load was 383 kN-m from the bridge model in SAP2000. Therefore, Caner and Zia's method over-estimated the bending moment by 16%. See Appendix B.1 for sample calculations.

Using the force method of indeterminate analysis, the link slab bridge can be analyzed when the link slab and bridge span are represented by beam elements. However, the eccentricity between the neutral axes of the link slab and bridge span must be taken into account, as shown in Figure 6-1, where the link slab is elevated from the bridge span.

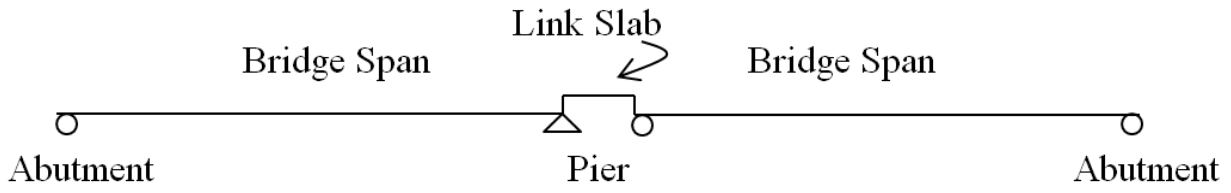

(a)

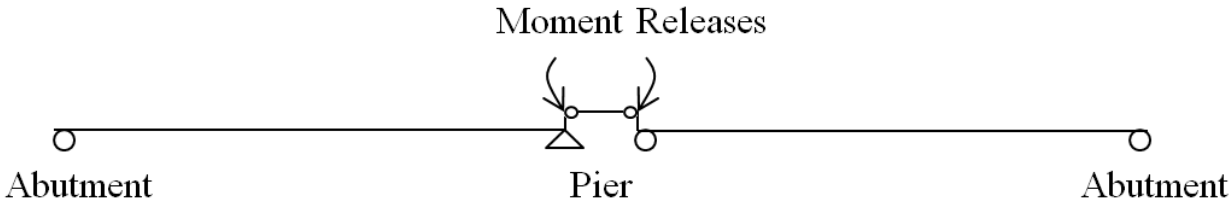

(b)

Figure 6-1 – Link slab bridge (a) simple beam model and (b) two rotational releases at link slab ends

For the RHRR support condition, the link slab bridge is two degrees indeterminate, and can be reduced into a statically determinate structure by releasing rotations at the link slab ends. The compatibility at the release can be restored later to find the force effects at the releases. In

forming a determinate structure, the relationship between the force effects at the releases, rotations and the stiffness of the structure can be described using Equation 6-2,

$$\begin{Bmatrix}\theta_1\\ \theta_2\end{Bmatrix}+\begin{bmatrix}f_{11} & f_{12}\\ f_{21} & f_{22}\end{bmatrix}\begin{Bmatrix}X_1\\ X_2\end{Bmatrix}=\begin{Bmatrix}0\\ 0\end{Bmatrix} \quad 6\text{-}2$$

where $f_{i,j}$ are flexibility coefficients based on the degrees of freedom i and j (e.g., i and j can be 1 or 2 for this case), θ_1 and θ_2 are the rotational degrees of freedom at the releases, and X_1 and X_2 are the bending moments at the releases. For the example shown in Figure 6-1, the degree of freedom 1 and 2 are the rotational releases provided at the left and right ends of the link slab, respectively. Equation 6-3 is the rearranged version of Equation 6-2 solving for the bending moment in the rotational release at the left end of the link slab.

$$X_1=\left(1-\frac{f_{11}^2}{f_{12}^2}\right)^{-1}\frac{f_{11}}{f_{12}^2}\cdot\theta_1 \quad 6\text{-}3$$

Equation 6-4 is the general form of the flexibility coefficient, where the area of bending moment due to unit rotation at "*i*" from the primary structure (i.e., determinate structure) is multiplied by the value of bending moment due to unit rotation at "*j*", divided by the stiffness of the bridge span *EI*. Appendix B.2 shows sample calculations of determining the flexibility coefficients.

$$f_{i,j}=\int m_i\frac{m_j(x)}{EI}dx \quad 6\text{-}4$$

Based on the idealized bridge configuration shown in Figure 6-1, The formulae for determining the flexibility coefficients $f_{i,j}$ are shown in Equations 6-5 and 6-6, where $L_{link\ slab}$ and L_{span} are the lengths of the link slab and bridge span, respectively, and $EI_{link\ slab}$ and EI_{span} are stiffness of the link slab and bridge span, respectively. Results of the coefficients are provided based on the geometry and material of the link slab bridge, which for this example can be found in Chapter 3

of the Camlachie Road Underpass as-designed condition. From Equation 6-3, the calculated bending moment is 391 kN-m, which is closer to the computational model result of 383 kN-m obtained from SAP2000 than compared to Caner and Zia's proposed equation (416 kN-m). See Appendix B.2 for sample calculations.

$$f_{11} = f_{22} = \frac{1}{3} \cdot \frac{L_{span}}{EI_{span}} + \frac{1}{3} \cdot \frac{L_{link\ slab}}{EI_{link\ slab}} = 14.0\left(10^{-6}\right) \frac{1}{\text{kN-m}} \qquad 6\text{-}5$$

$$f_{12} = f_{21} = \frac{1}{6} \cdot \frac{L_{link\ slab}}{EI_{link\ slab}} = 6.74\left(10^{-6}\right) \frac{1}{\text{kN-m}} \qquad 6\text{-}6$$

6.2.1.2 Simplified Analytical Model for RHRR Live Load

The generalized analytical model in Section 6.2.1.1 can be further simplified by assuming that the link slab acts as a rotational spring. In the RHRR model, there was no horizontal restraint in the structure. Thus, the axial component of the link slab did not need to be included in the analysis. The rotational spring can be solved using the force method as well, shown in Equation 6-7,

$$\theta + f_{11} \cdot M_{ls} = -\theta_{ls} \qquad 6\text{-}7$$

where θ is the girder rotation from the primary structure (similar to Equation 6-1), f_{11} is the flexibility coefficient from a virtual (unit) rotation of the primary structure at the pier, M_{ls} is the bending moment in the link slab (analogous to X_1 in Equation 6-3 of the generalized model), and θ_{ls} is the rotation of the bridge with the effects of the link slab. The rotation at the link slab is equal to the bending moment of the link slab divided by its rotational stiffness k_{ls}. Figure 6-2(a) is the pictorial representation of Equation 6-7.

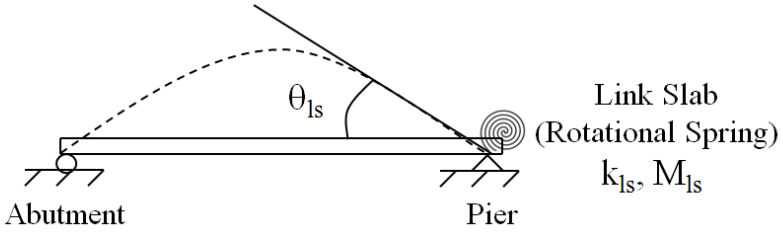

(a)

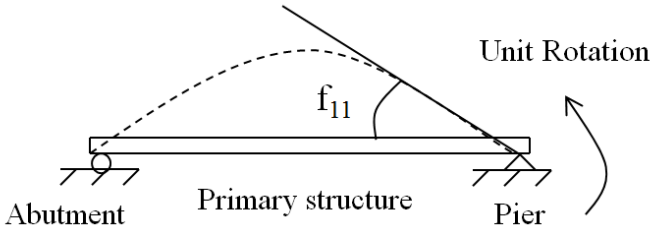

(b)

Figure 6-2 – The link slab bridge (a) as a rotational spring and (b) unit rotation of primary structure

Equation 6-7 can be simplified in terms of the bending moment in the link slab, which is shown in Equation 6-8.

$$\theta + f_{11} \cdot M_{ls} = -\frac{M_{ls}}{k_{ls}} \rightarrow M_{ls} = \frac{\theta}{1/k_{ls} + f_{11}} \qquad 6\text{-}8$$

Using the simplified equation and accounting for the rotational stiffness of the link slab, a result of 396 kN-m was obtained. Sample calculations for the proposed method can be found in Appendix B. The bending moment in the link slab was 3.4% higher than the link slab model using SAP2000. Results of the bending moments using SAP2000, generalized analytical model, simplified analytical model and Caner and Zia's method are summarized in Table 6-1.

Table 6-1 – Live load analysis comparing proposed equation to SAP2000 parametric study

	Bending Moment (kN-m)	Difference compared to SAP2000 (%)
SAP2000 results (parametric study)	383	-
Proposed generalized analytical model (Eq. 6-7)	391	2.1
Proposed simplified analytical model (Eq. 6-7)	396	3.4
Caner and Zia model (Eq. 6-1)	416	8.6

Therefore, both Equation 6-2 (generalized model) and Equation 6-7 (simplified model) can closely approximate the relationship between the force effect in the link slab and the imposed live load.

6.2.1.3 Analytical Model for RHRR Thermal Load

The force method can also be used for loading due to imposed strains, such as thermal and concrete shrinkage loads. Similar to live loads, the bending moment of the statically determinate primary structures can be found readily, and geometric compatibility then is restored to find the bending moment in the link slab.

From the parametric study in Section 5.2, the positive thermal load was the governing case in the RHRR model. Gradient thermal load was not considered because it acted in the opposite direction of the live load (i.e., beneficial effect) for the Camlachie Road Underpass. Figure 6-3 shows the positive thermal load for the composite section with steel girder elongating relative to the concrete deck.

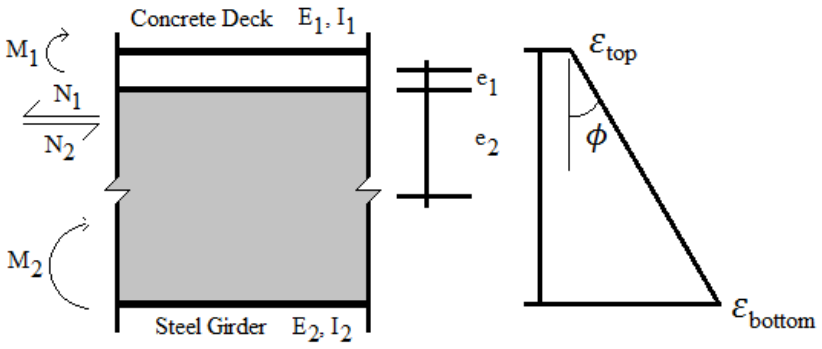

Figure 6-3 – Composite section behaviour under strain [41]

Equation 6-9 shows a closed-form solution for calculating the strains in the section as suggested by Huang et al. [41], where E is the elastic modulus of the sections, A is the area of the section, I is the moment of inertia of the section, e is the distance between the centroid of the section to the interface of the two sections, P is the axial force in the section and M is the bending moment in the section. The terms P/EA and Me/EI define the strain from axial force and bending moment, respectively. The term ε_T is the uniform strain in the concrete deck.

$$\frac{P_1}{E_1 \cdot A_1} + \frac{M_1 \cdot e_1}{E_1 \cdot I_1} = \varepsilon_T - \frac{P_2}{E_2 \cdot A_2} - \frac{M_2 \cdot e_2}{E_2 \cdot I_2} \qquad 6\text{-}9$$

For a composite bridge section, the expansion coefficient is greater for steel. Thus, for positive thermal loads, the bottom fibre of the bridge span expands more than the top fibre, causing bending in the same direction as the live load (i.e., thermal load causes positive curvature). For an unrestrained bridge such as the RHRR bridge model, the thermal strain ε_T can be calculated using Equation 6-10, where a is the thermal expansion coefficient of the material and ΔT is the thermal load. The curvature ϕ is the bending moment is divided by the bending stiffness $E \cdot I$ of the section shown in Equation 6-11, and illustrated in Figure 6-3, where M_T is the total bending moment in the section and $E \cdot I_T$ is the bending stiffness of the deck-girder section.

$$\varepsilon_T = (\alpha_1 - \alpha_2)\Delta T \quad 6\text{-}10$$

$$\phi = \frac{M_1}{E_1 \cdot I_1} = \frac{M_2}{E_2 \cdot I_2} = \frac{M_T}{E \cdot I_T} \quad 6\text{-}11$$

Since the section is unrestrained, there is zero net force or moment to satisfy force balance in the section. The sum of axial force and bending moment must be zero, shown in Equation 6-12.

$$\sum P = P_1 - P_2 = 0; \quad \sum M = P_1 e_1 + P_2 e_2 + M_1 + M_2 = 0 \quad 6\text{-}12$$

Substituting Equations 6-12 into Equation 6-11, the bending moments in the sections with respect to the axial forces are shown in Equation 6-13.

$$M_1 = \frac{P_1(e_1 + e_2) \cdot E_1 \cdot I_1}{E_1 \cdot I_1 + E_2 \cdot I_2}; \quad M_2 = \frac{P_2(e_1 + e_2) \cdot E_2 \cdot I_2}{E_1 \cdot I_1 + E_2 \cdot I_2} \quad 6\text{-}13$$

Finally, substituting Equation 6-13 into Equation 6-9 yields a closed-form solution to calculate the axial force in the concrete deck and steel girder, as shown in Equation 6-14. The section curvature is then used to calculate the end rotation in the bridge. For an unrestrained bridge span without link slab, the girder-end rotation can be approximated by the curvature multiplied by half of the bridge span length.

$$P_1 = P_2 = \frac{\varepsilon_T}{\frac{1}{E_1 \cdot A_1} + \frac{1}{E_2 \cdot A_2} + \frac{(e_1+e_2)^2}{E_1 \cdot I_1 + E_2 \cdot I_2}} \quad 6\text{-}14$$

For the Camlachie Road Underpass, which was subjected to a positive thermal load of 31^{o}C, the preceding model predicted a curvature of -3.98(10^{-8}) 1/mm and girder end rotation of -0.000764 radians. Calculations can be found in Appendix B.2. In comparison, a computer model of the simple span bridge (i.e., without link slab) predicted -0.00075 radians as the rotations for the positive thermal. Therefore, the closed-form equation for approximating an unrestrained bridge span is deemed valid.

Table 6-2 – Thermal load analysis comparing proposed equation to SAP2000 parametric study

	Bending Moment (kN-m)	Difference compared to SAP2000 (%)
SAP2000 results for pos. thermal load	-90	-
Proposed analytical model (Eq. 6-2)	-121	33
Caner and Zia method (Eq. 6-1)	-80	-12

From the parametric study in Section 5.2, it was found that the girder-end rotation in the link slab was -0.00059 radians for the positive thermal load. Using the proposed force method analytical model (i.e., Equation 6-2), the bending moment in the link slab was determined to be -121 kN-m with a difference of 33% when compared to SAP2000 results. Using Caner and Zia's method (Equation 6-1) gave a moment of -80 kN-m due to the positive thermal load with a difference of -12%, which means the bending moment was under-predicted in the link slab. The results of the bending moment from SAP2000, proposed analytical model and Caner and Zia's method for the positive thermal load are summarized in Table 6-2. Therefore, the proposed method resulted in a conservative prediction of the bending moment, while Caner and Zia's method under-predicted the bending moment.

6.2.1.4 Live load, Thermal and Shrinkage Load for RHHR and HRRH Models

The analysis of the RHHR and HRRH models are more complicated than the RHRR model due to higher indeterminacy in the bridge and horizontal restraints. Thus, the axial component of the link slab bridge cannot be ignored. Therefore, it is not trivial to represent the RHHR configuration with an analytical model by just considering the link slab as an axial spring. This

is because the link slab reaction is coupled by the bending moment and axial force, rather than considering the axial force and bending moment separately. In the RHHR model, the stiffness of the axial component with the moment arm is two magnitudes greater than the rotational stiffness of the link slab, which means the forces are likely to be distributed between the axial and bending components. Therefore, it is expected that less bending moment will occur in the link slab in the RHHR model in comparison to the RHRR model. Unfortunately, it was difficult to develop a closed-form solution for the RHHR and HRRH models, which required the coupling of bending and axial effects in the analytical model. It is therefore recommended to use a computer model to determine the behaviour of the RHHR and HRRH models, and more research is recommended to develop closed-form solutions for the RHHR and HRRH models.

Shrinkage in the link slab was not considered in the RHRR model because movement was allowed at the abutment and pier. Thus, shrinkage had no effect on the bridge model as the supports were free to move to accommodate the shrinkage. In the RHHR model, shrinkage was not considered because it acted in the opposite direction of the governing loads. Shrinkage load, however, is important in the HRRH model because it acted in the same direction as the governing live loads and the reactions in the link slab was significant. With shrinkage, it was found (from the parametric study in Section 5.2) that reactions higher than the live or thermal load were generated in the link slab due to abutment restraints at the bridge ends. A closed-form equation was not developed due to the coupling of axial and bending behaviour at the link slab (similar to the RHHR model). It is therefore recommended to use a computational model for analyzing the shrinkage behaviour of the bridge with this support configuration.

6.3 Derivation of Stress-strain Equations for FRC

The design of reinforced concrete in practice uses the stress-strain relationship of the concrete, and the same principle was used to determine the capacity of FRC with steel reinforcements in this research. It was discussed in Section 4.3 that the post-cracking tensile effects of FRC could be included using a rectangular tensile stress block in ultimate limit design as per the *fib* Model Code [14]. Additionally, it was found that the crack spacing and width were reduced through the use of fibres in concrete (see the experimental study in Chapter 5), which was supported by laboratory results in Chapter 4 and also by other researchers including Deluce and Vecchio [23] and Moffatt [24]. In developing the analytical model for link slab design, the Camlachie Road Underpass was used as a design example in this section. As reported previously in Chapter 3, the link slab dimensions are 190 mm in depth by 9754 mm wide with 2 rows of reinforcing steel at depths of 70 mm and 120 mm from the top surface of the link slab. These dimensions were used to demonstrate the use of the analytical model to analyze and design the FRC link slab in this research.

6.3.1 Ultimate Limit Design with FRC

The previous analyses indicated that the governing design condition for the link slab in most cases would be produced by live (truck) loads on the bridge, producing negative bending in the link slab. The tension side of the link slab is at the top surface of the slab due to bending in the negative curvature. This is to say that the tensile steel reinforcement layer is 70 mm from the top of the link slab, and the second layer of steel reinforcement is almost ineffective as it is quite close to the neutral axis of the link slab. Therefore, the stress in the steel reinforcement 120 mm from the top of the link slab can be neglected when considering the link slab in bending.

To better understand the response of the FRC link slab, an examination of the stress profile over the depth of the section using a layer-by-layer strain compatibility analysis is used to visualize the effects of fibres in reinforced concrete, as demonstrated by Figure 6-4. This figure shows the stress in the link slab versus link slab depth at ultimate (i.e., concrete at the extreme compression fibre has reached the crushing strain of $\varepsilon_{cu} = 0.0035$). See Appendix A.4 for a sample algorithm of the layer-by-layer analysis. Note that the compressive stress is at the bottom because the link slab is in negative bending. Three types of concrete were assessed, including reinforced concrete without fibres (denoted as normal concrete), reinforced concrete with polypropylene fibres (denoted as Polypropylene Fibres) and reinforced concrete with hooked steel fibres (denoted as Hooked Steel Fibres). The depth at 0 mm is the bottom of the link slab, which is in compression, and the depth at 190 mm is the top surface of the link slab, which is in tension. The steel reinforcement area was based on the as-designed condition of the Camlachie Road Underpass, which used approximately18200 mm^2 of steel reinforcement in one layer.

The top (tension) layer of steel reinforcement was used in calculating the bending capacity of the link slab because the contribution from the second layer of steel (120 mm from the top) was not significant, as it was very close to the neutral axis at ultimate. As a comparison, only accounting for the tensile reinforcement gives an ultimate bending moment capacity of 780 kN-m, while considering both steel reinforcement layers gives a bending capacity of 796 kN-m. The difference is only 2.1%, which is marginal. This means considering the tension reinforcement layer only (and not the compression steel) was sufficient for analysis. With the tension effect of fibres such as polypropylene and hooked steel fibres, it was found that the compression zone was increased to satisfy the force balance of the section.

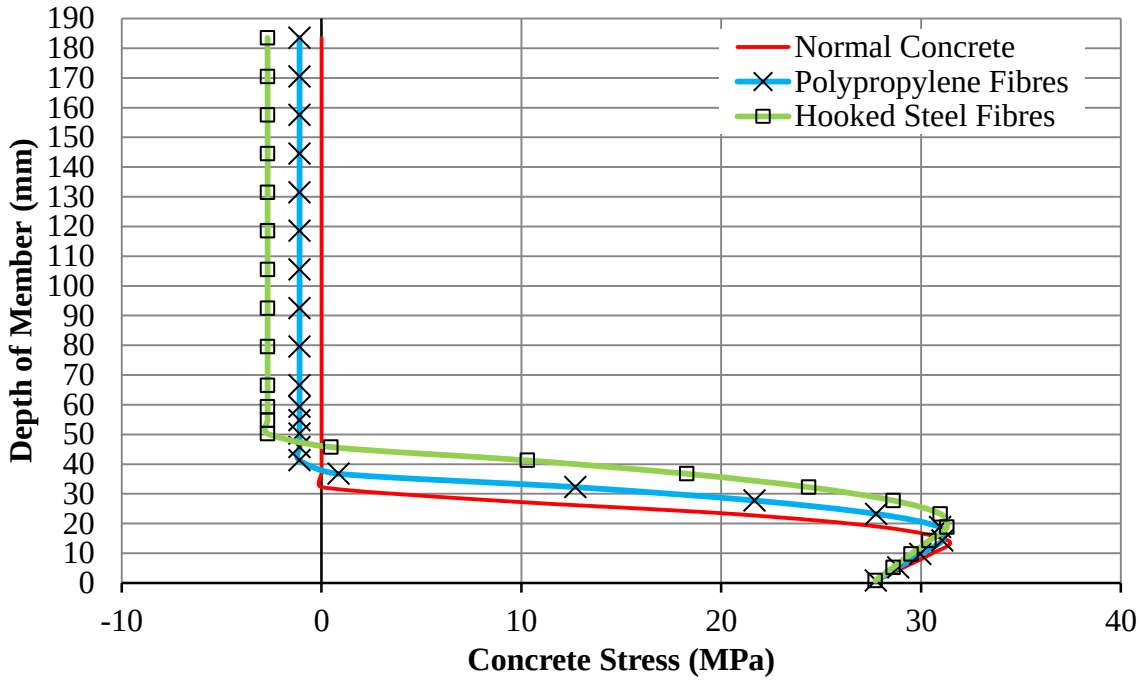

Figure 6-4 – Concrete stress versus depth of link slab at crushing strain from layer-by-layer analysis

From Figure 6-4, it can be seen that the compressive stress block in normal concrete is slightly smaller than the FRC stress blocks (polypropylene and hooked steel). This is because in order to achieve balance of forces at the cross-section, the compressive stress block must increase in size to accommodate the additional tensile stresses in the section due to the contribution of the fibres. The tensile stress from the polypropylene and hooked steel FRC were obtained from the experimental study in Section 4.3 based on methods described in RILEM TC 162 [15] and *fib* Model Code [14]. The tensile stresses for the stress blocks at ultimate load were 1.2 MPa and 2.8 MPa for polypropylene and hooked steel FRC, respectively. The tensile stress block is illustrated schematically as shown in Figure 6-5.

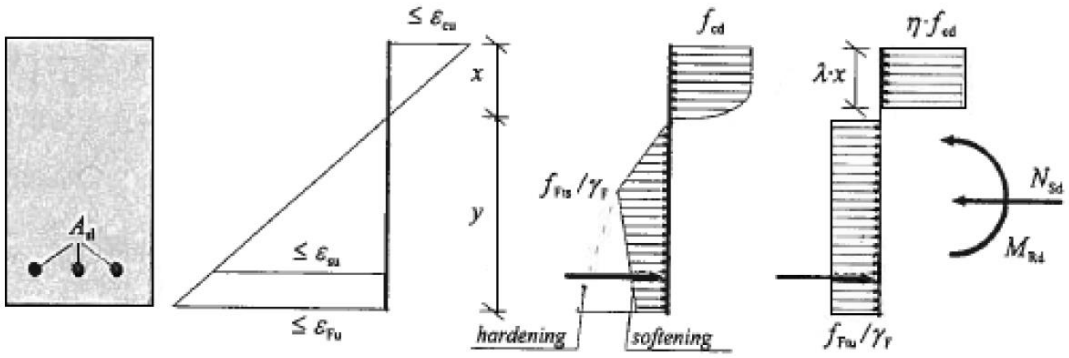

Figure 6-5 – *fib* Model Code approach for tensile stress blocks in FRC [14]

As mentioned previously, the additional tension component acting on the section due to the effects of fibres requires the concrete compression stress block to increase to maintain equilibrium. Based on equilibrium, the depth of the concrete compression block accounting for the addition of fibres with tensile stress f_t can be computed using Equation 6-15. Note that the compression block depth is denoted using "*a*" in Canadian standard (i.e., CSA A23.3), while it is indicated as λx by the *fib* Model Code in Figure 6-5,

$$C_c = T_s + T_c$$

$$\phi_c \cdot \alpha_1 \cdot f_c^{'} \cdot b \cdot a = \phi_s \cdot A_s \cdot f_y + \phi_{c,t} \cdot b \cdot h_t \cdot f_t \qquad 6\text{-}15$$

$$a = \frac{\phi_s \cdot A_s \cdot f_y + \phi_{c,t} \cdot b \cdot h_t \cdot f_t}{\phi_c \cdot \alpha_1 \cdot f_c^{'} \cdot b}$$

where C_c is the compressive resultant force of the concrete section, T_s is the tensile resultant force due to the steel reinforcement, T_c is the tensile resultant force due to the fibres in concrete, *a* is the depth of the concrete compression block, ϕ_c is the resistance factor for concrete, *b* is the width of the link slab section, α_1 is a stress block factor (the ratio of average stress in the compression block to the concrete compression strength), $f_c^{'}$ is the strength of concrete, ϕ_s is the

resistance factor for reinforcing steel, A_s is the area of steel reinforcement, f_y is the yield stress of steel reinforcement, $\phi_{c,t}$ is the resistance factor for concrete tensile stress, h_t is the depth of the rectangular tensile block, f_t is the effective concrete tensile stress in the rectangular tension block. The resistance factor $\phi_{c,t}$ is an assumed value this research that equals to the concrete safety factor (not defined in CSA 23.3 or CHBDC). Equation 6-16 gives the factored moment resistance of the FRC section and includes the additional effects from fibres with the tensile stress f_t, and z_t is the moment arm from the concrete tensile resultant force to the concrete compression resultant force.

$$M_r = \phi_s \cdot A_s \cdot f_y(d - a/2) + \phi_{c,t} \cdot h_t \cdot f_t \cdot z_t \qquad 6\text{-}16$$

Using a layer-by-layer analysis for normal concrete (i.e., without fibres), the nominal bending moment capacity of the link slab was found to be 780 kN-m. Using the conventional procedure from the CHBDC [32], the nominal moment resistance was 776 kN-m, which had an difference of 0.48% compared to the layer-by-layer analysis. Calculations can be found in Appendix C.1.

By including the tensile stress in concrete as a rectangular stress block in the layer-by-layer analysis, the bending moment capacities were 919 kN-m and 1104 kN-m for link slab with polypropylene fibres and hooked steel fibres, respectively. The moment resistances using the proposed methods given by Equations 6-15 and 6-16 were 912 kN-m and 1097 kN-m for link slab with polypropylene fibres and hooked steel fibres, respectively. The differences comparing the proposed method to the layer-by-layer analysis were 0.58% and 0.68%, respectively. The inclusion of fibres increased the capacity of the link slab by more than 10%. Results of the bending moments are summarized in Table 6-3. Calculations can be found in Appendix C.1. In

conclusion, the proposed equation to include a rectangular tensile stress block is a valid approach in estimating the bending moment in the link slab with fibres.

Table 6-3 – Moment capacity of link slab at ultimate with tension stiffening and effects of fibre

	Moment Capacity at Ultimate (kN-m)		Diff. (%)
	Eq. 6-16	Layer-by-layer Analysis	
Normal Reinforced Concrete (No Fibres)	776	780	0.48
Reinforced Concrete with Polypropylene Fibres	912	919	0.58
Reinforced Concrete with Hooked Steel Fibres	1097	1104	0.68

6.3.2 Service Load Analysis with FRC

The conventional method of calculating the bending moment at service load levels assumes that the concrete compression stress distribution is linear, as shown in Figure 6-6. The existing method used to calculate the properties of the reinforced concrete section at service needs to be revised to include the post-cracking tension contribution of the fibres.

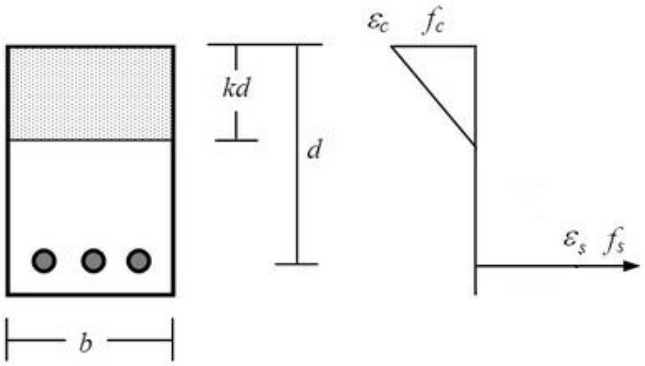

Figure 6-6 – Stress distribution in a reinforced concrete section at service load [42]

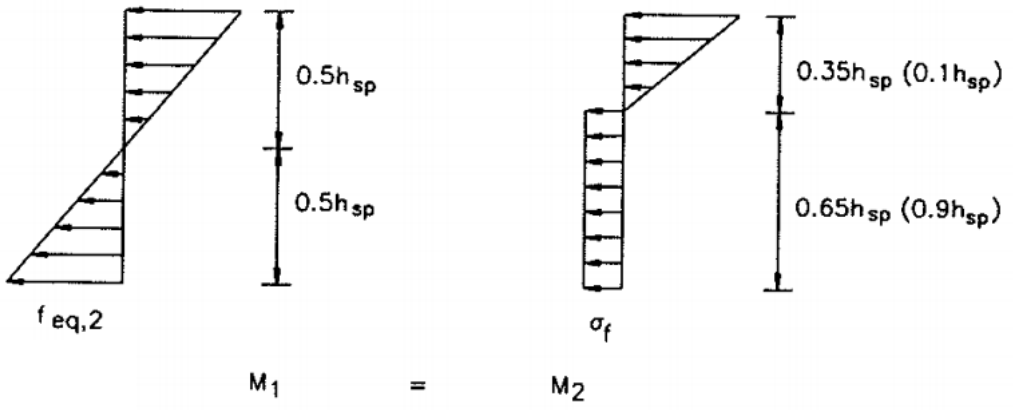

(a) (b)

Figure 6-7 – FRC stress distribution based on RILEM TC 162 for (a) before cracking (linear-elastic) and (b) after cracking [15]

The RILEM TC 162 method suggests that the tensile stress distribution at service is also assumed to be rectangular in shape, similar to that for ultimate. Figure 6-7shows the proposed stress blocks based on RILEM TC 162, where $f_{eq,2}$ is the stress before cracking, σ_f is the stress of FRC after cracking, and h_{sp} is the effective height of the section (i.e., excluding notches in the concrete section). Including the tensile stress in the reinforced concrete affects the compression

zone, and in order to satisfy the force balance of the section, the neutral axis will towards the tension face. An approach similar to the ultimate moment calculation in Section 6.3.1 was used, which accounted for the force balance of concrete in compression, steel reinforcement in tension and fibres in tension. With reference to Figure 6-6, the derivation of force balance of the section at service is shown in Equation 6-17, which assumes a linear compression stress and the tensile stress as a rectangular stress block effective below the neutral axis,

$$(C_c)_{serv} = (T_s)_{serv} + (T_c)_{serv}$$
$$0.5 \cdot b \cdot kd \cdot f_c = \rho \cdot b \cdot d \cdot f_s + b(h - kd) \cdot f_t \qquad 6\text{-}17$$

where b is the width of the section, kd is the position of the neutral axis of the concrete section, ρ is the reinforcing ratio, d is the depth of the reinforcement. Thus, $b \cdot kd$ is the area of the concrete in compression, $b(h - kd)$ is the area of concrete in tension and $\rho \cdot b \cdot d$ is the area of steel reinforcement.

For polypropylene and hooked steel FRC, the service level stresses in the equivalent tensile stress block were 1.3 MPa and 3.0 MPa, respectively. These values were determined previously in the experimental study in Section 4.3. Similar to the ultimate moment analysis in Section 6.3.1, the tensile stress block is treated as a uniform rectangular stress block effective below the neutral axis. This is bounded by a distance of $7.5d_b$ from the tensile steel reinforcement as recommended by *fib* Model Code [31] [14], but for the Camlachie Road Underpass link slab section this limit is within the depth of the neutral axis and thus does not govern. The term f_s is the stress in the steel reinforcement, which is now a variable depending on the magnitude of the bending moment. The compressive stress can be rearranged based on Equation 6-18.

$$\frac{f_c}{kd} = \frac{f_s/n}{d-kd} \rightarrow f_c = \frac{kd}{d-kd} \cdot \frac{f_s}{n} \qquad 6\text{-}18$$

Substituting the concrete stress from Equation 6-18 in the force balance equation in Equation 6-17, the final equation can be solved to obtain the neutral axis "kd", shown by Equation 6-19,

$$0.5 \cdot kd\left(\frac{kd}{d-kd}\right) \cdot \frac{f_s}{n} + kd \cdot f_t - \left(\rho \cdot d \cdot f_s + h \cdot f_t\right) = 0 \qquad 6\text{-}19$$

where *n* is the Elastic Modulus of steel to concrete. For tensile stress f_t, polypropylene and hooked steel FRC are constants, so reiteration of the neutral axis kd is not necessary, which means Equation 6-19 is a closed form solution. Summing the moment about the neutral axis gives the moment in service, shown in Equation 6-20.

$$M_T = A_s \cdot f_s(d-kd) + 0.5 \cdot b \cdot kd \cdot f_c(2 \cdot kd/3) + b(h-kd) \cdot f_t \cdot (h-kd)/2 \qquad 6\text{-}20$$

Table 6-4 – Moment capacity of link slab at yield with tension stiffening and effects of fibre

	Moment Capacity at Yield (kN-m)		Diff. (%)
	Eq. 6-20	Layer-by-layer Analysis	
Normal Reinforced Concrete (No Fibres)	755	754	0.13
Reinforced Concrete with Polypropylene Fibres	907	904	-0.33
Reinforced Concrete with Hooked Steel Fibres	1073	1107	3.1

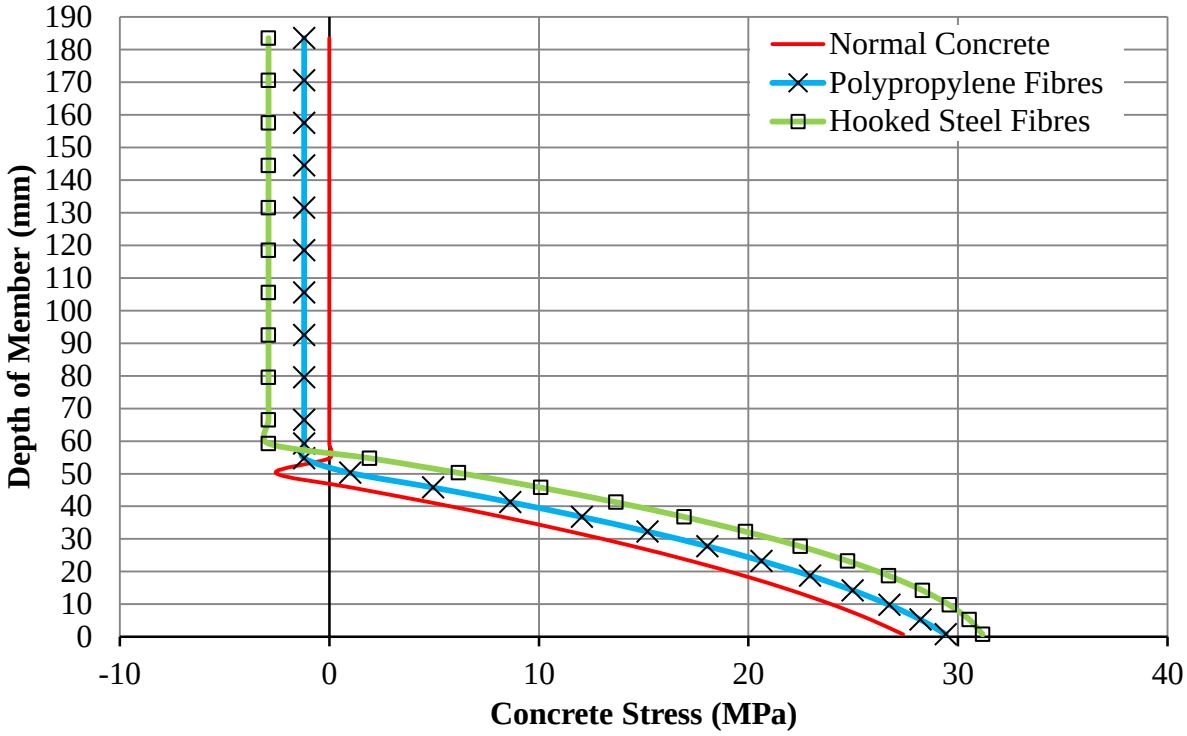

Figure 6-8 – Concrete stress versus depth of link slab at steel yielding from layer-by-layer analysis

A sample analysis has been conducted to find the yield moment in the link slab of the Camlachie Road Underpass. The calculations can be found in AppendixD.2. The yield moments obtained from the layer-by-layer analysis were 904 kN-m and 1107 kN-m for reinforced concrete with polypropylene fibres and hooked steel fibres, respectively. Using the proposed method (i.e., Equations 6-19 and 6-20), the yield moments were 907 kN-m and 1073 kN-m for reinforced concrete with polypropylene fibres and hooked steel fibres, respectively, with differences of -0.33% and 3.1% compared to its layer-by-layer results, respectively. Therefore, the answers obtained from the proposed equations were very close to the results from the layer-by-layer analysis. Figure 6-8 is the layer-by-layer stress of the cross-section of the link slab. Note that

the shape of the compressive stress is quite linear while tensile stress is rectangular, which follows the assumption for deriving the proposed method.

6.3.3 Design with Axial Forces for RHHR and HRRH Models

The RHHR and HRRH models are different than the RHRR model because of the presence of axial forces in the link slab of the RHHR and HRRH models. To include axial force in design, one method is to modify the compression area of concrete to satisfy the force balance of the section, which follows the same concept as the proposed method from Equation 6-15. The procedure to calculate the compression stress block depth, a, including the effect of an externally applied axial force, P_f, is shown in Equation 6-21,

$$\sum F_{int} = P_f$$

$$T_s + T_c - C_c = P_f$$

$$P_f = \phi_s \cdot A_s \cdot f_y + \phi_{c,t} \cdot b \cdot h_t \cdot f_t - \phi_c \cdot \alpha_1 \cdot f_c' \cdot b \cdot a \qquad \text{6-21}$$

$$a = \frac{\phi_s \cdot A_s \cdot f_y + \phi_{c,t} \cdot b \cdot h_t \cdot f_t - P_f}{\phi_c \cdot \alpha_1 \cdot f_c' \cdot b}$$

where $\sum F_{int}$ is the sum of forces in the concrete cross-section due to concrete and steel reinforcement (similar to Equation 6-15), P_f is the applied axial force, which is positive for tension and negative for compression. The next step is to calculate the bending moments taking the centre of area as the reference axis so that the applied axial force P_f has zero bending moment contribution at the centre of area.

6.4 Link Slab Design Example using Derived Stress-strain Equations

The Camlachie Road Underpass was used as the sample design case using the proposed models developed in Section 6.3. The design force effect results from the ULS 2 in Section 5.2 were used to determine the required reinforcements in design, and results from the SLS 1 were used to assess the serviceability requirements as per the CHBDC. The focus of the design in this section will be the design of link slab with the RHRR model, and the RHHR and HRRH models will only be briefly discussed. The difference between this section and Section 6.3 is the determination of steel reinforcement in designing the link slab with FRC. The ULS 2 and SLS 1 results were obtained from Section 5.2and summarized in Table 6-5.

Table 6-5 – ULS 2 and SLS 1 results from parametric study in SAP2000

	Bending moment in Link Slab (kN-m)		Axial force in Link Slab (kN)	
	ULS 2	SLS 1	ULS 2	SLS 1
RHRR	-881	-511	0	0
RHHR	-191	-107	6814	3985
HRRH	-1070	-634	22740	15502

6.4.1 Ultimate Limit State Design

The first step is to determine the required reinforcement in the link slab accounting for the contribution of the FRC. For polypropylene and hooked steel fibres, the stresses in the effective tensile stress block at ultimate were 1.2 MPa and 2.8 MPa, respectively. Let M_t be the additional bending in reinforced concrete due to effect of the fibres, as shown in Equation 6-22,

$$M_t = \phi_{c,t} \cdot b \cdot h_t \cdot f_t \cdot z_t \qquad 6\text{-}22$$

where $\phi_{c,t}$ is the resistance factor for concrete in tension, b is the width of the link slab, h_t is the height of the tensile stress block, and z_t is the moment arm between the concrete compression zone and the tensile stress block. By including the effect of fibres, the required steel reinforcement in tension, $A_{s,req}$, can be determined using Equation 6-23,

$$A_{s,req} = \frac{M_f - M_t}{\phi_s \cdot f_y \cdot 0.9 \cdot d} \qquad 6\text{-}23$$

where M_f is the factored bending moment from the ULS 2 load case, ϕ_s is the resistance factor for steel, f_y is the strength of steel reinforcement and d is the depth of the steel reinforcement. Based on the calculations, it was found that the required reinforcing steel areas were 22000 mm^2 and 18000 mm^2 for reinforced concrete with polypropylene fibres and hooked steel fibres, respectively. The steel reinforcement requirements are summarized in Table 6-6. Calculations for the ultimate limit designs are in Appendix D.1. The factored moment resistances based on these reinforcement areas and the FRC contributions were computed to be 885 kN-m and 899 kN-m for reinforced concrete with polypropylene fibres and hooked steel fibres, respectively, with differences of 0.56% and 0.55% compared to the layer-by-layer analysis (with CHBDC resistance factors). Therefore, the proposed method was deemed valid. The bending moment resistances are summarized in Table 6-7. Figure 6-9 shows the concrete stress distribution for the link slab at the ultimate limit state.

Without fibres, the required steel was found to be 22660 mm^2 (rounded to 22800mm^2). When hooked steel FRC was used, the required steel was reduced by 21%. Therefore, the inclusion of fibres in concrete had a significant impact on the reduction of required steel in the link slab, which would effectively reduce the construction cost of the link slab. Thus, the proposed method was valid in evaluating the bending capacity of the link slab at ultimate.

Table 6-6 – Required steel reinforcement with polypropylene and hooked steel fibres

	Eq. 6-23 Steel Reinforcing Area Required (mm2)	Percent Steel Reduced (%)
Normal Reinforced Concrete (No Fibres)	22800	-
Reinforced Concrete with Polypropylene Fibres	22000	3.5
Reinforced Concrete with Hooked Steel Fibres	18000	21

Table 6-7 – Moment resistance of link slab at ULS with polypropylene and hooked steel fibres

	Bending Moment Capacity (kN-m)		Diff. (%)
	Eq. 6-16	Layer-by-layer Analysis	
Normal Reinforced Concrete (No Fibres)	886	888	0.01
Reinforced Concrete with Polypropylene Fibres	885	890	0.56
Reinforced Concrete with Hooked Steel Fibres	899	904	0.55

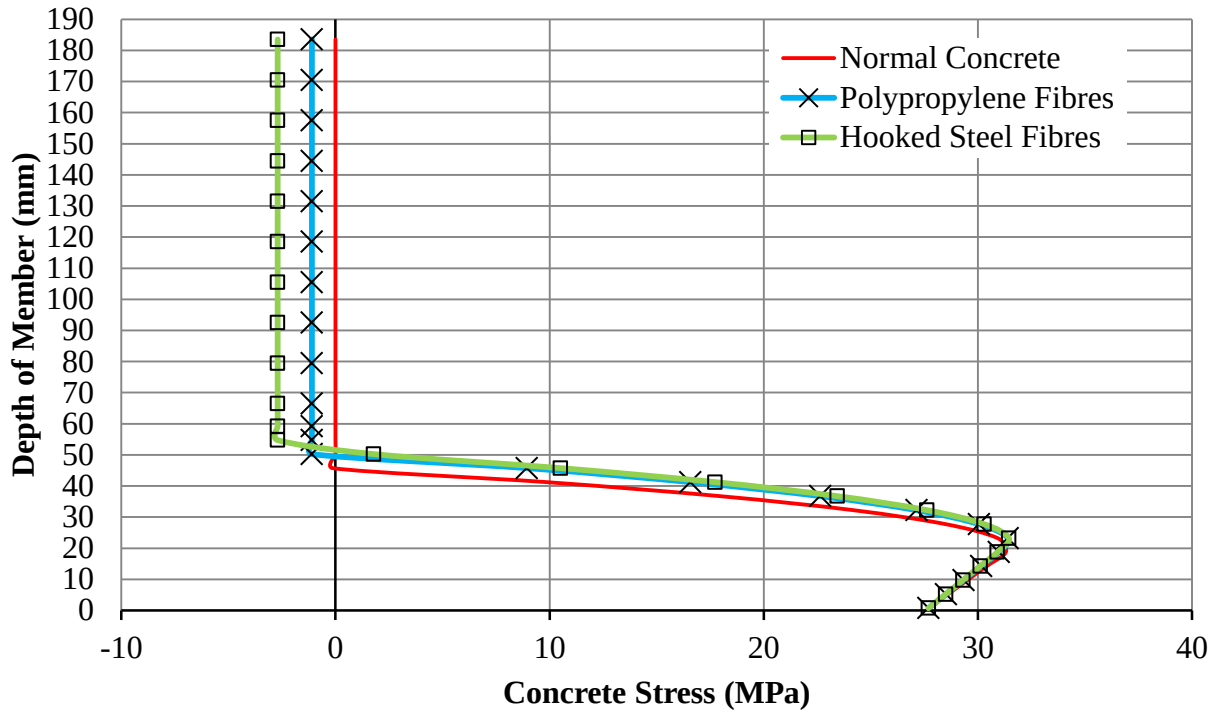

Figure 6-9 – Concrete stress at ultimate strength for design from layer-by-layer analysis

6.4.2 Yield Moment Calculation

The calculation of the yield moment assumed a linear strain profile in the concrete. Since the calculation was for bending moment capacity at service, material resistance factors were not used. The first step was to determine the neutral axis of the section i as described in Section 6.3.2. For polypropylene and hooked steel fibres, the stresses in the effective tensile stress block, f_t, were 1.3 MPa and 3.0 MPa, respectively. The equation to calculate the neutral axis is shown in Equation 6-24, which follows the same form as Equation 6-19, except that the stress in steel reinforcement f_s is replaced with the yield stress f_y for calculating the bending moment at yield.

$$0.5 \cdot kd\left(\frac{kd}{d-kd}\right) \cdot \frac{f_y}{n} + kd \cdot f_t - \left(\rho \cdot d \cdot f_y + h \cdot f_t\right) = 0 \qquad 6\text{-}24$$

The yield moment can be calculated after the neutral axis is found using Equation 6-25 (similar to Equation 6-20), which sums the resultant forces about the neutral axis kd.

$$M_T = A_s \cdot f_s(d - kd) + 0.5 \cdot b \cdot kd \cdot f_c(2 \cdot kd/3) + b(h - kd) \cdot f_t \cdot (h - kd)/2 \qquad 6\text{-}25$$

Sample calculations for the yield moment can be found in Appendix D.2. Table 6-8 shows the moment capacity of the link slab a yield.

Table 6-8 – Yield moment for link slab designs with fibres and tension stiffening

	Yield Moment (kN-m)		Diff. (%)
	Eq. 6-20	Layer-by-layer Analysis	
Normal Reinforced Concrete (No Fibres)	971	974	0.03
Reinforced Concrete with Polypropylene Fibres	1018	1037	1.8
Reinforced Concrete with Hooked Steel Fibres	1068	1099	2.8

The resultant yield moments were 1018 kN-m and 1068 kN-m for reinforced concrete with polypropylene fibres and hooked steel fibres, respectively, with differences of 1.8% and 2.8% compared to the layer-by-layer analysis (with CHBDC resistance factors). The proposed method was close to the layer-by-layer analysis. Thus, the proposed method was deemed valid in evaluating the yield moment for the link slab. Note that the bending moment at yield was higher than the ultimate moment in Table 6-7 because resistance factors were included in the calculation at ultimate, whereas resistance factors were not used at yield (i.e., service load conditions).

Additionally, the yield moment was much higher than the ultimate moment because the tensile stresses were higher at service load than at ultimate (refer to Chapter 4 for details). Figure 6-10 shows the concrete stress distribution of the link slab at yielding with fibres.

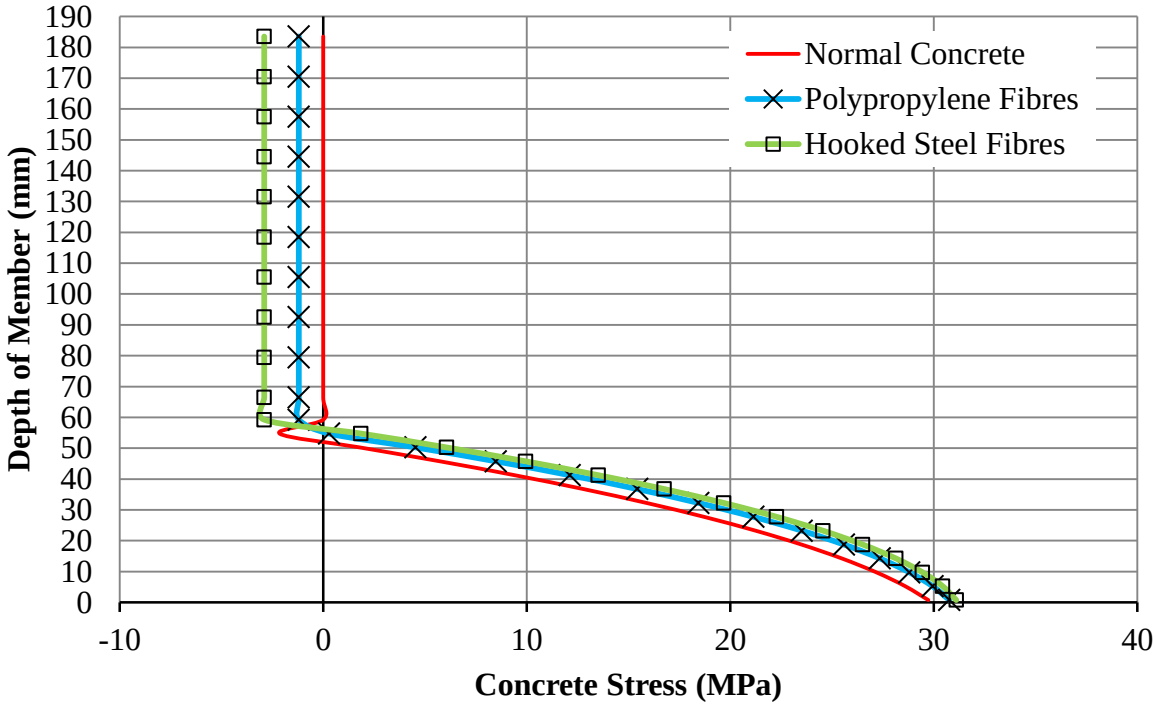

Figure 6-10 – Concrete stress versus depth of link slab at steel yielding from layer-by-layer analysis

6.4.3 Steel reinforcing Stress Check

The serviceability conditions of the link slab were assessed according to the CHBDC requirements. From the parametric study, the SLS 1 bending moment was 511 kN-m. The stress in the reinforcing steel is limited to 240 MPa (or $0.6 \cdot f_y$) as per Clause 8.6.2.7.4 of the CHBDC. Equation 6-26 checks the stress in the steel without accounting for the effects of the fibres.

$$f_s = \frac{M}{A_s(d - 2 \cdot kd/3)} \quad \text{6-26}$$

The next step was to check the steel reinforcement stresses when the tension stiffening effects of FRC were accounted for (i.e., including the tension stress block for polypropylene and hooked steel FRC). Equation 6-27 shows the service load bending moment, M , including contributions from the steel reinforcement, M_s, and FRC stress block in tension, M_t, which are found by multiplying the tensile resultants by the moment arm from the compression resultant force.

$$M = M_s + M_t = A_s \cdot f_s(d - 2 \cdot kd/3) + b(d - kd) \cdot f_t \cdot z_t \quad \text{6-27}$$

The tensile stress in concrete, as a function of the bending moment, is shown in Equation 6-28. For simplicity, the neutral axis *kd* can be assumed based on the yield load analysis in Section 6.4.2 as a conservative estimate to the neutral axis.

$$f_s = \frac{M - M_t}{A_s(d - 2 \cdot kd/3)} \quad \text{6-28}$$

It was found that for normal reinforced concrete, the stress in steel reinforcement was 263 MPa at the design service load moment of 511 kN-m, which exceeded the limits from Clause 8.6.2.7.4 of the CHBDC. For reinforced concrete with polypropylene fibres and hooked steel fibres, the stresses were 189 MPa and 102 MPa, respectively, which were reduced by 28% and 61% when compared to normal concrete, respectively. This demonstrates the significant tension stiffening effect of the FRC in reducing the stress in the steel reinforcement. The results are summarized in Table 6-9. Note that the steel reinforcement is different for each type of FRC link slab (see Table 6-6 for steel reinforcement).

Table 6-9 – Stress in steel reinforcement calculated for SLS 1

	Stress in Steel Reinforcement (MPa)		Difference (%)
	Eq. 6-28	Layer-by-layer Analysis	
Normal Reinforced Concrete (No Fibres)	263	267	-1.5
Reinforced Concrete with Polypropylene Fibres	189	158	20
Reinforced Concrete with Hooked Steel Fibres	102	85.7	19

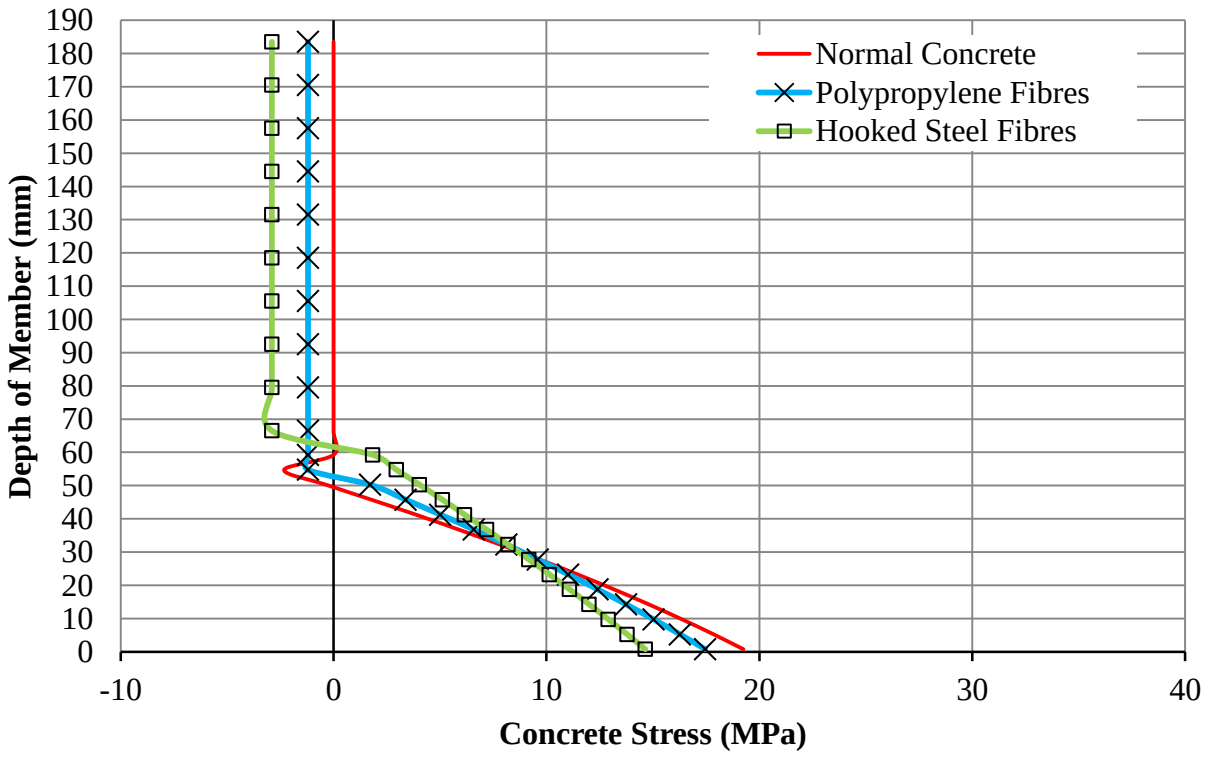

Figure 6-11 – Concrete stress versus depth of link slab for SLS 1 from layer-by-layer analysis

The effects of FRC decreased the stress in the reinforcement and the limits from the CHBDC were satisfied. The proposed equations were more conservative compared to the layer-by-layer analysis, but both methods showed that stress in the steel reinforcement did not exceed the limits from The CHBDC. Figure 6-11 shows the concrete stress distribution of the link slab at service with fibres and tension stiffening. Calculations can be found in Appendix D.3.

6.4.4 Crack Width Check

Two serviceability checks that are required from the CHBDC are Clause 8.6.2.7.4 [32], which states that the maximum stress in the reinforcement should not exceed 240 MPa in service, and Clause 8.12.3.1, which states that the maximum crack width allowed is 0.25 mm for concrete exposed to de-icing chemicals. The SLS 1 load case is used to determine the stress at service load in the steel reinforcement. The calculation of the crack width w using the CHBDC provisions is shown in Equation 6-29,

$$w = k_b \cdot \beta_c \cdot s_{rm} \cdot \varepsilon_{sm} \qquad 6\text{-}29$$

where k_b is 1.2 for epoxy-coated bars and 1.0 for all other components, β_c is 1.7 if the crack is due to loading or if the minimum cross-section dimension exceeds 800 mm, s_{rm} is the average spacing of cracks, and ε_{sm} is the average strain in the reinforcement. The average spacing crack is given by Equation 6-30,

$$s_{rm} = 50 + 0.25 \cdot k_c \cdot \frac{d_b}{\rho_c} \qquad 6\text{-}30$$

where k_c is 0.5 for bending and 1.0 for pure tension, d_b is the reinforcement diametre, ρ_c is the ratio of steel area to the lesser of 2.5 times the distance from the tensile fibre to the tensile

reinforcement or one third of the distance from the neutral axis to the extreme tensile fibre. The average strain in reinforcement is shown in Equation 6-31,

$$\varepsilon_{sm} = \frac{f_s}{E_s}\left[1 - \left(\frac{f_w}{f_s}\right)^2\right] \qquad 6\text{-}31$$

where f_s is the stress in steel reinforcement at the serviceability state, and f_w is the stress in reinforcement for initial concrete, both of which are calculated based on the cracked section of concrete. The value of f_s is also checked in Clause 8.6.2.7.4 from CHBDC to ensure that it does not exceed 240 MPa. The reinforcement stress in service can be calculated from the proposed equation in Section 6.3.2, which assumes a linear stress profile at service load with tension stiffening. The CHBDC equation for cracking will be used to check the serviceability limit state.

The CHBDC equations have the same form as the *fib* Model Code and RILEM TC 162. Therefore, the *fib* and RILEM TC 162 methods will be used to check the CHBDC results. The mean crack spacing "s_m" for non-fibrous concrete using the *fib* Model Code [14] is shown in Equation 6-32,

$$s_m = 2\left(c + \frac{s}{10}\right) + k_1\left(\frac{\varepsilon_1 + \varepsilon_2}{2\cdot\varepsilon_1}\right)\frac{d_b}{\rho_{eff}} \qquad 6\text{-}32$$

where c is the concrete cover, s is the spacing of reinforcements, k_1 is 0.8 for deformed reinforcing bars and 1.6 for smooth bars, d_b is the diametre of steel reinforcement, ρ_{eff} is the effective reinforcement, and ε_1 and ε_2 are the maximum and minimum tensile strains in the specimen, respectively. The RILEM Committee TC 162 equation [25] to calculate mean crack spacing for fibrous concrete is shown in Equation 6-33,

$$s_m = 50 + 0.25 \cdot k_1 \left(\frac{\varepsilon_1 + \varepsilon_2}{2 \cdot \varepsilon_1}\right)\left(\frac{50}{l_f/d_f}\right)\frac{d_b}{\rho_{eff}} \qquad 6\text{-}33$$

where l_f/d_f is the fibre aspect ratio, which is the fibre length to fibre diametre. The average strain in the reinforcement ε_{sm} is based on the loading, such as from the SLS 1 conditions. The crack spacing for normal reinforced concrete and reinforced concrete with polypropylene fibres and hooked steel fibres are summarized in Table 6-10. Note that from Table 6-10, the *fib* Model Code crack spacing equation (Equation 6-32) has a large error because it may not be applicable to bridge elements (such as the link slab), whereas the CHBDC crack equation (Equation 6-34) is for bridge decks. Calculations for the crack widths can be found in Appendix D.4 and D.5.

$$s_{rm} = 50 + 0.25 \cdot k_c \cdot \frac{d_b}{\rho_c} \qquad 6\text{-}34$$

Table 6-10 – Crack spacing results for concrete with tension stiffening and fibres

	Crack spacing (mm)		Diff. (%)
	CHBDC	*fib* Model Code	
Normal reinforced concrete (no fibres)	77.1	409	430
Reinforced Concrete with Polypropylene Fibres	78.1	96.4	23
Reinforced Concrete with Hooked Steel Fibres	84.3	119	41

The crack spacing is converted to crack width using Equations 6-32 and 6-33. It was found that the crack width for normal reinforced concrete was 0.169 mm. With polypropylene fibres and hooked steel fibres, the crack widths were 0.106 mm and 0.014 mm, respectively, both of which

were less than crack width of link slab with normal concrete. Table 6-11 is the summary of crack widths.

Table 6-11 – Crack width results for concrete with tension stiffening and fibres

	Crack Width (mm)	
	CHBDC	*fib* Model Code
Normal reinforced concrete (no fibres)	0.169	0.374
Reinforced Concrete with Polypropylene Fibres	0.106	0.088
Reinforced Concrete with Hooked Steel Fibres	0.014	0.109

It was found that the *fib* model gave a mean crack spacing of 409 mm, which corresponded to a crack width of 0.374 mm using Equation 6-28. This value exceeded the requirements of maximum crack width of 0.25 mm. Using Equation 6-34, which accounted for the presence of fibres in the concrete, the mean crack spacing were 96.4 mm and 119 mm for reinforced concrete with polypropylene and hooked steel fibre, respectively. The crack widths were 0.088 mm and 0.109 mm for the polypropylene FRC and hooked-steel FRC, respectively, according to the *fib* provisions. These crack widths were acceptable as per the CHBDC requirements. With fibres, the equations showed that the mean crack widths decreased by more than 270% compared to that of normal concrete (without fibres). In summary, the result showed that for normal concrete, the crack width was within the limits of CHBDC Clause 8.12.3.1 limit of 0.25 mm. Similarly, FRCs satisfied the CHBDC limits.

In conclusion, effects of FRC reduced the crack widths in reinforced concrete, which was calculated using CHBDC equations and checked with the *fib* Model Code and RILEM TC 162

methods. Both the CHBDC and *fib* Model Code showed reasonable crack width predictions (within one magnitude) and therefore both methods were valid.

6.4.5 Summary of Design Steps

A chart showing the design steps for the ultimate and serviceability limit states is shown in Figure 6-12. The design steps for ULS are as follows:

1. determine the effective FRC tensile stress block appropriate for ultimate limit design based on experimental tests;
2. assume a neutral axis of the section and calculate the concrete compression zone by including the tensile stress as a rectangular stress block; and
3. calculate the bending moment resistance of the section from the force resultants of concrete compression, steel reinforcement and tensile stress block from tension stiffening.

The design steps for SLS are as follows:

1. determine the effective FRC tensile stress block appropriate for service limit design based on experimental tests;
2. calculate the neutral axis depth for steel at yield assuming linear compression stress profile and rectangular tensile stress block;
3. use the neutral axis depth to approximate the stress and strain in steel reinforcement and calculate the crack spacing and width based on the stress in steel and check using CHBDC or *fib* Model Code; and
4. calculate the crack width based on the CHBDC or *fib* Model Code provisions.

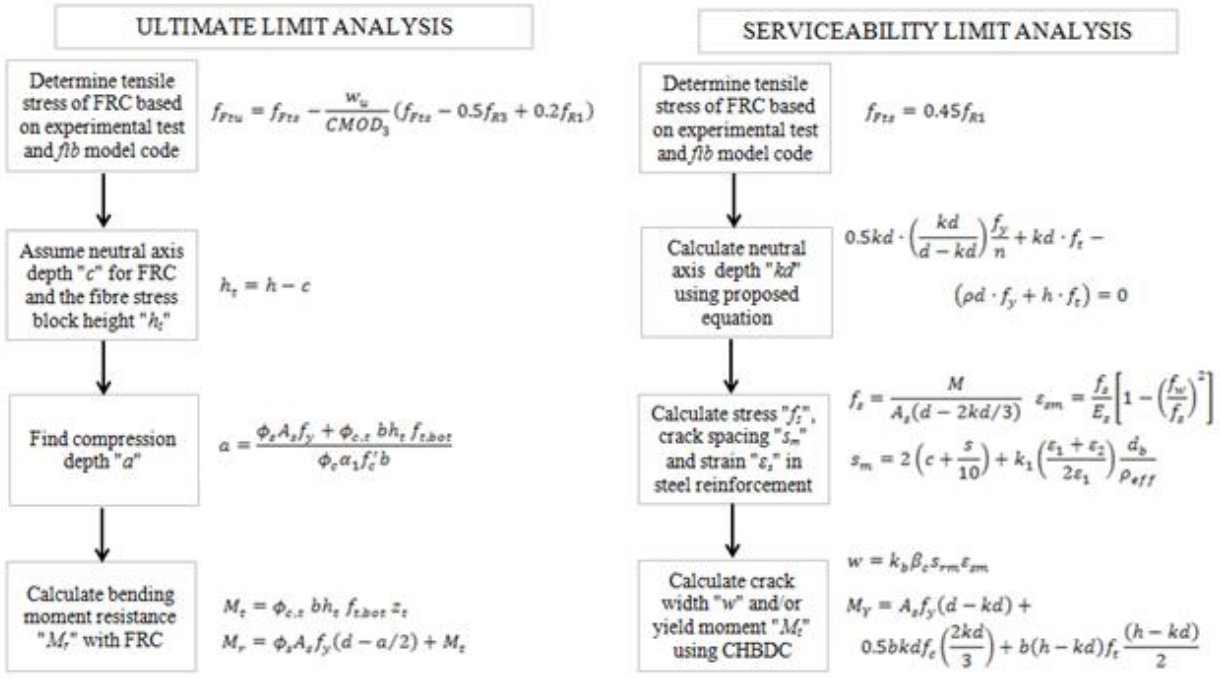

Figure 6-12 – Design steps for ULS and SLS

6.5 Summary of Analytical Model

From the analytical model to estimate the force effects in the link slab:

- The generalized analytical model showed a difference of 2-3% when compared to the SAP2000 model, whereas Caner and Zia's method showed a difference of 16% when compared to the SAP2000 model.
- The simplified analytical model for indeterminate analysis when considering the link slab as a rotational spring was valid in predicting the behaviour of the link slab bridge (i.e., Caner and Zia).
- The proposed method for calculating the thermal load was accurate when predicting the girder-end rotation for a simply-supported beam, but over-predicted the force effects in the link slab, similar to that of Caner and Zia's method.

From the analytical model accounting for the tension stiffening effects of FRC:

- The effect of FRC in reinforced concrete helped increase the bending moment capacity of the link slab by more than 10%, given that the internal steel reinforcement (bars) amount was kept the same. The increase in bending moment capacity was due to including the tensile stress block in the FRC concrete section analysis based on the *fib* Model Code and stress versus CMOD relationship obtained from tests on the FRC.
- The proposed method that used a rectangular tensile stress block in conjunction with concrete section analysis following typical procedures used for design was valid when compared to layer-by-layer analysis with less than 1% error.
- Using the proposed method and layer-by-layer analysis, it was found that the stress in the steel reinforcement was reduced by 28% and 61% with polypropylene and hooked steel FRC, respectively. As a result, the crack width of the link slab was reduced by more than 140% (2.4 times) when compared to normal reinforced concrete (without fibres) using the method described in the CHBDC.
- Crack spacing equations from the CHDBC were in agreement with the crack spacing equations that included FRC developed by *fib* and RILEM Committee TC 162. It was concluded that standard code provisions and analysis and design equations were valid when including the effects of FRC as tensile stress blocks.
- It was found that use of polypropylene fibres and hooked steel fibres in the link slab reduced the required steel reinforcement by 3.5% and 21%, respectively.

Chapter 7 Conclusions, Contributions and Recommendations

7.1 Conclusions

The primary conclusions and findings from the research are summarized in the following sections. Where appropriate, recommendations for the design of link slab bridges are included based on these conclusions.

7.1.1 Development of a Computational Model for a Link Slab Bridge

A computational model was developed using SAP2000 to model the behaviour of a two-span bridge with a link slab joining the two spans at the centre pier. The computational model considered the steel girder, concrete bridge deck and link slab as separate beam elements to account for the eccentricity between the centroid of the link slab and the centroid of the steel girder. The non-linear geometric response of the link slab was accounted for by debonding of the link slab from the steel girder using gap elements in SAP2000. The response of the computational model with elastic spring supports and idealized hinge (pinned) and roller supports were compared.

A preliminary parametric study was conducted to assess the effect of the assumed support conditions on the bridge response. As well, the predicted response of the bridge model was compared to the measured response of the Camlachie Road Underpass obtained during an MTO truck load test to provide an indication of the model accuracy and the appropriateness of the modelling approach. The primary findings of these preliminary analyses were:

- The support conditions for the Camlachie Road Underpass model with elastomeric bearing stiffness were modelled as spring supports (i.e., as-designed model or "elas" model) and had a similar response to the model with the roller-hinge-roller-roller support configuration (RHRR). This suggested that the as-designed bearing stiffness provided little or no horizontal restraint to the bridge, and indicated that bridges with elastomeric bearing supports could be modelled using the RHRR model.
- The RHRR model represented a bridge with no horizontal restraint at the supports, and therefore no axial forces were developed in the bridge when subjected to the design loading conditions. However, axial forces were developed in the link slab when there were two or more horizontal restraints at the supports (i.e., hinge supports). The magnitudes of these axial forces were significant for load cases that imposed a strain on the link slab (i.e., shrinkage).
- The bridge support conditions had significant influence on the force effects developed in the link slab, such that the assumed support conditions must be appropriately represented in a computational model for a reasonable estimation of the link slab force effects.
- The model developed in this study over-predicted the bridge deflections in comparison to the MTO truck load test result, but had better predictions than the MTO computational model. It was assumed that the actual bridge was stiffer than the computational model due to several possible factors, including:
    - the model did not account for the effect of the parapet (concrete barrier) walls on the bridge section properties;
    - the model did not include moment restraint at the abutment-ends for the semi-integral abutments; and

- the model used the design concrete strength to estimate the concrete modulus of elasticity rather than the as-constructed material properties.

- The predicted deflection was reasonably close to the MTO field measurements by within one magnitude. Therefore, the modelling approach was deemed accurate for representing the behaviour of the link-slab bridge for design and research purposes.

7.1.2 FRC Experimental Results and Parametric Study

The FRC experiment and parametric study were conducted to provide a better understanding of link slab behaviour as to assess the impact of design decisions on the bridge response. In the FRC experimental investigation, four-point bending tests results from Cameron were used to characterize the properties of FRC. The FRC properties were then used in the parametric study to study the effect of FRC in the link slab bridge response parametrically. The parametric study examined various design aspects of the link slab bridge, which were the design load combinations from the CHBDC, debonded length of the link slab, and the incorporation of FRC in the computational model.

The contribution of the FRC to the post-cracking and ultimate strength properties of a reinforced concrete structural element was examined using an experimental and analytical study. The *fib* Model Code was selected as the guideline for obtaining the tensile properties of FRC for structural design and analysis purposes. Because the standard FRC testing methods for use with the *fib* Model Code were not commonly used in North America, the ASTM C1609 test method was selected as a standard test method to establish the tensile properties of different FRC mixtures for use in design and analysis. This test method was used to assess the modulus of rupture and flexural toughness of FRC mixtures using rectangular prism specimens tested in

four-point bending, although it cannot be used directly with the *fib* Model Code procedures for FRC. The findings of this study were:

- The ASTM C1609 test method load-deflection results could be used to compute the stress versus crack mouth opening displacement (CMOD) properties for the FRC needed in the *fib* Model Code procedure. A plastic analysis procedure using virtual work was derived to compute the stress-CMOD response using the measured load-deflection results, allowing the effective tension stiffening properties of the FRC to be established using the *fib* Model Code procedures.
- The *fib* Model Code procedure used with FRC properties determined based on ASTM C1609 test results provided an accurate prediction of the load-deflection response of steel reinforced concrete beams made with FRC. This was demonstrated by comparison of the predicted response of reinforced concrete beams made using hooked steel fibres and polypropylene fibres to beam test results reported in a related project (Cameron 2013).

The following were the findings from the parametric analysis of the link slab bridge for the ultimate and service limit state load combinations from the CHBDC:

- The bridge dead loads generated significant force effects (bending moment and axial force) in the link slab if it was cast together with the bridge deck. Thus, it was recommended to cast the link slab after the casting and hardening of the bridge deck and parapet (barrier) walls to minimize the effect of dead loads on the link slab.
- Shrinkage of the concrete bridge deck in new bridge construction developed significant force effects (axial tension force and bending moment) in the computational model. Therefore, it was recommended to place the link slab concrete after the casting of the

bridge deck, which would minimize the effect of the concrete deck shrinkage on the link slab.

A parametric study was conducted on the debonded length of the link slab to determine the optimal debonded length in design, and also the economic benefits of using FRC in link slabs. The debonded lengths investigated were 0.5%, 2.5%, 5.0%, 7.5% and 10%. FRC with hooked steel and polypropylene fibres were compared to conventional concrete in terms of initial construction cost and the cracking characteristics of the link slab. The studies on the link slab debonded length revealed the following:

- As the debonded length increased, the design force effects in the link slab were reduced. As a result, the required area of reinforcement for the link slab cross-section decreased, although the total volume of steel required in the link slab increased (since the length of the link slab also increased). The required steel reinforcement (in terms of volume) for the RHRR support configuration was optimal anywhere from 2.5% to 7.5% debonded length, whereas the required steel reinforcement for the RHHR and HRRH support configurations were minimized at 2.5% debonded length.
- The predicted maximum crack width in the link slab at the service limit state decreased as the debonded length increased because the force effects (axial tension force and bending moment) in the link slab were reduced, thus the stress in the reinforcing bars reduced, which in turn reduced the crack width. The use of FRC also reduced the required amount of steel reinforcement for the link slab due to the tension-stiffening effect of the fibres. The tension-stiffening provided by the FRC reduced the stress in the steel reinforcing bars, which in turn reduced the crack width. Therefore, the use of FRC reduced the required steel reinforcement and the crack width of the link slab.

- When FRC was used with the RHRR support configuration, the optimal link slab debonded length was found to be 7.5% and 10% for hooked steel and polypropylene fibres, respectively. The optimal debonded length was selected by comparing the economic benefit of the link slab for initial construction and during its service life. The service life of the link slab was estimated based on the repair of cracks in the link slab.
- From the perspective of cost and serviceability, it was deemed that the hooked steel FRC was the best alternative for use in the link slab due to its superior crack control (i.e., lesser crack width). Since the hooked steel was selected as the best FRC alternative, 7.5% debonded length was recommended in this research for design of link slab with hooked steel FRC, which was optimal in terms of construction cost and crack control.

The contribution of the FRC to the post-cracking service load response and ultimate strength of the link slab was included in the model using plastic hinges. The plastic hinges were inserted in the link slab at expected cracking locations. The plastic hinge properties were estimated separately for service limit state (SLS) and ultimate limit state (ULS) analyses of the bridge. The following were the findings from the non-linear analyses:

- The bridge models with FRC had increased bending moment resistance and better cracking characteristics (reduced predicted crack widths) than bridge models without FRC. Thus, the addition of FRC in the link slab improved its strength and durability characteristics.
- In the HRRH ULS and SLS models, the horizontal restraint at the abutments created significant force effects (axial tension force and bending moment) in the link slab, which exceeded the predicted ultimate capacity of the plastic hinge. This suggested that the crack control and ductility provided by the FRC were not sufficient in compensating for

the force effects developed in the HRRH support configuration. In contrast, the force effects in the link slab for the RHRR and RHHR models did not exceed the yield moment capacity at SLS or the ultimate capacity at ULS. Thus, link slab bridges with HRRH support condition, such as an integral-abutment bridge, were not recommended for link slab bridge design.

- Plastic deformation of the hinges in the HRRH allowed deformation to occur in the link slab, therefore partially relieving the effect of the horizontal restraint in the abutments. However, the adverse effect of this was that the plastic deformation decreased the bending moment capacity in the link slab bridge. The same problem was not found in the RHRR and RHHR models since the plastic hinges did not undergo large plastic deformations.

The parametric computational analysis of the link slab bridge suggested the following design recommendations for link slab bridges:

- The link slab concrete should be placed after the placement of bridge deck concrete to avoid large force effects in the link slab from dead loads and bridge deck concrete shrinkage.
- The horizontal restraint at the abutment should be reduced through proper detailing of the abutment support so that the internal forces in the link slab could be minimized.
- The hooked steel FRC was the best alternative when compared to polypropylene FRC and conventional concrete in link slab design. Hooked steel FRC required the least amount of steel reinforcement in the link slab and had the best cracking characteristic. The most optimal debonded length was 7.5% for hooked steel, which took into consideration both the construction cost (i.e., steel reinforcement) and crack control.

- A bending test on FRC specimens was recommended to determine the CMOD versus load relationship, which would be used to establish the tensile stress values of the FRC using the *fib* Model Code. The *fib* Model Code was deemed to be accurate in calculating the FRC tensile stresses at service and ultimate conditions.

7.1.3 Analytical Model for Link Slab Design

The computational analysis (described in the preceding section) found that bridges with elastomeric bearing supports could be modelled assuming no horizontal restraint (e.g., RHRR model). Therefore, axial forces could be neglected in the link slab, which greatly reduced the degree of indeterminacy in the analysis. An analytical model was derived using the force method of indeterminate analysis, which was deemed suitable for "hand calculations" of the bridge force effects. The evaluation of the structural analysis analytical model showed the following:

- The proposed analytical model showed an error of 2-3% when compared to the SAP2000 model outputs, whereas the Caner and Zia's method showed an error of 16% when compared to the SAP2000 model. The proposed analytical model had better predictions because the analytical model accounted for the stiffness of the link slab as part of the link slab bridge structure, whereas Caner and Zia's method neglected the stiffness of the link slab in the bridge structure. Therefore, the proposed analytical model provided a better estimate of the force effects in the link slab than Caner and Zia's method.
- The proposed method for calculating the effects of thermal loading on the bridge was accurate when predicting the girder-end rotation for a simply-supported beam, but the force effect in the link slab was over-predicted by 33%. However, the proposed method

was deemed to be more reasonable than Caner and Zia's method, which under-predicted the bending moment by 12%. Therefore, the proposed method was more conservative than Caner and Zia's method in predicting the bending moment due to thermal load.

- An analytical model for the RHHR and HRRH models were difficult to derive due to the higher degree of indeterminacy for these support configurations. Therefore, it was recommended to use computational models to assess the link slab force effects when considering the RHHR and HRRH support conditions for link slab bridges.

Analytical procedures for the analysis and design of link slabs incorporating FRC were proposed and demonstrated. The analytical model for FRC analysis was based on the *fib* Model Code equations, which assumed a rectangular stress block for the concrete in tension (due to the fibres). The fibre stress equations from *fib* Model Code were used in conjunction with Canadian standards for concrete and bridge analyses, namely CSA 23.3 and CHBDC. The equations from the Canadian standards were modified to include effects of fibres as rectangular stress blocks. These analyses revealed the following:

- The effect of FRC in reinforced concrete increased the bending moment capacity of the link slab by over 10%, which was a notable increase in bending capacity compared to normal (i.e., no fibre) reinforced concrete. The increased bending moment was calculated based on tensile stress block assumptions from the *fib* Model Code, which was derived from the applied stress versus CMOD relationship of experiments on the FRC. The recommended setup for the experiment was a four-point bend test on rectangular specimens, which were described by RILEM TC 162.
- The proposed method of the *fib* Model Code rectangular stress block was used to calculate the bending moment resistance of FRC link slab with an error of less than 3%

compared to the layer-by-layer analysis. Using the proposed method, the stress in the steel reinforcement was reduced by 28% and 61% for polypropylene and hooked steel FRC, respectively, when compared to a link slab with normal reinforced concrete (without fibres). Because of the reduced reinforcement stress, the predicted crack width in the link slab was reduced by more than 1.5 times using the CHBDC equations, or 3 times using the *fib* Model Code crack width model. In both cases, it was suggested that fibres had significant impact on the control of cracks in reinforced concrete.

- The use of polypropylene fibres and hooked steel fibres reduced the required steel reinforcement in the link slab by 3.5% and 21%, respectively. Therefore, the addition of fibres in the link slab greatly enhanced the strength and cracking characteristics of the link slab, particularly when hooked steel fibres were used.

7.2 Research Contributions

The following is a summary of the main contributions of this thesis:

1. The examination of the eccentric effect of the link slab helped explain the development of the axial force in the link slab, which had not been modelled by others in 2-D. The centroid of the link slab is eccentric to the bridge span (i.e., steel girder with concrete bridge deck), which is found to develop axial forces in the link slab if there are horizontal restraints in the supports (i.e., RHHR and HRRH cases). Otherwise, for the RHRR case, it is found that there are no axial forces in the link slab.
2. It is concluded that the elastomeric bearings with low shear stiffness can be modelled as roller supports. Firstly, this means that axial forces in the link slab can be neglected, which greatly simplifies the analysis of the link slab bridge. Secondly, the modelling of

bridge supports with elastomeric bearings can be reduced to roller supports, which means the support condition is independent of the elastomeric bearing stiffness, and the parametric study of the link slab bridge can be simplified.

3. It is concluded that hooked steel fibres are beneficial in the design of link slabs and debonded lengths of 5% to 7.5% are the most optimal for design considering cost and serviceability. The hooked steel FRC is found to reduce the steel reinforcement by 21%, which reduces the cost of construction for both material use and labour cost. Additionally, the hooked steel FRC reduces the crack width of the link slab by 1.5 times when it is compared to conventional concrete, which is a substantial advantage in terms of crack control in link slabs.
4. The research is able to provide an analytical model for the link slab in design for both ULS and SLS design cases. This is achieved by modifying existing equations and methods from the Canadian standards CHBDC and CSA 23.3. The equations are validated using layer-by-layer analysis and computational models, and it is found that the proposed equations are deemed to predict the bending moment capacity of the link slab accurately.

7.3 Recommendations for Further Research

Based on the research from this thesis, the following is a list of recommendations for future work:

- A standardized test should be developed based on Canadian practices to determine the flexural strength of FRC similar to that of proposed method in this thesis (i.e., bending test similar to C1609 or RILEM TC 162). It is needed to validate the use of *fib* Model Code in combination with the C1609 test for calculating the tensile stress in FRC.

- There is need to conduct extensive experiments on polypropylene and hooked steel to check whether the results in this research are valid (i.e., the use of *fib* Model Code with C1609 tests). Additionally, it is needed to explore the use of other types of fibres in FRC and determine the optimal fibre type for use in FRC since only two fibre types are considered in this thesis.
- Experimental tests should be conducted on reinforced concrete as slabs (rather than beams) to determine the flexural and cracking characteristics of FRC in slabs rather than beams. Slab elements may behave differently than beams, and therefore validation is needed to confirm whether beam experiments (i.e., C1609) are appropriate for link slab research.
- Truck load tests should be conducted for bridges with elastomeric bearing supports to validate whether roller supports can be used to model elastomeric bearing supports. Moreover, multi-span bridges should be examined to check if the roller support assumption for the elastomeric bearings can be also used for bridges with higher degrees of indeterminacy.
- A life-cycle analysis on link slab bridges should be conducted for the use of FRC, and also considering long-term design characteristics of the link slab, such as fatigue and durability.

Chapter 8 References

[1] A. Caner and P. Zia, "Behavior and Design of Link Slabs for Jointless Bridge Deck," *PCI Journal*, vol. 43, no. 3, pp. 68-80, 1998.

[2] V. C. Li, M. D. Lepech, and M. Li, "Field Demonstration of Durable Link Slabs for Jointless Bridge Decks Based on Strain-Hardening Cementitious Composites," University of Michigan, Ann Arbor MI, 2005.

[3] A. M. Okeil and A. El-Safty, "Partial continuity in Bridge Girders with Jointless Decks," *Practice Periodical on Structurla Design and Construction*, vol. 10, no. 4, pp. 229-238, 2005.

[4] U.S. Department of Transportation. (2013, August) Current Practices in FRP Composites Technology. [Online]. http://www.fhwa.dot.gov/bridge/frp/frprepai.cfm

[5] Ministry of Transportation Ontario. (2011, Winter) Ontario's Transportation Technology Transfer Digest — Winter 2011 — Vol. 17, Issue 1. [Online]. http://www.mto.gov.on.ca/english/transtek/roadtalk/rt17-1/

[6] E. Ulku, U. Attanayake, and H. Aktan, "Jointless Bridge Deck with Link Slabs," *Journal of Transportation Research Board*, vol. 2131, pp. 68-78, 2009.

[7] V. C. Li and M. D. Lepech, "Application of ECC for bridge deck link slabs," *Materials and Structures*, vol. 42, pp. 1185-1195, 2009.

[8] A. Au and C. Lam, "Testing of Hwy 402/Camlachie Road Underpass," Ministry of

Transportation Ontario, Report No. BRO-045, Ontario, Canada, 2009.

[9] M. D. Lepech and V C Li, "Large Scale Processing of Engineerd Cementitious Composites," *ACI Materials Journal*, vol. 105, no. 4, pp. 358-366, 2008.

[10] AASHTO Highway Subcommittee on Bridges and Structures, "Standard Specifications for Highway Bridges, Sixteenth Edition," Washington, DC, 1996.

[11] Precast/Prestressed Concrete Institute, "PCI Design Handbook: Precast and Prestressed Concrete," Chicago, IL, 6th Edition, 2004.

[12] Michigan Department of Transportation, "Bridge Design Manual," Lansing, MI, 2005.

[13] M. A. Saadeghvaziri and R. Hadidi, "Cause and Control of Transverse Cracking in Concrete Bridge Decks," Department of Civil and Environmental Engineering, New Jersey Institute of Technology, Report No. FHWA-NJ-2002-019, Newark, 2002.

[14] the International Federation for Structural Concrete (fib), *fib Model Code Volume 1*. Lausanne, Switzerland: Ernst & Sohn publishing house, 2010.

[15] RILEM TC 162-TDF, "Test and design methods for steel fibre reinforced concrete by RILEM TC 162-TDF," *Materials and Structures*, vol. 36, pp. 560-567, 2003.

[16] the International Federation for Structural Concrete (fib), *fib Model Code Volume 2*. Lausanne, Switzerland: Ernst & Sohn publishing house, 2010.

[17] A. Jansson, "Analysis and design methods for fibre reinforced concrete: a state-of-the-art report," Chalmers University of Technology, Chalmers Report No. 2007:16, Göteborg,

2007.

[18] DAfStb UA SFB N 106, "DAfStb-Richtlinie Stahlfaserbeton-Draft march," (In German), Deutscher Ausschuss für Stahlbeton , Berlin, 2005.

[19] V. Gribniak, G. Kaklauskas, A. K. H. Kwan, D. Bacinskas, and D. Ulbinas, "Deriving stress-strain relationships for steel fibre concrete in tension from tests of beams with oridinary reinforcement," *Engineering Structures*, no. 42, pp. 387-395, 2012.

[20] I. Löfgren, "Fibre-reinforced Concrete for Industrial Construction-a fracture mechanics approach to material testing and structural analysis," PhD Thesis, Chalmers University of Technology, Göteborg, 2005.

[21] H. H. Abrishami and D. Mitchell, "Influence of Steel Fibers on Tension Stiffening," *ACI Structural Journal*, vol. 94, no. 6, pp. 769-775, 1997.

[22] P. H. Bischoff, "Tension Stiffening and Cracking of Steel Fiber-Reinforced Concrete," *Journal of Materials in Civil Engineering*, no. 15, pp. 174-182, 2003.

[23] J. R. Deluce and F. J. Vecchio, "Cracking Behavior of Steel Fiber-Reinforced Concrete Members Containing Conventional Reinforcement," *ACI Structural Journal*, vol. 110, no. 3, pp. 481-490, 2013.

[24] K. Moffatt, "Analyse de Dalles de Pont avec Armature Reduite et Beton de Fibres Metalliques," MASc Thesis (In French), École Polytechnique de Montréal, Montréal, QC, Canada, 2001.

[25] D. Dupont and L. Vandewalle, "Calculation of Crack Widths with the sigma-epsilon Method," International RILEM Workshop on Test and Design Methods for Steelfibre Reinforced Concrete, RILEM Publications SARL, Bochum, Germany, 2003.

[26] S.-C. Lee, J.-Y. Cho, and F. J. Vecchio, "Tension-Stiffening Model for Steel Fiber-Reinforced Concrete Containing Conventional Reinforcement," *ACI Structural Journal*, no. July-August, pp. 639-648, 2013.

[27] R. P. Dhakal, C. Wang, and J. B. Mander, "Behavior of steel fibre reinforced concrete in compression," Department of Civil Engineering, University of Canterbury, Christchurch, New Zealand, 2005.

[28] R. D. Neves and J. C. O. Fernandes de Almeida, "Compressive behaviour of steel fibre reinforced concrete," *Structural Concrete, fib*, vol. 6, no. 1, pp. 1464-4177, 2005.

[29] Z.-L. Wang, Y.-S. Liu, and R. F. Shen, "Stress-strain relationship of steel fiber-reinforced concrete under dynamic compression," *Construction and Building Materials*, no. 22, pp. 811-819, 2007.

[30] E. Hognestad, "A study on combined bending and axial load in reinforced concrete members," The University of Illinois, Urbana-Champaign, IL, Bulletin Series No. 399 1951.

[31] Canadian Standards Association, "Design of concrete structures," Mississauga, ON, 2004.

[32] Canadian Standards Association, *Canadian Highway Bridge Design Code*. Ontario, Canada: CSA S6-06, 2006.

[33] J. R. Deluce, "Cracking Behavior of Steel Fiber-Reinforced Concrete Members Containing Conventional Reinforcement," MASc Thesis, Department of Civil Engineering, University of Toronto, 2011.

[34] J. F. Cameron, "Engineered Fibre-Reinforced Concrete Systems for Innovative Structural Design Applications," MASc Thesis, Department of Civil and Environmental Engineering, The University of Waterloo, Waterloo, ON, 2013.

[35] Computers and Structures, Inc. (2005) CSI Analysis Reference Manual. docs.csiamerica.com/manuals/etabs/Analysis%20Reference.pdf.

[36] S. A. Civjan, C. Bonczar, S. F. Brena, J. DeJong, and D. Crovo, "Integral abutment bridge behavior: Parametric analysis of Massachusetts bridge," *Journal of Bridge Engineering*, vol. 12, no. 1, pp. 64-71, 2007.

[37] W. Kim and J. A. Laman, "Integral abutment bridge response under thermal loading," *Engineering Structures*, vol. 32, no. 6, pp. 1495-1508, 2010.

[38] H. Aktan, U. Attanayake, and E. Ulku, "Combining Link Slab, Deck Sliding over Backwall, and Revising Bearings," Department of Civil & Construction Engineering, Western Michigan University, Report No. MDOT RC-1514, Lansing, MI, 2008.

[39] R. S. Means Online. (2013, December) Search Data for Unit Prices on Commercial Construction in Toronto. Reed Construction Data Inc.

[40] Computers and Structures. Temperature-gradient loading for bridge objects. [Online].

https://wiki.csiberkeley.com/display/tp/Temperature-gradient+loading+for+bridge+objects

[41] H. Huang, Z. Xiang, and S. Liu, "Analysis method of internal force distribution on composite section for arch bridge strengthening," *6th International Conference on Arch Bridges*, pp. 860-865, 2010.

[42] City of Boston Building Department, *The Building Code Of The City Of Boston*. Boston: City of Boston, 1970.

Appendix A Parametric Study and FRC Experimental Calculations

A.1 Dead Load Calculations

The area of the reinforced concrete of the link slab is

$$\text{R. C. Area} = 190 \times 7924 + 2 \times (600 \times 300) + 2 \times (900 \times 380) = 2549560\ \text{mm}^2 = 2.55\ \text{m}^2$$

$$\text{R. C. Dead Load} = 2.55\ \text{m}^2 \times 24\ \text{kN/m}^3 = 61.2\ \text{kN/m}$$

The area and load of the asphalt wearing surface per length of the bridge is

$$\text{Asphalt (wearing surface) Area} = 90 \times 7924 = 713160\ \text{mm}^2 = 0.713\ \text{m}^2$$

$$\text{Asphalt Dead Load} = 0.713\ \text{m}^2 \times 23.5\ \text{kN/m}^3 = 16.8\ \text{kN/m}$$

The total girder steel area and load per length of the bridge is

$$\text{Steel Area} = 16 \times (1315 \times 2 + 508 \times 2 + 2032) \times 2 = 181696\ \text{mm}^2 = 0.182\ \text{m}^2$$

$$\text{Dead load in Girder} = 0.182\ \text{m}^2 \times 77\ \text{kN/m}^3 = 14.0\ \text{kN/m}$$

A.2 Live Load and Influence Line

Qualitative influence line from SAP2000, used CL-625-ONT truck to determine largest loading

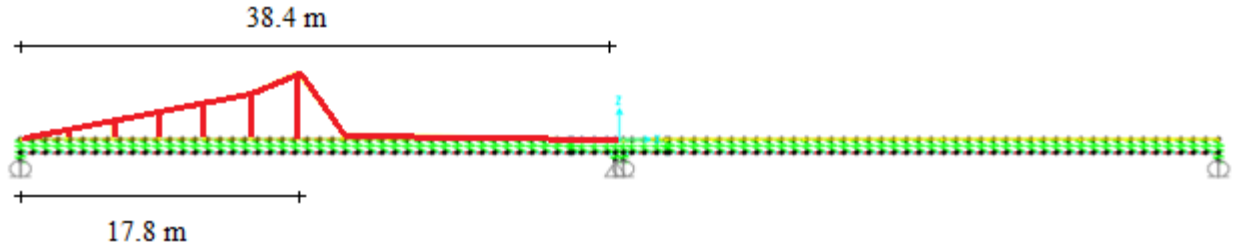

(a)

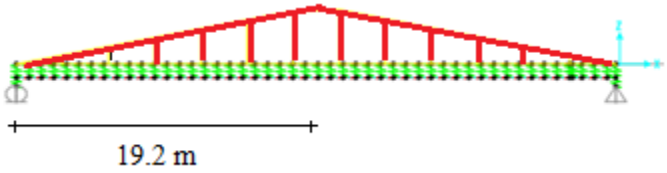

(b)

Figure A-1 – Influence line of (a) link slab bridge and (b) simply supported bridge

A.3 Shrinkage Load Calculations

$$\varepsilon_{cs0} = \beta_{RH}\left[160 + 50\left(9 - \frac{f_c' + a}{10}\right)\right]10^{-6};\ \beta_{RH} = -1.55\left[1 - \left(\frac{RH}{100}\right)^3\right]$$

The relative humidity (RH) in the region is 60 (based on the CHBDC), the link slab concrete strength (f_c') is 35 MPa, and it is assumed that the theoretical link slab concrete strength does not vary from the actual strength (i.e., the variable "*a*" equals to zero).

$$\varepsilon_{cs0} = -1.55\left[1-\left(\frac{60}{100}\right)^3\right]\cdot\left[160+50\left(9-\frac{35+0}{10}\right)\right]\cdot 10^{-6} = -529\left(10^{-6}\right)$$

To apply the strain in the structural model, the values can be converted to an equivalent temperature, such that

$$\varepsilon = \alpha\Delta T;\ \alpha = 9.9\left(10^{-6}\right)/℃;\ \Delta T_{cs0} = \frac{\varepsilon}{\alpha} = \frac{-529\left(10^{-6}\right)}{9.9\left(10^{-6}\right)} = -53.40℃$$

Therefore, the equivalent thermal load for concrete shrinkage at ultimate is -53.4°C in the bridge deck and/or link slab.

A.4 Layer-by-layer Analysis

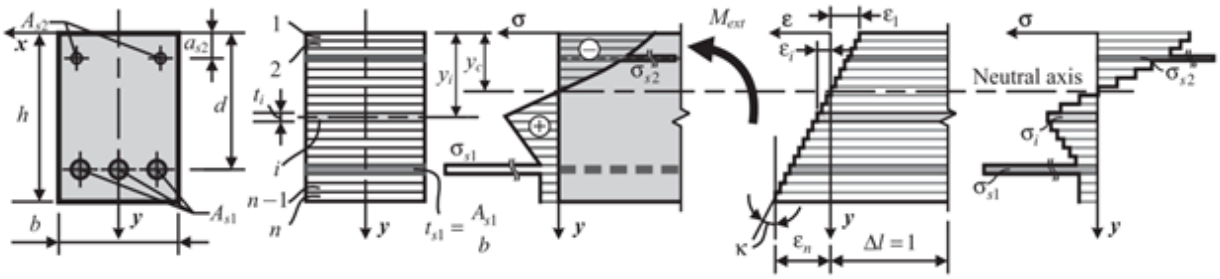

Figure A-2 – Layer-by-layer analysis diagram [19]

Table is an example of the layer-by-layer analysis with excel. The layer-by-layer analysis is driven by the compressive strain that is defined at the top layer, defined as ε_{top}. The strains in each of the layer

ε_i is a function of ε_{top} and the compression depth *c*, which is

$$\varepsilon_i = \frac{c-y_i}{c}\varepsilon_{top}$$

Table A-1 – Sample layer-by-layer analysis for normal concrete (no fibres)

Layer	t_i	b_i	y_i	ε_i	A_n	f_i	F_i	M_i
	mm	mm	mm		mm2	MPa	kN	kN-m
1	1.5	9754	0.75	1.31E-03	1.46E+04	27.82	407.00	37.93
2	1.5	9754	2.25	1.27E-03	1.46E+04	27.34	400.06	36.68
3	1.5	9754	3.75	1.22E-03	1.46E+04	26.84	392.70	35.42
4	1.5	9754	5.25	1.18E-03	1.46E+04	26.31	384.92	34.14
5	1.5	9754	6.75	1.14E-03	1.46E+04	25.75	376.72	32.85
⋮	⋮	⋮	⋮	⋮	⋮	⋮	⋮	⋮
48	13	9754	157.5	-3.13E-03	1.27E+05	-177.15	0	0
49	13	9754	170.5	-3.50E-03	1.27E+05	-208.24	0	0
50	13	9754	183.5	-3.87E-03	1.27E+05	-241.49	0	0
A_{s1}	-	-	50	-8.57E-05	1.09E+05	-	-312.11	-13.72
A_{s2}	-	-	120	-2.07E-03	1.09E+05	-	-7280.00	189.69
A_{s3}	-	-	120	-2.07E-03	0	-	0.00	0.00
A_{s4}	-	-	100	-1.50E-03	0	-	0.00	0.00

Layers labeled with numbers are concrete layers, and layers with A_s are steel layers (i.e., bottom 4 rows). The variable t_i is the height of layer i, b_i is the width, y_i is the location of layer i from the top of section, ε_i is the strain in layer i, A_n is the transformed area of the section (i.e., steel is multiplied by E_s/E_c). f_i is the stress, F_i is the force and M_i is the bending moment in layer i.

$$A_{n,i} = b_i \cdot t_i \cdot \frac{E_i}{E_c}$$

For concrete, Hognestad equation (taken 0.0134 as max compressive strain based on findings from experimental study in Section 4.4.

$$\text{If } 0 < \varepsilon_i \leq \varepsilon_c;\ f_c = 0.9 f_c' \left[2\frac{\varepsilon_i}{\varepsilon_c'} - \left(\frac{\varepsilon_i}{\varepsilon_c'}\right)^2 \right]$$

$$\text{If } \varepsilon_t < \varepsilon_i \leq 0;\ f_c = \varepsilon_i \cdot E_c$$

$$If\ \varepsilon_c < \varepsilon_i \leq 0.0134;\ f_c = 0.9f_c^{'} - \left(\frac{0.135f_c^{'}}{0.0038\text{-}\varepsilon_c^{'}}\right)(\varepsilon_i - \varepsilon_c)$$

$If\ \varepsilon_i \leq \varepsilon_t;\ f_c$ has tensile value with effects of fibres, $f_c = 0$ for normal concrete

For steel layers

$$f_t = \varepsilon_i \cdot E_s;\ \text{Bounded by} \pm f_y$$

Force, moment and strain

$$F_i = A_n \cdot f_i;\ M_i = F_i \cdot \left(y_i\text{-}y_{ref}\right);\ y_{ref} = \text{Reference point, taken at centre of section}$$

$$\varepsilon_i = \frac{c\text{-}y_i}{c} \cdot \varepsilon;\ c = \text{Compression depth}$$

Iterate until sum of the forces in the layers are zero $\sum F_i = 0$, which will require the iteration of compression depth c until sum of forces are zero. To define a moment-curvature plot of the reinforced concrete section, the top compression strain ε_{top} is increased from 0 to a desired value, which is 0.0035 for normal concrete and 0.0134 for FRC.

A.5 Virtual Work and Displacement of Beams

Given a beam in four-point loading at distances 500 mm from the support, the bending moment diagram from four-point bending $M(x)$ and the virtual bending moment diagram $m(x)$ for mid-span deflection is shown in Figure A-3.

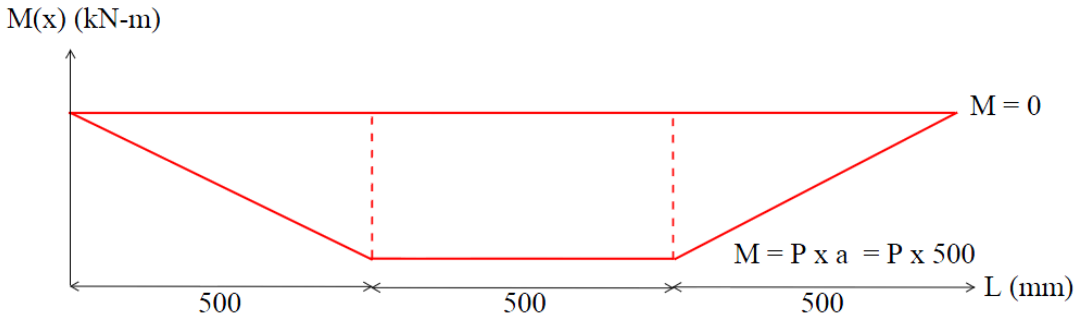

(a)

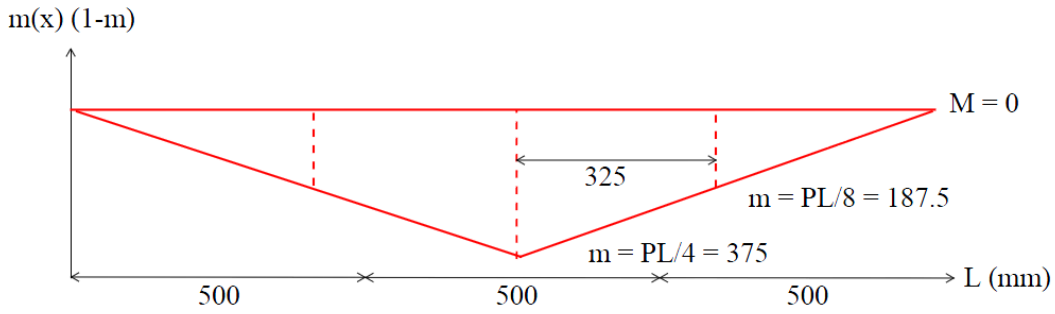

(b)

Figure A-3 – Bending moment diagram for (a) four-point bending and (b) virtual work

To calculate the theoretical deflection of FRC beam in plasticity, assume apportion of the beam in plasticity, which is the "plastic hinge". The remainder of the concrete beam is in linear elastic behaviour. Since four-point bending generates the largest load in the middle one-third of the beam, assume that the middle section is in plasticity.

The property of the plastic hinge can be found from the moment-curvature ($M - \varphi$) relationship using the layer-by-layer analysis. The Plastic Modulus defines the stiffness of the plastic hinge using the Secant Modulus method, which is

$$EI_p = \frac{M}{\varphi}$$

Therefore, the deflection of the reinforced beam is

$$\Delta = \int \frac{M(x)m}{EI} = \sum \frac{\text{Area from } M(x) \cdot \text{Value from } m(x)}{EI}$$

For four-point bending, the equation is

$$\Delta = 2 \cdot \frac{M \cdot a}{2 \cdot E \cdot I_e} \cdot \frac{2}{3} m + \frac{M \cdot a}{E \cdot I_p} \cdot m = \frac{1}{2} \cdot \frac{M \cdot a^2}{E \cdot I_e} + \frac{3}{4} \cdot \frac{M \cdot a}{E \cdot I_p}$$

A.6 Concrete Cracking Compared to Lab Data

$$w = k_b \cdot \beta_c \cdot s_{rm} \cdot \varepsilon_{sm} = 1.0 \cdot 1.7 \cdot s_{rm} \cdot \varepsilon_{sm}$$

Loads at 25 kN and 35 kN, assume service stresses in fibre (2.8 MPa for polypropylene and 6.7 MPa for hooked steel). From layer-by-layer analysis, strain values for normal concrete, polypropylene and hooked steel are

	Strain at 15 kN	Strain at 25 kN	Strain at 35 kN
Normal Concrete	0.00108	0.00182	-
Polypropylene	0.000460	0.00119	0.00196
Hooked Steel	0.0000388	0.000407	0.00114

For normal concrete, the cover was 45 mm, the reinforcement spacing was 50 mm, the bar diametre was 11.3 mm, the reinforcing ratio was 0.0133, k_1 is 0.8. At yield load, net strain is -0.00145 without tension stiffening. At half of the load, strain is -0.000618.

$$s_m = 2 \cdot \left(c + \frac{s}{10} \right) + k_1 \cdot \frac{d_b}{\rho_{eff}} \cdot \left(\frac{\varepsilon_1 + \varepsilon_2}{2 \cdot \varepsilon_1} \right)$$

$$s_m = 2\left(45+\frac{50}{10}\right)+0.8\cdot\frac{11.3}{0.0133}\cdot\left(\frac{\varepsilon_1}{2\cdot\varepsilon_1}\right) = 100+340 = 440 \text{ mm}$$

For polypropylene, the aspect ratio is 74. At yield load, net strain is -0.00110 with tension stiffening. At half of the load, strain is -0.000365.

$$s_m = 50+0.25\cdot k_1\cdot\frac{d_b}{\rho_{eff}}\cdot\left(\frac{50}{l_f/d_f}\right)\cdot\left(\frac{\varepsilon_1+\varepsilon_2}{2\cdot\varepsilon_1}\right)$$

$$s_m = 50+0.25\cdot(0.8)\cdot\frac{11.3}{0.0133}\cdot\left(\frac{50}{74}\right)\cdot\left(\frac{\varepsilon_1}{2\varepsilon_1}\right) = 50+57 = 107 \text{ mm}$$

For hooked steel, the aspect ratio is 50

$$s_m = 50+0.25\cdot(0.8)\cdot\frac{11.3}{0.0133}\cdot\left(\frac{50}{50}\right)\cdot\left(\frac{\varepsilon_1}{2\varepsilon_1}\right) = 50+85 = 135 \text{ mm}$$

	Crack (mm) at 15 kN	Crack (mm) at 25 kN	Crack (mm) at 35 kN
Normal Concrete	0.81	1.4	-
Polypropylene	0.084	0.22	0.36
Hooked Steel	0.0089	0.093	0.26

A.7 Concrete Cracking SAP2000

For normal concrete, the cover was 32 mm, the reinforcement spacing was 90 mm, the bar diametre was 16 mm, the reinforcing ratio was 0.00982, k1 is 0.8. At ultimate load, net strain is 0.00483

$$s_m = 2\cdot\left(32+\frac{90}{10}\right)+0.8\cdot\frac{16}{0.00982}\cdot\left(\frac{\varepsilon_1}{2\cdot\varepsilon_1}\right) = 82+652 = 734 \text{ mm}$$

$$w_m=734\cdot(0.00483)=3.55 \text{ mm}$$

For polypropylene, the aspect ratio is assumed to be50. At ultimate load, net strain is -0.00431.

$$s_m = 50+0.25\cdot(0.8)\cdot\frac{16}{0.00982}\cdot\left(\frac{50}{50}\right)\cdot\left(\frac{\varepsilon_1}{2\varepsilon_1}\right) = 50+163 = 193 \text{ mm}$$

$$w_m = 193\cdot(0.00431) = 0.832 \text{ mm}$$

A.8 Stress Calculations from C1609 using *fib* Model Code

$$f_{Fts} = 0.45\cdot f_{R1}$$

$$f_{Ftu} = f_{Fts}-\frac{w_u}{CMOD_3}\cdot\left(f_{Fts}-0.5\cdot f_{R3}+0.2\cdot f_{R1}\right)\geq 0$$

Polypropylene, f_{R1} = 2.7 MPa, f_{R3} = 2.0 MPa, w_u = 0.25 mm

$$f_{Fts} = 0.45\cdot(2.7) = 1.2 \text{ MPa}$$

$$f_{Ftu} = 1.2-\frac{0.25}{2.5}[1.2-0.5\cdot(2.0)+0.2\cdot(2.7)] = 1.1 \text{ MPa}$$

Hooked steel, f_{R1} = 6.4 MPa, f_{R3} = 4.1 MPa, w_u = 0.25 mm

$$f_{Fts} = 0.45 \cdot (6.4) = 2.9 \text{ MPa}$$

$$f_{Ftu} = 2.9 - \frac{0.25}{2.5} \cdot [2.9 - 0.5 \cdot (4.1) + 0.2 \cdot (6.4)] = 2.7 \text{ MPa}$$

A.9 Debonded Length Crack Width Calculations

b=9753 mm; h=190 mm; d=120 mm; $I_g = b \cdot h^3 / 12 = 5.575 \left(10^9\right) \text{mm}^4$

E_s=200,000 MPa; f_c'=35 MPa

$$M_{cr} = \frac{f_r \cdot I_g}{y_t} = \frac{0.4 \cdot \sqrt{35} \cdot (5.575) \cdot \left(10^9\right)}{95} \cdot \left(10^{-6}\right) = 139 \text{ kN-m}$$

For 5% debonded length with normal concrete:

$f_{s,SLS1}$=250 MPa; A_s=26200 mm^2 (assume 1 layer); kd=53 mm

$$\rho_c = \frac{A_s}{A_{ct}} = \frac{26200}{b \cdot \min[2.5(h-d), h/6]} = \frac{26200}{9754 \cdot \min[2.5(190-120), 190/6]} = 0.085$$

$$s_{rm} = 50 + 0.25 \cdot (0.5) \cdot \frac{16}{0.085} = 74 \text{ mm}$$

$$f_w = \frac{M_{cr}}{A_s \cdot jd} = \frac{M_{cr}}{A_s \cdot (d - kd/3)} = \frac{139\left(10^6\right)}{26200 \cdot (120 - 53/3)} = 51.8 \text{ MPa}$$

$$\varepsilon_{sm} = \frac{f_s}{E_s} \cdot \left[1 - \left(\frac{f_w}{f_s}\right)^2\right] = \frac{250}{200000} \cdot \left[1 - \left(\frac{51.8}{250}\right)^2\right] = 0.00119$$

$$w=k_b \cdot \beta_c \cdot s_{rm} \cdot \varepsilon_{sm};\ k_b=1.0;\ \beta_c=1.7$$

$$w= 1.0\cdot(1.7) \cdot (0.00119) \cdot (74) = 0.149 \text{ mm}$$

For 5% debonded length with hooked steel FRC:

$$f_{s,SLS1}=115 \text{ MPa};\ A_s=26200 \text{ mm}^2 \text{(assume 1 layer)};\ kd=67 \text{ mm}$$

$$\rho_c=0.085;\ s_{rm}=74 \text{ mm}$$

$$f_w = \frac{M_{cr}}{A_s \cdot jd} = \frac{M_{cr}}{A_s \cdot (d - kd/3)} = \frac{139(10^6)}{26200\cdot(120 - 67/3)} = 52.6 \text{ MPa}$$

$$\varepsilon_{sm} = \frac{f_s}{E_s} \cdot \left[1 - \left(\frac{f_w}{f_s}\right)^2\right] = \frac{115}{200000} \cdot \left[1 - \left(\frac{52.6}{115}\right)^2\right] = 0.00087$$

$$w=k_b \cdot \beta_c \cdot s_{rm} \cdot \varepsilon_{sm};\ k_b=1.0;\ \beta_c=1.7$$

$$w= 1.0\cdot(1.7) \cdot (0.00087) \cdot (74) = 0.056 \text{ mm}$$

A.10 Non-linear Model Results for ULS

Axial is plastic axial load at hinge, moment is plastic moment at hinge, U1 is plastic axial displacement at hinge, R3 is plastic rotation at hinge, and State is the hinge state at the load between linear and failure load.

Hinge states: A is starting point, B is cracking load, C is yielding load, D is ultimate load and E is failure load

State A to B is linear, B to C is between cracking and yielding, C to D is between yielding and ultimate load, D to E is between ultimate and failure load

Table A-2 – Hinge results for RHRR model, ULS loading, no fibre

Hinge	RHRR Model, ULS Loading				
	No Fibre				
	Axial	Moment	U1	R3	State
	KN	kN-m	m	Radians	
H1	0	371.36	0	0	A to B
H2	0	-223.63	0	0	A to B
H3	0	-527.19	0	0	A to B
H4	0	-829.00	2.90E-05	-5.77E-04	B to C
H5	0	-743.01	0	0	A to B
H6	0	-657.02	0	0	A to B
H7	0	-413.97	0	0	A to B
H8	0	-172.68	0	0	A to B
H9	0	300.26	0	0	A to B

Table A-3 – Hinge results for RHRR model, ULS loading, polypropylene and hooked steel FRC

Hinge	RHRR Model, ULS Loading									
	Polypropylene					Hooked Steel				
	Axial	Moment	U1	R3	State	Axial	Moment	U1	R3	State
	KN	kN-m	m	Radians		KN	kN-m	m	Radians	
H1	0	388.44	0	0	A to B	0	388.44	0	0	A to B
H2	0	-239.71	0	0	A to B	0	-239.71	0	0	A to B
H3	0	-560.19	0	0	A to B	0	-560.19	0	0	A to B
H4	0	-878.82	0	0	A to B	0	-878.82	0	0	A to B
H5	0	-787.61	0	0	A to B	0	-787.61	0	0	A to B
H6	0	-696.40	0	0	A to B	0	-696.40	0	0	A to B
H7	0	-438.60	0	0	A to B	0	-438.60	0	0	A to B
H8	0	-182.66	0	0	A to B	0	-182.66	0	0	A to B
H9	0	318.98	0	0	A to B	0	318.98	0	0	A to B

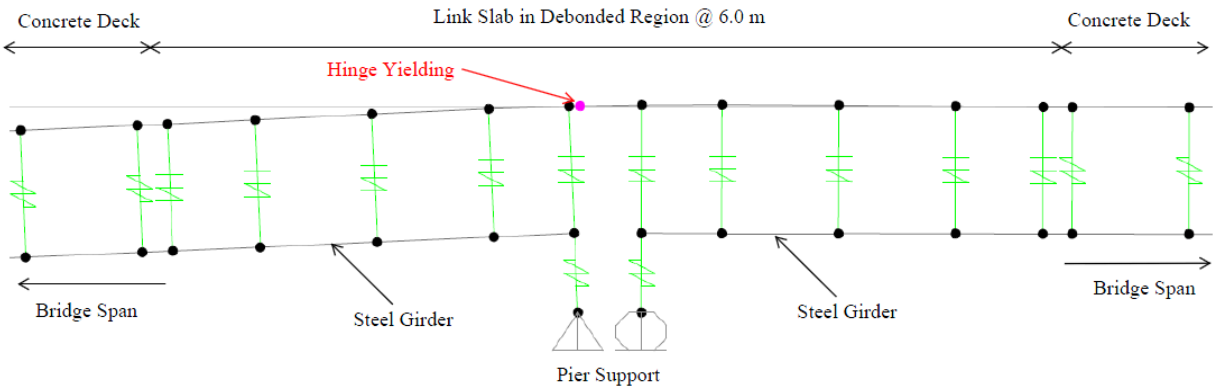

(a)

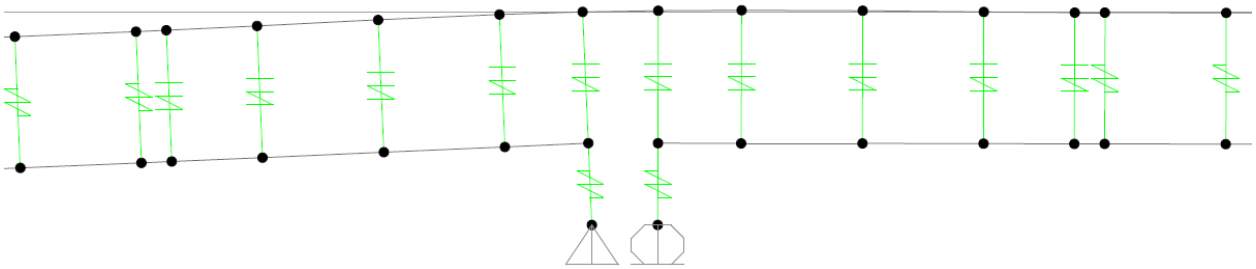

(b)

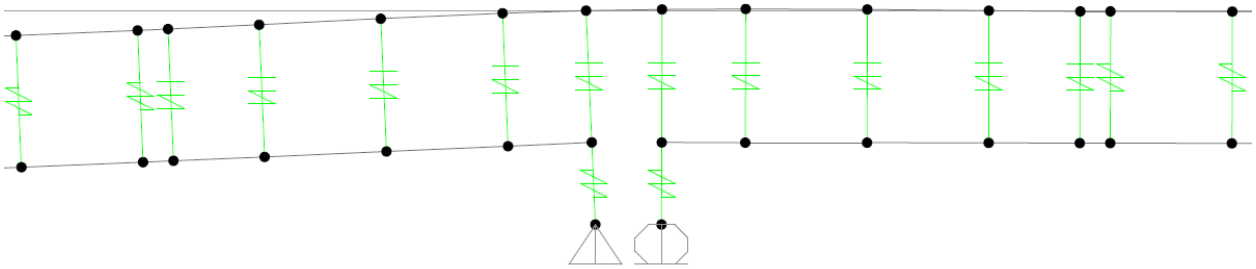

(c)

Figure A-4 – RHRR ULS non-linear model deflection diagrams for (a) no fibre, (b) polypropylene FRC and (c) hooked steel FRC

Table A-4 – Hinge results for RHHR model, ULS loading, no fibre

Hinge	RHHR Model, ULS Loading				
	No Fibre				
	Axial	Moment	U1	R3	State
	KN	KN-m	m	Radians	
H1	6814	78.15	0	0	A to B
H2	6814	-54.63	0	0	A to B
H3	6814	-122.94	0	0	A to B
H4	6814	-190.85	0	0	A to B
H5	6814	-170.22	0	0	A to B
H6	6814	-149.59	0	0	A to B
H7	6814	-91.27	0	0	A to B
H8	6814	-33.39	0	0	A to B
H9	6814	78.95	0	0	A to B

Table A-5 – Hinge results for RHHR model, ULS loading, polypropylene and hooked steel FRC

Hinge	RHHR Model, ULS Loading									
	Polypropylene					Hooked Steel				
	Axial	Moment	U1	R3	State	Axial	Moment	U1	R3	State
	KN	KN-m	m	Radians		KN	KN-m	m	Radians	
H1	6814	78.15	0	0	A to B	0	388.44	0	0	A to B
H2	6814	-54.63	0	0	A to B	0	-239.71	0	0	A to B
H3	6814	-122.94	0	0	A to B	0	-560.19	0	0	A to B
H4	6814	-190.85	0	0	A to B	0	-878.82	0	0	A to B
H5	6814	-170.22	0	0	A to B	0	-787.61	0	0	A to B
H6	6814	-149.59	0	0	A to B	0	-696.40	0	0	A to B
H7	6814	-91.27	0	0	A to B	0	-438.60	0	0	A to B
H8	6814	-33.39	0	0	A to B	0	-182.66	0	0	A to B
H9	6814	78.95	0	0	A to B	0	318.98	0	0	A to B

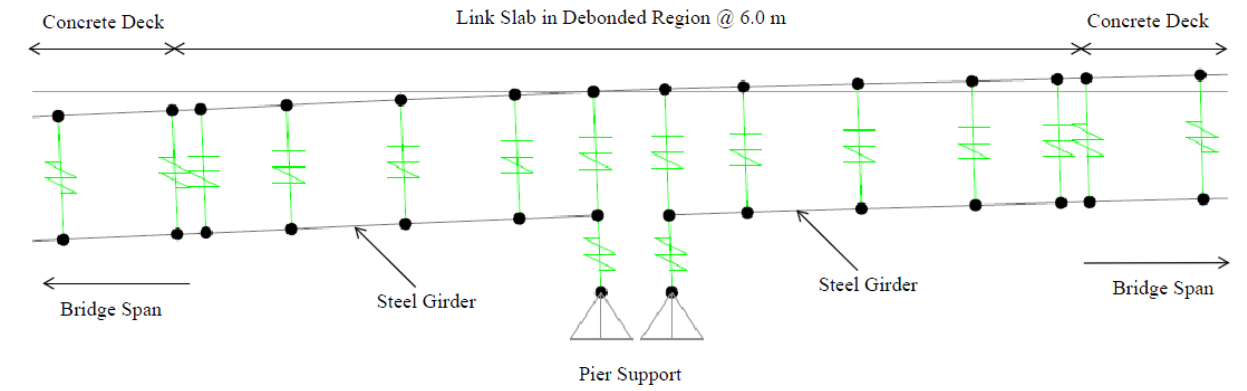

(a)

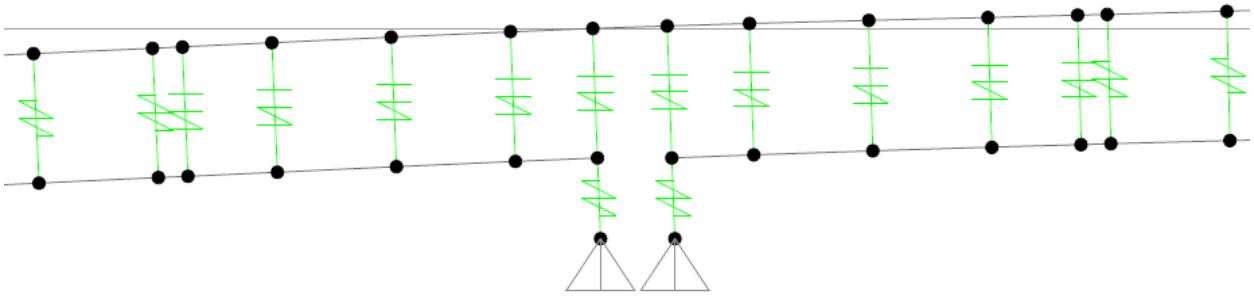

(b)

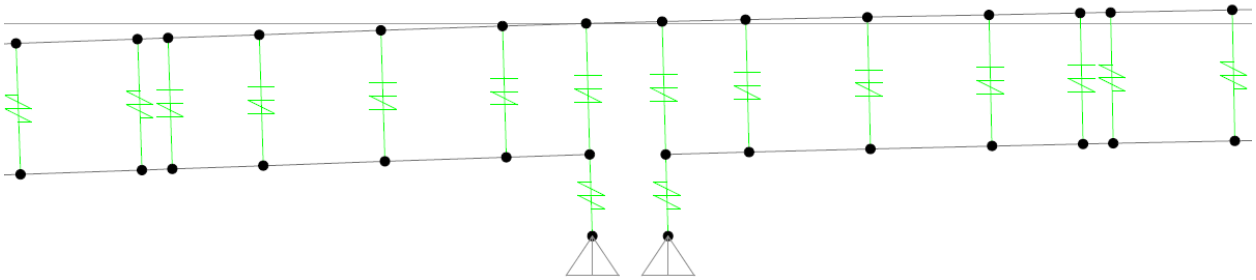

(c)

Figure A-5 – RHHR ULS non-linear model deflection diagrams for (a) no fibre, (b) polypropylene FRC and (c) hooked steel FRC

Table A-6 – Hinge results for HRRH model, ULS loading, no fibre

Hinge	HRRH Model, ULS Loading				
	No Fibre				
	Axial	Moment	U1	R3	State
	KN	KN-m	m	Radians	
H1	14970	3.73	3.30E-05	6.46E-04	B to C
H2	14970	2.89	1.20E-05	1.97E-04	B to C
H3	14969	2.12	2.42E-06	-4.40E-05	B to C
H4	14967	0.98	4.80E-04	-8.79E-03	B to C
H5	14967	0.74	1.13E-04	-1.43E-03	B to C
H6	14967	0.50	2.87E-04	4.64E-06	B to C
H7	14969	0.66	2.19E-03	-1.22E-03	B to C
H8	14969	0.35	1.02E-03	5.18E-04	B to C
H9	14969	-0.57	1.70E-05	3.34E-04	B to C

Table A-7 – Hinge results for HRRH model, ULS loading, polypropylene and hooked steel FRC

Hinge	HRRH Model, ULS Loading									
	Polypropylene					Hooked Steel				
	Axial	Moment	U1	R3	State	Axial	Moment	U1	R3	State
	KN	KN-m	m	Radians		KN	KN-m	m	Radians	
H1	14791	9.88	4.10E-05	5.16E-04	B to C	14717	33.60	4.40E-05	4.00E-04	B to C
H2	14791	0.43	1.28E-03	7.39E-04	B to C	14720	9.20	2.40E-05	6.03E-04	B to C
H3	14791	1.37	2.29E-04	-7.57E-04	B to C	14717	-3.54	4.80E-05	-6.10E-04	B to C
H4	14791	2.53	7.52E-04	-9.41E-03	B to C	14717	-15.32	8.20E-04	-8.84E-03	B to C
H5	14791	2.30	1.63E-04	0.00E+00	B to C	14717	-13.31	1.81E-06	-1.50E-05	B to C
H6	14791	2.08	1.68E-03	5.37E-06	B to C	14717	-11.29	0.00E+00	0.00E+00	B to C
H7	14791	1.45	1.87E-04	-9.56E-04	B to C	14717	-5.58	1.18E-04	-1.63E-03	B to C
H8	14791	1.09	2.01E-03	-5.53E-04	B to C	14717	0.08	4.72E-03	-7.24E-04	B to C
H9	14791	-0.42	2.29E-04	7.45E-04	B to C	14717	11.18	6.70E-05	1.06E-03	B to C

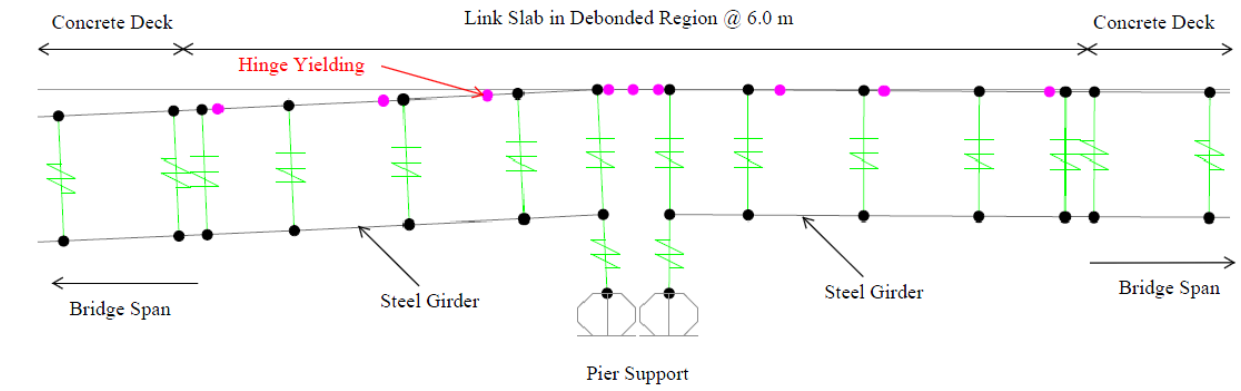

(a)

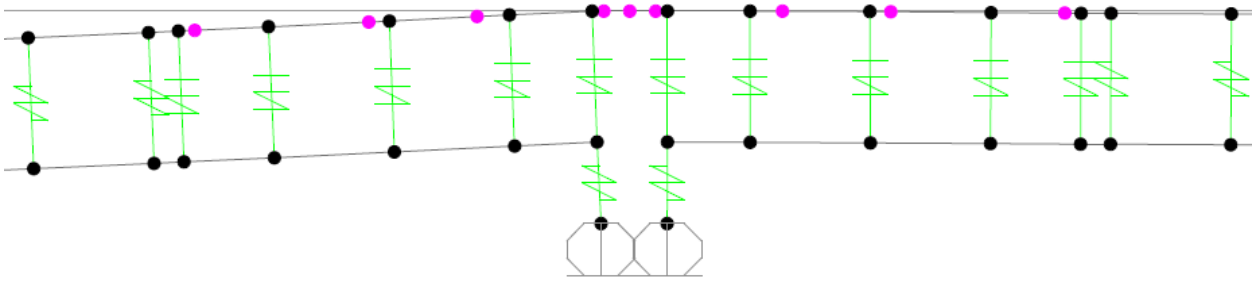

(b)

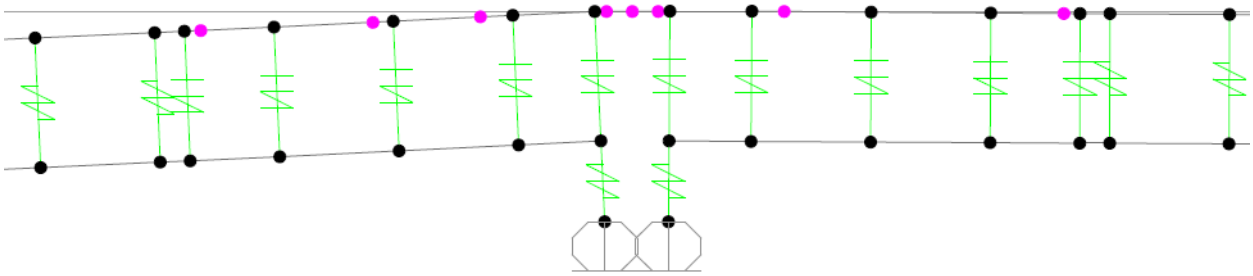

(c)

Figure A-6 – HRRH ULS non-linear model deflection diagrams for (a) no fibre, (b) polypropylene FRC and (c) hooked steel FRC

A.11 Non-linear Model Results for SLS

Table A-8 – Hinge results for RHRR model, SLS loading, no fibre and tension stiffening

Hinge	RHRR Model, SLS Loading				
	No Fibre				
	Axial	Moment	U1	R3	State
	KN	kN-m	m	Radians	
H1	0	132.84	0	0	A to B
H2	0	-54.30	0	0	A to B
H3	0	-149.78	0	0	A to B
H4	0	-244.74	7.70E-05	-2.48E-03	B to C
H5	0	-219.28	1.90E-05	-6.58E-04	B to C
H6	0	-193.81	0	0	A to B
H7	0	-121.84	0	0	A to B
H8	0	-50.39	0	0	A to B
H9	0	89.67	0	0	A to B

Table A-9 – Hinge results for RHRR model, SLS loading, polypropylene and hooked steel FRC

Hinge	RHRR Model, SLS Loading									
	Polypropylene					Hooked Steel				
	Axial	Moment	U1	R3	State	Axial	Moment	U1	R3	State
	KN	kN-m	m	Radians		KN	kN-m	m	Radians	
H1	0	135.53	0	0	A to B	0	139.09	0	0	A to B
H2	0	-56.75	0	0	A to B	0	-60.10	0	0	A to B
H3	0	-154.85	0	0	A to B	0	-161.73	0	0	A to B
H4	0	-252.42	6.70E-05	-2.17E-03	B to C	0	-262.79	6.50E-05	-2.08E-03	B to C
H5	0	-225.98	2.60E-05	-9.04E-04	B to C	0	-235.29	2.60E-05	-8.75E-04	B to C
H6	0	-199.55	0	0	A to B	0	-207.79	0	0	B to C
H7	0	-124.84	0	0	A to B	0	-130.07	0	0	A to B
H8	0	-50.67	0	0	A to B	0	-52.90	0	0	A to B
H9	0	94.70	0	0	A to B	0	98.35	0	0	A to B

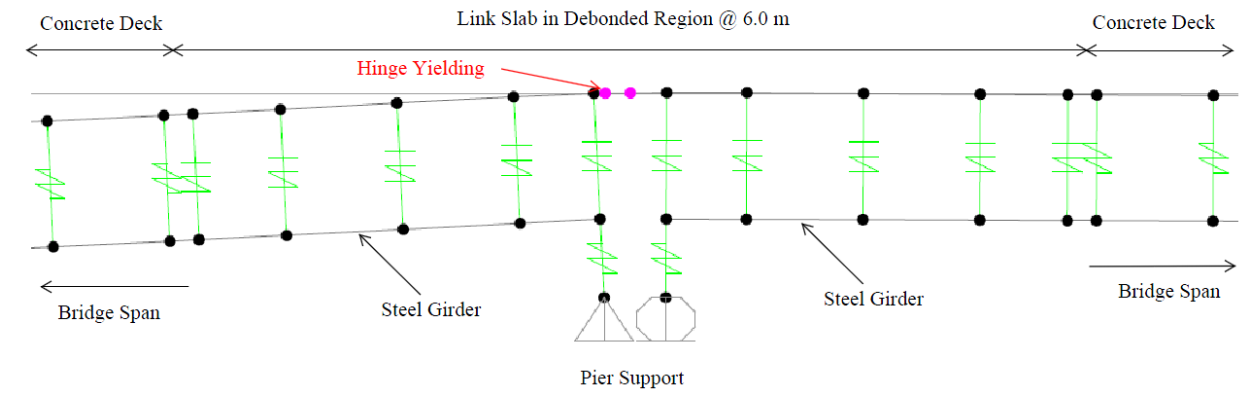

(a)

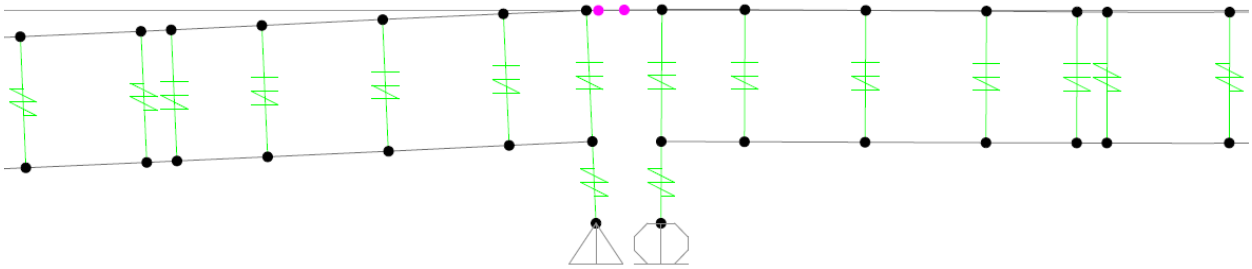

(b)

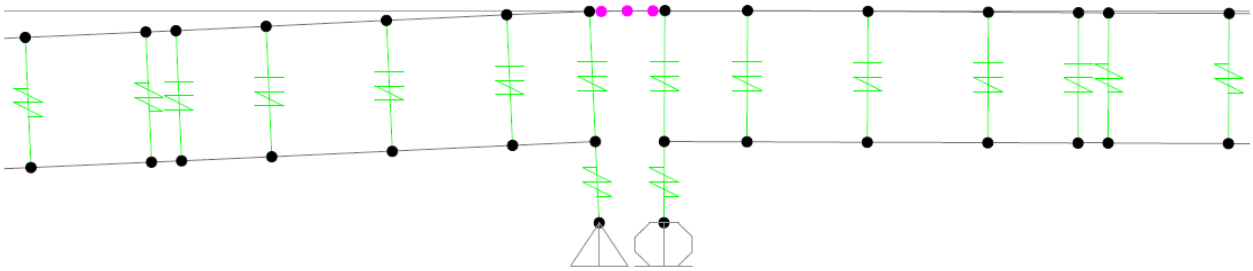

(c)

Figure A-7 – RHRR SLS non-linear model deflection diagrams for (a) no fibre, (b) polypropylene FRC and (c) hooked steel FRC

Table A-10 – Hinge results for RHHR model, SLS loading, no fibre and tension stiffening

Hinge	RHHR Model, SLS Loading				
	No Fibre				
	Axial	Moment	U1	R3	State
	KN	KN-m	m	Radians	
H1	3993	35.29	0	0	A to B
H2	3993	-25.66	0	0	A to B
H3	3993	-57.15	0	0	A to B
H4	3993	-88.45	5.71E-06	-2.06E-04	B to C
H5	3993	-78.92	0	0	A to B
H6	3993	-69.38	0	0	A to B
H7	3993	-42.43	0	0	A to B
H8	3993	-15.68	0	0	A to B
H9	3993	35.98	0	0	A to B

Table A-11 – Hinge results for RHHR model, SLS loading, polypropylene and hooked steel FRC

Hinge	RHHR Model, SLS Loading									
	Polypropylene					Hooked Steel				
	Axial	Moment	U1	R3	State	Axial	Moment	U1	R3	State
	KN	KN-m	m	Radians		KN	KN-m	m	Radians	
H1	3993	35.84	0	0	A to B	3992	36.23	0	0	A to B
H2	3993	-26.10	0	0	A to B	3992	-26.41	0	0	A to B
H3	3993	-58.10	0	0	A to B	3992	-58.77	0	0	A to B
H4	3993	-89.91	5.27E-06	-1.90E-04	B to C	3992	-90.93	4.96E-06	-1.79E-04	B to C
H5	3993	-80.22	0	0	A to B	3992	-81.13	0	0	A to B
H6	3993	-70.53	0	0	A to B	3992	-71.34	0	0	A to B
H7	3993	-43.14	0	0	A to B	3992	-43.65	0	0	A to B
H8	3993	-15.97	0	0	A to B	3992	-16.18	0	0	A to B
H9	3993	36.53	0	0	A to B	3992	36.91	0	0	A to B

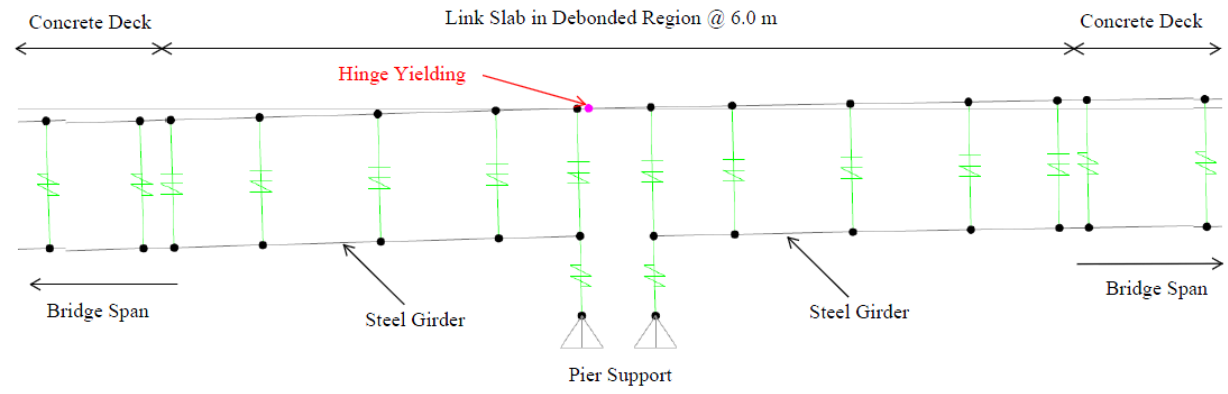

(a)

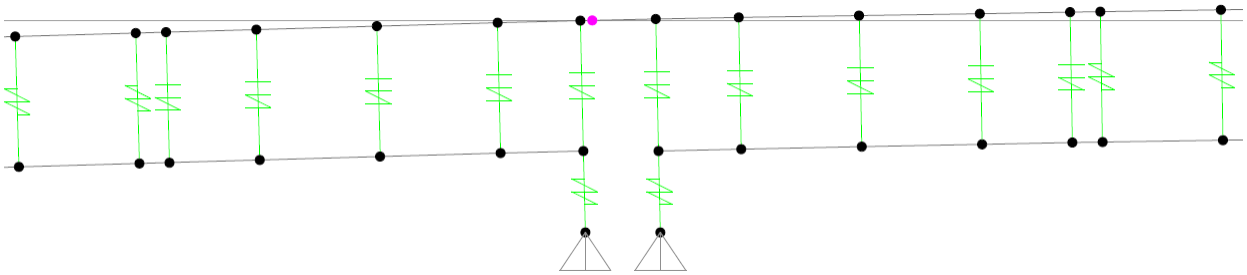

(c)

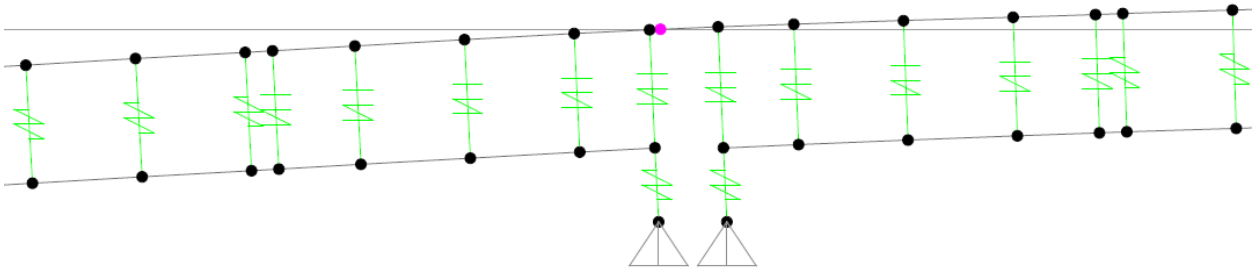

(d)

Figure A-8 – RHHR SLS non-linear model deflection diagrams for (a) no fibre, (b) polypropylene FRC and (c) hooked steel FRC

Table A-12 – Hinge results for HRRH model, SLS loading, no fibre and tension stiffening

Hinge	HRRH Model, SLS Loading				
	No Fibre				
	Axial	Moment	U1	R3	State
	KN	KN-m	m	Radians	
H1	12592	-8.18	1.75E-04	1.81E-03	C to D
H2	12592	-7.01	3.69E-04	2.12E-03	D to E
H3	12592	-6.41	5.99E-04	-5.21E-03	D to E
H4	12592	-5.80	3.57E-03	-3.50E-03	D to E
H5	12592	-5.59	8.01E-04	-7.40E-04	D to E
H6	12592	-5.38	1.37E-04	-5.28E-04	C to D
H7	12591	-4.77	1.58E-04	-1.52E-04	C to D
H8	12592	-4.17	2.35E-04	-1.61E-04	C to D
H9	12592	-3.00	2.04E-04	4.31E-04	C to D

Table A-13 – Hinge results for RHHR model, SLS loading, polypropylene and hooked steel FRC

Hinge	HRRH Model, SLS Loading									
	Polypropylene					Hooked Steel				
	Axial	Moment	U1	R3	State	Axial	Moment	U1	R3	State
	KN	KN-m	m	Radians		KN	KN-m	m	Radians	
H1	7523	19.23	2.00E-05	5.11E-04	B to C	10030	8.57	2.80E-05	6.65E-04	B to C
H2	7523	18.94	5.28E-06	-1.59E-04	B to C	10030	7.15	6.40E-05	-1.75E-04	C to D
H3	7523	18.80	7.96E-06	-1.11E-04	B to C	10030	6.42	4.20E-05	2.50E-05	B to C
H4	7519	1.32	2.08E-04	-3.52E-03	D to E	10027	-6.51	4.61E-04	-3.69E-03	D to E
H5	7523	18.58	5.50E-05	-1.52E-03	B to C	10030	5.43	7.10E-05	-1.62E-03	B to C
H6	7523	18.52	2.60E-05	-7.00E-04	B to C	10030	5.17	6.60E-05	-1.01E-03	B to C
H7	7523	18.40	9.69E-06	-1.73E-04	B to C	10030	4.44	4.70E-05	-1.89E-04	B to C
H8	7523	18.25	1.10E-05	-3.52E-04	B to C	10030	3.71	7.90E-05	-2.14E-04	C to D
H9	7523	17.97	2.10E-05	5.18E-04	B to C	10030	2.28	3.90E-05	6.88E-04	B to C

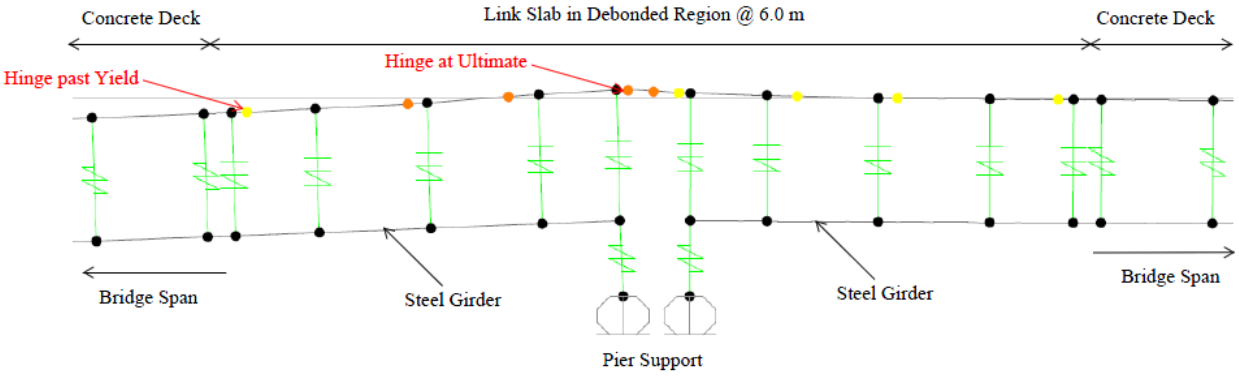

(a)

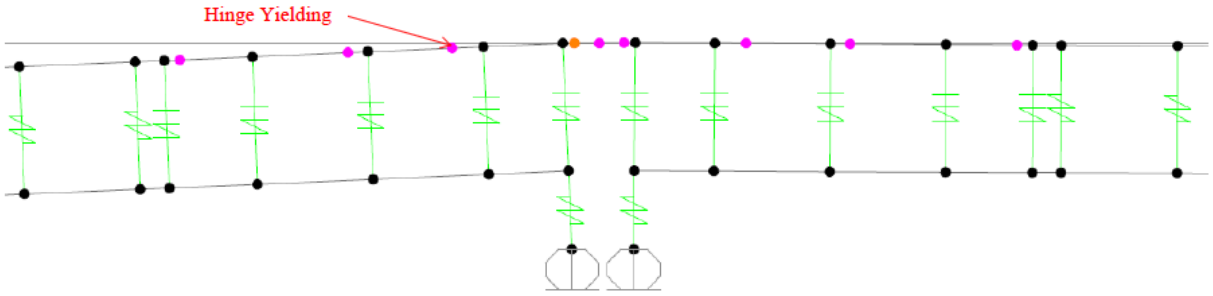

(c)

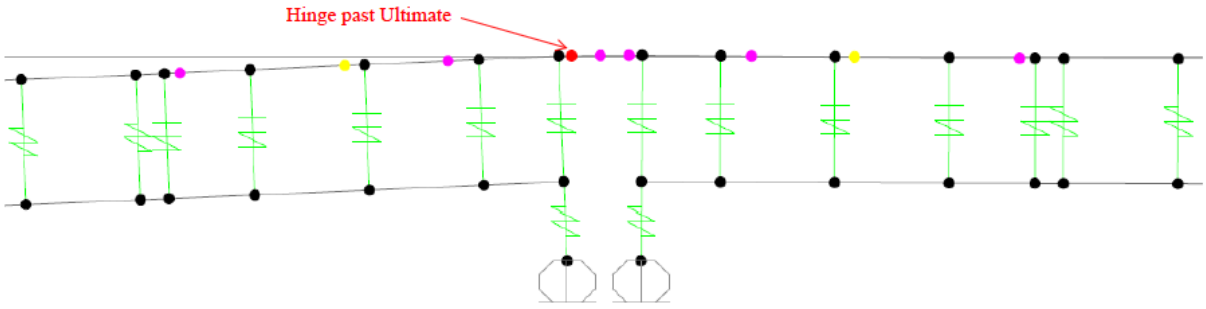

(d)

Figure A-9 – HRRH SLS non-linear model deflection diagrams for (a) no fibre, (b) polypropylene FRC and (c) hooked steel FRC

Appendix B Analytical Model– Load Analysis

B.1 Caner and Zia Method and Calculations

Live load can be approximated from the end girder rotation, $L = 3000$ mm

$$M_a = 2 \cdot \frac{E_c \cdot I_g}{L} \theta$$

$$E_c = 4500 \cdot \sqrt{f'_c} = 26622 \text{ MPa}; \quad I_g = b \cdot h^3/12 = 9754 \cdot (190)^3/12 = 5.575 \cdot (10^9) \text{mm}^4$$

$$M_a = 2 \frac{(26622) \cdot (5.575 \cdot 10^9) \cdot 10^{-6}}{3000} \cdot \theta = 98945 \cdot \theta \text{ kN-m}$$

Bending moment from simply-supported analysis

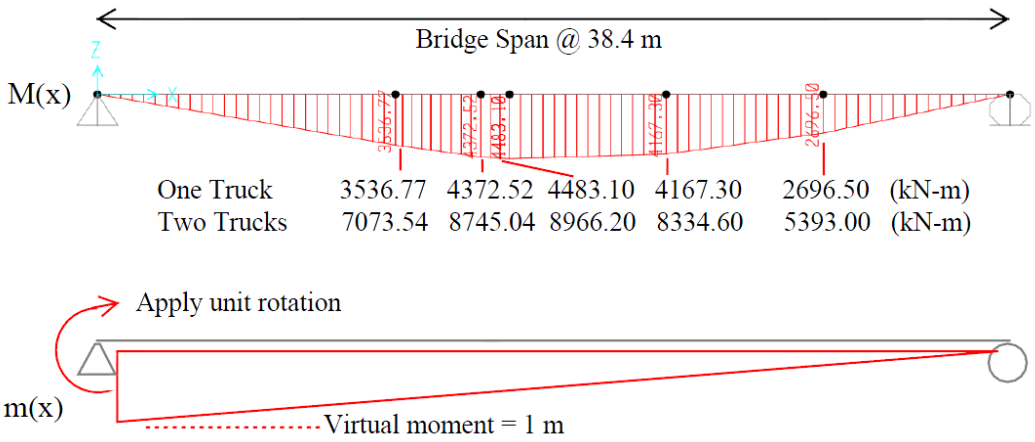

Use virtual work to determine spring load at end of girder

Bridge stiffness, approximated from Camlachie Road Underpass conditions:

$$I = 125.9 \cdot (10^9) \text{ mm}^4; \quad E = 200 \text{ GPa}$$

Results, "M_t" is the triangular bending area, "M_r" is the rectangular bending area

M (kN-m)	x (m)	M_t (kN-m*m2)	m_t (m)	M_r (kN-m*m2)	m_r (m)	∫Mm (Nm4)
7073.54	12.535	44333	0.218	0	0.163	9648
8745.04	16.135	3009	0.389	25465	0.373	10676
8966.20	17.335	133	0.441	10494	0.436	4632
8334.60	23.935	2084	0.509	55008	0.537	30620
5393.00	30.535	9707	0.681	35594	0.709	31851
-	38.4	21208	0.863	0	0.898	18312
					Total	105740

$$\theta = \sum \frac{M \cdot m}{E \cdot I} = \frac{105740}{200\left(10^{8}\right) \cdot 125.9\left(10^{-3}\right)} = 0.00420 \text{ rad}$$

$$M_a = 98945 \cdot (-0.00420) = -416 \text{ kN-m}$$

B.2 Force Method for RHRR Model with Live Load

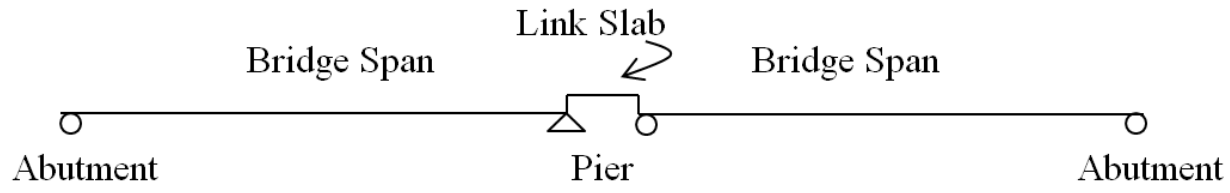

$$\theta_i + f_{ij} \cdot X_j = 0$$

θ_i = Bending moment of primary structures with applied loads

f_{ij} = Flexibility fromunit rotation at releases

X_i = Bending moment at releases

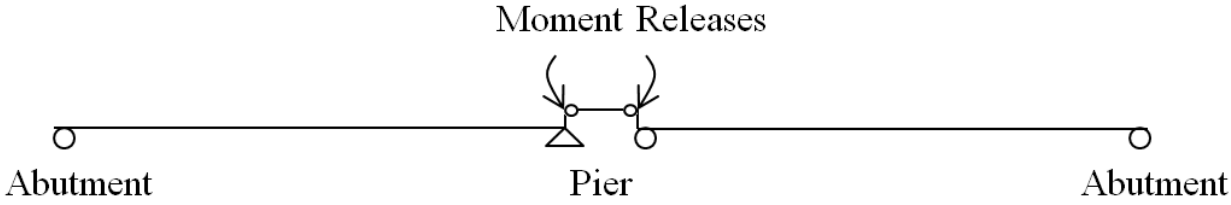

Two degrees indeterminate, release #1 at pier support of loaded span, release #2 at end of link slab:

$$\begin{cases} \theta_1 + f_{11} \cdot X_1 + f_{12} \cdot X_2 = 0 \\ \theta_2 + f_{21} \cdot X_1 + f_{22} \cdot X_2 = 0 \end{cases}$$

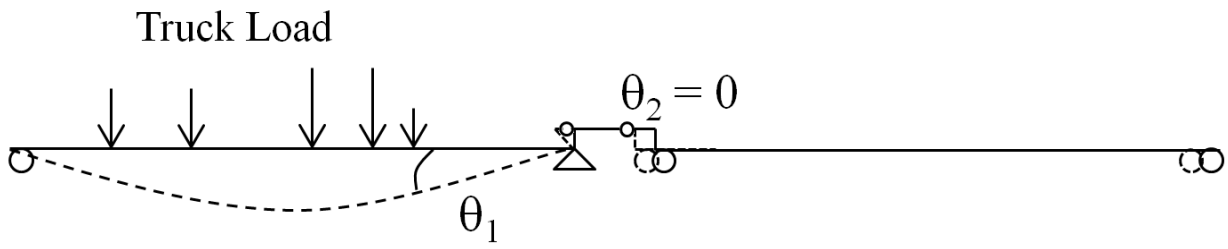

θ_1 = rotation at release #1, at pier of girder end of loaded span

$\theta_2 = 0$ = rotation at release #2, at pier of girder end of unloaded span

Bending moment (M_1) for loaded span of primary structure (from SAP2000):

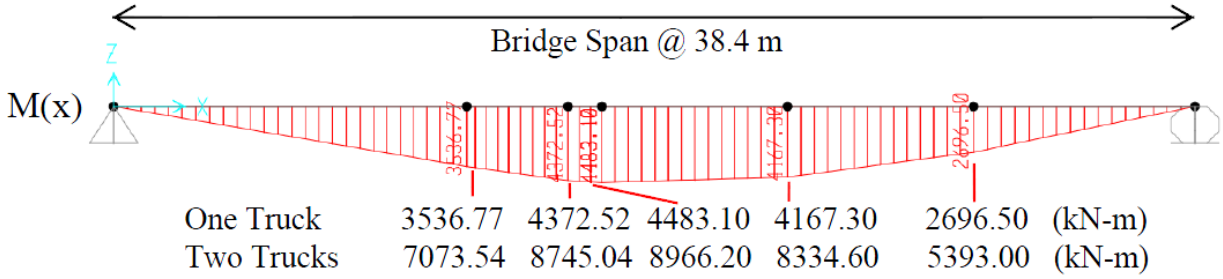

One Truck	3536.77	4372.52	4483.10	4167.30	2696.50	(kN-m)
Two Trucks	7073.54	8745.04	8966.20	8334.60	5393.00	(kN-m)

Bending moment (m_1) for the unit rotations at release #1

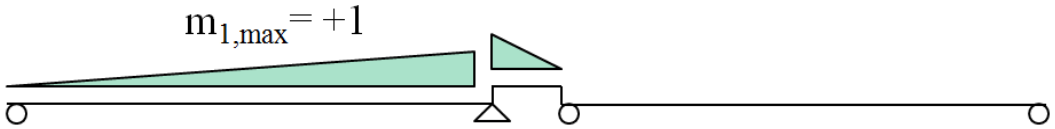

Bending moment (m_2) for the unit rotations at release #2

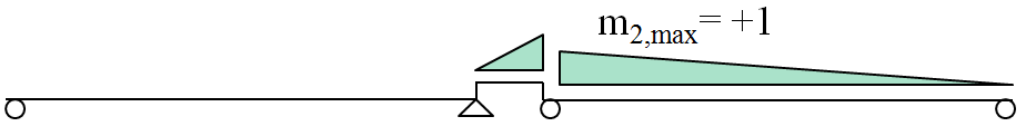

Bridge span and link slab stiffness:

$$\text{Bridge span: } I_{bs} = 126(10^{-3})\text{m}^4;\ E_s = 200(10^8)\text{kPa};\ L_{bs} = 38.4\text{ m}$$

$$\text{Link slab: } I_{ls} = 5.58(10^{-3})\text{m}^4;\ E_s = 26.6(10^8)\text{ kPa};\ L_{ls} = 6\text{ m}$$

Results, "M_t" is the triangular bending area, "M_r" is the rectangular bending area

M (kN-m)	x (m)	M_t (kN-m*m2)	m_t (m)	M_r (kN-m*m2)	m_r (m)	∫Mm (Nm4)
7073.54	12.535	44333	0.218	0	0.163	9648
8745.04	16.135	3009	0.389	25465	0.373	10676
8966.20	17.335	133	0.441	10494	0.436	4632
8334.60	23.935	2084	0.509	55008	0.537	30620
5393.00	30.535	9707	0.681	35594	0.709	31851
-	38.4	21208	0.863	0	0.898	18312
					Total	105740

First find rotation of primary structure, which is

$$\theta_1 = \int m_1 \frac{M_1(x)}{EI} dx = \frac{105740}{126\left(10^{-3}\right)\cdot 200\left(10^{8}\right)} = 0.00420 \text{ rad}$$

$\theta_2 = \int m_2 \frac{M_1(x)}{E \cdot I} dx = 0 \rightarrow$ Consistent with primary structure (no rotation at unloaded span)

Flexibility coefficients

$$f_{11} = \int m_1 \frac{m_1(x)}{E \cdot I} d\,x = \frac{(1/2) \cdot (38.4) \cdot (2/3)}{126\left(10^{-3}\right) \cdot 200\left(10^{8}\right)} + \frac{(2/3) \cdot (1/2) \cdot (6)}{5.58\left(10^{-3}\right) \cdot 26.6\left(10^{8}\right)} = 14.0\left(10^{-6}\right) \frac{1}{\text{kN-m}}$$

$$f_{12} = f_{21} = \int m_1 \frac{m_2(x)}{E \cdot I} dx = \frac{(1/3) \cdot (1/2) \cdot (6)}{5.58\left(10^{-3}\right) \cdot 26.6\left(10^{8}\right)} = 6.74\left(10^{-6}\right) \frac{1}{\text{kN-m}}$$

Final results

$$\begin{Bmatrix} \theta_1 \\ \theta_2 \end{Bmatrix} + \begin{bmatrix} f_{11} & f_{12} \\ f_{21} & f_{22} \end{bmatrix} \begin{Bmatrix} X_1 \\ X_2 \end{Bmatrix} = \begin{Bmatrix} 0 \\ 0 \end{Bmatrix}$$

$$\begin{Bmatrix} X_1 \\ X_2 \end{Bmatrix} = - \begin{bmatrix} 14.0\left(10^{-6}\right) & 6.74\left(10^{-6}\right) \\ 6.74\left(10^{-6}\right) & 14.0\left(10^{-6}\right) \end{bmatrix}^{-1} \begin{Bmatrix} 0.00420 \\ 0 \end{Bmatrix} = \begin{Bmatrix} \text{-391 kN-m} \\ \text{188 kN-m} \end{Bmatrix}$$

From SAP2000, bending moment at pier (X_1) is -383 kN-m, bending moment at end of link slab (X_2) is 182 kN-m

The equation can be simplified to

$$X_1 \cdot \left(1 - \frac{f_{11} \cdot f_{22}}{f_{12} \cdot f_{21}}\right) = \frac{f_{22}}{f_{12} \cdot f_{21}} \cdot \theta_1$$

The coefficient for the releases provided is symmetric, so that $f_{11}=f_{22}$ and $f_{12}=f_{21}$

$$X_1 = \left(1 - \frac{f_{11}^2}{f_{12}^2}\right)^{-1} \frac{f_{11}}{f_{12}^2} \theta_1$$

Simplification:

From the analysis, it was found that the contribution due to the link slab was small and the effect of the adjacent span is negligible. Thus, to simplify the analysis, one can simply treat the link slab as a rotational spring

$$I_{ls}=5.575\left(10^{9}\right)\text{mm}^4;\ E_c=26622\text{ MPa};\ L=3000\text{ mm}$$

$$k_s = 2\frac{EI}{L} = 2\frac{5.575\left(10^{9}\right)\cdot 26622}{3000}10^{-6} = 98950\text{ kN-m/rad}$$

First find the moment area of the simply-supported beam and the flexibility coefficient

$$\theta_1 = \int m\frac{M(x)}{E\cdot I}dx;\ f_{11} = \int m\frac{m(x)}{E\cdot I}dx = 5.08\left(10^{-7}\right)\frac{1}{\text{kN-m}}$$

It was found that the girder end rotation using virtual work is about 0.00420 radians, which is very close to the structural analysis with a difference of 0.0003 radians. The bending moment of the link slab is therefore

$$X_1 = \frac{\theta_1}{1/k_s + f_{11}} = \frac{0.00420}{1/98950 + 5.08\left(10^{-7}\right)} = 396\text{ kN-m}$$

B.3 Force method for RHHR Model with Live Load

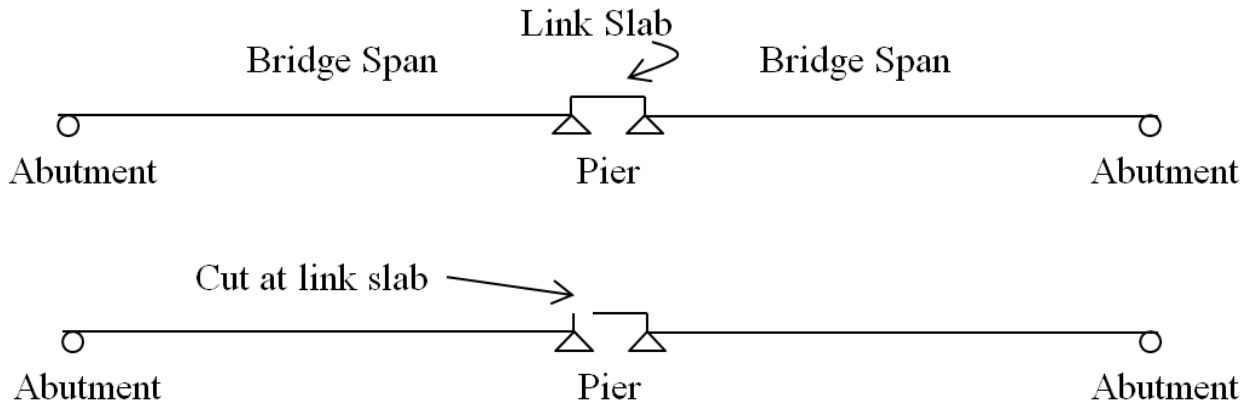

Three degrees indeterminate, release at link slab above pier support of loaded span. Release #1 is the rotation, release #2 is the shear, and release #3 is the axial force. Distance between span to link slab is 0.38 m

$$\begin{cases} \theta_1 + f_{11} \cdot X_1 + f_{12} \cdot X_2 + f_{13} \cdot X_3 = 0 \\ \theta_2 + f_{21} \cdot X_1 + f_{22} \cdot X_2 + f_{23} \cdot X_3 = 0 \\ \theta_3 + f_{31} \cdot X_1 + f_{32} \cdot X_2 + f_{33} \cdot X_3 = 0 \end{cases}$$

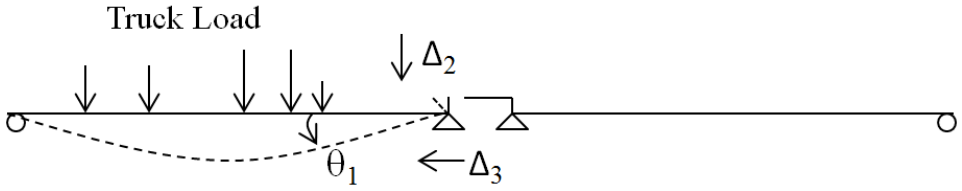

Bending moment (m_1) for the unit rotations at release #1

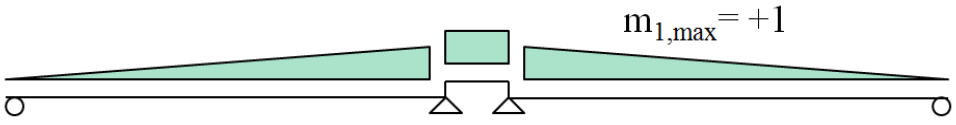

Bending moment (m_2) for the unit rotations at release #2

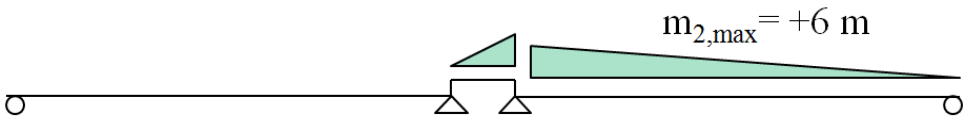

Bending moment (m_3) for the unit rotations at release #3

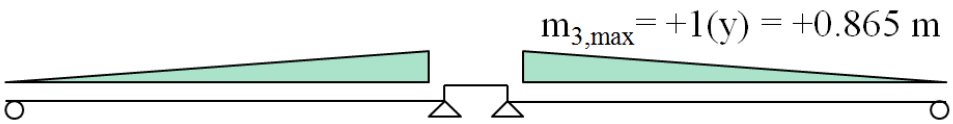

Bridge span and link slab stiffness:

Bridge span: $I_{bs}=126\left(10^{-3}\right)\text{m}^4$; $E_s=200\left(10^8\right)\text{kPa}$; $L_{bs}=38.4$ m

Link slab: $I_{ls}=5.58\left(10^{-3}\right)\text{m}^4$; $A_{ls}=1.85\ \text{m}^4$; $E_s=26.6\left(10^8\right)$ kPa; $L_{ls}=6$ m

First find rotation of primary structure, which is

$$\theta_1=\int m_1\frac{M_1(x)}{E\cdot I}dx=\frac{105740}{126\left(10^{-3}\right)\cdot 200\left(10^8\right)}=0.00420\ \text{rad}$$

Use geometry to determine displacement at support, d = distance from pier support to link slab centroid

$$\Delta_2\approx 0\ \text{m}$$

$$\Delta_3=\int m_3\frac{M_3(x)}{E\cdot I}dx=\frac{105740}{126\left(10^{-3}\right)\cdot 200\left(10^8\right)}(0.38)=0.00160\ \text{m}$$

Flexibility coefficients

$$f_{11}=\int m_1\frac{m_1(x)}{E\cdot I}dx=2\times\frac{(2/3)\cdot(1/2)\cdot(38.4)}{126\left(10^{-3}\right)\cdot 200\left(10^8\right)}+\frac{(1)\cdot(1)\cdot(6)}{5.58\left(10^{-3}\right)\cdot 26.6\left(10^8\right)}=41.4\left(10^{-6}\right)\frac{1}{\text{kN-m}}$$

$$f_{22}=\int m_2\frac{m_2(x)}{E\cdot I}dx=\frac{6\cdot(2/3)\cdot 6\cdot(1/2)\cdot(38.4)}{126\left(10^{-3}\right)\cdot 200\left(10^{8}\right)}+\frac{6\cdot(2/3)\cdot 6\cdot(1/2)\cdot(6)}{5.58\left(10^{-3}\right)\cdot 26.6\left(10^{8}\right)}=503\left(10^{-6}\right)\frac{1}{\text{kN-m}}$$

$$f_{33}=\int m_3\frac{m_3(x)}{E\cdot I}dx=2\times\frac{0.865\cdot(2/3)\cdot 0.38\cdot(1/2)\cdot(38.4)}{126\left(10^{-3}\right)\cdot 200\left(10^{8}\right)}=0.147\left(10^{-6}\right)\frac{1}{\text{kN-m}}$$

$$f_{12}=f_{21}=\int m_1\frac{m_2(x)}{E\cdot I}dx=\frac{6\cdot(2/3)\cdot(1/2)\cdot(38.4)}{126\left(10^{-3}\right)\cdot 200\left(10^{8}\right)}+\frac{6\cdot(1)\cdot(1/2)\cdot(6)}{5.58\left(10^{-3}\right)\cdot 26.6\left(10^{8}\right)}1.24\left(10^{-4}\right)\frac{1}{\text{kN-m}}$$

$$f_{13}=f_{31}=\int m_1\frac{m_3(x)}{E\cdot I}dx=2\times\frac{1\cdot(2/3)\cdot 0.38\cdot(1/2)\cdot(38.4)}{126\left(10^{-3}\right)\cdot 200\left(10^{8}\right)}=0.386\left(10^{-6}\right)\frac{1}{\text{kN}}$$

$$f_{23}=f_{32}=\int m_2\frac{m_3(x)}{E\cdot I}dx=\frac{6\cdot(2/3)\cdot 0.38\cdot(1/2)\cdot(38.4)}{126\left(10^{-3}\right)\cdot 200\left(10^{8}\right)}=1.16\left(10^{-6}\right)\frac{1}{\text{kN}}$$

Final results

$$\begin{Bmatrix}\theta_1\\ \Delta_2\\ \Delta_3\end{Bmatrix}+\begin{bmatrix}f_{11} & f_{12} & f_{13}\\ f_{21} & f_{22} & f_{23}\\ f_{31} & f_{32} & f_{33}\end{bmatrix}\begin{Bmatrix}X_1\\ X_2\\ X_3\end{Bmatrix}=\begin{Bmatrix}0\\ 0\\ 0\end{Bmatrix}$$

$$\begin{Bmatrix}X_1\\ X_2\\ X_3\end{Bmatrix}=-\begin{bmatrix}f_{11} & f_{12} & f_{13}\\ f_{21} & f_{22} & f_{23}\\ f_{31} & f_{32} & f_{33}\end{bmatrix}^{-1}\begin{Bmatrix}\theta_1\\ \Delta_2\\ \Delta_3\end{Bmatrix}=\begin{Bmatrix}\text{290 kN-m}\\ \text{-96.6 kN-m}\\ \text{-10870 kN (Tension)}\end{Bmatrix}$$

From SAP2000, bending moment at pier (X_1) is -96 kN-m, axial force in the link slab (X_3) is 2836 kN (Tension)

B.4 Thermal Load

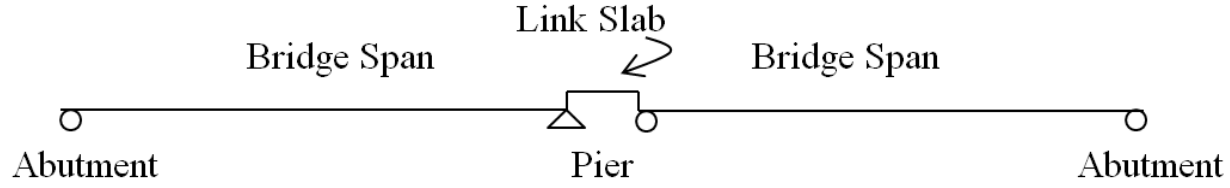

General equation:

$$\theta_i + f_{ij} X_j = 0$$

θ_i=Bending moment of primary structures with applied loads

f_{ij}=Flexibility fromunit rotation at releases

X_i=Bending moment at releases

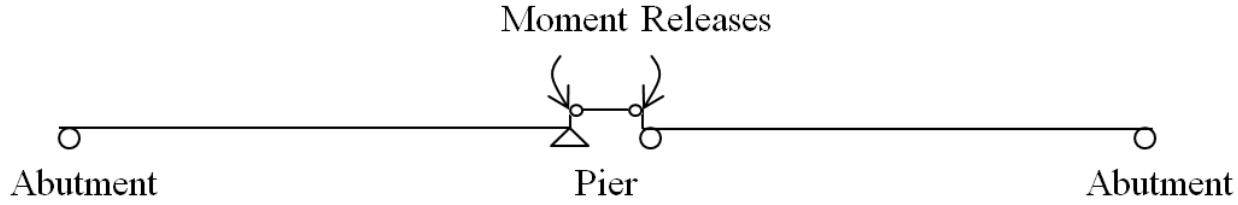

Two degrees indeterminate, release #1 at pier support of loaded span, release #2 at end of link slab:

$$\begin{cases} \theta_1 + f_{11} \cdot X_1 + f_{12} \cdot X_2 = 0 \\ \theta_2 + f_{21} \cdot X_1 + f_{22} \cdot X_2 = 0 \end{cases}$$

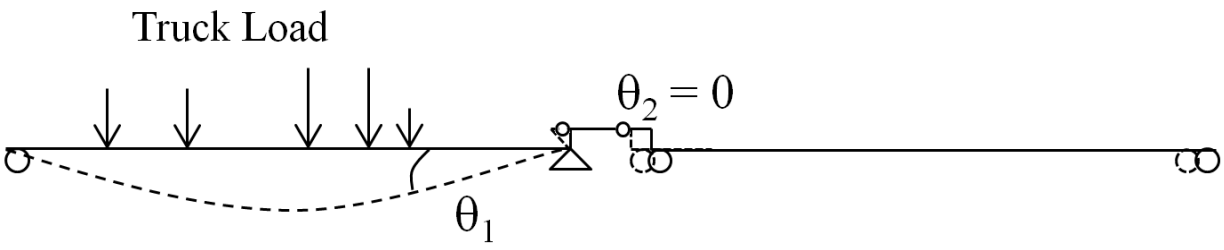

θ_1=rotation at release #1, at pier of girder end of loaded span

θ_2=0=rotation at release #2, at pier of girder end of unloaded span

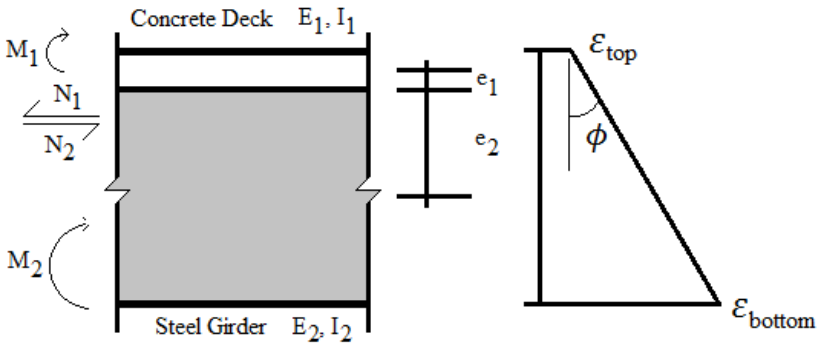

$$\frac{P_1}{E_1 \cdot A_1} + \frac{M_1 \cdot e_1}{E_1 \cdot I_1} = \varepsilon_T - \frac{P_2}{E_2 \cdot A_2} - \frac{M_2 \cdot e_2}{E_2 \cdot I_2}$$

$$\phi = \frac{M_1}{E_1 \cdot I_1} = \frac{M_2}{E_2 \cdot I_2}$$

$$\sum P = P_1 - P_2 = 0; \quad \sum M = P_1 \cdot e_1 + P_2 \cdot e_2 + M_1 + M_2 = 0$$

$$M_1 = \frac{P_1 \cdot (e_1+e_2) \cdot E_1 \cdot I_1}{E_1 \cdot I_1 + E_2 \cdot I_2}; \quad M_2 = \frac{P_2 \cdot (e_1+e_2) \cdot E_2 \cdot I_2}{E_1 \cdot I_1 + E_2 \cdot I_2}$$

$$P_1 = -P_2 = \frac{\varepsilon_T}{\frac{1}{E_1 \cdot A_1} + \frac{1}{E_2 \cdot A_2} + \frac{(e_1+e_2)^2}{E_1 \cdot I_1 + E_2 \cdot I_2}}$$

For positive thermal of 31°C and negative thermal of 42.5°C

Concrete deck properties:

$$E_1=26622 \text{ MPa};\ I_1=5.58(10^9)\text{mm}^4;\ A_1=1944977 \text{ mm}^2$$

$$e_1=95 \text{ mm};\ \alpha_1=9.90(10^{-6})\ ℃$$

Steel girder:

$$E_2=200000 \text{ MPa};\ I_2=4.88(10^{10})\text{mm}^4;\ A_2=180793 \text{ mm}^2$$

$$e_2=770 \text{ mm};\ \alpha_2=1.17(10^{-5})\ ℃$$

Find axial first

Positive and negative temperature strains, both steel and concrete are expanding or contracting, and since concrete has lower thermal expansion coefficient

<u>Positive thermal load:</u>

$$\varepsilon_{T+}=(\alpha_1-\alpha_2)\cdot\Delta T=\left[9.90(10^{-6})-1.17(10^{-5})\right]\cdot(31)=-5.58(10^{-5})$$

$$P_1=\frac{-5.58\cdot(10^{-5})\cdot(10^{-3})}{\frac{1}{26622(1944977)}+\frac{1}{200000(180793)}+\frac{(95+770)^2}{26622\cdot5.58(10^9)+200000\cdot4.88(10^{10})}}=-452 \text{ kN}$$

$$M_1=\frac{-452\cdot(95+770)\cdot26622\cdot5.58(10^9)}{26622\cdot5.58(10^9)+200000\cdot4.88(10^{10})}\cdot(10^{-3})=-5.90 \text{ kN-m}$$

$$M_2=\frac{452\cdot(95+770)\cdot200000\cdot4.88(10^{10})}{26622\cdot5.58(10^9)+200000\cdot4.88(10^{10})}\cdot(10^{-3})=385 \text{ kN-m}$$

Total bending moment

$$M_{T+} = P_2(e_1+e_2)+M_1+M_2 = 452(95+770)\left(10^{-3}\right)\text{-}5.90+385 = \text{-}770 \text{ kN-m}$$

Bending moment (m_1) for the unit rotations at release #1

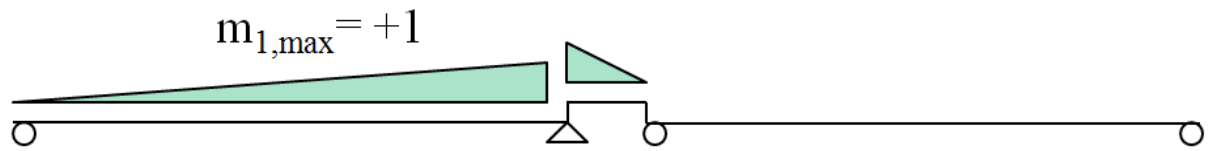

Bending moment (m_2) for the unit rotations at release #2

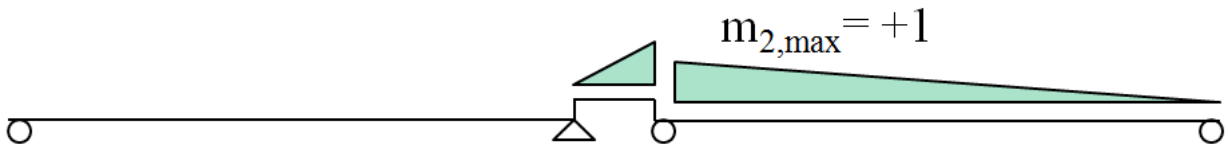

Bridge span and link slab stiffness:

Bridge span: $I_{bs}=126\left(10^{-3}\right)\text{m}^4$; $E_s=200\left(10^{8}\right)\text{kPa}$; $L_{bs}=38.4$ m

Link slab: $I_{ls}=5.58\left(10^{-3}\right)\text{m}^4$; $E_s=26.6\left(10^{8}\right)$ kPa; $L_{ls}=6$ m

First find rotation of primary structure, which is

$$\theta_1 = \int m_1 \frac{M_1(x)}{EI} dx = \left(\frac{1}{2}\right)\frac{770}{126\left(10^{-3}\right)\cdot 200\left(10^{8}\right)} = 0.000587 \text{ rad}$$

$$\theta_2 = \int m_2 \frac{M_1(x)}{EI} dx = \theta_1 = \text{-}0.000587 \text{ rad} \rightarrow \text{Rotation in opposite direction}$$

Flexibility coefficients

$$f_{11} = \int m_1 \frac{m_1(x)}{EI} dx = \frac{(1/2)\cdot(38.4)\cdot(2/3)}{126(10^{-3})\cdot 200(10^{8})} + \frac{(2/3)\cdot(1/2)\cdot(6)}{5.58(10^{-3})\cdot 26.6(10^{8})} = 14.0(10^{-6})\frac{1}{\text{kN-m}}$$

$$f_{12} = f_{21} = \int m_1 \frac{m_2(x)}{EI} dx = \frac{(1/3)\cdot(1/2)\cdot(6)}{5.58(10^{-3})\cdot 26.6(10^{8})} = 6.74(10^{-6})\frac{1}{\text{kN-m}}$$

Final results

$$\begin{Bmatrix}\theta_1\\ \theta_2\end{Bmatrix} + \begin{bmatrix}f_{11} & f_{12}\\ f_{21} & f_{22}\end{bmatrix}\begin{Bmatrix}X_1\\ X_2\end{Bmatrix} = \begin{Bmatrix}0\\ 0\end{Bmatrix}$$

$$\begin{Bmatrix}X_1\\ X_2\end{Bmatrix} = -\begin{bmatrix}14.0(10^{-6}) & 6.74(10^{-6})\\ 6.74(10^{-6}) & 14.0(10^{-6})\end{bmatrix}^{-1}\begin{Bmatrix}0.000587\\ -0.000587\end{Bmatrix} = \begin{Bmatrix}\text{-81.1 kN-m}\\ \text{81.1 kN-m}\end{Bmatrix}$$

Using Caner and Zia's method

$$M_{a,T} = 2\cdot E_c \cdot I_g \cdot \theta/L = 53000(0.000587) = \text{-58.1 kN-m}$$

Negative thermal load, Force method M = 111 kN-m, Caner and Zia's method M = 80 kN-m. From SAP2000, link slab moment = -90 kN-m for positive thermal, 42 kN-m for negative thermal.

B.5 Strain Load Calculations

Link slab bending for T+, T- and Tg are -90 kN-m, 42 kN-m and 47 kN-m, model rotations:

$$M_{a,T+} = 53000\cdot(-0.00059) = 62.5 \text{ kN-m};\quad M_{a,T-} = 53000\cdot(0.00086) = 91.1 \text{ kN-m}$$

$$M_{a,Tg} \approx 0$$

Simply-supported results for service load

$$M_{a,T+} = 53000\cdot(-0.00075) = \text{-79.5 kN-m};\quad M_{a,T-} = 53000\cdot(0.00103) = 109.1 \text{ kN-m}$$

With load factors

$$M_{T+} = \alpha_K \cdot M_{a,T+} = (1.15) \cdot (-79.5) = -91.4 \text{ kN-m};$$

$$M_{T-} = \alpha_K \cdot M_{a,T+} = (1.15) \cdot (109.1) = 125.5 \text{ kN-m}$$

B.6 Shrinkage

Strain from shrinkage "ε_{cs0}" was found to be -529μ. Shrinkage will be treated as a uniform axial strain applied to the link slab, and both layers of the steel will be used for the analysis.

$$\varepsilon_{concrete} = \varepsilon_{steel}$$

$$\frac{f_c}{E_c} = \frac{f_s}{E_s};\ f_s = nf_c$$

$$F_{sh} = \left(A_g - A_s\right) \cdot \varepsilon_{cs0} \cdot E_c = [190(9754) - 2 \cdot 18200] \cdot (529)\left(10^{-6}\right) \cdot (26622)\left(10^{-3}\right) = 26879 \text{ kN}$$

$$F_{sh} = A_s f_s + \left(A_g - A_s\right) f_c = A_s n f_c + \left(A_g - A_s\right) f_c = 18200 \cdot (7.51) f_c + [190(9754) - 2 \cdot (18200)] \cdot f_c$$

$$f_c = \frac{26879\left(10^3\right)}{2 \cdot 18200 \cdot (7.51) + [190(9754) - 2 \cdot (18200)]} = 12.3 \text{ MPa}$$

$$f_s = nf_c = 7.51 \cdot (12.32) = 92.5 \text{ MPa}$$

The shrinkage load in the serviceability case is multiplied by a factor of 0.8. Thus, the resulting stress and strain in both layers of steel is

$$0.8 f_s = 0.8 \cdot 92.5 \text{ MPa} = 74.0 \text{ MPa}$$

$$\varepsilon_s = \frac{f_s}{E_s} = \frac{74.0}{200000} = 0.000370$$

Appendix C Analytical Model – Link Slab Section Analysis

C.1 Ultimate Load Analysis

C.1.1 Normal Concrete

Assume 91-15M at depth of 120 mm, slab height 190 mm, 35 MPa concrete

f_c'=35 MPa; f_y=400 MPa; d=120 mm; b=9754 mm; A_s=18200 mm^2; E_c=26622 MPa

$$\alpha_1 = 0.85\text{-}0.0015 \cdot f_c' = 0.85\text{-}0.0015(35) = 0.7975$$

$$\beta_1 = 0.97\text{-}0.0025 \cdot f_c' = 0.97\text{-}0.0025(35) = 0.8825$$

Calculation for nominal bending moment, factors are:

$$\phi_c = \phi_s = 1$$

First assume no tensile stress to approximate compression zone:

$$a = \frac{\phi_s \cdot A_s \cdot f_y}{\phi_c \cdot \alpha_1 \cdot f_c' \cdot b} = \frac{(1)(18200)(400)}{(1)(0.7975)(35)(9754)} = 26.7 \text{ mm}$$

$$c = \frac{a}{\beta_1} = \frac{26.7}{0.8825} = 30.3 \text{ mm}; \quad \frac{700}{700+f_y} = 0.636 > \frac{c}{d} = 0.254 \therefore \text{O.k.}$$

$$M_r = \phi_s \cdot A_s \cdot f_y(d - a/2) = (1) \cdot (18200) \cdot (400) \cdot (120 - 26.7/2) \cdot \left(10^{-6}\right) = 776 \text{ kN-m}$$

M_r=780 kN-m from layer-by-layer analysis; 0.48% error

C.1.2 With Polypropylene Fibres

For polypropylene, f_{Ftu} = 1.1 MPa:

Assume h_t=159.7 mm

$$a = \frac{\phi_s \cdot A_s \cdot f_y + \phi_{c,t} \cdot b \cdot h_t \cdot f_t}{\phi_c \cdot \alpha_1 \cdot f_c' \cdot b} = \frac{(1) \cdot (18200) \cdot (400) + 1 \cdot (9754) \cdot (159.70) \cdot (1.1)}{(1) \cdot (0.7975) \cdot (35) \cdot (9754)} = 38.62 \text{ mm}$$

New h_t=152.8 mm ∴ O.k. close to previous answer

$$z_t = c + h_t/2 - a/2 = 97.2 \text{ mm}$$

$$M_t = \phi_{c,t} \cdot b \cdot h_t \cdot f_{t,bot} \cdot z_t = 1 \cdot (9754) \cdot (152.8) \cdot (1.1) \cdot (97.2) \cdot \left(10^{-6}\right) = 159 \text{ kN-m}$$

$$M_{r,final} = M_r + M_t = (1) \cdot (18200) \cdot (400) \cdot \left(10^{-6}\right) \cdot (120 - 38.6/2) + 159 = 912 \text{ kN-m}$$

Comparison with layer-by-layer analysis:

M=919 kN-m from layer-by-layer analysis; 0.58% error

C.1.3 With Hooked Steel Fibres

For hooked steel fibres, f_{Ftu} = 2.7 MPa:

Assume h_t=152.8 mm

$$a = \frac{\phi_s \cdot A_s \cdot f_y + \phi_{c,t} \cdot b \cdot h_t \cdot f_t}{\phi_c \cdot \alpha_1 \cdot f_c' \cdot b} = \frac{(1) \cdot (18200) \cdot (400) + 1 \cdot (9754) \cdot (152.8) \cdot (2.7)}{(1) \cdot (0.7975) \cdot (35) \cdot (9754)} = 41.5 \text{ mm}$$

New h_t=143.0 mm∴Reiterate

$$a = \frac{\phi_s \cdot A_s \cdot f_y + \phi_{c,t} \cdot b \cdot h_t \cdot f_t}{\phi_c \cdot \alpha_1 \cdot f_c' \cdot b} = \frac{(1) \cdot (18200) \cdot (400) + 1 \cdot (9754) \cdot (143.0) \cdot (2.7)}{(1) \cdot (0.7975) \cdot (35) \cdot (9754)} = 40.6 \text{ mm}$$

New h_t=144.0 mm ∴ O.k. close to previous answer

$$z_t = c + h_t/2 - a/2 = 97.7 \text{ mm}$$

$$M_t = \phi_{c,t} \cdot b \cdot h_t \cdot f_{t,bot} \cdot z_t = 1 \cdot (9754) \cdot (144.0) \cdot (2.7) \cdot (97.7) \cdot \left(10^{-6}\right) = 371 \text{ kN-m}$$

$$M_{r,final} = M_r + M_t = (1) \cdot (18200) \cdot (400)\left(10^{-6}\right) \cdot (120 - 40.6/2) + 371 = 1097 \text{ kN-m}$$

Comparison with layer-by-layer analysis:

M=1104 kN-m from layer-by-layer analysis; 0.68% error

C.2 Yield Load Analysis

C.2.1 Normal Concrete

f_c'=35 MPa; f_y=400 MPa; d=120 mm; b=9754 mm

A_s=18200 mm^2; E_c=28511 MPa

$$\rho = \frac{A_s}{b \cdot d} = \frac{18200}{9754(120)} = 0.0155; \; n = \frac{E_s}{E_c} = \frac{200000}{26622} = 7.51; \; \rho n = 0.1168$$

$$k = \sqrt{2 \cdot \rho n + (\rho n)^2} - \rho n; \; kd = 49.0 \text{ mm}$$

$$M_y = A_s \cdot f_y (d - kd/3) = 755 \text{ kN-m}$$

Comparison with layer-by-layer analysis:

$M = 754$ kN − m from layer − by − layer analysis; 0.13% error; $kd = 47.0$ mm

C.2.2 With Polypropylene Fibres

For polypropylene, f_{Fts} = 1.2 MPa:

$$0.5 \cdot b \cdot kd \cdot f_c = A_s \cdot f_y + b(h - kd) \cdot f_t$$

$$0.5kd \cdot \left(\frac{kd}{120\text{-}kd}\right)\frac{400}{7.51} + kd \cdot 1.2 - (0.0155 \cdot 120 \cdot 400 + 190 \cdot 1.2) = 0 \rightarrow \text{Cubic function}$$

kd=49.3 mm→Goal Seek

$$f_c = \frac{kd}{d\text{-}kd}\frac{f_y}{n} = \frac{49.3}{120\text{-}49.3}\left(\frac{400}{7.51}\right) = 37.1 \text{ MPa} \rightarrow \text{Assume } f_c = f_c' = 35 \text{ MPa}$$

$$M_T = A_s \cdot f_y(d - kd) + 0.5 \cdot b \cdot kd \cdot f_c(2 \cdot kd/3) + b \cdot (h - kd) \cdot f_t \cdot (h\text{-}kd)/2$$

$$M_T = 18200 \cdot (400) \cdot (120\text{-}49.3) + 0.5 \cdot (9754) \cdot (49.3) \cdot 35\left(\frac{2 \cdot 49.3}{3}\right) + 9754 \cdot (1.50) \cdot \frac{(190\text{-}49.3)^2}{2}$$

$$M_T = 907\left(10^{-6}\right) = 907 \text{ kN-m}$$

Comparison with layer-by-layer analysis:

M=904 kN-m from layer-by-layer analysis; -0.33% error; kd=51.3 mm

C.2.3 With Hooked Steel Fibres

For polypropylene, f_{Fts} = 2.9 MPa:

$$0.5kd \cdot \left(\frac{kd}{120\text{-}kd}\right)\frac{400}{7.51} + kd \cdot 2.9 - (0.0155 \cdot 120 \cdot 400 + 190 \cdot 2.9) = 0 \rightarrow \text{Cubic function}$$

kd=53.4 mm→Goal Seek

$$f_c = \frac{kd}{d\text{-}kd} \cdot \frac{f_y}{n} = \frac{53.4}{120\text{-}53.4}\left(\frac{400}{7.51}\right) = 42.8 \text{ MPa} \rightarrow \text{Assume } f_c = f_c' = 35 \text{ MPa}$$

$$M_T = A_s f_y (d - kd) + 0.5 \cdot b \cdot kd \cdot f_c (2 \cdot kd/3) + b \cdot (h - kd) \cdot f_t \cdot (h\text{-}kd)/2$$

$$M_T = 18200 \cdot (400) \cdot (120\text{-}53.4) + 0.5(9754) \cdot (53.4) \cdot 35 \cdot \left(\frac{2 \cdot 53.4}{3}\right) + 9754 \cdot (1.50) \cdot \frac{(190\text{-}53.4)^2}{2}$$

$$M_T = 1073\left(10^{-6}\right) = 1073 \text{ kN-m}$$

Comparison with layer-by-layer analysis:

M=1107 kN-m from layer-by-layer analysis; 3.1% error; kd=56.7 mm

Appendix D Analytical Model – Link Slab Design

D.1 Ultimate Load Design and Calculations

f_c'=35 MPa; f_y=400 MPa; d=120 mm; b=9754 mm

E_c=26622 MPa; M_f=881 kN-m

α_1=0.7975; β_1=0.8825; ϕ_s=0.90; ϕ_c=0.75; Assume $\phi_{c,t}$=0.75

If the link slab is designed normally without the effects of fibres, the reinforcement is:

$$A_{s,req} = \frac{M_f}{\phi_s \cdot f_y \cdot 0.9 \cdot d} = \frac{881}{0.9 \cdot (400) \cdot (0.9 \cdot 120)} 10^6 = 22660 \text{ mm}^2$$

$$M_f = 881 \text{ kN-m} = M_r + M_t = \phi_s \cdot A_s \cdot f_y \cdot (d - a/2) + M_t$$

D.1.1 With Polypropylene Fibres

<u>For polypropylene, i = 1.1 MPa:</u>

Assume compression zone is 35% of height (checked later):

$$h_t = h - c \approx h - 0.35h = 0.65(190) = 123.5 \text{ mm}$$

$$z_t \approx h_t/2 + 0.35h/2 = 123.5/2 - 0.35(190)/2 = 95 \text{ mm}$$

$$M_t = \phi_{c,t} \cdot b \cdot h_t \cdot f_{t,bot} \cdot z_t = 0.75 \cdot (9754) \cdot (123.5) \cdot (1.1) \cdot (95) \cdot 10^{-6} = 94.4 \text{ kN-m}$$

$$A_{s,req} = \frac{M_f - M_t}{\phi_s \cdot f_y \cdot 0.9 \cdot d} = \frac{881 - 94.4}{0.9 \cdot (400) \cdot (0.9 \cdot 120)} 10^6 = 20231 \text{ mm}^2 \rightarrow \text{Try 110-15M}$$

Recalculate the stress in concrete:

$$\phi_c \cdot \alpha_1 \cdot f_c^{'} \cdot b \cdot a = \phi_s \cdot A_s \cdot f_y + \phi_{c,t} \cdot b \cdot h_t \cdot f_t$$

$$a = \frac{\phi_s \cdot A_s \cdot f_y + \phi_{c,t} \cdot b \cdot h_t \cdot f_t}{\phi_c \cdot \alpha_1 \cdot f_c^{'} \cdot b} = \frac{(0.9) \cdot (22000) \cdot (400) + (0.75) \cdot (9754) \cdot (123.5) \cdot (1.1)}{(0.75) \cdot (0.7975) \cdot (35) \cdot (9754)} = 43.7 \text{ mm}$$

$$c = \frac{a}{\beta_1} = \frac{43.7}{0.8825} = 49.5 \text{ mm}; \quad \frac{700}{700 + f_y} = 0.636 > \frac{c}{d} = 0.412 \therefore \text{O.k.}$$

$$h_t = h - c = 141 \text{ mm}; \quad z_t = c + h_t/2 - a/2 = 97.9 \text{ mm} \rightarrow \text{Re-iterate}$$

From next iteration:

$$a = 44.3 \text{ mm}; \quad c = 50.2 \text{ mm}; \quad h_t = 140 \text{ mm}; \quad z_t = 98.0 \text{ mm}$$

Final bending moment:

$$M_t = \phi_{c,t} \cdot b \cdot h_t \cdot f_{t,bot} \cdot z_t = 0.75(9754)(140)(1.1)(98)\left(10^{-6}\right) = 110 \text{ kN-m}$$

Total moment:

$$M_r = \phi_s \cdot A_s \cdot f_y \cdot (d - a/2) + M_t = 0.9(21000)(400)(120 - 42.7/2)10^{-6} + 112 = 885 \text{ kN-m}$$

$$M_r = 885 \text{ kN-m} > M_f = 881 \text{ kN-m} \therefore \text{O.k.}$$

Spacing, Cl 8.6.2.7.4, Cl 8.14.2.1.1:

$$s_{max} = 250 \text{ mm and } s_{min} = \max\left(1.5d_b, 1.5a_g, 40\right) = 40 \text{ mm}$$

$$s = \frac{b - 2 \cdot c - n \cdot d_b}{n - 1} = \frac{9754 - 2(50) - 110(16)}{110 - 1} = 73 \text{ mm} > s_{min} = 40 \text{ mm} \therefore \text{O.k.}$$

From layer-by-layer analysis: M_u = 890 kN-m, c = 50.4 mm

D.1.2 With Hooked Steel Fibres

Assume compression zone is 35% of height (checked later):

$$h_t \approx h - 0.35 \cdot h = 0.65 \cdot (190) = 123.5 \text{ mm}$$

$$z_t \approx h_t/2 + 0.35 \cdot h/2 = 123.5\ /2 - 0.35 \cdot (190)/2 = 95 \text{ mm}$$

$$M_t = \phi_{c,t} \cdot b \cdot h_t \cdot f_{t,bot} \cdot z_t = 0.75(9754)(123.5)(2.7)(95)10^{-6} = 232 \text{ kN-m}$$

$$A_{s,req} = \frac{M_f - M_t}{\phi_s \cdot f_y \cdot 0.9 \cdot d} = \frac{881 - 232}{0.9 \cdot (400) \cdot (0.9 \cdot 120)} 10^6 = 16700 \text{ mm}^2 \rightarrow \text{Try 90-15M}$$

Recalculate the stress in concrete:

$$a = \frac{\phi_s \cdot A_s \cdot f_y}{\phi_c \cdot \alpha_1 \cdot f_c' \cdot b} = \frac{(0.9) \cdot (18000) \cdot (400) + (0.75) \cdot (9754) \cdot (123.5) \cdot (2.7)}{(0.75) \cdot (0.7975) \cdot (35) \cdot (9754)} = 43.7 \text{ mm}$$

$$c = \frac{a}{\beta_1} = \frac{43.7}{0.8825} = 49.5 \text{ mm};\ \ \frac{700}{700 + f_y} = 0.636 > \frac{c}{d} = 0.412 \therefore \text{O.k.}$$

Iterate, moment increased by tension stress block, assume resistance factor is 0.75:

$$h_t = h - c = 141 \text{ mm};\ \ z_t = c + h_t/2 - a/2 = 97.9 \text{ mm} \rightarrow \text{Iterate}$$

From next iteration:

$$a = 45.4 \text{ mm};\ \ c = 51.4 \text{ mm};\ \ h_t = 139 \text{ mm};\ \ z_t = 98.0 \text{ mm}$$

Final bending moment:

$$M_t = \phi_{c,t} \cdot b \cdot h_t \cdot f_{t,bot} \cdot z_t = 0.75 \cdot (9754) \cdot (139) \cdot (2.7) \cdot (98.0) \cdot \left(10^{-6}\right) = 268 \text{ kN-m}$$

Total moment:

$$M_r = \phi_s \cdot A_s \cdot f_y \cdot (d - a/2) + M_t = 0.9 \cdot (18000) \cdot (400) \cdot (120 - 37.0/2) 10^{-6} + 268 = 899 \text{ kN-m}$$

$$M_r = 899 \text{ kN-m} > M_f = 881 \text{ kN-m} \therefore \text{O.k.}$$

Spacing, Cl 8.6.2.7.4, Cl 8.14.2.1.1:

$$s_{max} = 250 \text{ mm and } s_{min} = \max(1.5d_b, 1.5a_g, 40) = 40 \text{ mm}$$

$$s = \frac{b - 2 \cdot c - n \cdot d_b}{n - 1} = \frac{9754 - 2 \cdot (50) - 90 \cdot (16)}{90 - 1} = 93 \text{ mm} > s_{min} = 40 \text{ mm} \therefore \text{O.k.}$$

From layer-by-layer analysis: M_u = 904 kN-m, c = 51.0 mm

D.2 Yield Moment Calculations

f_c'=35 MPa; f_y=400 MPa; d=120 mm; b=9754 mm; E_c=28511 MPa

M_f=511 kN-m

D.2.1 With Polypropylene Fibres

For polypropylene, f_{Fts} = 1.2 MPa:

From ultimate limit design, reinforcement is A_s=22000 mm^2

$$\rho = \frac{A_s}{b \cdot d} = \frac{22000}{9754(120)} = 0.0188; \; n = \frac{E_s}{E_c} = \frac{200000}{26622} = 7.51$$

Calculate force in the concrete:

$$\frac{f_c}{kd} = \frac{f_y/n}{d-kd};\ f_c = \frac{kd}{d-kd}\cdot\frac{f_y}{n}$$

$$0.5\cdot kd\cdot\left(\frac{kd}{d-kd}\right)\frac{f_y}{n}+kd\cdot f_t-\left(\rho d\cdot f_y+h\cdot f_t\right)=0\rightarrow\text{Cubic function}$$

kd=52.2 mm→Goal Seek

$$f_c = \frac{kd}{d-kd}\cdot\frac{f_y}{n} = \frac{52.2}{120\text{-}52.2}\left(\frac{400}{7.51}\right) = 40.9\text{ MPa} > f_c' = 35\text{ MPa}\rightarrow\text{Assume } f_c = 35\text{ MPa}$$

Calculate yield moment, no resistance factors:

$$M_Y = A_s\cdot f_y(d-kd)+0.5\cdot b\cdot kd\cdot f_c(2\cdot kd/3)+b\cdot(h-kd)\cdot f_t\cdot(h-kd)/2$$

$$M_Y = 21000\cdot 400\cdot(120-52.2)+0.5\cdot 9754\cdot 52.2\cdot 35\cdot\left(\frac{2\cdot 52.2}{3}\right)+9754\cdot(1.2)\frac{(190-52.2)^2}{2}$$

$$M_Y = 1018\text{ kN-m}$$

From layer-by-layer analysis: M_Y = 1037 kN-m, kd = 55.0 mm

D.2.2 With Hooked Steel Fibres

For hooked steel, f_{Fts} = 2.9 MPa

From ultimate limit design, reinforcement is A_s=18000 mm^2:

$$\rho = \frac{A_s}{b \cdot d} = \frac{18000}{9754 \cdot (120)} = 0.0188; \; n = \frac{E_s}{E_c} = \frac{200000}{26622} = 7.51$$

Calculate force in the concrete:

$$\frac{f_c}{kd} = \frac{f_y / n}{d - kd}; \; f_c = \frac{kd}{d - kd} \cdot \frac{f_y}{n}$$

$$0.5 \cdot kd \cdot \left(\frac{kd}{d - kd}\right) \cdot \frac{f_y}{n} + kd \cdot f_t - \left(\rho d \cdot f_y + h \cdot f_t\right) = 0 \rightarrow \text{Cubic function}$$

kd=53.3 mm→Goal Seek

$$f_c = \left(\frac{kd}{d - kd}\right) \cdot \frac{f_y}{n} = \frac{53.3}{120 - 53.3} \cdot \frac{400}{7.51} = 42.6 \text{ MPa} > f_c' = 35 \text{ MPa} \rightarrow \text{Assume } f_c = 35 \text{ MPa}$$

Calculate yield moment, no resistance factors:

$$M_Y = A_s \cdot f_y (d - kd) + 0.5 \cdot b \cdot kd \cdot f_c (2 \cdot kd / 3) + b \cdot (h - kd) \cdot f_t \cdot (h - kd) / 2$$

$$M_Y = 21000 \cdot 400 \cdot (120 - 52.2) + 0.5 \cdot 9754 \cdot 52.2 \cdot 35 \cdot \left(\frac{2 \cdot 52.2}{3}\right) + 9754 \cdot (2.7) \frac{(190 - 52.2)^2}{2}$$

$$M_Y = 1068 \text{ kN-m}$$

From layer-by-layer analysis: M_Y = 1099 kN-m, kd = 56.7 mm

D.3 Serviceability Checks for Stress in Steel Reinforcement

Serviceability is well below the yield moment, so check the stress in the reinforcement, assume no tension stiffening for easy computation, if it exceeds stress, then include tension stiffening

$$f_s = \frac{M}{A_s(d - 2\cdot kd/3)} = \frac{511(10^6)}{22800(120 - 2/3\cdot 52.5)} = 263 \text{ MPa} \rightarrow \text{Stress exceeded } 0.6f_y$$

D.3.1 With Polypropylene Fibres

For polypropylene, f_{Fts} = 1.2 MPa:

Assume *kd* yield load analysis, *kd* = 52.2 mm:

$$M = A_s \cdot f_y \cdot (d - 2\cdot kd/3) + b \cdot h_t \cdot f_{t,bot} \cdot z_t$$

$$z_t = (h - kd)/2 + 2 \cdot kd/3 = (190 - 52.2)/2 + 2 \cdot (52.2)/3 = 103.7 \text{ mm}$$

$$511(10^6) = 22000 \cdot f_s \cdot (120 - 2 \cdot 52.2/3) + 9754 \cdot (190 - 52.2) \cdot (1.2) \cdot 103.7$$

$$f_s = 183 \text{ MPa} = 0.46 \cdot f_y$$

Check *kd* using cubic function:

$$0.5 \cdot kd \cdot \left(\frac{kd}{d - kd}\right)\frac{f_y}{n} + kd \cdot f_t - \left(\rho d \cdot f_y + h \cdot f_t\right) = 0 \rightarrow \text{Cubic function}$$

kd = 55.1 mm→Recalculate stress in steel

$$511(10^6) = 22000 \cdot f_s \cdot (120 - 2 \cdot 55.1/3) + 9754 \cdot (190 - 55.1) \cdot (1.2) \cdot 104.2$$

$$f_s = 189 \text{ MPa} = 0.47 \cdot f_y \rightarrow \text{Close to previous guess} \therefore \text{O.k.}$$

From layer-by-layer analysis, for *M* = 511 kN-m, *kd* = 55.0 mm, e_{top} = 0.00067, f_s = 158 MPa

D.3.2 With Hooked Steel Fibres

For hooked steel, f_{Fts} = 2.9 MPa

Assume *kd* yield load analysis, *kd* = 53.3 mm:

$$M = A_s \cdot f_y \cdot (d - 2 \cdot kd/3) + b \cdot h_t \cdot f_{t,bot} \cdot z_t$$

$$z_t = (h - kd)/2 + 2 \cdot kd/3 = (190 - 53.3)/2 + 2 \cdot (53.3)/3 = 103.9 \text{ mm}$$

$$511\left(10^6\right) = 18000 \cdot f_s \cdot (120 - 2 \cdot 53.3/3) + 9754 \cdot (190 - 53.3) \cdot (1.2) \cdot 103.9$$

$$f_s = 71.9 \text{ MPa} = 0.18 \cdot f_y$$

Check *kd* using cubic function:

$$0.5 \cdot kd \cdot \left(\frac{kd}{d - kd}\right)\frac{f_y}{n} + kd \cdot f_t - \left(\rho d \cdot f_y + h \cdot f_t\right) = 0 \rightarrow \text{Cubic function}$$

kd = 66.0 mm → Recalculate stress in steel

$$511\left(10^6\right) = 18000 \cdot f_s \cdot (120 - 2 \cdot 66.0/3) + 9754 \cdot (190 - 66.0) \cdot (2.9) \cdot 106.0$$

$$f_s = 102 \text{ MPa} = 0.25 \cdot f_y \rightarrow \text{Next iteration is similar} \therefore \text{O.k.}$$

From layer-by-layer analysis, for *M* = 511 kN-m, *kd* = 66.4 mm, e_{top} = 0.00053, f_s = 85.7 MPa

D.4 Crack width check

$$w=k_b \cdot \beta_c \cdot s_{rm} \cdot \varepsilon_{sm}$$

k_b=1.0; β_c=1.7; ε_{sm}=0.00164

$$w = 1 \cdot (1.7) \cdot (0.000538) \cdot s_{rm}$$

The normal concrete equation is

$$s_{rm} = 50+0.25 \cdot k_c \cdot \frac{d_b}{\rho_c}$$

k_c assume to be 0.5 for governing case in bending

Crack width without fibres

$f_{s,SLS1}$=278 MPa; A_s=22660 mm^2→Round to 22800 mm^2

$$\rho_c=\frac{A_s}{A_{ct}} = \frac{22800}{b\cdot \min[2.5(h\text{-}d), h/6]} = \frac{22800}{9754\cdot \min[2.5(190\text{-}120), 190/6]} = 0.0738$$

$$s_{rm}=50+0.25 \cdot (0.5) \cdot \frac{16}{0.0738}=77.1 \text{ mm}$$

$$\varepsilon_{sm} = \frac{f_s}{E_s} \cdot \left[1\text{-}\left(\frac{f_w}{f_s}\right)^2\right] = \frac{278}{200000} \cdot \left[1\text{-}\left(\frac{75.7}{278}\right)^2\right] = 0.00129$$

$$w = 1 \cdot (1.7) \cdot (0.00129) \cdot (77.1) = 0.169 \text{ mm}$$

D.4.1 With Polypropylene Fibres

$$f_{s,SLS1}=198 \text{ MPa}$$

$$f_w = \frac{M_{cr}}{A_s \cdot jd} = \frac{f_{cr} \cdot I_g / y_t}{A_s(d - 2 \cdot kd/3)} = \frac{0.4 \cdot \sqrt{35} \cdot (190)^3 \cdot 9754/12}{22000 \cdot (85.2) \cdot 190/2} = 74.1 \text{ MPa}$$

$$\varepsilon_{sm} = \frac{f_s}{E_s} \cdot \left[1 - \left(\frac{f_w}{f_s}\right)^2\right] = \frac{189}{200000} \cdot \left[1 - \left(\frac{74.1}{189}\right)^2\right] = 0.000769$$

Crack spacing equation is:

$$s_{rm} = 50 + 0.25 \cdot k_c \cdot \frac{d_b}{\rho_c}$$

k_c assume to be 0.5 for governing case in bending

$$\rho_c = \frac{A_s}{A_{ct}} = \frac{22000}{b \cdot \min[2.5(h\text{-}d), h/6]} = \frac{22000}{9754 \cdot \min[2.5(190\text{-}120), 190/6]} = 0.0712$$

$$s_{rm} = 50 + 0.25 \cdot (0.5) \cdot \frac{16}{0.0712} = 78.1 \text{ mm}$$

Crack width equation is:

$$w = k_b \cdot \beta_c \cdot s_{rm} \cdot \varepsilon_{sm}$$

$$k_b = 1.0;\ \beta_c = 1.7;\ \varepsilon_{sm} = 0.000769$$

$$w = 1 \cdot (1.7) \cdot (0.000769) \cdot (78.1) = 0.106 \text{ mm} < w_{max} = 0.25 \text{ mm} \ \therefore \text{O.k.}$$

D.4.2 With Hooked Steel Fibres

$$f_{s,SLS1}=102 \text{ MPa}$$

$$f_w = \frac{M_{cr}}{A_s \cdot jd} = \frac{f_{cr} \cdot I_g / y_t}{A_s(d - 2 \cdot kd/3)} = \frac{0.4 \cdot \sqrt{35} \cdot (190)^3 \cdot 9754/12}{22000 \cdot (84.5) \cdot 190/2} = 91.4 \text{ MPa}$$

$$\varepsilon_{sm} = \frac{f_s}{E_s} \cdot \left[1 - \left(\frac{f_w}{f_s}\right)^2\right] = \frac{102}{200000} \cdot \left[1 - \left(\frac{91.4}{102}\right)^2\right] = 0.0000994$$

Crack spacing equation is:

$$s_{rm} = 50 + 0.25 \cdot k_c \cdot \frac{d_b}{\rho_c}$$

k_c assume to be 0.5 for governing case in bending:

$$\rho_c = \frac{A_s}{A_{ct}} = \frac{18000}{b \cdot \min[2.5(h-d), h/6]} = \frac{18000}{9754 \cdot \min[2.5(190\text{-}120), 190/6]} = 0.0583$$

$$s_{rm} = 50 + 0.25 \cdot (0.5) \cdot \frac{16}{0.0583} = 84.3 \text{ mm}$$

Crack width equation is:

$$w = k_b \cdot \beta_c \cdot s_{rm} \cdot \varepsilon_{sm}$$

$$k_b = 1.0;\ \beta_c = 1.7;\ \varepsilon_{sm} = 0.0000994$$

$$w = 1 \cdot (1.7) \cdot (0.0000994) \cdot (84.3) = 0.014 \text{ mm} < w_{max} = 0.25 \text{ mm} \therefore \text{O.k.}$$

D.5 Secondary Checks with Crack Width with Other Literature

First, calculate strain due to SLS 1 loading for RHRR

The *fib* code equation for crack spacing is:

$$s_m = 2\left(c+\frac{s}{10}\right)+k_1 \cdot \frac{d_b}{\rho_{eff}} \cdot \left(\frac{\varepsilon_1+\varepsilon_2}{2\varepsilon_1}\right)$$

$$\rho_{eff} = \frac{A_s}{A_{ct}} = \frac{A_s}{b\cdot(c+7.5d_b)} = \frac{2\cdot 21600}{9754\cdot(70+16\cdot 7.5)} = 0.0233$$

$$s_m = 2\left(62+\frac{50}{10}\right)+0.8 \cdot \frac{16}{0.0233} \cdot \left(\frac{\varepsilon_1}{2\cdot\varepsilon_1}\right) = 409 \text{ mm}$$

$\frac{\varepsilon_1+\varepsilon_2}{2\varepsilon_1} = 0.5$ because the SLS 1 dominates the strain in bending

$$w = 1 \cdot (1.7) \cdot (0.000538) \cdot (409) = 0.374 \text{ mm} > 0.25 \text{ mm} \therefore \text{Fail}$$

The FRC from RILEM is:

$$s_m = 50+0.25 \cdot k_1 \cdot \frac{d_b}{\rho_{eff}} \cdot \left(\frac{50}{l_f/d_f}\right) \cdot \left(\frac{\varepsilon_1+\varepsilon_2}{2 \cdot \varepsilon_1}\right)$$

Polypropylene fibres: $s_m = 50+0.25 \cdot (0.8) \cdot \frac{16}{0.0233} \cdot \left(\frac{50}{74}\right) \cdot \left(\frac{\varepsilon_1}{2 \cdot \varepsilon_1}\right) = 96.4$ mm

$$w = 1 \cdot (1.7) \cdot (0.000538) \cdot (96.4) = 0.088 \text{ mm}$$

Hooked Steel fibres: $s_m = 50+0.25 \cdot (0.8) \cdot \frac{16}{0.0233} \cdot \left(\frac{50}{50}\right)\left(\frac{\varepsilon_1}{2 \cdot \varepsilon_1}\right) = 119$ mm

$$w = 1 \cdot (1.7) \cdot (0.000538) \cdot (119) = 0.109 \text{ mm} < 0.25 \text{ mm} \therefore \text{O.k.}$$

D.6 Calculate with Axial Force

Using CSA 23.3 method with factors from CHBDC:

f_c'=35 MPa; f_y=400 MPa; d=120 mm; b=9754 mm; E_c=26622 MPa

M_f=191 kN-m; P_f=6814 kN;

α_1=0.7975; β_1=0.8825; ϕ_s=0.90; ϕ_c=0.75; Assume $\phi_{c,t}$=0.75

Normal concrete $A_s = 22800$ mm^2

$$a = \frac{\phi_s \cdot A_s \cdot f_y - P_f}{\phi_c \cdot \alpha_1 \cdot f_c' \cdot b} = \frac{0.9 \cdot (22800) \cdot (400) - 6814}{0.75 \cdot (0.7975) \cdot (35) \cdot (9754)} = 6.83 \text{ mm};\ c = \frac{a}{\beta_1} = 7.74 \text{ mm}$$

$$M_s = \phi_s \cdot A_s \cdot f_y \cdot (d - a/2) = 205.2 \text{ kN-m}$$

$$M_c = \phi_c \cdot \alpha_1 \cdot f_c' \cdot b \cdot a \cdot (h/2 - a/2)$$

$$= (0.75) \cdot (0.7975) \cdot (35) \cdot (9754) \cdot (6.83) \cdot (190/2 - 6.83/2) = 127.7 \text{ kN-m}$$

$$M_r = 205.2 + 127.7 = 333 \text{ kN-m}$$

Polypropylene FRC A_s=22000 mm^2, $f_{t,bot}$=1.2 MPa, assume initially a=8.6 mm

$$\text{Iteration 1: } a = \frac{\phi_s \cdot A_s \cdot f_y + \phi_{c,t} \cdot b \cdot h_t \cdot f_{t,bot} - P_f}{\phi_c \cdot \alpha_1 \cdot f_c' \cdot b} = 12.5 \text{ mm};\ c = 14.2 \text{ mm}$$

Iteration 2: a = 12.5 mm; c = 14.2 mm→Converges

$$h_t = h - c = (190 - 14.2) = 176 \text{ mm};\ z_t = h/2 - h_t/2 = 7.1 \text{ mm}$$

$$M_t = \phi_{c,t} \cdot b \cdot h_t \cdot f_{t,bot} \cdot z_t = 10.0 \text{ kN-m}$$

$$M_s = \phi_s \cdot A_s \cdot f_y \cdot (d - h/2) = 198 \text{ kN-m}$$

$$M_c = \phi_c \cdot \alpha_1 \cdot f_c' \cdot b \cdot a \cdot (h/2 - a/2) = 227 \text{ kN-m}$$

$$M_r = 10+198+227 = 435 \text{ kN-m}$$

Hooked steel FRC, A_s=22000 mm^2, $f_{t,bot}$=2.8 MPa, assume initially a=8.6 mm

Iteration 1: a = $\dfrac{\phi_s \cdot A_s \cdot f_y + \phi_{c,t} \cdot b \cdot h_t \cdot f_{t,bot} - P_f}{\phi_c \cdot \alpha_1 \cdot f_c' \cdot b}$ = 15.4 mm; c=17.5 mm

Iteration 2: a=15.7 mm; c=17.8 mm→Converges

$$h_t = h - c = (190 - 14.2) = 172 \text{ mm}; \; z_t = h/2 - h_t/2 = 8.8 \text{ mm}$$

$$M_t = M_t = \phi_{c,t} \cdot b \cdot h_t \cdot f_{t,bot} \cdot z_t = 31.2 \text{ kN-m}$$

$$M_s = \phi_s \cdot A_s \cdot f_y \cdot (d - h/2) = 162 \text{ kN-m}$$

$$M_c = \phi_c \cdot \alpha_1 \cdot f_c' \cdot b \cdot a \cdot (h/2 - a/2) = 278 \text{ kN-m}$$

$$M_r = 131.2+162+278 = 471 \text{ kN-m}$$

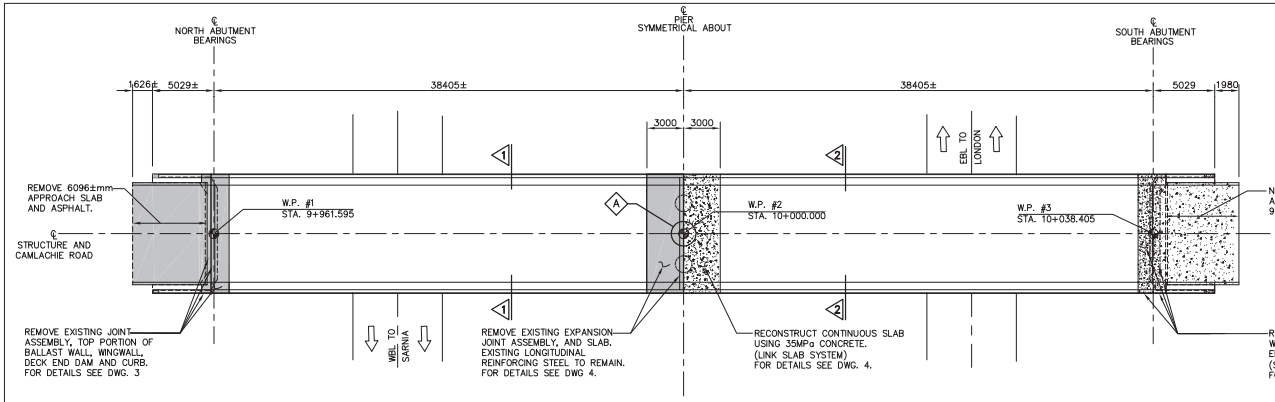

PLAN
SCALE 1 : 200

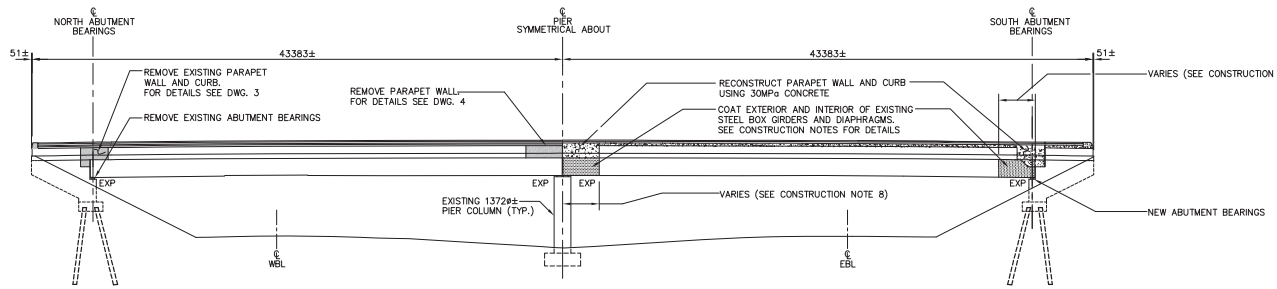

ELEVATION
SCALE 1 : 200

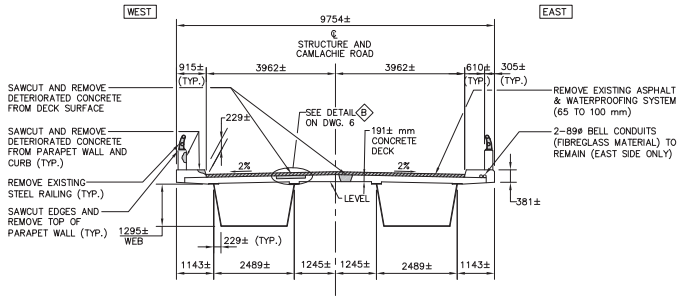

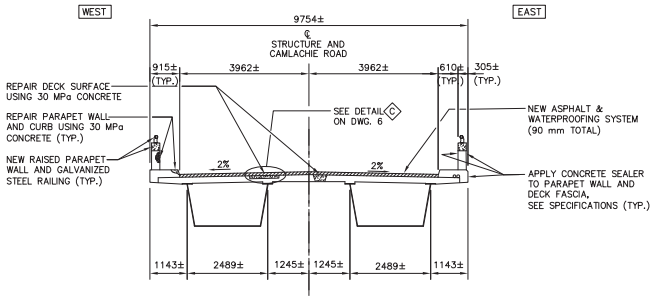

DRAWING NOT TO BE SCALED
100 mm ON ORIGINAL DRAWING

METRIC

DIMENSIONS ARE IN METRES AND/OR MILLIMETRES UNLESS OTHERWISE SHOWN

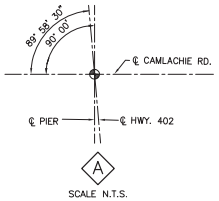

DIST. No HWY.402
CONT No XXXX-XXXX
WP No 3301-03-01

CAMLACHIE ROAD UNDERPASS

SHEET XXX

GENERAL ARRANGEMENT

DILLON CONSULTING

GENERAL NOTES

1. **CLASS OF CONCRETE**

DECK (AT PIER ONLY)	35 MPa
REMAINDER	30 MPa

2. **CLEAR COVER TO REINFORCING STEEL**

DECK	TOP	70±20 (TO MATCH EXISTING)
	BOTTOM	40±10
REMAINDER		70±20 UNLESS OTHERWISE NOTED

CONCRETE COVER ON PATCH REPAIRS SHALL REMAIN THE SAME AS EXISTING UNLESS OTHERWISE NOTED.

3. **REINFORCING STEEL**

REINFORCING STEEL SHALL BE GRADE 400 UNLESS OTHERWISE SPECIFIED.

BAR MARKS WITH THE PREFIX 'C' DENOTE COATED BARS.

UNLESS SHOWN OTHERWISE, TENSION LAP SPLICES SHALL BE CLASS 'B'.

CONSTRUCTION NOTES

1. SEE ROADWAY DRAWINGS FOR CONSTRUCTION STAGING ON HWY. 402 CAMLACHIE ROAD SHALL BE CLOSED DURING CONSTRUCTION
2. TYPICAL AREAS OF REPAIR ARE INDICATED ON DRAWINGS. WHERE REPAIR LIMITS ARE NOT SHOWN, LIMITS SHALL BE IDENTIFIED BY THE CONTRACT ADMINISTRATOR
3. THE CONTRACTOR SHALL VERIFY ALL DIMENSIONS OF THE PROPOSED WORK AND ALL DETAILS ON SITE AND REPORT ANY DISCREPANCIES TO THE CONTRACT ADMINISTRATOR BEFORE PROCEEDING WITH THE REPAIR WORK
4. THE EXISTING DECK IS WATERPROOFED WITH RUBBERIZED ASPHALT MEMBRANE
5. SAWCUTS SHALL BE 25 mm DEEP OR TO THE FIRST LAYER OF REINFORCING STEEL, WHICHEVER IS LESS
6. ALL CONCRETE SURFACES TO BE ABRASIVE BLAST CLEANED AND A BONDING AGENT SHALL BE APPLIED BEFORE CASTING NEW CONCRETE
7. ABRASIVE BLAST CLEAN ALL REINFORCING STEEL THAT IS TO BE RETAINED
8. COAT EXTERIOR OF EACH STEEL BOX GIRDER AND DIAPHRAGMS FOR 3000mm TYPICAL AT ABUTMENT AND PIER (8 LOCATIONS TOTAL). COAT INTERIOR OF EACH GIRDER AND DIAPHRAGMS FOR 10000mm TYPICAL AT ABUTMENT AND PIER (8 LOCATIONS TOTAL).
9. xxx

LIST OF DRAWINGS

1. GENERAL ARRANGEMENT
2. REMOVE AND REPAIR DETAILS I
3. REMOVE AND REPAIR DETAILS II
4. REMOVE AND REPAIR DETAILS III
5. REMOVE AND REPAIR DETAILS IV
6. REMOVE AND REPAIR DETAILS V
7. PARAPET WALL DETAILS
8. RAILING FOR PARAPET WALL
9. APPROACH SLAB
10. AS CONSTRUCTED ELEVATIONS AND DIMENSIONS

APPLICABLE STANDARD DRAWINGS

OPSD-2302.040	EMBEDDED WORK IN STRUCTURE
OPSD-3906.020	BRIDGE DECK WATERPROOFING - HOT APPLIED ASPHALT MEMBRANE WITH PROTECTION BOARD
OPSD-3906.030	BRIDGE DECK WATERPROOFING DETAILS - AT ACTIVE WIDE CRACKS (GREATER THAN 2mm) AND CONSTRUCTION JOINTS
OPSD-4010.000	GUIDE RAIL AND CHANNEL ANCHORAGE
OPSD-4601.000	LOCATION OF SITE NUMBER AND DATE FIGURE

REVISIONS

DATE	BY	DESCRIPTION

DESIGN	CTW	CHK	PLL	CODE	CHBDC 2000	LOAD	CL625ONT
DRAWN	ABH	CHK	CTW	SITE	14-348		

DATE NOV 05
DWG 1

METRIC

DIMENSIONS ARE IN METRES AND/OR MILLIMETRES UNLESS OTHERWISE SHOWN

DIST. No	HWY.402
CONT No	XXXX–XXXX
WP No	3301–03–01
CAMLACHIE ROAD UNDERPASS	SHEET XXX
REMOVE AND REPAIR DETAILS III	

DILLON CONSULTING

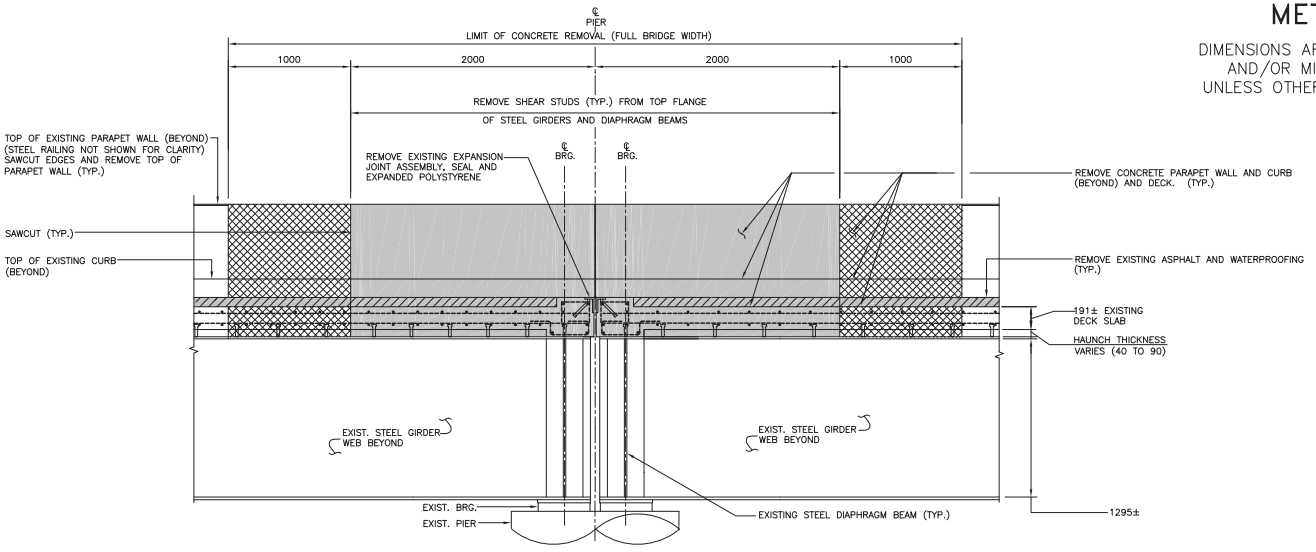

EXISTING CONDITION

4

SCALE 1 : 20

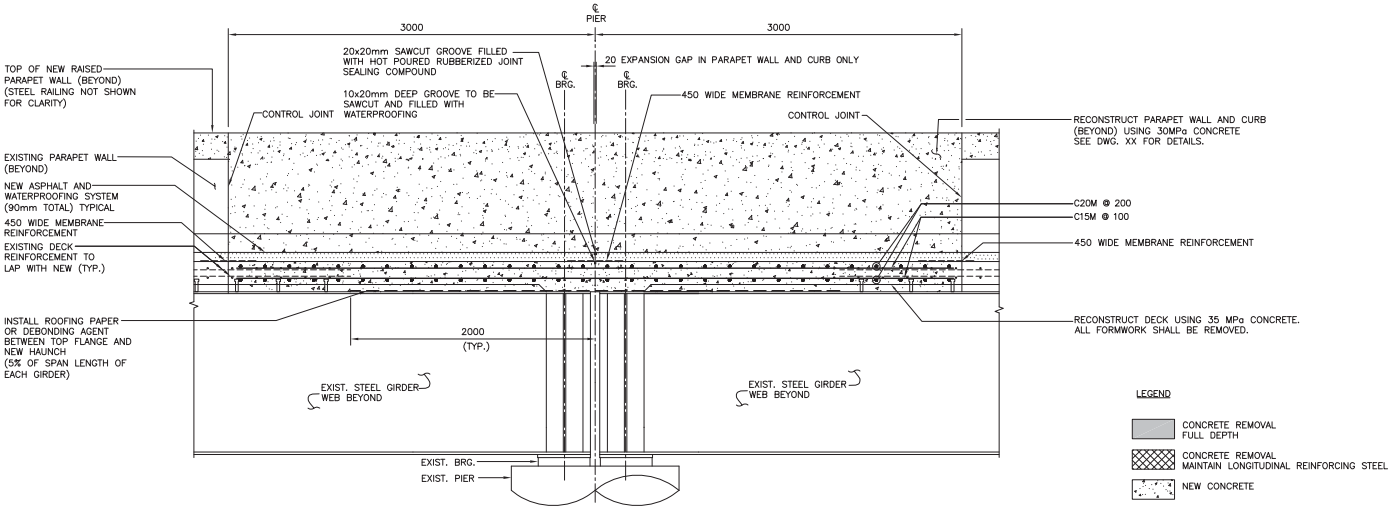

REHABILITATED CONDITION

5

SCALE 1 : 20

LEGEND

- CONCRETE REMOVAL FULL DEPTH
- CONCRETE REMOVAL MAINTAIN LONGITUDINAL REINFORCING STEEL
- NEW CONCRETE

DRAWING NOT TO BE SCALED
100 mm ON ORIGINAL DRAWING

REVISIONS		
DATE	BY	DESCRIPTION

DESIGN	PLL	CHK	BRC	CODE	CHBDC 2000	LOAD	CL625ONT
DRAWN	ABH	CHK	PLL	SITE	14–348		

DATE OCT 05
DWG 4

METRIC

DIMENSIONS ARE IN METRES AND/OR MILLIMETRES UNLESS OTHERWISE SHOWN

DIST. No	HWY.402
CONT No	2006-3029
WP No	3301-03-01
CAMLACHIE ROAD UNDERPASS	SHEET 263
REMOVE AND REPAIR DETAILS III	

DILLON CONSULTING

LICENSED PROFESSIONAL ENGINEER — CAI K. P. LOH — PROVINCE OF ONTARIO

LICENSED PROFESSIONAL ENGINEER — B.R. CRAIG — PROVINCE OF ONTARIO

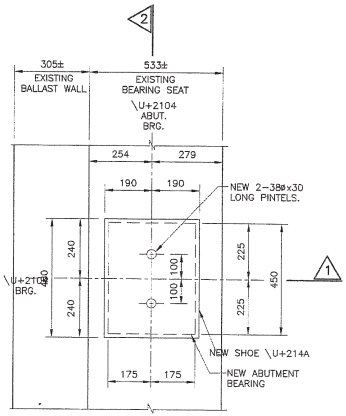

PLAN

SCALE 1:10

BEARING DETAILS

BEARING AND SHOE PLATE DATA	REQUIREMENTS AT SERVICEABILITY LIMIT STATES LOADING
	ABUTMENTS
DEAD LOAD (kN)	540
TOTAL LOAD (kN)	880
MOVEMENT (mm)	+/-17
MAXIMUM SHEAR RATE (kN / mm) @ -40°C	2.59
BEARING SIZE	450x350x110
SHOE PLATE SIZE	480x380x25
NUMBER REQUIRED	8
BEARING TYPE	LAMINATED ELASTOMERIC
NUMBER REQUIRED AT NORTH ABUTMENT	4
NUMBER REQUIRED AT SOUTH ABUTMENT	4

*THE CONTRACTOR SHALL MEASURE THE THICKNESS OF THE EXISTING BEARINGS PRIOR TO FABRICATING THE NEW BEARINGS. ANY DISCREPANCIES SHALL BE REPORTED TO THE CONTRACT ADMINISTRATOR.

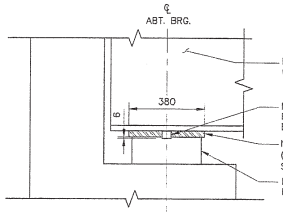

SCALE 1 : 10

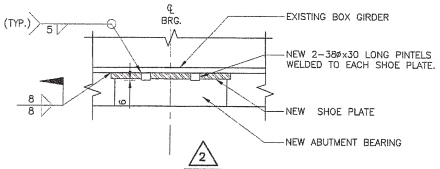

SCALE 1 : 10

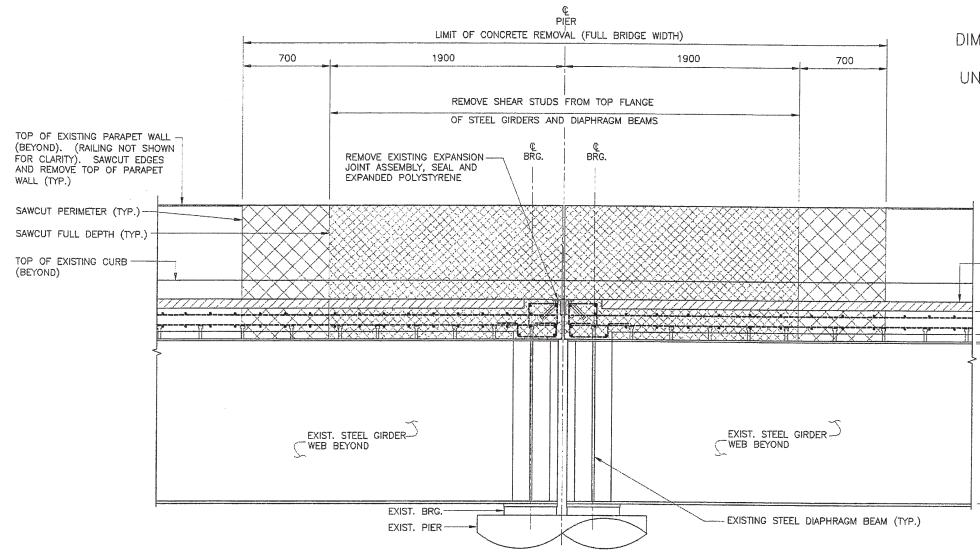

EXISTING CONDITION

4

SCALE 1 : 20

LEGEND

- CONCRETE REMOVAL FULL DEPTH
- CONCRETE REMOVAL MAINTAIN LONGITUDINAL REINFORCING STEEL
- NEW CONCRETE

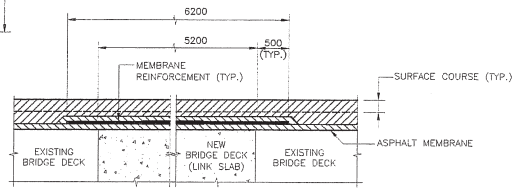

JOINT IN BRIDGE DECK

A

SCALE N.T.S.

NOTES:

1. THIS DETAIL IS TO BE READ IN CONJUNCTION WITH OPSD-3370.100
2. PROTECTION BOARD IS NOT SHOWN FOR CLARITY
3. MEMBRANE REINFORCEMENT SHALL BE SPUN BONDED SHEET STRUCTURE COMPOSED OF 100% CONTINUOUS FILAMENT POLYESTER FIBERS BONDED TOGETHER AT THEIR CROSSOVER POINTS, AS DESCRIBED IN THE SPECIFICATIONS

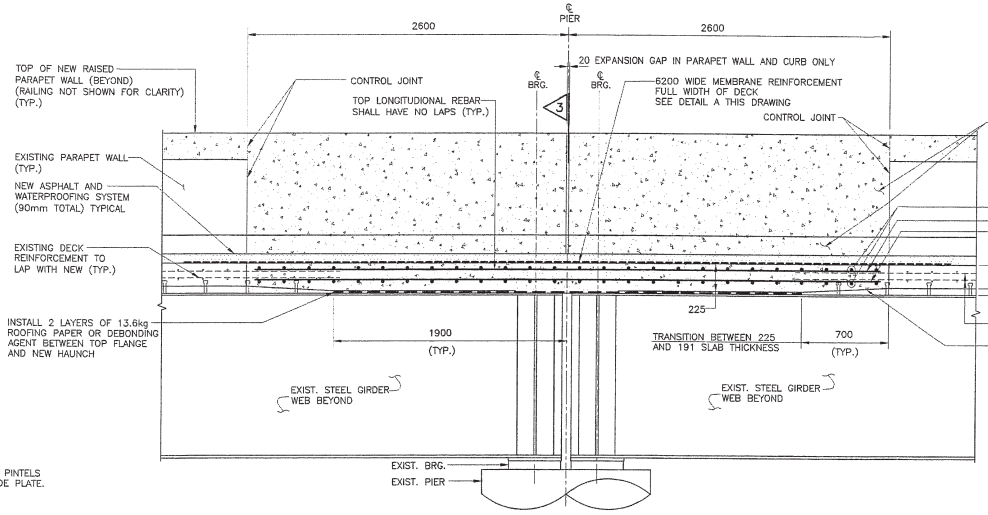

REHABILITATED CONDITION

5

SCALE 1 : 20

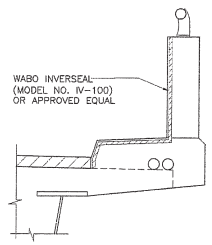

3

SCALE 1:20

DRAWING NOT TO BE SCALED
100 mm ON ORIGINAL DRAWING

REVISIONS			
	DATE	BY	DESCRIPTION
DESIGN PLL	CHK BRC	CODE CHBDC 2000	LOAD CL625ONT	DATE NOV 05
DRAWN ABH	CHK PLL	SITE 14-348		DWG 4

256